Unraveling the antioxidant protection mechanisms in the radiation resistant bacterium *Deinococcus radiodurans*

Cross-talk between Dps proteins triggers manganese distribution as a defense strategy against oxidative stress

Sandra Isabel Pereira dos Santos

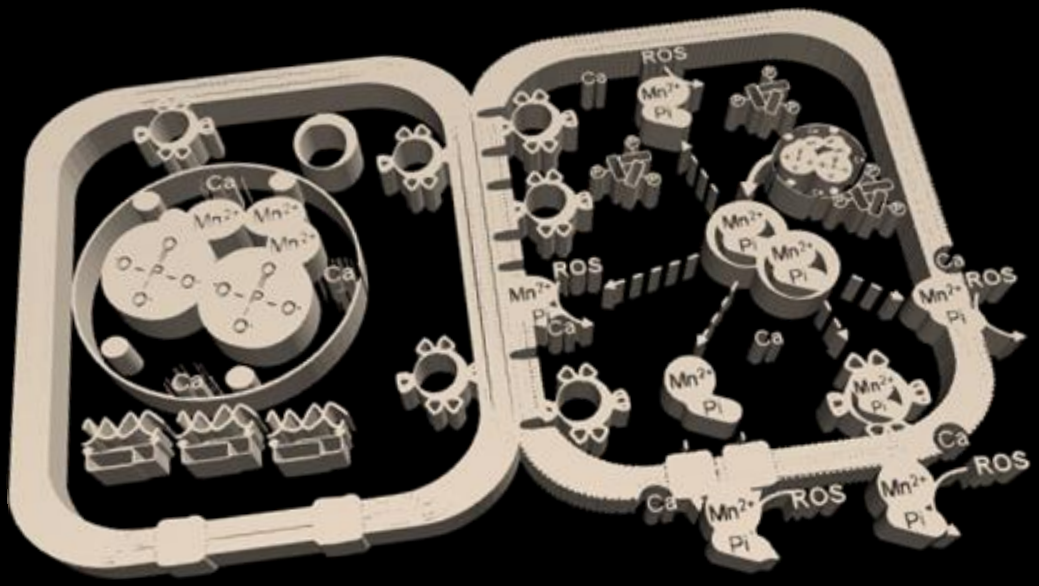

Dissertation presented to obtain the Ph.D degree in Biochemistry

Instituto de Tecnologia Química e Biológica António Xavier | Universidade Nova de Lisboa

Oeiras,
June 2017

UNIVERSIDADE NOVA DE LISBOA

Unraveling the antioxidant protection mechanisms in the radiation resistant bacterium *Deinococcus radiodurans*

Cross-talk between Dps proteins triggers manganese distribution as a defense strategy against oxidative stress

Sandra Isabel Pereira dos Santos

Supervisor: Dr. Célia V. Romão

Co-Supervisor: Prof. Miguel Teixeira

Dissertation presented to obtain the Ph.D degree in Biochemistry

Instituto de Tecnologia Química e Biológica António Xavier | Universidade Nova de Lisboa

FCT Fundação para a Ciência e a Tecnologia
MINISTÉRIO DA CIÊNCIA, TECNOLOGIA E ENSINO SUPERIOR

Oeiras, June 2017

ITQB UNIVERSIDADE NOVA DE LISBOA

Apoio financeiro da Fundação para a Ciência e Tecnologia do Programa Operacional Potential Humano do Fundo Social Europeu POPH/FSE no âmbito do quadro comunitário de apoio (Bolsa de Doutoramento SFRH/BD/78870/2011).

From left to right: Fernando Antunes, Ligia Saraiva, Miguel Castanho, Nuno Empadinhas, Sandra Santos, Miguel Teixeira, Célia Romão, Maria Arménia Carrondo.

09th June 2017

Second Edition, July 2017

Cover: Model of the protection mechanism of *D. radiodurans* against oxidative stress conditions, linking *Dr*Dps1 and *Dr*Dps2 cellular function with manganese homeostasis.

Metalloenzymes and Molecular Bioenergetics laboratory
Metalloproteins and Bioenergetics Unit
Instituto de Tecnologia Química e Biológica, António Xavier
Universidade Nova de Lisboa
Av. da República (EAN)
2780-157 Oeiras
Portugal

Thesis Outline

The present thesis entitled “Unraveling the antioxidant protection mechanisms in the radiation resistant bacterium *Deinococcus radiodurans*, cross-talk between Dps proteins triggers manganese distribution as a defense strategy against oxidative stress” is the result of research done at the Metalloenzymes and Molecular Bioenergetics, Metalloproteins and Bioenergetics Unit at the Instituto de Tecnologia Química e Biológica António Xavier from Universidade Nova de Lisboa, under the supervision of Célia Valente Romão and Professor Miguel Teixeira.

The work, realized during four years, focuses on two Dps proteins from radiation resistant organism *Deinococcus radiodurans* and is comprised of three parts. Part I is an introduction which is divided in fours chapters. Chapter I and II are a general introduction about reactive oxygen species and metals respectively, chapter III describes the organism used in this work, *Deinococcus radiodurans*, and chapter IV gives a description about *Dr*Dps family proteins. Part II shows the experimental results, and includes chapters V and VI, mainly about *in vitro* studies aiming to understand the *Dr*Dps functions, and chapter VII, mainly about *in vivo* studies showing the link between *Dr*Dps proteins and manganese, contributing for protection mechanisms observed in *D. radiodurans*. Part III is a general discussion that integrates all results obtained during the four years of Ph.D.

Acknowledgements

I would like to express my gratitude to the people that contributed to this work:

- Doctor **Célia Romão**, my supervisor, for her presence, determination and friendship. For her knowledge, critical sense and ideas supporting my all work. For her availability, 24 hours a day, to answer questions or simply just to hear me in bad and good times. For her optimism in all times, even when an experiment failed she always saw a positive side. For giving me the opportunity to grow at scientific and personal level and all the time believing in me and in my work. Thanks for everything "chefe".

- Professor **Miguel Teixeira**, my co-supervisor, for giving me the opportunity to work in his lab, developing my work. For his knowledge and fruitful discussion and advices which contributed to improve my work.

- Professor Maria Arménia Carrondo, for giving me the opportunity to attend the Structural Genomics laboratory, using available resources, especially the purification systems and materials required to obtain crystals. A special thanks for the support demonstrated during my PhD thesis.

- Isabel Abreu, Margarida Rosa and Mafalda Rodrigues, for all their support, not just during the mRNA assay performed in Proteome Regulation in Plants lab but also in the discussions about all work, a special thanks to Isabel Abreu for the long long discussion and helpful advices, mainly during the experiments realized in ID16A beam line at ESRF, and of course for providing a good working environment.

- Collaborators, for receiving me in their laboratories: Doctor Emilia Chianchone and Pierpaolo Ceci for receiving me and for their collaboration and advice on the electrophoretic mobility shift assays. Doctor Miguel Castanho and Henri Franquelim for receiving me and for their help during Atomic Force Microscopy. Doctor Adam Round for his helpful acknowledgments about Small angle scattering X-ray when receiving me at ESRF. Doctor Mariana Pinho and Helena Veiga for their advice in cell preparation support when using fluorescence microscopy. Doctor Peter Cloetens and Yang Yang for receiving me at the ID16A beamline and for their help during all fluorescence microscopy X-ray experiment.

- Doctor Lígia Saraiva and, again, Isabel Abreu, for following the work developed during these years and promoting productive discussions.

- Doctor Tiago Bandeiras, for passing his knowledge and providing support during the thermofluor work.

- Doctor Pedro Matias by critical thesis revision.

- Doctor Elin Moe, for her help in parts of my work, protein stabilization and for her availability to discuss about everything.

- To all my Metalloproteins and Bioenergetics Unit colleagues, Afonso Duarte, Ana Filipa Pinto, Ana Patrícia Refoso, Ana Paula Batista, Andreia Silva, Bruno Marreiros, Cecília Miranda, Filipa Calisto, Filipa Sena, Filipe Sousa, Joana Carrilho, João Carita, Liliana Pinto, Manuela Pereira, Miguel Ribeiro, for providing a great environment at work.

- To everyone at the Macromolecular Crystalography Unit, Ana Teresa Gonçalves, Bernardo Canico, Bruno Correia, Carlos Frazão, Colin McVey, Elin Moe, Cristiana Sousa, Dalila Fernandes, Denise Pinel, Diogo Athayde, Filipe Rollo, João Vicente, José Brito, José Silva, Karim Zuhra, Margarida Acher, Margarida Silva, Micael Freitas, Patricia Borges, Paulo Espirito Santo, Pedro Matias, Pedro Sousa, Rute Chitas, Sara Silva, Sónia Zacarias, Tiago Bandeiras, for providing a good work environment all the time.

- A special thanks to Cristiana Sousa, Dalila Fernandes, José Silva, Liliana Pinto and Patricia Borges, who became my friends in these last years, for the great conversations, great moments and camaraderie and being present in all the moments when I needed it.

- To Denise Pinel, for the long discussions about *Dr*Dps work, for “forcing” me to think about small details in all of my work and for her gaiety providing a good environment and good moments in th lab.

- A todos os meus familiares, que sempre me apoiaram neste percurso, especialmente aos meus tios, Glória Silva, João Silva, Ermelinda Medeiros, Joaquim Medeiros e Jorge Almeida, e às minha primas, Liliana Silva, Steffi Silva, Fernando Almeida e Cristiana Almeida.

- Finalmente, à minha irmã Vera Santos, pais António Figueira e Alice Santos e ao meu filho Gustavo Fonseca por todo o seu amor, carinho, compreensão e por estarem sempre presentes em todos os momentos deste meu percurso, por me darem forças suficente para continuar sempre em frente sem nunca desistir e por sempre acreditarem em mim.

Para os meus pais

Para o meu filho

Thesis publications

1. **Santos S. P**, Cuypers M. G., Round A., Finet S., Narayanan. T., Mitchell E. P., Romão C. V. (2017) SAXS structural studies of Dps from *Deinococcus radiodurans* highlights the conformation of the mobile N-terminal extensions, *J. Mol. Biol.,* 429(5), 667-687.
http://dx.doi.org/10.1016/j.jmb.2017.01.008

2. **Santos S. P.**, Mitchell E.P. Franquelim H.G. , Castanho M.A.R.B. , Abreu I.A., Romão C.V. (2015) Dps from *Deinococcus radiodurans*: oligomeric forms of Dps1 with distinct cellular functions and Dps2 involved in metal storage, *FEBS,* 282 (22), 4307-27. *J*. http://dx.doi.org/10.1111/febs.13420

One manuscript is in preparation, based on the studies in chapter VII.

3. **Santos S. P.**, Yang Y., Rosa M., Rodrigues M., . De La Tour C. B., Sommer S., Teixeira M., Carrondo Maria A., Cloetens P., Abreu I. A., and V. Romão C.V. Cross-talk between Dps in Deinococcus radiodurans triggers Mn distribution.

Other publications not included in this thesis

3. **Santos S. P.**, Marques A. T., Rosa M. G., Rodrigues M. A. A., Abreu I. A., Frazão C., Romão C. V. (2014) Expression, purification and crystallization of MnSOD from *Arabidopsis thaliana***,** Acta Cryst. F70, 669-72.
http://dx.doi.org/10.1107/S2053230X14007687.

4. Borges P. T., Miranda C. S., **Santos S. P.**, Carita J. N., Frazao C., Romão C. V. (2014) Purification, crystallization and phase determination of the DR1998 haem b catalase from *Deinococcus radiodurans***,** *Acta Cryst*. F70, 659-662.
http://dx.doi.org/10.1107/S2053230X1400764X

5. **Santos S. P.**, Bandeiras T.M., Pinto A.F., Teixeira M., Carrondo M.A., Romão C.V. (2012) Thermofluor-based optimization strategy for the stabilization and crystallization of *Campylobacter jejuni* desulforubrerythrin *Protein Expression and Purification*, 81, 193-200. http://dx.doi.org/10.1016/j.pep.2011.10.001

x

Dissertation abstract

Deinococcus radiodurans is a radiation resistant bacterium. For this reason, it has been a focus of several studies over the years. The aim has been to understand what makes this organism so resistant to different extreme conditions. Several protection mechanisms are present, such as enzymatic and non-enzymatic systems, namely Mn^{2+}-Pi complexes. These mechanisms work synergistically, thereby conferring higher protection to this extraordinary organism.

The present thesis is focused on the biochemical characterisation of the two **D**NA-binding **p**roteins from **s**tarved conditions, known as **Dps,** from ***D. radiodurans.*** This work started with studies performed under *in vitro* conditions, which were complemented with several *in vivo* experiments, establishing the function of these proteins in the cell and their role in the protection mechanism of this bacterium.

D. radiodurans contains two genes coding for two Dps: *Dr*Dps1 (*dr*2263) and *Dr*Dps2 (*dr*b0092). *Dr*Dps share a high structural homology, namely a dodecameric hollow sphere in the crystal form composed of monomeric four-helix bundles and both share the typical properties of Dps: iron storage and DNA binding and protection ability. However, the *Dr*Dps1 protein is unique for *Deinococcus* genus whilst *Dr*Dps2 has high similarity with Dps present in others genus, including organisms from Bacteria and Archaea domains.

Compared to the other family members known to date these two proteins have unique long N-terminal tails. *Dr*Dps1 has 54 amino acid residues in these tails while *Dr*Dps2 contains 42 amino acid residues. The crystal structures previously determined for *Dr*Dps lack electron density for the full or partial length of these N-terminal tails, probably due to disorder and/or flexibility. In the present work we have used a low-resolution structural approach, small angle X-ray scattering (SAXS), to determine the structural position of the N-terminal tails in solution. For the first time was shown that the N-terminal tails are flexible regions protruding from the spherical shell of both proteins.

The DNA binding ability of Dps proteins has been associated with the positively charged amino acid residues present at the N- or C-terminal tails, and the flexibility and location of these tails. In fact, both *Dr*Dps bind to DNA. *Dr*Dps1 binding occurs directly through N-terminal tails which contains seven positively charged amino acid residues, while for *Dr*Dps2 these N-terminal tails have one positively charged amino

acid residue, and are not directly involved in DNA-binding but are associated with the selection of DNA conformation type. *Dr*Dps1 binds to linear and supercoiled DNA, forming complexes with DNA looping from a central aggregate, whilst *Dr*Dps2 only binds to supercoiled DNA forming complexes with toroidal morphology.

In the iron storage process *Dr*Dps are able to oxidise iron using oxygen and hydrogen peroxide as oxidants, leading to iron incorporation in the hollow cavity of the *Dr*Dps dodecamer. The maximum capacity for *Dr*Dps1 and *Dr*Dps2 is 270 and 500 iron atoms per dodecamer, respectively. Under reducing conditions this metal is released.

The iron storage capacity coupled with the DNA binding/condensation, leads to DNA protection. For *Dr*Dps1 this occurs *via* its iron storage capacity and DNA condensation, whilst for *Dr*Dps2 this happens mostly due to its DNA-binding ability, since iron oxidation is decreased when *Dr*Dps2-DNA complexes are formed.

Since *D. radiodurans* contains a high intracellular manganese concentration that has been associated with the cell protection against oxidative damage, in this work was also demonstrated that these two proteins have the capacity to store and release this metal.

Based in our *in vitro* results, we hypothesise that these two proteins play distinct functions in the cell. In order to address if *Dr*Dps proteins are involved in iron-manganese homeostasis and in cell protection against damage promoted by oxidative stress, a multidisciplinary approach was used, centered upon gene and protein expression levels, and cellular location of the proteins and metals. This work was performed in *D. radiodurans* wild-type and in *dps* knockout mutant strains: Δ*dps1*, Δ*dps2* and Δ*dps1*Δ*dps2*, under different conditions: hydrogen peroxide, methyl viologen, iron, manganese, and manganese followed by methyl viologen.

D. radiodurans is rich in a variety of elements, including: manganese, calcium, phosphorus, zinc, potassium, iron and sulphur as shown in our X-ray fluorescence imaging results. Under control conditions it was observed that manganese, phosphorus and calcium elements are concentrated in small phosphate granules which, upon stress conditions, are re-distributed to the cytosol and membrane region. Since manganese and phosphorus elements are co-localised in the different conditions, it is suggested that they are in the form of Mn^{2+}-Pi complexes, which has been described to be involved in reactive oxygen species (ROS) detoxification, protecting the macromolecules against oxidation. Both *Dr*Dps are implicated in this

storage/re-distribution of manganese and phosphorus, from/to the phosphate granules. This mechanism is regulated by conformational changes of both *Dr*Dps. *Dr*Dps1 was detected with different oligomeric states, namely dimer and trimer. Under control conditions, *Dr*Dps1 binds as a dimer to DNA whilst under external stimulus, such as manganese or compounds that induce an oxidative stress condition to the cell, is activated a mechanism leading to conformational changes of *Dr*Dps1, to a trimeric form. This dimer-trimer conversion is regulated by post-translation phosphorylation modification. The regulation of this mechanism is proposed to be dependent upon calcium, as our X-ray fluorescence imaging results suggest. Moreover the oligomeric state change is associated with a different cellular localisation of *Dr*Dps1 from the nucleoid region to the cytosol and phosphate granules. Thus *Dr*Dps1 structural dynamic plasticity between dimer-trimer coupled with a change in its cellular localisation, leads to a regulation of the intracellular distribution of Mn^{2+}-Pi complexes.

*Dr*Dps2 contains a signal peptide suggesting a non-cytoplasmic localisation for protein. In fact this protein was localised mostly in the membrane region. However, under growth conditions submitted to an excess of manganese or oxidative stress, the protein appears in both membrane (*Dr*Dps2$_M$) and cytosol regions (*Dr*Dps2$_C$). These two forms have different molecular masses. *Dr*Dps2$_C$ has a lower molecular mass that corresponds to the protein without N-terminal tails whilst *Dr*Dps2$_M$ corresponds to the full length protein containing N-terminal tails and which is proposed to interact with the cellular membrane. These two forms are suggested to have different functions: *Dr*Dps2$_C$ is able to store Mn^{2+}-Pi complexes inside the hollow cavity and is also to be involved in the Mn^{2+}-Pi complex trafficking from and to the phosphate granules while *Dr*Dps2$_M$ protects the membrane contributing for cell division.

Furthermore, *Dr*Dps are also implicated in iron homeostasis. Under growth conditions submitted to an excess of iron, *Dr*Dps1 changes its oligomeric state from dimer to dodecamer. In that case *Dr*Dps1 acts as a typical Dps being able to store iron.

Both *Dr*Dps are dependent upon each other. *Dr*Dps1 as a trimer regulates indirectly a cytosolic *Dr*Dps2 form and the formation of *Dr*Dps1 dodecamer is dependent upon *Dr*Dps2.

To complement our studies, we analysed the enzymatic ROS scavenging system, namely catalase and manganese superoxide dismutase enzymes (MnSOD). These

enzymes have an important role mainly during the stationary phase, where the catalase activity was observed to increase and a new MnSOD isoform band activity was detected.

This work has revealed for the first time the mechanism protection from *D. radiodurans* that involves the Mn^{2+}-Pi complex regulation which plays a crucial role against oxidative stress. This regulation is orchestrated by the two *Dr*Dps, which have different functions driven by their structural changes.

The protection mechanism identified through Mn^{2+}-Pi complexes and the crosstalk between the two *Dr*Dps were the missing key components that help to understand the protection mechanism of this bacterium.

Resumo da dissertação

Deinococcus radiodurans é uma bactéria resistente a elevadas doses de radiação. Por este motivo, tem sido o foco de vários estudos ao longo dos anos. O objetivo é compreender os mecanismos de resistência desta bactéria a condições extremas. Neste organismo, estão presentes vários mecanismos de protecção, tanto enzimáticos como não enzimáticos, nomeadamente complexos na forma de Mn^{2+}-Pi. Estes mecanismos funcionam sinergicamente, assim conferindo elevada proteção a esta extraordinária bactéria.

O trabalho apresentado nesta tese centrou-se na caracterização bioquímica de duas **Dps**, denominadas como "DNA binding protein from starved conditions" de ***D. radiodurans***. Inicialmente, baseou-se em estudos realizados em condições *in vitro*, que foram depois complementados com vários ensaios em condições *in vivo*. Desta forma, foi possível determinar as funções destas proteínas na célula e o seu papel no mecanismo de proteção contra o stress oxidativo.

D. radiodurans contém dois genes que codificam para as Dps: *Dr*Dps1 (*dr2263*) e *Dr*Dps2 (*drb0092*). As *Dr*Dps possuem uma elevada homologia estrutural, nomeadamente dodecameros na forma cristalina, formando uma esfera com uma cavidade central oca, sendo cada monómero composto por um conjunto de quatro hélices-α. Pará além disso, as proteínas têm características típicas da família das Dps: capacidade de armazenar ferro e de ligar e proteger e o ADN. No entanto, a *Dr*Dps1 é única para o género *Deinococcus*, enquanto a *Dr*Dps2 tem elevada similaridade com Dps presentes em outros géneros, incluindo os domínios Bactéria e Arquea.

Comparativamente a outros membros da família das Dps conhecidos até à data, estas duas proteínas têm longos N-terminais. Nesta região, a *Dr*Dps1 tem 54 resíduos de aminoácido enquanto a *Dr*Dps2 contém 42 resíduos. Nas estruturas cristalográficas previamente determinadas, para as duas *Dr*Dps, não foi possível observar densidade electrónica para parte ou mesmo a totalidade da zona dos N-terminais, provavelmente devido a uma desordem e/ou flexibilidade destes. No presente trabalho, utilizou-se uma abordagem estrutural de baixa resolução, o espalhamento de raios-X a baixos ângulos (SAXS) para determinar a posição estrutural dos N-terminais em solução. Pela primeira vez, foi demonstrado que os N-

terminais são regiões flexíveis sobressaindo da superfície esférica de ambas as proteínas.

A capacidade de ligação das *Dr*Dps ao ADN tem sido associada com os resíduos de aminoácido carregados positivamente, presentes nas zonas dos N- ou C-terminais, bem como à flexibilidade e localização destas zonas. De facto, ambas as *Dr*Dps ligam ADN. Para a *Dr*Dps1, esta ligação ocorre diretamente com os N-terminais, que contêm sete resíduos de aminoácido carregados positivamente, enquanto para a *Dr*Dps2, os N-terminais, que apenas contêm um resíduo de aminoácido carregado positivamente, não estão directamente envolvidos na ligação ao ADN, mas sim implicados na seleção do tipo de conformação do ADN. A *Dr*Dps1 liga ADN linear e enrolado, formando complexos constituídos por um agregado central de *Dr*Dps1-ADN, na qual partes do ADN sobressaem do agregado. Por sua vez, a *Dr*Dps2 só liga ADN enrolado, ligando-se à volta deste, formando complexos *Dr*Dps2-ADN com uma morfologia toroidal.

Durante o processo de armazenamento de ferro, as *Dr*Dps enquanto dodecameros são capazes de oxidar o ferro usando oxigénio e peróxido de hidrogénio como oxidantes, levando à incorporação daquele metal na sua cavidade oca. A capacidade máxima de armazenar ferro por dodecamero é de 270 e 500 para a *Dr*Dps1 e para a *Dr*Dps2, respetivamente. O metal é libertado para o exterior quando as proteínas são submetidas a condições redutoras.

A capacidade das Dps de armazenar ferro, juntamente com a ligação/enrolamento do ADN, permite a proteção do ADN. De facto, para a *Dr*Dps1 esta proteção ocorre pela sua capacidade de armazenar ferro e ligar ADN enquanto, para a *Dr*Dps2, acontece principalmente pela sua ligação ao ADN, uma vez que a sua capacidade para oxidar ferro diminui aquando da formação dos complexos *Dr*Dps2-ADN.

Sabe-se que *D. radiodurans* contém uma elevada concentração intracelular de manganês, a qual tem sido associada à proteção celular contra os danos oxidativos, neste trabalho, foi também demonstrado que ambas as *Dr*Dps têm a capacidade de armazenar e libertar este metal.

Tendo como base os nossos resultados obtidos em condições *in vitro*, nós formulámos a hipótese de que estas duas proteínas poderiam desempenhar funções distintas na célula. De modo a perceber se as *Dr*Dps estão envolvidos na homeostase do ferro-manganês e na proteção celular contra os danos provocados pelo stress

oxidativo, foi utilizada uma abordagem multidisciplinar, centrada na análise da expressão dos genes e das proteínas e na localização celular das *Dr*Dps e dos metais. Este trabalho foi efetuado usando as estirpes de *D. radiodurans* do tipo selvagem e três deletadas nos genes que codificam para as *Dr*Dps: Δ*dps1*, Δ*dps2* e Δ*dps1Δdps2*. As diferentes estirpes foram submetidas a diversas condições: peróxido de hidrogénio, metil viologénio, manganês, ferro, e manganês seguido de metil viologénio.

D. radiodurans é rico numa variedade de elementos incluindo: manganês, cálcio, fósforo, zinco, potássio, ferro e enxofre, como demonstrado pelos nossos resultados de varrimento de fluorescência de raios-X. Em condições de controlo, observou-se que os elementos, manganês, fósforo e cálcio estão armazenados em pequenos grânulos de fosfato. Em condições de stress, estes elementos são redistribuídos para a região citosólica e da membrana. Uma vez que o manganês e o fósforo estão co-localizados nas diferentes condições, sugere-se que estejam na forma de complexos de Mn^{2+}-Pi, os quais têm sido descritos estarem envolvidos na desintoxicação de espécies reativas de oxigénio (ROS), protegendo as macromoléculas contra a oxidação. Ambas as *Dr*Dps estão implicadas neste armazenamento/redistribuição do manganês e fosfato de/para os grânulos de fosfato. Este mecanismo é regulado por alterações conformacionais de ambas as *Dr*Dps. A *Dr*Dps1 mostrou existir em diferentes estados oligoméricos, nomeadamente dímero e trímero. Em condições de controlo, a *Dr*Dps1 liga ADN, na sua forma dimérica, contudo, estímulos externos, tais como adição de manganês ou compostos que levam a uma condição de stress oxidativo para a célula, induzem uma alteração do estado oligomérico da *Dr*Dps1, de dímero para trímero. Esta conversão dímero-trímero é regulada por uma modificação pós-traducional, a fosforilação. A regulação deste mecanismo poderá ser dependente de cálcio, como é sugerido pelos nossos resultados de varrimento de fluorescência de raios-X. Além disso, a alteração do estado oligomérico está associada a uma mudança na localização celular da *Dr*Dps1, da região do nucleoide para o citosol bem como para os grânulos de fosfato. Desta forma, existe uma correlação entre a dinâmica estrutural, dímero-trímero da *Dr*Dps1, com uma mudança na sua localização celular, o que leva a uma regulação da distribuição intracelular dos complexos de Mn^{2+}-Pi.

A *Dr*Dps2 contém um sinal peptídico, sugerindo uma localização não-citosólica para a proteína. De facto, em condições controlo esta proteína foi localizada

principalmente na região da membrana. No entanto em condições de crescimento celular submetidas a excesso de manganês ou stress oxidativo, a proteína aparece tanto na região da membrana (*Dr*Dps2$_M$) como citosólica (*Dr*Dps2$_C$). Estas duas formas apresentam diferentes massas moleculares: a *Dr*Dps2$_C$ tem uma massa molecular inferior, correspondendo à proteína sem os N-terminais, enquanto que a *Dr*Dps2$_{M,}$ com uma massa molecular superior, corresponde à proteína completa, contendo os N-terminais, os quais são propostos servir como âncoras para a membrana celular. A existência destas duas formas para a *Dr*Dps2 sugere que esta proteína desempenha diferentes funções. A *Dr*Dps2$_C$ é capaz de armazenar os complexos de Mn^{2+}-Pi dentro da cavidade oca e posteriormente estar envolvida na sua distribuição de/para os grânulos de fosfato, ao passo que a *Dr*Dps2$_M$ protege a membrana, ajudando na divisão celular.

Para além das funções supracitadas, a associação de ambas as *Dr*Dps à homeostase do ferro também foi estudada. Em condições de crescimento celular com excesso de ferro, a *Dr*Dps1 altera o seu estado oligomérico de dímero para dodecamero. Neste caso, a *Dr*Dps1 funciona como uma típica Dps, sendo capaz de armazenar ferro.

Ambas as *Dr*Dps são dependentes uma da outra. A *Dr*Dps1 na sua forma trimérica indiretamente regula a forma citosólica da *Dr*Dps2, enquanto a formação do dodecamero da *Dr*Dps1 é dependente da *Dr*Dps2.

Este estudo foi complementado com uma análise do sistema enzimático de desintoxicação de ROS, designadamente, as catalases e as superóxido dismutases de manganês (MnSOD). Estas enzimas mostraram ser fundamentais na fase estacionária do crescimento de *D. radiodurans*, uma vez que a atividade catalase aumentou nesta fase e uma nova banda com atividade MnSOD foi detetada.

Este trabalho revelou, pela primeira vez, que o mecanismo de proteção de *D. radiodurans* envolve a regulação dos complexos de Mn^{2+}-Pi, desempenhando um papel crucial contra o stress oxidativo. Esta regulação é controlada pelas duas *Dr*Dps, que mostraram diferentes funções, impulsionadas pelas suas alterações estruturais.

A identificação do mecanismo de proteção contra os danos oxidativos, através dos complexos de Mn^{2+}-Pi e a intercomunicação entre as duas *Dr*Dps, eram os pontos chave em falta, para a compreensão dos mecanismos de proteção desta bactéria.

Abbreviations

AbDps	Polyclonal antibodies against Dps
AFM	Atomic force microscopy
APBS	Adaptive Poisson-Boltzmann Solver
ATP	Adenosine triphosphate
ATPase	Adenosine triphosphatase
BER	Base excision repair system
Bfr	Bacterioferritins
CAT	Catalase
CP	Cetylpyridinium chloride
Ctr	Control
DAG	Diacylglycerol
D_{max}	Maximal particle size
DMSO	Dimethyl sulfoxide
DNA	Deoxyribonucleic acid
Dps	DNA-binding proteins from starved cells
Dr	*Deinococcus radiodurans*
DSBs	Double-strand breaks
EMPO	2-ethoxycarbonyl-2-methyl-3,4-dihydro-2H-pyrrole-1-oxide
EMSA	Electrophoretic mobility shift assay
EPR	Electron paramagnetic resonance
ER	Endoplasmic reticulum
ETRC	Electron transfer respiratory chain
FDPs	Flavodiiron proteins
FMN	Flavin mononucleotide
Ftn	Classical ferritins
GBS	Guillain–Barré syndrome
GPCR	G protein-coupled receptors
GTP	Guanosine-5'-triphosphate
HAA	Amino acid hydrolase
HO^-	Hydroxide ion
Hpi	Hexagonally Packed Intermediate protein
$h\nu$	Energy absorption
ICP-AES	Inductively coupled plasma atomic emission spectroscopy
IP_3	Inositol trisphosphate
IPTG	Isopropyl β-D-1-thiogalactopyranoside
kGy	Kilogray
mntE	Manganese efflux pump
mntH	Manganese transporter
MOPS	3-(N-morpholino) propansulfonic acid
M-Pi	Divalent ions phosphate complex
Mrg	Metalloregulation DNA-binding stress protein
Mv	N,N´-dimethyl-4,4´-bipyridinium dichloride (Methyl viologen)
ggNAD	Nicotinamide adenine dinucleotide
Nap	Neutrophil activating protein
NER	Nucleotide excision repair system
Nramp	Natural resistance-associated macrophage protein
NSD	Normalized Spatial Discrepancy
O_2R	Oxygen reductases
P(r)	Pair distance distribution function
PAGE	Polyacrylamide gel electrophoresis
PDB	Protein Data Bank
PIP_2	Phosphatidylinositol 4, 5 bisphosphate
Pit	Low affinity phosphate inorganic transporter
PKC	Activate protein kinase C
PLC	Phospholipase C
PMSF	Phenylmethylsulfonyl fluoride
polyP	Polyphosphate
PPase	Inorganic pyrophosphatase
PPi	Pyrophosphate
PPK	Polyphosphate kinase
PPX	Exopolyphosphatase
PS	Phosphatidylserine
Pst	High affinity phosphate specific transporter
PVDF	Polyvinylidene fluoride membrane
Pxd	Peroxidase
Rbr	Rubrerythrin
Rec	Recombinase protein
R_f	Goodness of fit of simulated data versus experimental data
R_g	Radius of gyration
RNA	Ribonucleic acid
ROS	Reactive oxygen species
SAXS	Small angle X-ray scattering
SDS-PAGE	Sodium dodecyl sulfate- Polyacrylamide gel electrophoresis
SEC	Size exclusion chromatography
SLH	Surface layer homology motif
SlpA	S-Layer Protein A
SOD	Superoxide dismutase
SOR	Superoxide reductase
SSBs	Single-strand breaks
TEV	Tobacco Etch Virus
TpF1	Antigen growth factor
UV	Ultraviolet
UVDE	UV damage endonuclease pathway
UvrABC	Classical nucleotide excision repair system
V	Volts
V-H^+- PPase	Vacuolar H^+-pyrophosphatase

Table of contents

Part I – General Introduction

Chapter I

Chapter II

Chapter III

Chapter IV

Part II – Experimental results

Chapter V

Chapter VI

Chapter VII

Part III – General Discussion and conclusion

Chapter VIII

Part I

General Introduction

CHAPTER I

Reactive oxygen species

1.1 ROS formation

All aerobic organisms are surrounded by oxygen and as a consequence reactive oxygen species (ROS) can be generated. The production of these molecules can occur as indispensable intermediates in a diversity of normal biochemical reactions having vital roles, such as cell signaling (*1-4*). However, when their concentration increases above a threshold level exceeding the capacity of the cell defense mechanisms, ROS become toxic leading to the general phenomenon known as oxidative stress (*5-7*).

The electronic structure of the oxygen molecule, with two unpaired electrons with parallel spins in the antibonding molecular orbitals ($\pi^*_{y,z}$) results in a triplet ground state and restricts its reactivity (*8-9*). ROS are chemically reactive molecules containing oxygen including free radicals, namely superoxide anion radical ($O_2^{\bullet -}$), hydroxyl radical ($HO^{\bullet}$), peroxyl radical ($ROO^{\bullet}$), and the non-radical molecules hydrogen peroxide (H_2O_2), and singlet oxygen ($^1O_2$) (Fig. 1.1) (*1, 7-8, 10*).

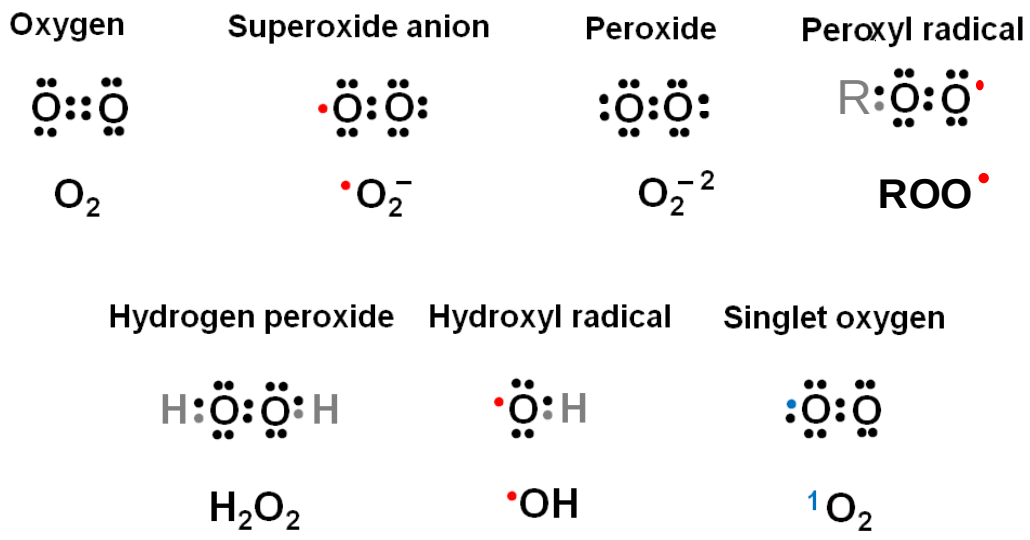

Figure 1.1 - Electronic structures of reactive oxygen species. The names and chemical formulas for each structure are presented. Red dots represent an unpaired electron, and blue dots represent an electron that jumped from one orbital to another. Adapted from Lee *et al.* and Imlay, 2003 (*8, 11*).

The formation of ROS from O_2 can occur by sequential reduction of oxygen through the addition of electrons, which leads to the formation of superoxide anion, hydrogen peroxide, and hydroxyl radical (Reaction 1.1) (*7, 9*). The major source of ROS formation in aerobic cells comes from electron transfer in respiratory chain complexes. In that case, ROS can be formed during normal cellular respiration metabolism, under physiological conditions and neutral pH (*12*).

Reaction 1.1

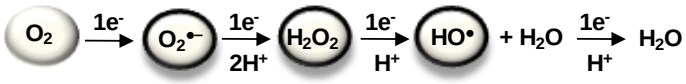

Reduction of O_2 to H_2O

Reaction 1.2

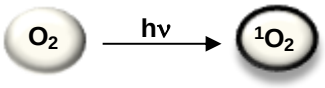

Reaction 1.3

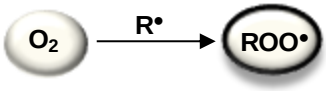

Reduction of O_2 to singlet oxygen and peroxyl radical

Singlet oxygen ($^1O_2$) is an excited form of oxygen in which the absorbed energy ($h\nu$) is enough to invert the spin of one of the unpaired electrons, and then this electron jumps to another orbital (Reaction 1.2) (*8, 13*).

Peroxyl radical ($ROO^{\bullet}$) can be formed when O_2 reacts with an alkyl radical ($R^{\bullet}$) (Reaction 1.3) (*8*). This alkyl radical can be formed when cells are subjected, for example, to ionizing radiation, (Chapter III).

1.2 ROS and their chemical targets

ROS lead to diverse reversible or irreversible redox modifications on all types of biomolecules, such as proteins, lipids, carbohydrates, DNA and RNA. However, ROS have different chemical reactivities, damaging specific biomolecules (Fig. 1.2) (*1, 9*).

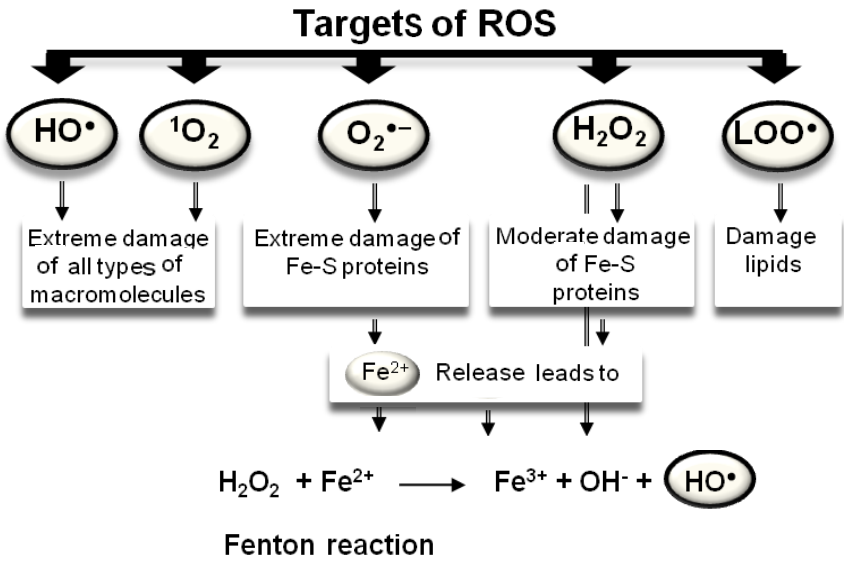

Figure 1.2 - Reactive oxygen species and most known cellular targets (*4, 14-15*).

1.2.1 Hydroxyl radical

The hydroxyl radical is the most reactive oxygen species, with a short half-life of approximately 10 nanoseconds (ns). This radical oxidizes and damages indiscriminately all biomolecules: DNA, RNA, proteins, and lipids (Fig. 1.2). Due to its short lifetime this radical damages the molecules near by where it is being formed and there are no detoxification enzymes known to date (*1, 16*).

1.2.2 Superoxide anion

The superoxide anion is a moderately reactive ROS with a half-life approximately of 1 microsecond (µs) (*15*). In aqueous solution, these species can act as a reducing or oxidizing agent. As a reductant, it can reduce hemes in cytochromes or Cu^{2+} in copper proteins while, as an oxidant it can oxidize enzymes containing iron sulfur clusters (Fig. 1.2), such as aconitase or fumarase (*11, 15, 17*).

1.2.3 Hydrogen peroxide

The hydrogen peroxide does not have unpaired electrons (Fig. 1.1), its reactivity being basically dependent on its low energy bonds (H-OOH, 376 kJ/mol; HO-OH, 213 kJ/mol) when compared with the bond energies of O_2 or $O_2^{\bullet-}$ (493 and 393 kJ/mol, respectively) (*18*). Due to its solubility in lipids, it can cross the cell membrane and penetrate in the cell causing oxidative damage in thiol groups, such as cysteine (-SH) or methionine (-SCH_3) amino acids present in different proteins generating sulfenic acid or even sulfinic and sulfonic acid adducts in proteins (*19-20*). It is also a general oxidant for most metalloproteins (Fig. 1.2) (*14*).

Both hydrogen peroxide and the superoxide anion may participate in some reactions that will generate the most reactive oxygen species, $HO^{\bullet}$, by Fenton (Reaction 1.4) and Haber-Weiss reactions (Reaction 1.5). The Fenton reaction can be potentiated when both hydrogen peroxide and superoxide anion damage proteins with iron sulfur clusters. This damage leads to Fe^{2+} release, which reduces H_2O_2 thereby generating the hydroxyl radical (Fig. 1.2) (*1, 9, 15*). Moreover, in the presence of $O_2^{\bullet-}$ Fe^{3+} can be reduced to Fe^{2+} (Reaction 1.5). The combination of these two reactions (1.4 and 1.5) gives the Haber-Weiss reaction (Reaction 1.6). This reaction generates hydroxyl radicals from hydrogen peroxide and superoxide anion catalyzed by iron (*21-22*).

Reaction 1.4 $Fe^{2+} + H_2O_2 \longrightarrow Fe^{3+} + HO^{\bullet} + HO^-$

Fenton reaction

Reaction 1.5 $Fe^{3+} + O_2^{\bullet-} \longrightarrow Fe^{2+} + O_2$

Reaction 1.6 $H_2O_2 + O_2^{\bullet-} \longrightarrow O_2 + HO^{\bullet} + HO^-$

Haber-Weiss reaction

1.2.4 Singlet oxygen

The singlet oxygen has a half-life of approximately of 4 μs in water and 100 μs in a nonpolar environment. It is quite reactive, oxidizing mainly proteins but also lipids, RNA and DNA (Fig. 1.2). It has been observed that when singlet oxygen reacts with proteins, hydrogen peroxide is formed as a byproduct (*15*).

It was demonstrated that tryptophan is the most damaged amino acid residue by the action of singlet oxygen. However, tyrosine, histidine, cysteine, and methionine are also affected, leading to protein carbonyls (common marker for protein oxidation) (*13*).

1.2.5 Peroxyl radical

The peroxyl radical is a highly reactive radical that can be involved in lipid peroxidation. However, the formation of this radical is proceeded by a lipid radical formation ($L^{\bullet}$) that in the presence of oxygen leads to the production of lipid peroxyl radical ($LOO^{\bullet}$) (Reaction 1.7). This radical can interact with a new lipid, forming the lipid hydroperoxide (LOOH) and a second lipid radical (*4, 8*).

Reaction 1.7

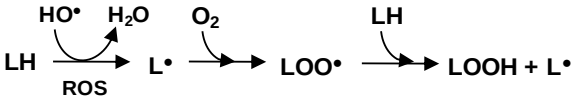

Lipid peroxidation

1.3 ROS Scavengers

Bacteria have mechanisms to directly reduce dioxygen to water (Fig. 1.3). Respiratory oxygen reductases (O_2R) and flavodiiron proteins (FDPs) are two enzymatic systems which reduce dioxygen to water without ROS formation (*23*). However, under certain conditions ROS can be generated, and systems involved in its detoxification can be divided in enzymatic or non-enzymatic.

The superoxide anion can be dismutated into hydrogen peroxide and oxygen by superoxide dismutase enzyme (SOD, Chapter II) or reduced to hydrogen peroxide by superoxide reductase (SOR). The hydrogen peroxide can be converted into water

and oxygen by catalase (Kat) (Chapter II) or reduced to water by rubrerythrin (Rbr) and peroxidase (Pxd) (Fig. 1.3) (*24*).

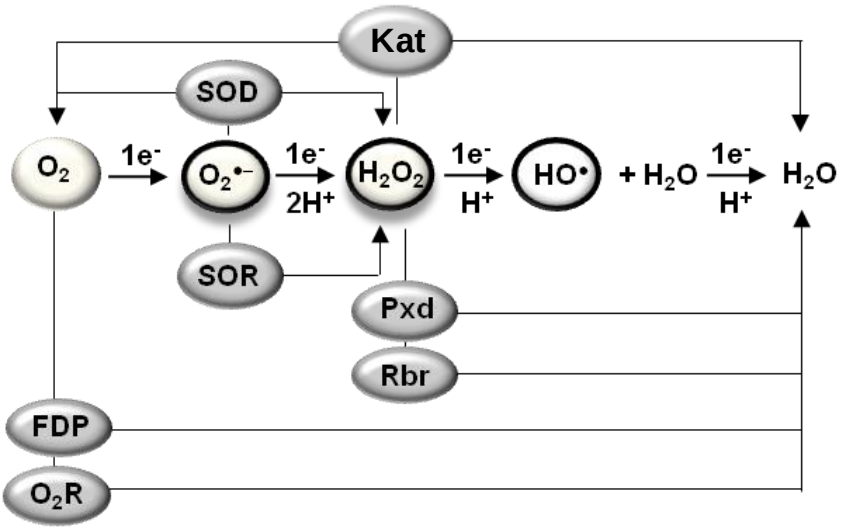

Figure 1.3 - Enzymatic systems involved in the reduction of oxygen and in the detoxification of ROS. O_2R - Oxygen reductase; FDP - Flavodiiron protein; SOR - Superoxide reductase; SOD - Superoxide dismutase; Kat - Catalase; Pxd - Peroxidase; Rbr - Rubrerythrin. Figure adapted from Romão *et al.* 2016 (*23*).

The low molecular weight non-protein thiol glutathione is an excellent example for the non-enzymatic systems which can react with ROS (superoxide anion, hydrogen peroxide and hydroxyl radical) with the capacity to scavenge these species (*15, 25*). Tocopherols and carotenoids (Chapter III) are lipophilic antioxidants which can be present in the membrane and prevent lipidic peroxidation by quenching the $^1O_2$ and thus protecting all membrane components (*15, 25*). Polyphosphates have also been observed to protect the cell, forming small complexes, for instance with manganese, that have the ability to scavenge ROS. This will be further discussed in chapter II (*26*).

In summary, these enzymatic and non-enzymatic systems can act synergistically to protect the cell from degradation promoted by ROS.

CHAPTER II

Metals in biology

2.1 Metals in biological systems

The elements that are most abundant in the Earth´s crust (Fig. 2.1, blue colour) are essential elements in living systems (Fig. 2.1, pink colour), with few exceptions, such as silicon and aluminum. In addition to the abundance, the availability and functional efficiency of the different elements also contribute to the element selection by organisms (*22, 27-28*).

The most abundant elements present in organisms are hydrogen, oxygen, carbon and nitrogen. The human body is 99 % constituted by these elements. However these elements by themselves do not enable life and the inclusion of inorganic elements, such as metals, is vital (*22*).

In fact, it has been observed that several metals are essential for the growth and development of cells, thus serving as micronutrients, and are essential for multiple metabolic pathways (Fig. 2.1, pink colour). Each metal has distinct chemical features that can be implicated in different physiological roles (*22, 27-30*).

Sodium (Na) and potassium (K) are essential alkali metals, which belong to Group 1 of the periodic table. They have in common an outer *s*-electron shell which is not fully occupied; therefore the electron can be easily lost leading to a +1 oxidation state (Table 2.1) (*22, 27, 31*).

Magnesium (Mg) and calcium (Ca) are essential alkaline earth metals from the Group 2 of the periodic table. These elements share an outer *s*-electron shell fully occupied, forming cations with charge +2 (Table 2.1) (*22, 27, 31*).

The majority of transition metals that are essential belong to period 4 of the periodic table, with exception of molybdenum and tungsten (Fig. 2.1, represented in pink colour). Due to incomplete *d*-orbitals, these elements can form cations with charges that can vary between +1 and +7 (Table 2.1). However, in biological systems the oxidation states of +2 and +3 are the most common (*22, 27, 31*). Zinc is an exception, since it contains only one stable oxidation state (+2) and acts mainly as a structural element and as a Lewis acid in catalysis (Table 2.1) (*22, 27*).

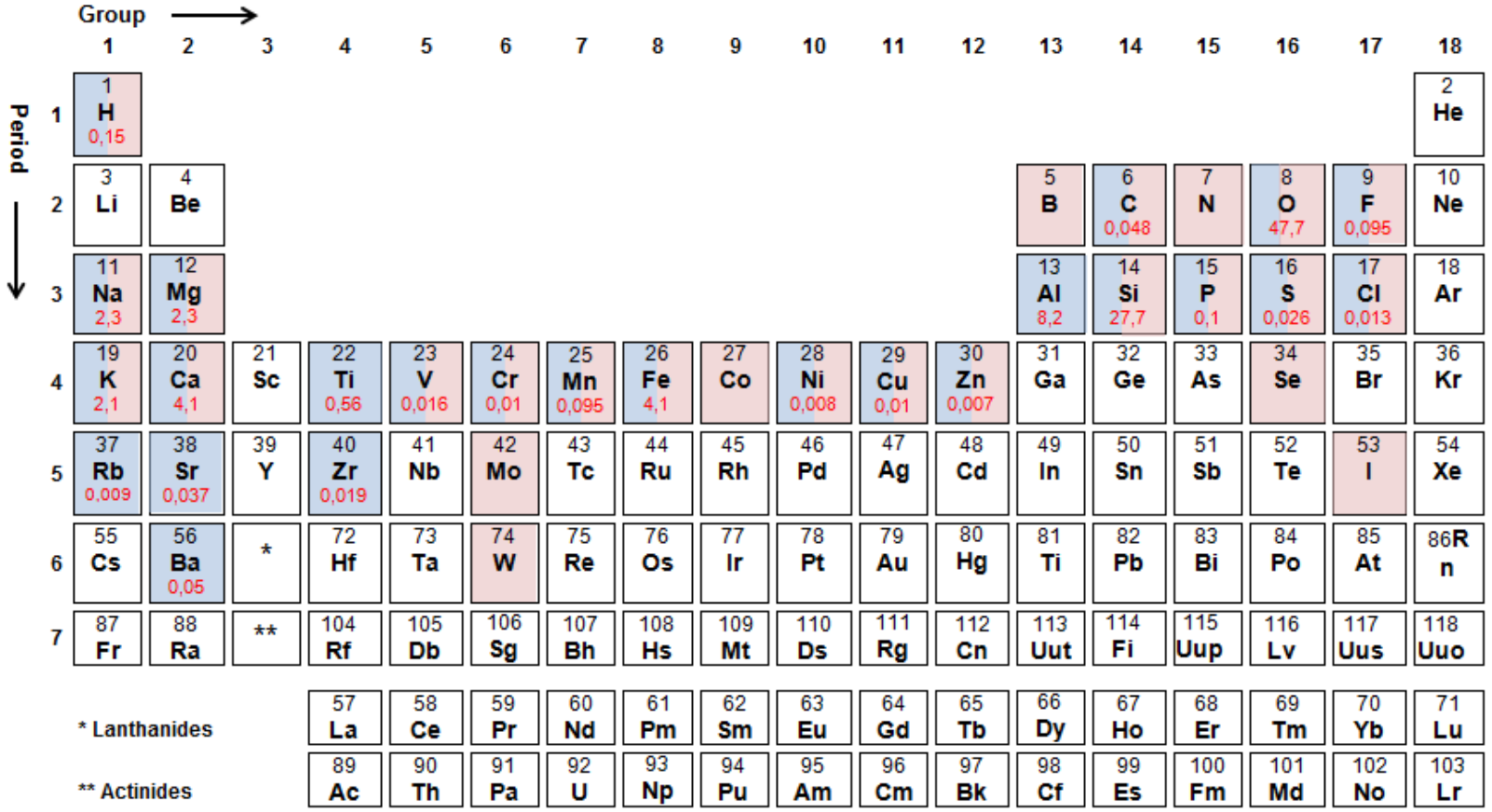

Figure 2.1 - Periodic table. Blue colour represents the most abundant elements in Earth´s crust (The abundance is shown in percentage by mass – red colour values) and pink colour represents the most essential elements for biological metabolism (*27*).

able 2.1 - Chemical properties of the most essential metals for organisms (*27*).

	Alkali metals	Alkaline earth metals	Transition metals	
Metal ions	Na, K	Mg, Ca	Mn**, Fe, Co, Cu, Mo	Zn
Valence electron configuration	$3s^1$; $4s^1$	$3s^2$; $4s^2$	$4s^23d^5$; $4s^23d^6$; $4s^23d^7$; $4s^13d^{10}$; $5s^14d^5$	$4s^23d^{10}$
Most common oxidation state	+1	+2	Variable	+2
Complex stability	Weak	Moderate	Strong	Moderate
Mobility	High	Intermediate	Low	Intermediate
Donor atoms*	O	O	N,O,S	N,O,S
Coordination number *	6 (Na) 8 (K)	6	4-6	4-6

* Most common, **Mn is not coordinated by sulfur atoms

2.2 Essentiality and toxicity

All the essential metals are indispensable for the cell metabolism. However, the intracellular concentration of these metals has to be controlled in order to maintain cell viability.

Cells can have physiological and metabolic modifications at a low level of metals. However, after addition of essential metals to the medium, the cell recovers. On the other hand, at high concentration these essential metals become toxic, leading to the disruption of biological functions and lethal effects (*27, 32*). In addition, other metals such as silver, cadmium, gold, or aluminum, that have no biological role, are potentially toxic to organisms. Their toxicity is related to their capacity to bind at specific sites for essential metals, disrupting protein function (*27, 32-33*).

The requirement of metals is not homogenous for all organisms and each organism has a need for specific metals at different levels (*29-30, 34*). This difference

can be related with environmental conditions (that can contain different essential or toxic metals) and in that case the organism has the capacity to adapt to these conditions, controlling the uptake or efflux of different metals (*33, 35*).

The present chapter is mainly focused on metals that are essential for *Deinococcus radiodurans*, such as potassium, calcium, zinc, iron and manganese.

2.3 Sodium and potassium

Sodium (Na) is the 11th and potassium (K) is the 19th chemical element belonging to the 1st group and 3rd or 4th periods respectively (Fig. 2.1). These two elements bind weakly to biomolecules, thus having a particular higher mobility in cell (Table 2.1).

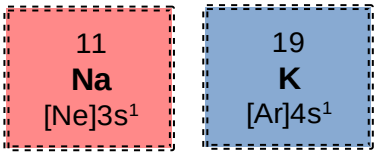

These two elements form complexes coordinated by oxygen when bound to biomolecules, but potassium can have a higher coordination number (up to 8) than sodium (up to 6) (Table 2.1), since potassium has a higher ionic radius (*27*). Both metals contribute to the regulation of osmotic pressure, to guarantee the electroneutrality of compartments, and to establish membrane potentials (*22, 27*).

In general, organisms have the tendency to perform the efflux of sodium and the uptake of potassium in cells. The passage of these metals through the membrane occurs at specific sites, such as channels (Fig. 2.2, A,B), pumps (Fig. 2.2, C) and exchangers known as antiporters (Fig. 2.2, D) (*22, 27*). For example, the Na^+/K^+-ATPase (sodium-potassium adenosine triphosphatase, also known as Na^+/K^+ pump) is an enzyme found in the plasma membrane of cells which pumps sodium out and potassium into the cell, both against their concentration gradients, using energy from ATP (Fig. 2.2, C) (*22, 36*).

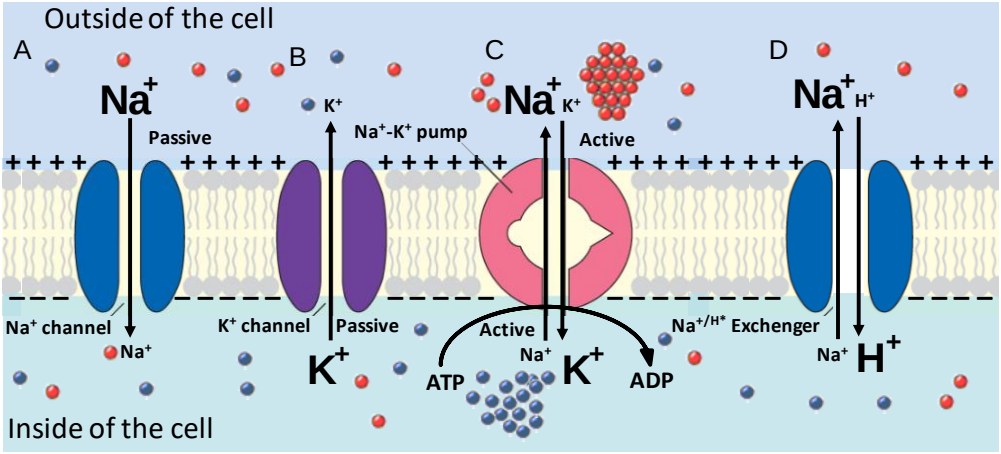

Figure 2.2 - Schematic representation of passive and active fluxes of potassium and sodium. **(A, B)** Na^+ and K^+ channels; **(C)** Na^+-K^+ pump; **(D)** Na^+/H^+ exchanger. Adapted from Epstein 2003 (*37*).

Potassium is also vital for phosphate uptake in the cell. In *E. coli* it was observed that in absence of potassium in the medium, the bacteria did not present the capacity for phosphate uptake (*38*). The inverse, it was also observed, meaning that the uptake of potassium is dependent on phosphate. *E. coli* mutants impaired in phosphate accumulation demonstrated to have a low potassium concentration inside the cell (*39*). These results showed that the uptake of potassium and phosphate are dependent on each other.

2.4 Calcium as a signaling ion

Calcium (Ca) is the 20th chemical element belonging to the 2th group, 4th period (Fig. 2.1). Calcium form complexes coordinated by oxygen when bound to biomolecules with 6 coordination number. This metal has higher binding constants than alkali metals such as Na and K, but lower than transition metals (Table 2.1) (*27, 31*). These properties confer to this metal the ability to function as a protein cofactor and is essential as a structural or catalytic element (*40-41*). For example, calcium is vital to maintain the structure of

20
Ca
[Ar]4s^2

serine proteases (*40*), but has also been recognized as an intracellular signaling messenger.

It has been demonstrated in Eukaryotic organisms that the intracellular calcium concentration is very low (10^{-7} M), thus preventing the precipitation of phosphorylated or carboxylated calcium complexes, many of which are insoluble (*22, 42-43*). The intracellular calcium levels can be controlled by calcium efflux from the cytosol to the extracellular space, where the concentration can reach 10^{-3} M. The low intracellular calcium concentration in the cytosol can also be controlled by its accumulation in intracellular Ca^{2+} stores, like the endoplasmic reticulum (ER), mitochondria, Golgi vesicles or even endosomes, lysosomes and secretory granules. In these compartments calcium concentration can vary from µM to mM, similar to the calcium concentration found in the extracellular space (Fig. 2.3). These differences in calcium concentration generate a concentration gradient, which is tightly controlled by the presence of pumps and exchangers present in the membranes that allow the flux of this metal. Calcium efflux to the extracellular side occurs by ATP-dependent calcium pumps (Fig. 2.3, step 1) and Ca^{2+}/Na^{+}-exchangers (Fig. 2.3, step 2). Calcium influx to ER and Golgi occurs *via* ATPase pumps (Fig. 2.3, step 4), while the influx to mitochondria involves calcium channels (Fig. 2.3, step 5) (*22, 27, 44*).

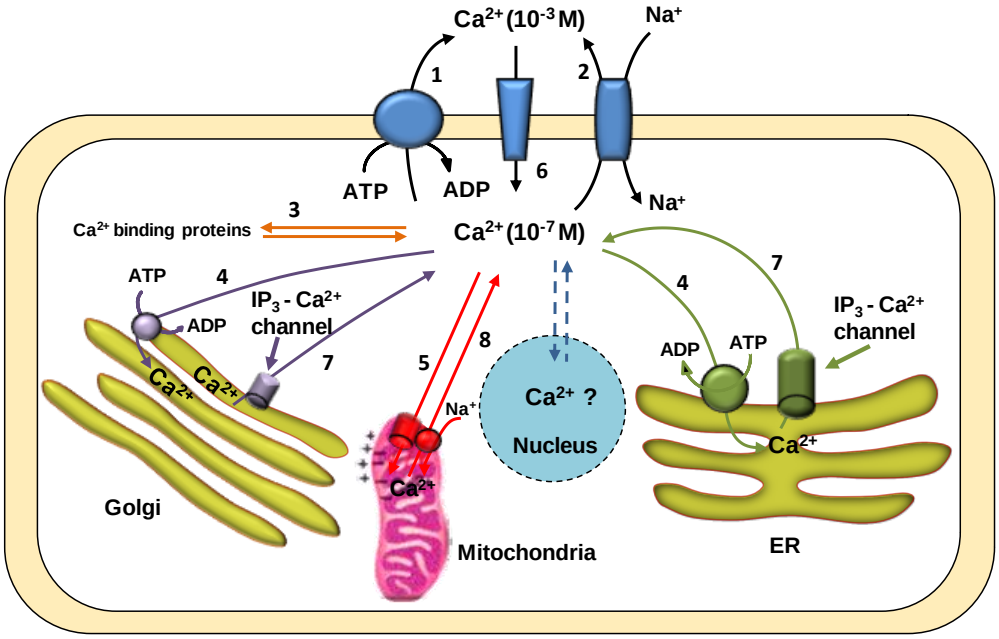

Figure 2.3 - Intracellular Ca^{2+} homeostasis. Low intracellular Ca^{2+} level is maintained by Ca^{2+}

efflux to the extracellular space, which can occur by energy dependent mechanisms using Ca^{2+} pumps (step 1), by Na^{+}/Ca^{2+} exchangers (step 2), or by Ca^{2+} influx to organelles using Ca^{2+} pumps present in endoplasmic reticulum (ER), and Golgi membrane (step 4) or by Ca^{2+} channel present in the mitochondria membrane (step 5) and also by Ca^{2+} binding proteins (step 3). Transient high Ca^{2+} levels occur by the uptake from the extracellular space via Ca^{2+} channel (step 6), by Ca^{2+} release from ER or Golgi via inositol trisphosphate channels (IP3-Ca^{2+}) (step 7) or from mitochondria via Ca^{2+}/Na^{+} exchanger (step 8). Figure adapted from Clapham 2007 [43].

The internal calcium concentration can be affected by external signals that induce a transient increase in calcium levels, activating intracellular signal-transducing pathways. The intracellular increase can occur by external calcium uptake, via calcium channels (Fig. 2.3, step 6) or by releasing the metal from intracellular compartments through inositol trisphosphate (IP_3) channels present in the ER or the Golgi membrane (Fig. 2.3, step 7) or by Na^{+}/Ca^{2+}-exchangers present in mitochondrial membranes (Fig. 2.3, step 8) (*22, 27, 44*).

In Prokaryotic organisms such as *E. coli* it was observed that intracellular calcium concentration is tightly controlled and the levels can vary between 100 and 300 nM (*44-45*). In this organism the presence of ion channels, pumps (P-type Ca^{2+}-ATPase) and Ca^{2+} binding proteins that could be involved in the homeostasis of this metal was identified (*44*).

As in Eukaryotic organisms, the intracellular calcium concentration in bacteria can be altered by external factors, such as: addition of calcium or H_2O_2; heat or cold shock stress, salinity and osmotic stress (*45-46*). For example, in *E. coli* it was observed that the free intracellular calcium concentration increased up to 2 µM after 1 mM of calcium addition to the medium. However, after 80 min the intracellular concentration of this metal stabilized at physiological levels (*47*). Addition of H_2O_2 to *Bacillus subtilis* led to the raising of intracellular calcium concentration, inducing the expression of several proteins, including alkyl hydroperoxide reductase that is modulated by Ca^{2+} (*43*).

In cyanobacteria the intracellular calcium concentration changes under heat or cold shock conditions. In cold shock conditions, calcium uptake occurs mostly via the extracellular space; while under heat shock conditions, the intracellular calcium levels increases due to the uptake from extracellular and the release from intracellular compartments. Subsequently, the intracellular Ca^{2+} levels start to stabilize in this organism (*46*) , as described above for *E.coli*.

In Eukaryotic organisms, the Ca^{2+} signaling mechanism known as phosphoinositide cascade, consists on its release from intracellular compartments, such as the ER (Fig. 2.4). In this case, an external stimulus activates the cell surface receptors (Fig. 2.4, step 1), including G-protein coupled receptors (GPCR) that activate the G-protein, which depends on guanosine-5'-triphosphate (GTP) (Fig. 2.4, step 2). The qα subunits of G-protein activate the phospholipase C (PLC) which then hydrolyses phosphatidylinositol 4, 5 bisphosphate (PIP_2) into 1,4,5-inositol trisphosphate (IP_3) and diacylglycerol (DAG) (Fig. 2.4, step 3). Then, IP_3 activates the calcium channel present in the ER membrane, inducing a calcium release to the cytosol (Fig. 2.4, step 4). As a result, calcium activates numerous cellular processes through Ca^{2+} binding proteins, such as calmodulin (CaM) which can activate other proteins by phosphorylation (Fig. 2.4, step 5).

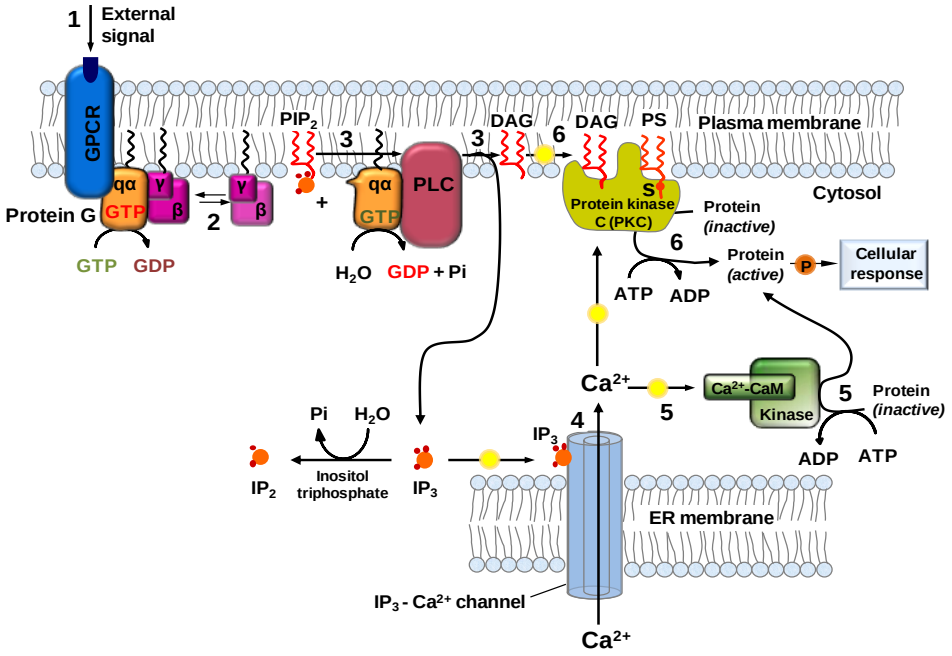

Figure 2.4 - Schematic representation of the phosphoinositide cascade for eukaryotic organisms. External stimulus (step 1) can activate the G-protein coupled receptors, (GPCR - Blue) (step 2), followed by the activation of phospholipase C (PLC - red) by G-protein, hydrolysing the phosphatidylinositol 4, 5 bisphosphate (PIP_2) into 1,4,5-inositol triphosphate (IP_3) and diacylglycerol (DAG) (step 3). IP_3 is a ligand for the intracellular IP_3-Ca^{2+} channel which span the ER membrane (step 4). Calcium released from the ER can bind proteins such as calmodulin (step 5) or kinase C proteins that can be recruited by DAG and phosphatidylserine (PS) (step 6) starting a signaling pathway. Figure adapted from Clapham 2007 (*42*).

The membrane associated diacylglycerol (DAG) and phosphatidylserine (PS) cofactors are required in some cases to activate protein kinase C (PKC) located in the membrane. Afterwards, PKC is released to the cytosol inducing the phosphorylation of other proteins (Fig. 2.4, step 6). The activation of PKC is also dependent on calcium. (*42*).

2.5 Zinc

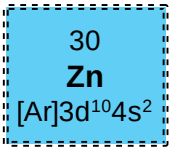

Zinc (Zn) is the 30th chemical element belonging to the 12th group, 4th period (Fig. 2.1). This element is a transition metal with complete 3*d* orbitals existing only as Zn^{2+} in solution. Although this metal has only one stable oxidation state as the alkali metals and alkaline earth metals, the nature of this element is different. Zinc forms complexes with higher binding constants due to its higher electronegativity and can act as a strong Lewis acid (Table 2.1) (*22, 27, 31, 48*).

This element can play structural, catalytic or co-catalytic roles in proteins and it has been found in more than 300 enzymes (*29, 49-50*). Examples of proteins that require zinc are: alcohol dehydrogenase or superoxide dismutase (oxidoreductases), carboxypeptidase or alkaline phosphatase (hydrolases), carbonic anhydrase (lyases), RNA polymerase (transferases), phosphomannose isomerase (isomerase), and amino acyl-tRNA synthetase (ligase) (*22, 49, 51-53*).

Catalytic zinc is generally coordinated by one water molecule and by three or four amino acid residues, which are usually cysteines or histidines, but can also be aspartic or glutamic acids. Therefore Zn^{2+} can bind oxygen (H_2O, Asp, Glu), sulfur (Cys) and nitrogen (His) ligands (Table 2.1) (*49, 54*).

Zinc as a structural element is coordinated by four amino acids residues with tetrahedral geometry, and no water molecules are involved in the coordination (*55*). It is known that zinc can stabilize several protein structures such as aspartate carbamoyltransferase from *E. coli,* ferrodoxin from *Sulfolobus sp*. and zinc finger proteins (*49, 55*). Zinc finger proteins are small proteins with a structural anti-parallel hairpin motif making tandem interactions with the target molecule. This motif can have one or more zinc ions in order to stabilize the protein conformation, and is coordinated by four amino acids residues, the most common coordination is 2 Cys and 2 His, known as the classical zinc finger coordination (*55*). Zinc finger proteins containing this classical coordination are the most abundant proteins in eukaryotic organisms.

The majority of these proteins are transcription factors which recognize a specific DNA sequence, but this motif is also essential to bind RNA, proteins and lipids (*55*). Therefore, this zinc finger motif is involved in different functions such as: DNA replication and repair, gene transcription and translation, protein folding, proliferation, cell adhesion, and apoptosis (*55*).

Zinc as a co-catalytic element occurs in enzymes that contain two or more zinc atoms in close proximity. In addition, several sites contain Zn in combination with other metals, such as Mg, Cu or Fe (*22*). An example of this function is the copper/zinc CuZnSOD superoxide dismutase. This enzyme is involved in protection of the cell against the superoxide radical (Fig. 2.5) where zinc is the structural element and copper is the catalytic element (*22, 56*).

2.6 Iron

Iron (Fe) is the 26th chemical element belonging to the 8th group and 4th period (Fig. 2.1). This element has an electronic configuration of [Ar]3d^{6}4s^2. Since this metal has incomplete 3*d* orbitals, it can exist in several oxidation states (Table 2.1). The most stable valence states in biology are ferrous (Fe^{2+}) and ferric (Fe^{3+}) forms, however the ferryl form (Fe^{4+}) has been also described to be important in enzymatic intermediates (*31, 57-60*).

26
Fe
[Ar]3d^{6}4s^2

Iron forms stable complexes with different coordination numbers (up to 6) and geometries (Table 2.1).

Iron can be in a high- or low-spin state when it is octahedrally coordinated. The high-spin state occurs when the electrons are distributed by the five *d* orbitals: three t_{2g} and two e_g. According to the Pauli Exclusion Principle, the final spin state of Fe^{3+} or Fe^{2+} is S=5/2 or S=2, respectively. However, iron can also be in a low-spin state: this occurs when the interaction between the electrons and the ligand field is strong, favoring the pairing of the electrons in the lowest energy levels (t_{2g} orbitals), with a final spin state of S= 1/2 for Fe^{3+} or S=0 for Fe^{2+}. On the other hand, when iron present a tetrahedral coordination, only the high spin state is possible.

These different spin states of iron is an advantage in studies to understand iron centers in proteins using spectroscopic techniques, such as electron paramagnetic resonance (EPR) spectroscopy (*61*).

2.6.1 Iron availability and toxicity

Iron is the fourth most abundant element in Earth´s crust and is required by all organisms. In reducing conditions which existed at the origin of life, the soluble Fe^{2+} form predominated, and in this way iron was available for organisms. However the atmosphere transition to oxidative conditions, due to the presence of dioxygen caused a problem in iron availability, since Fe^{2+} was oxidized to insoluble Fe^{3+}. Under these conditions and despite its abundance, the availability of this element for the organisms became limited. The insolubility of Fe^{3+} is due to the fact that under aerobic conditions ferric iron forms insoluble ferric hydroxides ($Fe(OH)_3$) with a solubility product of $K_{sp}=2.79x10^{-39}$ (*22, 62*).

In addition, under oxidative conditions, free iron in cells potentiate oxygen toxicity by its interaction with oxygen or its reduction products, forming in this way highly reactive oxygen species, toxic for the cells (Fig. 2.5) (described in Chapter I).

To overcome the problem of iron availability and prevent ROS formation under oxidative conditions, organisms have mechanisms to sequester and store iron. Proteins involved in the storage of this metal are known as iron storage proteins, which include Ferritins, Bacterioferritins and Dps proteins. In the presence of O_2 or H_2O_2, Fe^{2+} is oxidized to Fe^{3+}, which is stored in the cavity of these proteins as ferric hydroxides form, without ROS formation (Fig. 2.5). When cells have the need for iron, this metal can be released from these iron storage proteins and be “re-used” in the cell (*63-65*).

2.6.2 Iron as an essential element

Due to its chemical properties, iron is involved in a wide range of biological functions. It can interact directly with proteins regulating the expression of some genes. This metal can also act as a cofactor for several proteins and enzymes, for instance heme, iron-sulfur clusters, mixed metal centers, mononuclear and binuclear centers (*22*).

One of the most important characteristics of iron is to promote electron transfer due to its redox properties. For example, it is present in several proteins from the oxidative phosphorylation pathway, containing iron sulfur clusters or hemes that are involved in the reduction of dioxygen to water (*66*).

Iron metal is also an essential cofactor of enzymes that scavenge ROS, such as iron superoxide dismutase enzymes (FeSOD) or heme catalase enzymes (*59*). Iron SOD contains a mononuclear iron site which is reduced from Fe^{3+} to Fe^{2+} followed by its reoxidation. These two steps are consecutive and require $O_2^{\bullet-}$, which undergoes disproportionation into H_2O_2 and O_2 (Reaction 2.1 and 2.2, Fig. 2.5) (*59*).

Reaction 2.1 $Fe^{3+} + O_2^{\bullet-} \longrightarrow Fe^{2+} + O_2$

Reaction 2.2 $Fe^{2+} + O_2^{\bullet-} + 2H^+ \longrightarrow Fe^{3+} + H_2O_2$

FeSOD disproportionation

Catalases that are dependent of iron contain heme and are divided into monofunctional (only catalase activity) or bifunctional catalases (catalase-peroxidase activity). The monofunctional catalases have a heme *b* cofactor (FeP) which is a redox cofactor. During the turnover, the $Fe^{3+}P$ is oxidized to an oxo-ferryl porphyrin π-cation radical complex (complex I - $Fe^{4+}OP^{\bullet}$) by one H_2O_2 molecule, releasing one H_2O molecule, and then is reduced to $Fe^{3+}P$ by another H_2O_2 molecule. During this turnover two hydrogen peroxide molecules are catalytically dismutated into one oxygen and two water molecules, protecting the cell against ROS (Reaction 2.3 and 2.4, Fig. 2.5) (*57-58*). Bifunctional catalases form the same radical, complex I (Reaction 2.3), but with two intermediate steps, that react with two organic electron donors (RH_2) forming an intermediate species, $^{\bullet}RH$, releasing two water molecules (Reaction 2.5 and 2.6) (*24*).

Reaction 2.3 $Fe^{3+}P + H_2O_2 \longrightarrow Fe^{4+}OP^{+\bullet} + H_2O$

Reaction 2.4 $Fe^{4+}OP^{+\bullet} + H_2O_2 \longrightarrow Fe^{3+}P + H_2O + O_2$

Monofunctional, heme-containing catalases

Reaction 2.5 $Fe^{4+}OP^{+\bullet} + RH_2 \longrightarrow Fe^{4+}OP + {}^{\bullet}RH$

Reaction 2.6 $Fe^{4+}OP + RH_2 \longrightarrow Fe^{3+}P + H_2O + {}^{\bullet}RH$

Bifunctional, heme-containing catalases

Iron is also essential for several proteins that contain mixed metal centers or binuclear centers. For example the most known group that contains a binuclear center (di-iron centers) is the four helix bundle protein family. This family includes proteins with distinct functions, such as monooxygenases, erythrin, rubrerythrin, ferritins and bacterioferritins (*22, 65*).

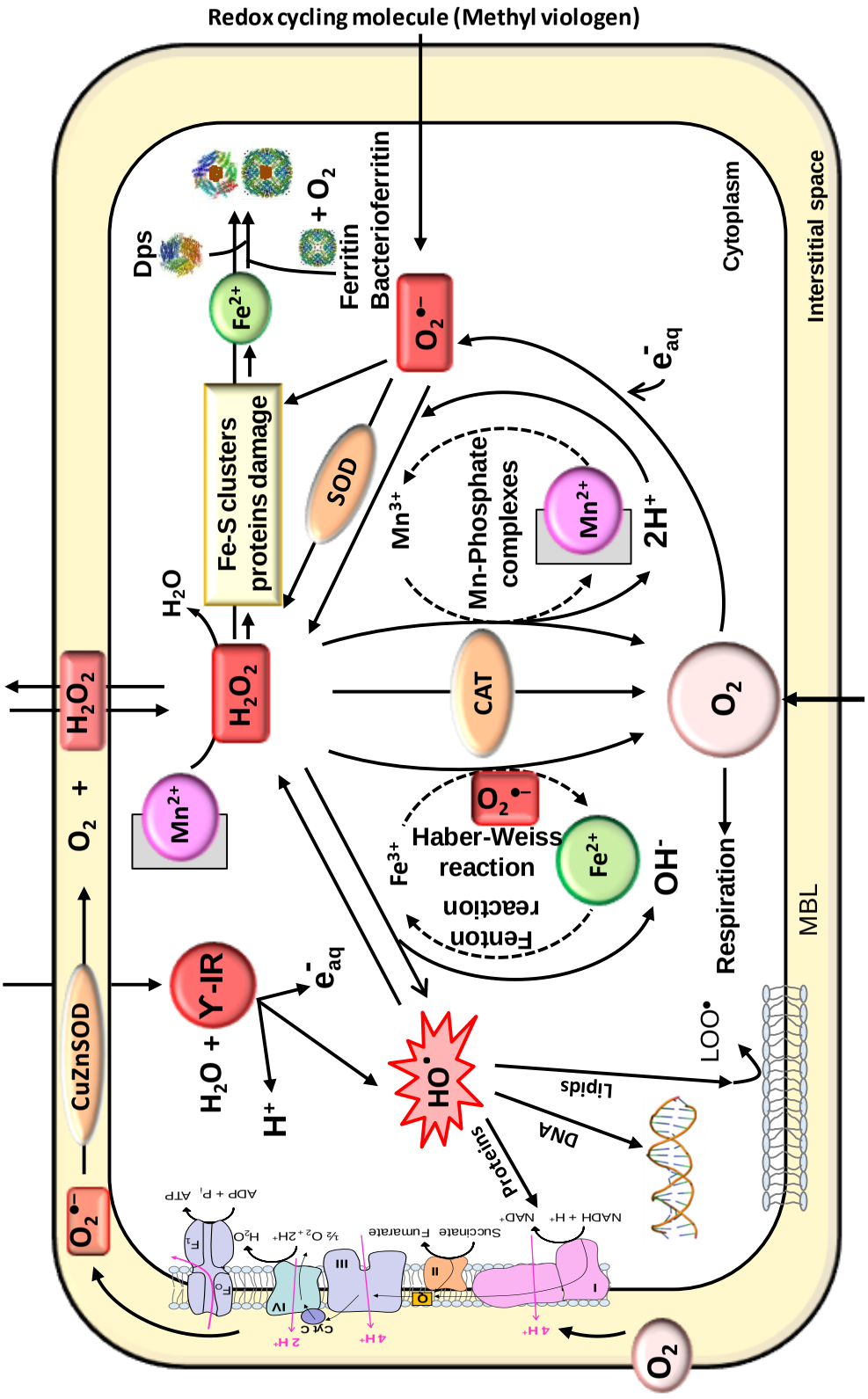
Redox cycling molecule (Methyl viologen)
Interstitial space
Cytoplasm
Dps
Ferritin
Bacterioferritin
+ O2
Fe2+
O2•−
e-aq
Fe-S clusters proteins damage
SOD
Mn3+
Mn-Phosphate complexes
Mn2+
2H+
H2O
H2O2
CAT
O2
Haber-Weiss reaction
Fenton reaction
Fe3+
OH-
Respiration
MBL
LOO•
Lipids
DNA
Proteins
HO•
Y-IR
H2O +
H+
CuZnSOD
O2 +
ADP + Pi ATP
NADH + H+
NAD+
Succinate
Fumarate
½ O2 + 2H+
H2O
2 H+
4 H+

Figure 2.5 - Model for manganese (pink colour) and iron (green colour) redox cycling. Manganese and iron are cofactors of superoxide dismutase (SOD) and catalase (CAT) (orange colour), respectively. Iron is a toxic element (Fenton reaction and Haber-Weiss reaction) and manganese is an antioxidant (Phosphate manganese complexes - pink colour with grey box). ROS production, hydrogen peroxide (H_2O_2), superoxide anion ($O_2^{\bullet -}$) and hydroxyl radical ($HO^{\bullet}$) (red colour), from external sources (gamma radiation - γ-IR, H_2O_2 and redox cycling molecule (Methyl viologen)) or from internal sources (Electron transfer respiratory chain - ETRC). Hydroxyl radical can damage proteins, DNA and lipids ($LOO^{\bullet}$ - Lipid peroxidation) and H_2O_2 or $O_2^{\bullet -}$ can damage iron-sulfur cluster proteins (yellow colour) that release ferrous iron (green colour) which can be incorporated by iron storage proteins (Dps, Ferritins and bacterioferritins). MLB – membrane lipid bilayer. Adapted from Daly 2007 and 2009, Lisher 2013 and Ghosal 2005 (*34, 67-69*).

2.7 Manganese

25
Mn
$[Ar]3d^5 4s^2$

The transition metal manganese (Mn) is the 25th chemical element belonging to the 7th group and the 4th period (Fig. 2.1), with an electronic configuration of $[Ar]3d^5 4s^2$. Since it has 5 electrons in 3*d* orbitals it can exist in several oxidation states, that can vary between +2 and +7 (Table 2.1); however only the Mn^{2+} and Mn^{3+} states have been identified in biological systems (*31, 50*). The Mn^{2+} form is more stable than Mn^{3+}, whereas for iron, Fe^{3+} is more stable relative to Fe^{2+}. This fact is due to the existence of a half-filled d^5 in both, Mn^{2+} and Fe^{3+} that confer thermodynamic stability. In this way, the presence of high amounts of free Mn^{2+} for cells does not have any consequence in ROS formation (*22*).

Among transition metals, Mn^{2+} is the one with highest ionic radius. In this case, manganese forms complexes with low binding constants when compared with other transition metals, and can be coordinated by nitrogen or oxygen atoms (Table 2.1). Also, Mn^{2+} has higher exchange rates where water can be easily replaced by other ligands. This behavior can be favorable to the formation of Mn-complexes, as described in section 2.7.1.2 (*22*).

2.7.1 Role of manganese in biological systems

2.7.1.1 Manganese metalloenzymes

Manganese is an essential cofactor for several manganese metalloenzymes and can function as a Lewis acid or as a redox catalyst element (*22, 24, 59, 70-73*).

As a Lewis acid, a manganese cofactor does not play a part in the redox reaction, but accepts a pair of electrons, for example the di-nuclear manganese center in the arginase enzyme (*74*). Manganese is present in redox centers of different enzymes for example those involved in the detoxification of ROS such as mononuclear manganese superoxide dismutase (MnSOD) and non-heme di-nuclear manganese catalase (*24, 59, 70-71*). MnSOD contains a mononuclear manganese center which is involved in the dismutation of $O_2^{\bullet-}$, converting this radical into H_2O_2 and O_2 by reduction of Mn^{3+} to Mn^{2+} and its re-oxidation (Reaction 2.7 and 2.8, Fig. 2.5) (*59*).

Reaction 2.7 $Mn^{3+} + O_2^{\bullet-} \longrightarrow Mn^{2+} + O_2$

Reaction 2.8 $Mn^{2+} + O_2^{\bullet-} + 2H^+ \longrightarrow Mn^{3+} + H_2O_2$

MnSOD disproportionation

Non-heme catalases contain a di-nuclear manganese active site. During turnover this protein converts H_2O_2 into H_2O and O_2, through two electron catalytic cycle between reduced ($Mn^{2+}Mn^{2+}$) and oxidized ($Mn^{3+}Mn^{3+}$) stages (Reaction 2.9 and 2.10, Fig. 2.5) (*24, 70*).

Reaction 2.9 $Mn^{3+} + H_2O_2 \longrightarrow Mn^{2+} + O_2 + 2H^+$

Reaction 2.10 $Mn^{2+} + H_2O_2 + 2H^+ \longrightarrow Mn^{3+} + 2H_2O$

Non-heme catalase

2.7.1.2 Manganese complexes

Under physiological pH and oxidative conditions Fe^{2+} can produce ROS while Mn^{2+} is thermodynamically stable (half-filled d^5 shell), and can be involved in the

protection of cells by acting as a ROS scavenger. Thus, its protecting role is not only limited to being a cofactor in proteins, such as SOD or catalase, but is extended to Mn^{2+}-non-protein complexes which play a crucial role as a protection mechanism in cells (Fig. 2.5). This protection occurs by cycling between the divalent (Mn^{2+}) and trivalent states (Mn^{3+}). The oxidation of Mn^{2+} occurs in the presence of $O_2^{\bullet-}$ or peroxyl radicals ($HO_2^{\bullet}$ and $R\text{-}O_2^{\bullet}$), releasing hydrogen peroxide as an intermediate (reaction 2.11). Also, oxidation of Mn^{2+} occurs in the presence of H_2O_2, releasing two water molecules (reaction 2.12) (*69, 75*). The reduction of Mn^{3+} can occur by electron donors such as thiols, hydroquinones and glutathione (*25, 69, 75*).

Reaction 2.11 $Mn^{2+} + O_2^{\bullet-} + 2H^+ \longrightarrow Mn^{3+} + H_2O_2$

Reaction 2.12 $Mn^{2+} + H_2O_2 + 2H^+ \longrightarrow Mn^{3+} + 2H_2O$

Manganese oxidation

In solution, free manganese is hexagonally coordinated by six water molecules and can react poorly with $O_2^{\bullet-}$. But when it is coordinated by various anion molecules, it loses the hexagonal coordination and can act as a potential scavenger of superoxide radical (*75*). It was been observed that Mn^{2+} can bind a diversity of small ligands (L) such as organic molecules (lactate, succinate, malate, citrate and pyruvate), phosphate (orthophosphate and pyrophosphate) and bicarbonate (*71, 75*).

Mn^{2+} complexed with pyrophosphate or citrate acts as a stoichiometric scavenger of the superoxide radical (Reaction 2.13 and 2.14) whereas complex with orthophosphate or bicarbonate it serves as a catalytic scavenger (Reaction 2.15 and 2.16) removing the superoxide with 2-3 orders of magnitude slower rates than SOD enzymes (Table 2.2) (*71, 75-76*). On the other hand, it was reported that in Mn^{2+}-polyphosphate complex is not a ROS scavenger (*77*).

Reaction 2.13 $Mn^{2+}\text{-}L + O_2^{\bullet-} \longrightarrow MnOO^{1+} + L$

Reaction 2.14 $MnOO^{1+} + L + 2H^+ \longrightarrow Mn^{3+}\text{-}L + H_2O_2$

Stoichiometric scavenger; L - Citrate or Pyrophosphate

Reaction 2.15 $Mn^{2+}\text{-}L + O_2^{\bullet -} \longrightarrow MnOO^{1+}\text{-}L$

Reaction 2.16 $MnOO^{1+}\text{-}L + MnOO^{1+}\text{-}L + 2H^{+} \longrightarrow 2Mn^{2+}\text{-}L + H_2O_2 + O_2$

Catalytic scavenger; L - Bicarbonate or orthophosphate

Table 2.2 – Rate constants for the non-catalytic and catalytic disproportionation of superoxide (*71, 75-76*).

	Compounds	Rates constants
Non-catalytic mechanism Mn^{2+}-complexes	Mn^{2+}-pyrophosphate	$> 2.0x10^4\ s^{-1}$
	Mn^{2+}-Citrate	$2.0x10^3\ s^{-1}$
Catalytic mechanism Mn^{2+}-complexes	Mn^{2+}-orthophosphate	$8.9x10^6\ M^{-1}s^{-1}$
	Mn^{2+}-Bicarbonate	$1.5x10^6\ M^{-1}s^{-1}$
Catalytic mechanism SOD enzymes	CuZnSOD	$6.9x10^9\ M^{-1}s^{-1}$
	FeSOD	$6.6x10^8\ M^{-1}s^{-1}$
	MnSOD	$6.8x10^8\ M^{-1}s^{-1}$

Furthermore, it was also observed that the Mn^{2+}-bicarbonate complex can perform H_2O_2 dismutation, but in the presence of amino acids this complex becomes a much more efficient scavenger (reaction 2.17) (*78*).

Reaction 2.17 $RCHNH_3^{+}COO^{-} + 2H_2O_2 \xrightarrow{Mn^{2+}\text{-}L} RCOO^{-} + CO_2 + NH_4^{+} + 2H_2O$

L - Bicarbonate (HCO_3^-)

The high protection ability of these complexes has been reported. Addition of Mn^{2+}-orthophosphate complex protects endonuclease *Bam*HI or glutamine synthetase activities up to an ionizing radiation dose of 10 kGy. Furthermorer, addition of peptides (Mn^{2+}-orthophosphate-peptides), free amino acids (Mn^{2+}-orthophosphate-amino acids) or free nucleotides (Mn^{2+}-orthophosphate-nucleotides) strongly induces the protection of proteins, which maintain 100 % of their activity when submitted to approximately 22.5 kGy of ionizing radiation. Nevertheless, under these conditions and in the presence of these manganese complexes, the damage of plasmid DNA is not prevented (*79*). DNA is damaged mainly by the $HO^{\bullet}$ radical, while proteins are mainly damaged by the superoxide radical, as mentioned in chapter I (*11*). These results

clearly demonstrate that Mn^{2+}-complexes function as scavengers of superoxide anion and hydrogen peroxide. However, Mn^{2+}-complexes do not have the ability to scavenge hydroxyl radicals.

Most organisms can accumulate micromolar quantities of manganese, but several organisms can accumulate millimolar levels. This high intracellular level of manganese has been associated with resistance to radiation (Chapter III, Table 3.1) (*69, 79-83*).

The first report that showed the importance of Mn^{2+} complexes is from studies in bacterium *Lactobacillus plantarum*. This organism does not contain any genes coding for SOD enzymes (*84*) but accumulates high intracellular manganese levels, approximately 20 mM, that are required for the survival under UV conditions. Also, this bacterium accumulates high intracellular levels of lactate during the fermentation metabolism (*80, 85*). The high accumulation of manganese and lactate can contribute to the protection, since it was observed that manganese can form complexes with lactate which scavenge the superoxide radical (*75*). This organism also accumulates high levels of polyphosphate (60 mM) (*86*) that do not have the ability to scavenge superoxide radical when complexed with Mn^{2+} (*77*). However, these polyphosphates can be hydrolyzed to pyrophosphate or to orthophosphate by exopolyphosphatase (PPX) (*87-88*), and both phosphate forms when complexed with manganese have the ability to scavenge superoxide (*75, 89*).

E. coli Δ*sodA*Δ*sodB* double mutant (MnSOD and FeSOD) is sensitive to oxidative damage. However, when manganese was added to the growth medium, the oxidative damage was abolished. In that case, it is suggested that Mn^{2+} forms complexes with orthophosphate and pyrophosphate that are found in this bacterium with concentrations of 10 mM and 2.5 mM, respectively (*90-91*). Also, it is interesting to note that addition of manganese to *B. subtilis* Δ*sodA* (MnSOD) mutant protects cells under oxidative stress (*92*).

Furthermore, the presence of Mn^{2+}-orthophosphate complexes has been associated with the survival of *Deinococcus radiodurans* under extreme ionizing, ultraviolet radiation and desiccation conditions that will be discussed in chapter III.

The manganese complexes have also been found in Eukaryotic organisms and their formation in *Saccharomyces cerevisiae* has been studied. The survival of this

organism in the presence of manganese is associated with the formation of Mn^{2+}-orthophosphate or Mn^{2+}-bicarbonate complexes that protect the organism against oxidative stress (*77*). In fact, *S. cerevisiae* Δ*sodC* mutant (CuZnSOD) is more sensitive to oxidative damage, which is suppressed by the external addition of manganese (*93*).

It was observed that the formation of Mn^{2+}-complexes is a tightly regulated process that occurs by nutrient or stress signaling pathways, which consists of a series of kinases that sense and respond to changes in the environment. In nutrient condition Rim15 kinase (serine/threonine kinase) is repressed while in stress conditions it is activated by its desphosphorylation, activating transcriptional factors (Msn2, Msn4 and Gis1). These transcriptional factors can activate Mn^{2+}-complexes via Msn2 and Msn4 or repress them via Gis1, thus controlling the intracellular assembly of these complexes without alteration of the manganese levels (scheme 2.1) (*94-96*). This regulated process can occur via calcium signaling since during stress conditions the vacuolar ion channel is highly activated releasing calcium (*97*).

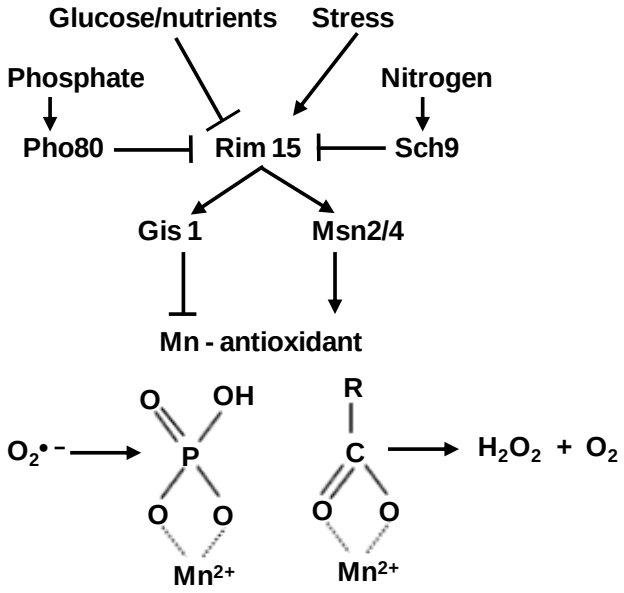

Scheme 2.1 - Schematic representation of the tight regulation of Mn^{2+}-orthophosphate complexes or Mn^{2+}-bicarbonate complexes in *Saccharomyces cerevisiae*. Rim15 kinase can be controlled by external factors, such as nutritional and stress factors, directly (Glucose and stress) or indirectly (Phosphate and nitrogen). Rim15 can activate three transcriptional factors

(Gis1 and Msn2/4) that regulate the levels of complexes. Scheme adapted from Aguirre and Culotta (*95*).

To sum up, manganese can form complexes with small molecules, such as orthophosphate, pyrophosphate, bicarbonate, and lactate which can synergistically scavenge superoxide or peroxyl radicals, protecting proteins or even lipids, in a tightly regulated process.

-

CHAPTER III

Deinococcus radiodurans

3.1 General considerations

Deinococcus radiodurans belongs to the family of *Deinococcaceae.* This organism was the first of this family to be discovered. In 1956, it was found in a canned food after being submitted to sterilization conditions using high doses of gamma radiation, which would supposedly kill all known forms of life (*98*).

Initially, this organism was named *Micrococcus radiodurans* based on its morphological and physiological features (*98*). Later on, it was renamed *Deinococcus radiodurans* after an analysis of its 16S rRNA (*99*). The name *Deinococcus* comes from the Greek word *deinos* that means strange or unusual, and *coccus* means grain or berry (*100*).

D. radiodurans R1 is an aerobic, red-pigmented, gram positive coccus, nonsporulating and mesophilic bacterium with approximately 1.5 - 3.5 µm in diameter (*100*). This bacterium can form single of pair cells but appears frequently in the form of tetrads (Fig. 3.1). The division occurs alternately in two planes; first the formation of two septa in opposite sides occurs perpendicularly to the cell wall forming two cells, and then two new septa starts to form in another plane before the previous two are finished. In this situation the tetrad cells can communicate between them until the division is complete (*101*).

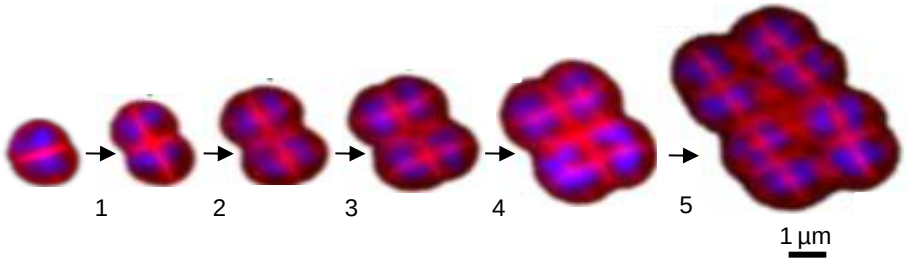

Figure 3.1 - *D. radiodurans* cell division. ***Step 1***, septa formation perpendicularly to the cross wall, forming two diads. ***Step 2***, new septa formation in opposite planes to the cross wall. ***Step 3***, complete formation of the septa, forming two tetrads. ***Step 4***, new septa formation perpendicularly to the previously formed cross wall, leading to four tetrads. ***Step 5***, next step of cell division forming eight tetrads. The nucleoids are represented in blue, and the membranes in red. Figure adapted from Slade and Radman (*100*).

The complete genome sequence of *D. radiodurans* was published in 1999 and it was the first genome to be sequenced from a radiation resistant organism (*102*). The genome is composed of four DNA molecules: chromosome I (2,648,615 base pairs),

chromosome II (412,340 bp), a megaplasmid (177,466 bp), and a plasmid (45,702 bp) yielding a total genome with 3.28 megabase pairs (Mbp) with a high GC content of 66.6 % (*102*).

3.2 Radiation resistant organisms

Most bacteria do not have the capacity to survive to the presence of 200 Gray (Gy, is a derived unit of ionizing radiation dose in the International System of Units), such as *Escherichia coli or Shewanella oneidensis* and a dose of 10 Gy is enough to kill most invertebrate animals (Fig. 3.2) (*103*).

To date several radiation resistant organisms that have been isolated belong to the *Deinococcaceae* family such as: *D. radiodurans* (*98*), *D. roseus* (*104*), *D. misaseusis* (*104*), *D. deserti* (*105*), *D. geothermalis* (*106*), *D. murraryi* (*106*), *D. hopiensis* (*107*), *D. sonorensis* (*107*) and *D. ficus* (*108*). These bacteria have been isolated from a variety of habitats, such as animal gut, hot springs, deserts, hospital air, alpine environments, and Antarctica (*105-107*).

However, radiation resistance ability is not restricted to the *Deinococcaceae* family. Organisms belonging to the three domains of life have been identified as being radiation resistant. *Halobacterium salinarum* sp. NRC-1, *Pyrococcus furiosus*, *Thermococcus marinus*, *Thermococcus radiotolerans*, and *Thermococcus gammatolerans* are examples from Archaea (*109-112*), *Kineococcus radiotolerans, Cyanobacterium chroococcidiopsis* and *Acinetobacter radioresistens* are example from Bacteria (*113-115*), *Philodina roseola*, and *Ustilago maydis* are example from Eukarya (*116-117*). However *D. radiodurans* is still the most radiation resistant organism known to date, which can survive to the doses of more than 12 kGy (Fig. 3.2) (*67, 118-119*). Moreover, this organism is also extremely resistant to high levels of desiccation (*119-120*), ultraviolet light (*121*), and oxidative stress (hydrogen peroxide) (*122*).

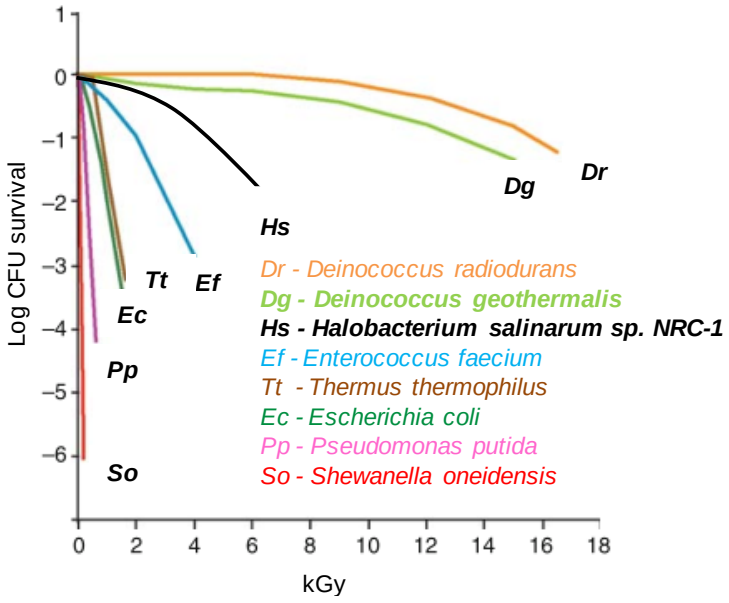

Figure 3.2 - Ionizing radiation survival curves from different organisms. Figure adapted from Daly, 2009 (*67*).

3.3 Reactive oxygen species formation by exogenous sources

There are several exogenous sources that can cause cell damage. However, here we will focus in the description of exogenous sources which are fundamental for this work which include: ionizing radiation, ultraviolet radiation, and desiccation (Scheme 3.1).

3.3.1 Ionizing and non-ionizing radiation

Ionizing radiation (IR) is a radiation that has energy high enough to ionize atoms and molecules (*123*). The different types of radiation can be differentiated by their frequency, wavelength, and energy (Fig. 3.3). The ionizing radiation has a high frequency and can be divided into gamma (0.001-0.1nm) and X-ray radiation (0.1-1 nm). The ultraviolet radiation (UV) can be divided into UVA (400-320 nm), UVB (280-295 nm) and UVC (295-100 nm), in which the first two are considered non-ionizing radiation while the latter is more powerful and dangerous than UV-A and UV-B and it is consider ionizing (*100, 124*).

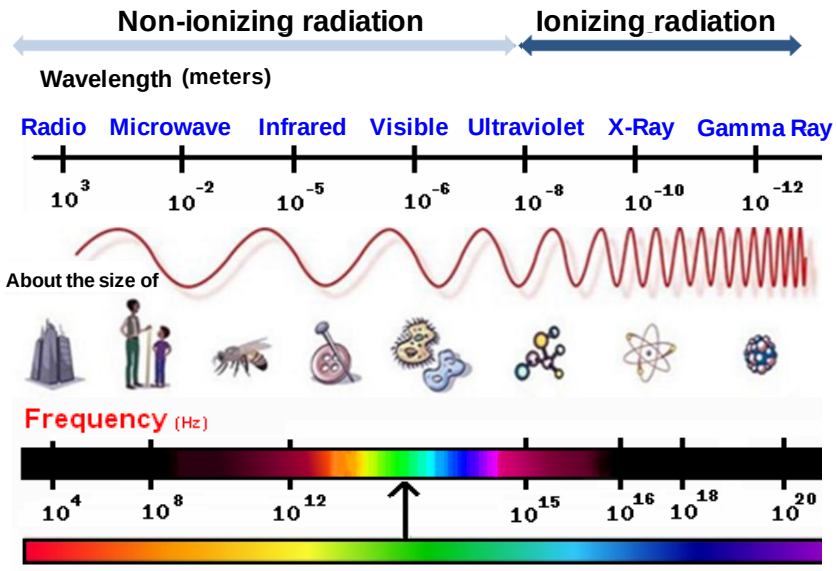

Figure 3.3 - Electromagnetic spectrum.

Ionizing radiation (IR) can damage molecules directly or indirectly through radiolysis of water leading to ROS formation (Scheme 3.1) (*125*). It has been observed that damage occurs primarily via ROS production (80%) formed by radiolysis of water while the remaining 20% comes from the direct effect of IR (*68, 126*).

During radiolysis of water, the radical $HO^{\bullet}$ is immediately formed, releasing 1 proton (H^+) and 1 hydrated electron (e^-_{aq}) with a rate constant (theoretical) of 5.9 x 10^{-8} mol/s (Scheme 3.1, reaction 3.1). Besides this radical, other ROS are formed, but with lower rate constants than the one described above. H_2O_2 is generated from two $HO^{\bullet}$ radicals (Scheme 3.1, reaction 3.2), while superoxide anion is produced when O_2 reacts with one electron (Scheme 3.1, reaction 3.3), and $HOO^{\bullet}$ is formed from $O_2^{\bullet-}$ in the presence of 1 H^+ (Scheme 3.1, reaction 3.4) (*67, 126*).

UV radiation induces ROS production which promotes oxidative damage (Scheme 3.1) (*127-128*). The $^1O_2$ radical is the main ROS source formed from UV radiation. However, under this condition other ROS can also be formed, such as $HO^{\bullet}$, H_2O_2 and $ROO^{\bullet}$ inducing the oxidation of lipids, proteins and DNA (*128-133*).

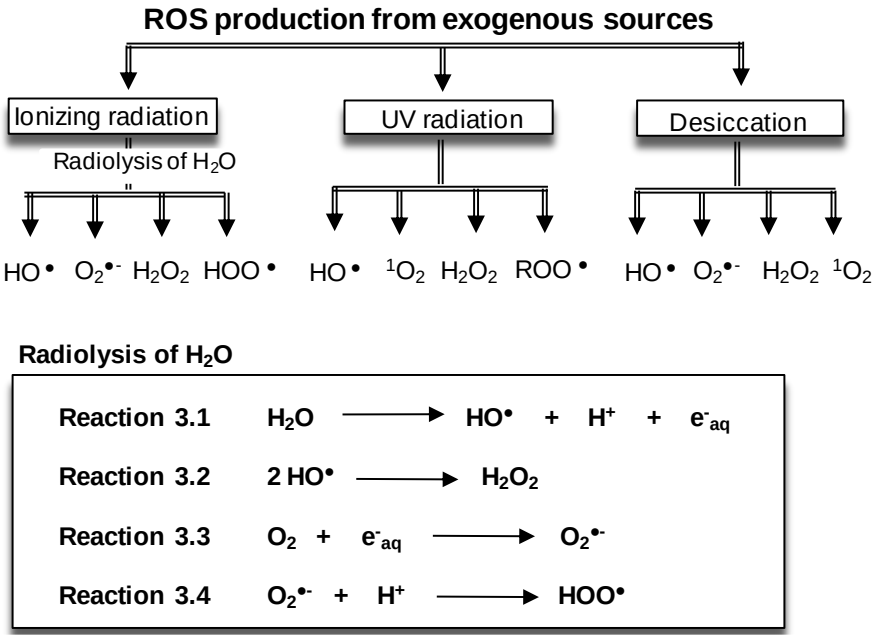

Scheme 3.1 - Reactive oxygen species production from exogenous sources.

3.3.2 Desiccation

Desiccation is a dehydration process that leads to a decrease of water content below 0.1 g H_2O/g dry mass, a phenomenon frequently observed in plants. Under this condition the production of $O_2^{\bullet-}$, H_2O_2, $HO^{\bullet}$ and $^1O_2$ was observed (Scheme 3.1) (*100, 134*). Consequently the oxidative damage of protein, lipid and DNA was also observed, due to the side effects of ROS.

3.4 Factors that can contribute for the *D. radiodurans* survival

Since high levels of ionizing radiation do not occur in natural environments, some studies proposed that the extreme IR resistance of *D. radiodurans* is a consequence of its high resistance to desiccation (*119-120*). Studies in *D. radiodurans* showed that IR and desiccation are the most severe conditions that promote DNA damage. Both can induce multiple types of DNA damage, namely: base damage, single-strand breaks (SSBs) as well as the most severe form of DNA damage, double-strand breaks (DSBs) (*100, 120, 135*). Reinforcing the link between IR resistance and desiccation, it

was observed that after *D. radiodurans* being submitted to ionizing radiation or desiccation, the genes induced during the recovery period are similar, and belong to the category of DNA/RNA metabolism, stress response, heat-shock response and transport (*119*). Moreover, it has been reported that most IR resistant organisms are also resistant to desiccation (*107, 114*) .

The link between IR and desiccation suggests that this organism has a common defense mechanism to survive to extreme conditions, which is centered in the protection against oxidative stress. Thus, under ionizing, UV radiation, desiccation, and hydrogen peroxide conditions *D. radiodurans* survives by its ability to detoxify ROS and protection against degradation. Multiple factors contribute to this, that will be described in the next sections.

3.4.1 DNA repair systems

As mentioned above, ionizing radiation can damage DNA, and one of the effects is to generate double-strand breaks (DSBs) (*120*). The first focus of several studies aimed to understand the radiation resistance mechanisms was based, during many years, in the DNA repair systems and consequently in their high efficiency to repair DSBs leading to the reconstruction of an integral genome in a few hours (*136-137*). IR can induce DSBs not only in radiation resistant but also in radiation sensitive organisms. However, *D. radiodurans* can withstand about 160 DSBs without any mutation while the radiation sensitive organism *E. coli* can undergo only 6 DSBs in its genome prior to the onset of mutations (*138-140*).

D. radiodurans has several DNA repair systems which include the base excision repair (BER) / nucleotide excision repair system (NER), mismatch repair system and double-strand break repair system. During ionizing radiation and desiccation the involvement of BER and NER systems was observed, as well as of the homologous recombination repair pathway to repair DSBs, including RecFOR (Rec-recombinase) and RecA pathways (*100, 141*). *D. radiodurans* Δ*recF*, Δ*recO*, Δ*recR* and Δ*recA* mutants demonstrated that these two pathways are essential for DNA repair (*142-144*). Under UV radiation conditions, two different excision repair systems were activated; classical nucleotide excision repair system (UvrABC) and also UV damage endonuclease pathway (UVDE) (*100, 136*). However, a transcriptome analysis of this organism did not reveal any DNA repair system unique to *D. radiodurans*, but identical

repair systems to those present in IR sensitive organisms such as *S. oneidensis* or *E. coli* (*102, 145-147*). In fact, *D. radiodurans* mutant strains defective in DNA polymerase are ionizing and UV radiation sensitive, but their resistance to radiation is restored when complemented with the homologous DNA polymerase I from *E. coli* (*148*). These results demonstrate that DNA repair systems can contribute to the repair of DNA, protecting the cell from DNA damage. Nevertheless, similar DNA repair systems are found in radiation sensitive organisms, suggesting that other factors contribute to the protection mechanism in this organism.

D. radiodurans contains a high genome copy number, 4-10 haploid genome copies per cell, which have been suggested to facilitate the repair of DSBs (*149*). However, *E. coli* also contains 4-8 haploid genome copies per cell (*150*). Moreover, the high levels of chromosomal condensation forming ring-like nucleoid morphology was proposed to be associated with DNA repair (*151*), but this model has been contested, since it was observed that *D. radiodurans* is less IR resistant in the stationary phase where the ring-like nucleoid morphology is more pronounced (*152*). Therefore, it is unlikely that the radiation resistance of *D. radiodurans* is due to DNA ring-like morphology.

3.4.2 The cell wall

The cell wall is an essential component of organisms and confers resistance and protection to the organism when submitted to diverse environmental conditions (*153*).

D. radiodurans has an unusual cell wall with multilayers and a different lipid composition. It is a gram positive bacterium because it contains a peptidoglycan multilayer. However, its cell wall is more similar to those of gram negative bacteria due to the presence of outer membranes (*153-154*). This organism has at least six membrane layers with a total thickness of 150 nm, identified by electron microscopy (Fig. 3.4) (*100, 154*). These layers can be divided into two innermost layers and four outermost layers that have been characterized as an open network structure (*154*). The first layer is an inner membrane and the second is a peptidoglycan layer penetrated by many holes, but until now no physiological significance for this holes is known (*154*). The innermost layers are only involved in the septum formation during the cell division (*154*). The third layer is an interstitial layer, a fine matrix compartmentalized, composed of soluble proteins such as S-Layer Protein A (SlpA)

(*155*). The fourth is a lipid-rich backing layer followed by a surface layer (S-layer) composed by S-layer proteins in which the Hexagonally Packed Intermediate protein (Hpi) is the major constituent. These two membranes are known as the "pink envelope" and the S-layer penetrates into a lipid-rich baking and interstitial layers (*156*). Finally, the sixth layer is the carbohydrate coat (Fig. 3.4) (*157*).

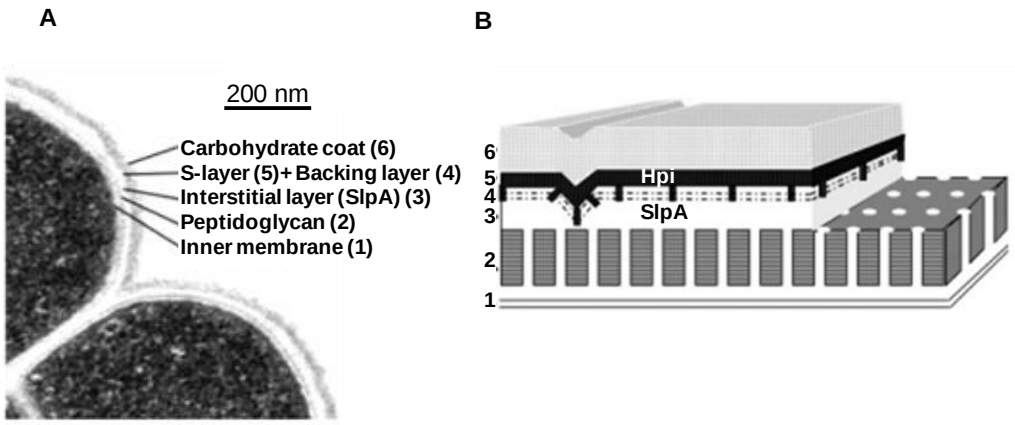

Figure 3.4 - Cell wall composition of *Deinococcus radiodurans* showing six layers (1-6). **(A)** Thin section electron micrograph of the cell wall. **(B)** Schematic representation of the cell wall. Figure adapted from Rothfuss *et al.*, 2006 (*155*).

The *D. radiodurans* cell wall contains in general in its composition 1% of phosphorus, 4.3 % of lipids and 3.3 % of polysaccharides (of which 2.6 % is D-galactose and 0.5 % is D-glucose), the presence of rhamnose and mannose was also observed but at lower concentrations (*154*).

In the inner membrane, 43 % of lipids present are phosphoglycolipids that contain alkylamines which differ from the common bacterial phospholipids and are exclusive of *D. radiodurans* (*158*).

The peptidoglycan layer of this organism is composed of mucopeptides containing glucosamine, muramic acid, and the following amino acids: glutamic acid, alanine, glycine and diamino acid L-ornitine (*154*). This last amino acid is characteristic of the *Deinococcaceae* family members. In addition, this layer also contains phosphorus, glucose and meso and LL-diaminopimelic acid (*154*).

The pink envelope (lipid-rich backing and S-layers) is constituted by carotenoids, mainly deinoxanthine that confers the pink colour to *D. radiodurans. In vitro*, this *D.*

radiodurans carotenoid showed high capacity to scavenge all types of ROS, including, $^1O_2$, ROO·, OH·, $O_2\cdot^-$, H_2O_2 consequently protecting the membrane from lipid peroxidation, proteins against carbonylation and DNA against oxidative damage (*129, 159*). When the carotenoid biosynthesis was blocked in *D. radiodurans* (DcrtB – *dr0862* mutant), the mutant showed to be more sensitive to ionizing and UV radiation and hydrogen peroxide when compared with the wild type strain (*129, 160*). These results showed that the carotenoids are important for the survival of *D. radiodurans*, but it is not the major protection mechanism.

It has been reported that ionizing radiation changes the composition of the cell wall, releasing nucleases, proteases and polysaccharides from the cell wall middle layers (lipid-rich backing and S- layers) to the surrounding media while the constitution of the peptidoglycan layer is maintained (*161-163*). The major polysaccharides released are glucose and N-acylated glucosamine, but a small amount of rhamnose and mannose was also observed (*162*). One known example from a protein that is released is a calcium nuclease (*drb0067*). Mitchel R. E. J. and co-authors observed, in 1975, that this nuclease enzyme is essential during the recovery from ionizing radiation and that nucleoside-5'-monophosphate is the final product of the degradation reaction (*161*). Consequently, when this extracellular nuclease gene (*drb0067*) was deleted, *D. radiodurans* became more sensitive to H_2O_2 and gamma radiation (*164*).

3.4.3 Carbohydrate and phosphate granules

Two types of granules were observed in *D. radiodurans* using electron microscopy: carbohydrate and phosphate granules, known as electron-low and electron-dense granules, respectively (*165-166*).

The carbohydrate granules are oval or circular with a small size that can vary between 10-100 nm in diameter and they are stained with periodic acid-Schiff reagent, specific for carbohydrate molecules. These granules do not appear to have surrounding membranes and are present in a high quantity but in variable number from cell to cell. Some cells appeared crowded with this type of granules (Fig. 3.5) (*165*).

Phosphate granules showed to have a darker edge, which is proposed to have a membrane (*165*). Earlier electron microscopy studies estimated the diameter of these granules to vary between 30-90 nm. However, using cryoelectron microscopy of

vitreous sections with fully hydrated biological material was possible to identify the electron-dense granules more closely to the natural cell conditions. Under these conditions, it was observed that these granules have a spherical form and their diameter can vary between 100 and 400 nm and are localized in the central part of the cells (*167*). Contrarily to the carbohydrate granules, each cell contains only one phosphate granule (Fig. 3.5).

The presence of these structures was observed only in the exponential growth phase. However, in the stationary phase structures was observed that resemble phosphate granules, but without phosphate (*167*).

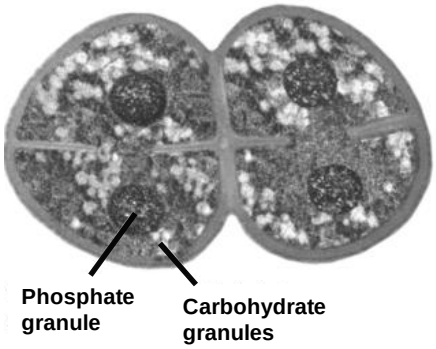

Figure 3.5 - Schematic representation of four *D. radiodurans* cells. One large electron-dense phosphate granule for each cell (dark circles) and several small carbohydrate granules (white circles). Figure adapted from Slade and Radman, 2011 (*100*).

3.4.3.1 Phosphate granules in other organisms

Phosphate granules were observed in organisms belonging to all three life domain, from bacteria to human platelets. They are also known as metachromatic granules, volutin granules and acidocalcisomes (*168-169*), and they can be stained in pink using basic toluidine blue. These granules contain a high amount of phosphate in the form of polyphosphate (short-chain and long-chain) or even pyrophosphate (PPi) (*168-170*). The polyphosphate (polyP) is a linear polymer of orthophosphate residues linked by phosphoanhydride bonds that can vary in size, between ten to one thousand orthophosphate (Pi) residues (*171*) (Fig. 3.6). Moreover it has been observed that these granules contain also high amounts of calcium (Fig. 3.7) (*168, 170, 172*).

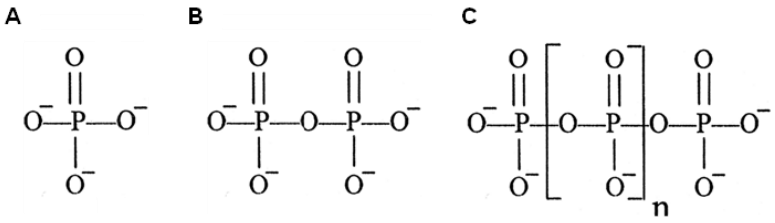

Figure 3.6 – Structure of different phosphate forms. **(A)** Linear orthophosphate, **(B)** Linear pyrophosphate, **(C)** Linear polyphosphate linked by phosphoanhydride bounds. *n* represents the number of phosphate molecules that is repeated in a linear long chain.

For example, in *Rhodospirillum rubrum* and *Agrobacterium tumefaciens*, the granules also contain other cations such as magnesium and potassium, besides pyrophosphate and calcium (Fig. 3.7) (*173-174*). In *Micrococcus lysodeikticus,* phosphate granules contain 27 % of polyphosphate and metals, calcium, sodium, magnesium, potassium, manganese, iron and copper (*175*). In addition, in this organism, the granules also contains 24 % of protein and 30 % of lipids (*175*). Furthermore, several studies performed in Eukaryotic organisms, such as *Trypanosoma cruzi* and *Dictyostelium discoideum*, demonstrated that the granules contain soluble proteins involved in the synthesis or hydrolysis of phosphate, such as polyphosphate kinase (PPK), exopolyphosphatase (PPX) and inorganic pyrophosphatase (PPase) (Fig. 3.7) (see section 3.4.3.2) (*176-178*).

In the membranes of phosphate granules present in some organisms, such as *Rhodospirillum rubrum* and *Trypanosoma cruzi* a number of pumps, channels, including V-H^+-PPase V-H^+-ATPase and V-Ca^{2+}-ATPase (*173-174, 179-180*), cation exchangers, including Na^+/H^+ and Ca^{2+}/H^+ (*181-182*), and an aquaporin were also identified (*183*) (Fig. 3.7).

In conclusion, the discovery of soluble proteins, channels, pumps, cation exchangers, and an aquaporin in these granules shows that they can be regarded subcellular structures with a surrounding membrane, demonstrating that they can be considered as organelles, in which the levels of different metals and phosphate can be regulated (Fig. 3.7).

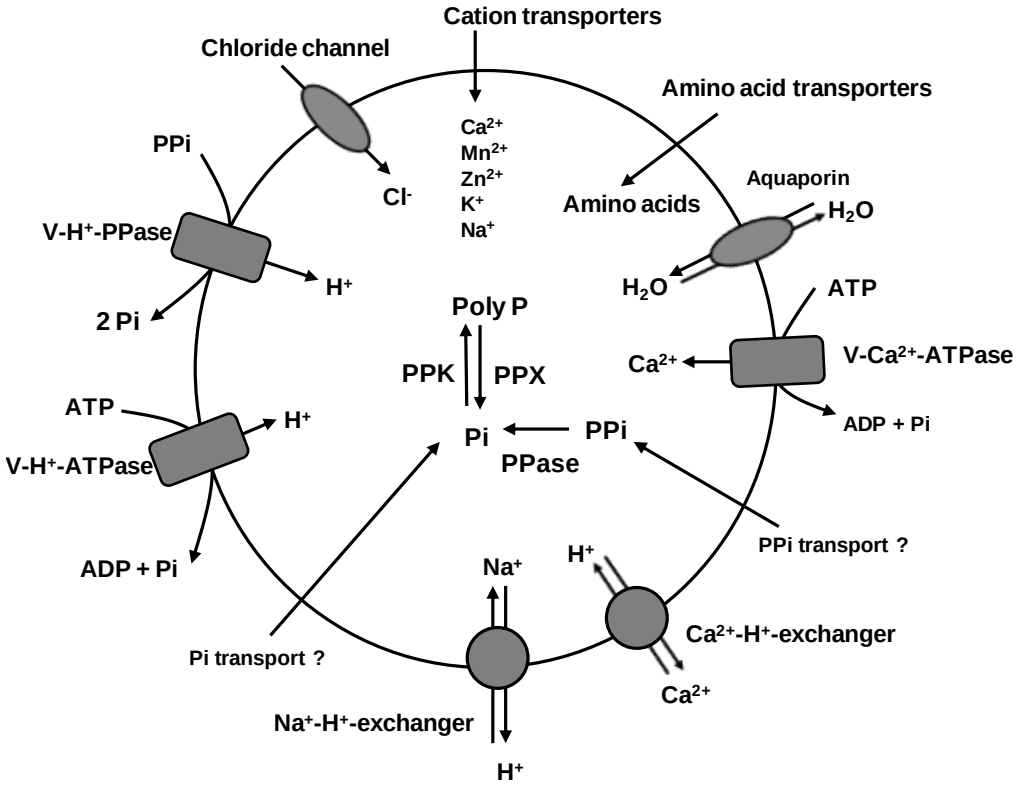

Figure 3.7 - Schematic representation of an acidocalcisome/ phosphate granule from an eukaryote. Phosphate granules can be rich in pyrophosphate (PPi) and/or polyphosphate (polyP), and metals such as manganese, magnesium, calcium, sodium, potassium and zinc. Proteins involved in the polyphosphate (poly P) synthesis and hydrolysis can be present, such as polyphosphate kinase (PPK) and exopolyphosphatase (PPX), or those involved in the hydrolysis of pyrophosphate into orthophosphate (Pi), namely pyrophosphatase (PPase). The presence of different metals in granules can be controlled by pumps, channels and exchangers. For example Ca^{2+} can enter via a vacuolar Ca^{2+}-ATPase and released via Ca^{2+}/H^{+} exchanger that is favored by the interchange of Na^{+}/H^{+}. H^{+} gradient is performed via a vacuolar H^{+}-ATPase and a vacuolar H^{+}-pyrophosphatase (V-H^{+}- PPase). Other transporters can be present, for example for inorganic phosphate (Pi), pyrophosphate transporters (PPi), and amino acids. Aquaporin acts as a water channel. Question marks represent the lack of biochemical evidence for Pi and PPi transporters. Figure adapted from Docampo *et al.*, 2010 (*172*).

3.4.3.2 Enzymes for the synthesis and hydrolysis of polyphosphate

The synthesis of polyphosphate in prokaryotic organisms involves mostly polyphosphate kinase (PPK).

PPK1 enzyme (polyphosphate:ADP phosphotransferase) transfers a terminal phosphate of adenosine triphosphate (ATP) to a $polyP_n$ chain. Although this reaction can be reversible, the synthesis of $polyP_{(n+1)}$ is favorable (reaction 3.5). PPK1 synthesizes polyP using ATP, and Mg^{2+} is also essential for the activation of this enzyme (*72*).

Reaction 3.5

$$ATP + polyP_n \xrightleftharpoons{PPK1\,(Mg^{2+})} ADP + polyP_{n+1}$$

Phosphotransferase reaction catalyzed by PPK1 enzyme

The second polyphosphate kinase, known as PPK2 was identified in a *Pseudomonas aeruginosa* PPK1 knockout mutant. This enzyme synthesizes polyP from ATP or guanosine triphosphate (GTP) and its activity is increased when the growth medium is rich in polyP and when Mg^{2+} is replaced by Mn^{2+}. PPK2 also catalyzes the reversible reaction but more slowly, and in that case it is dependent of Mg^{2+} (Reaction 3.6) (*72*).

Reaction 3.6

$$ATP/GTP + polyP_n \underset{PPK2\,(Mg^{2+})}{\overset{PPK2\,(Mn^{2+})}{\rightleftharpoons}} ADP/GDT + polyP_{n+1}$$

Phosphotransferase reaction catalyzed by PPK2 enzyme

PPK1 has been mostly related with the synthesis of polyphosphate and with pathogenicity of bacteria, however the function of PPK2 is still unknown (*184-185*). PPK are proteins highly conserved in Bacteria and Archaea that are also found in a few Eukaryotes (*87*). However, the study of these proteins has been mainly from bacteria. The presence of PPK1 and/or PPK2 depends on the organism. There are bacteria with only PPK1 such as *E. coli* and *H. pylori*, only PPK2 such as *Staphylococcus aureus* and *K. radiotolerans* or both PPK1 and PPK2 such as *Campylobacter jejuni* and *D. radiodurans* (*87*).

Exopolyphosphatase enzyme (PPX) is responsible for most of the terminal phosphate polyP chain hydrolysis in prokaryotic organisms (Reaction 3.7) (*87-88*).

Reaction 3.7

$$H_2O + polyP_n \xrightarrow{PPX} Pi + polyP_{n-1}$$

Hydrolysis reaction catalyzed by PPX enzyme

PPX1 is found in Bacteria, fungi and protozoa while PPX2 occurs in Bacteria and Archaea. The latter has been demonstrated to have an important role during starvation conditions (*87*). In *E. coli*, two different PPXs were identified, PPX1 and PPX2. PPX1 activity in *E. coli* depends on Mg^{2+} and KCl (*88*), while Ca^{2+} is suggested to be required for the PPK2 activity (*186*). PPX2 from *Corynebacterium glutamicum* requires Mg^{2+} or Mn^{2+} for its activity (*187*).

The uptake and storage of polyphosphate and also its hydrolysis implies phosphate flux inside the cell. The two major transporter systems found in bacteria are the low-affinity phosphate inorganic transporter (Pit system) and the high-affinity phosphate specific transporter (Pst system) (*188*). The Pit transporter is a single transmembrane protein while Pst is formed by five subunits, one phosphate binding protein positioned in the periplasmic space (PstS), two cytoplasmic proteins (ATPases and PstB) and two membrane permeases (PstA and PstC) (*188*).

The Pit transporter allows the influx and the efflux of neutral divalent ions, including Mn^{2+}, Ca^{2+}, Mg^{2+} and Co^{2}, complexed with phosphate (M-Pi). The Pst system is a unidirectional phosphate transporter, but as mentioned above has a higher affinity for phosphate (*188*).

In *D. radiodurans,* synthesis and hydrolysis of polyphosphate can be performed by the two PPK (PPK1-*dr1939* and PPK2-*dr0132*), and one PPX (PPX2-*dra0185*), respectively (*102*). A gene (*dr2576*) that encodes for a putative manganese-dependent inorganic pyrophosphatase (PPase), that converts the pyrophosphate to orthophosphate, was also found is this organism (*170*). The uptake of phosphate can be controlled in *D. radiodurans* by the PitA (*dr0925*) and Pst (PstA, PstB, PstC and PstS) systems (*dra0159, dra0160, dra0158* and *dra0157*) (*102*).

3.4.3.3 Polyphosphate functions

Phosphate granules have been associated with different functions, such as phosphate storage, energy source, cations sequestration and storage, and virulence.

When phosphate reaches a high concentration it can be stored in the granules, for instance in the polyphosphate form. Under phosphate depletion these polyphosphates can then be hydrolyzed by PPX enzyme (*189*).

Polyphosphate can be used as an energy source. It has been reported that in energy rich conditions, accumulation of polyphosphate increases during growth, while

in energy starvation conditions polyphosphate is hydrolyzed (*189-190*). Van Veen *et al.* in 1994 suggested that in *Acinetobacter johnsonii*, the orthophosphate obtained from the polyphosphate hydrolysis by the PPX enzyme can be transported out of the cell originating a transmembrane proton gradient, consequently preserving the energy of the phosphoanhydride bond (*191*).

In the stationary phase the nutrients available decrease, therefore phosphate is used as an energy source. This was shown in the *E. coli ppk* knockout mutant, where only 7 % of the mutant cells survived after two days growth in a limited carbon source medium, when compared with the wild-type strain (*192*).

Polyphosphate that is stored in the phosphate granules can also be associated with sequestration and storage of cations (*173, 193*). For example, the concentration of calcium increases in the granules of *Agrobacterium tumefaciens* in the presence of extracellular calcium (*173*). Furthermore, adaptation (long lag phase) of *Vibrio cholerae ppk* knockout mutant to the media decreases in the presence of high calcium levels when compared with the wild type, suggesting that the phosphate is necessary for metal homeostasis into granules (*194*). Moreover, when different metals, namely magnesium, barium, manganese and strontium were added to the growth medium of *Plectonema boryanum,* all the metals were uptake and incorporated in these granules (*193*). Accumulation of heavy metals in granules was also observed in the bacterium *Acidithiobacillus ferrooxidans*, which tolerates high levels of heavy metals. The mechanism for metal detoxification occurs via hydrolysis of polyphosphate catalyzed by the PPX enzyme, that is stimulated by heavy metals, thus the metal-phosphate complexes are transported out from the cell by phosphate transporters (*195*).

Polyphosphate has also been associated with virulence. It has been observed that polyphosphate is a component of cell capsule and increases the virulence of *Neisseria gonorrhoeae* and *N. meningitides*; *ppk* knockout mutants of these bacteria are more sensitive to the action of human serum (*184, 196*). Polyphosphate present in phosphate granules from *Helicobacter pylori* are involved in the host colonization by this organism (*185*). It is also interesting that the *V. cholera ppk* knockout mutant demonstrates lower motility and attachment to abiotic surfaces (*194*).

In *D. radiodurans*, until now, the function of polyphosphate in granules has not been characterized.

3.4.4 Enzymatic ROS scavenging - SOD and catalases

D. radiodurans has an enzymatic antioxidant system to scavenge ROS which include catalases, superoxide dismutases (SODs) and peroxidases (*100, 102, 146*).

SODs belong to the group of metalloenzymes that catalyze the dismutation of $O_2^{\bullet-}$ to O_2 and H_2O_2 described in chapter II (*197*).

The genome of this organism encodes for four SODs: *dr1279* (MnSOD) with 23.4 kDa, *dr1546* (Cu/ZnSOD$_1$) with 18.7 kDa, *dra0202* (Cu/ZnSOD$_2$) with 48.3 kDa, and *dr0644* with 20.9 kDa (*102*).

In this organism the SOD activity is 32-fold and 19-fold higher in the exponential and stationary phases, respectively, when compared with SOD activity from *E. coli* (*198*). The SOD activity in *D. radiodurans* is also increased (5-fold) when manganese is added (*198*).

MnSOD is constitutively expressed and was shown to be able to efficiently eliminate higher $O_2^{\bullet-}$ concentrations *in vitro* when compared with the MnSODs from *E. coli* and human (*199-200*).

In the *D. radiodurans* Δ*Mnsod* mutant, the SOD activity was completely abolished and this mutant is more sensitive to the effects of ionizing radiation and methyl viologen addition (superoxide radical production) (*201*). These results suggested that MnSOD is the major SOD involved in the neutralization of $O_2^{\bullet-}$ in *D. radiodurans*. However, when *D. radiodurans* was submitted to ionizing radiation, the *Cu/Znsod$_2$* gene was strongly induced in the early stages of stress, suggesting that this SOD is also important for ROS detoxification (*160*).

D. radiodurans genome encodes for three catalases, *dr1998* (KatA) with 60.5 kDa, *dra0259* (KatB) with 84.0 kDa and *dra0146* (KatC) with 40.2 kDa (*100, 102, 146*). It has been reported that KatA and KatB are constitutively expressed enzymes (*122, 198-199*), and in *D. radiodurans* extracts collected during the exponential phase, the catalase activity detected is only due to KatA and KatB. Under these conditions, no catalase activity attributed to KatC. These results were obtained using *D. radiodurans* catalase knockout mutants, Δ*dr1998*, Δ*dra0146*, and Δ*dra0259* (*202*).

This organism has higher catalase activity than *E. coli*, 127-fold higher in the exponential phase and 32-fold higher in the stationary phase (*122*). In the presence of 10 mM H_2O_2 the catalase activity increases in *D. radiodurans*, and under this

condition, this bacterium is much more resistant than *E. coli* (*122*). Catalase activity in *D. radiodurans* is also increased by the addition of 2.5 μM manganese (*198*). Furthermore, the *D. radiodurans* Δ*katA* mutant showed to be sensitive when submitted to high IR doses, 16 and 32 kGy (*201*).

3.4.5 DNA binding proteins from starved conditions (Dps)

D. radiodurans contains two genes that encode for Dps proteins: *Dr*Dps1 (*dr2263*) and *Dr*Dps2 (*drb0092*) (*102*). These two proteins are dodecamers sharing only 16 % amino acid sequence identity (*203-204*) and are structurally similar to Dps from others organisms (Chapter IV). This organism does not possess any gene encoding for ferritins or bacterioferritins, suggesting that in *D. radiodurans* these Dps could play a major role in metal storage (*102*).

Previous studies showed that both *Dr*Dps bind and protect DNA against ROS (*205-206*). However, in *in vitro* conditions *Dr*Dps1 changes its oligomeric state between dimeric and dodecameric forms and only the dimeric form is able to protect the DNA against ROS (*205*). The DNA protection by both *Dr*Dps could be related with its capacity to bind DNA (*205-206*) and/or its capacity to incorporate iron avoiding the Fenton reaction (*203-205*). Furthermore, based on *in vivo* studies *Dr*Dps1 is weakly associated with DNA and is not involved in DNA compaction (*207*). Although the cellular function of *Dr*Dps2 is not yet known, this protein was suggested to be involved in iron storage due to the cellular localization of *Dr*Dps2 and iron, which are both close to the membrane (*69, 206*). The *drdps2* gene is highly induced during recovery, 5-fold immediately after being submitted to 3 kGy of ionizing radiation and 8-fold after 30 min recovery (*119*), suggesting that *Dr*Dps2 can also be involved in cell protection against IR.

The genetic regulation of both *Dr*Dps proteins is not yet clarified. The transcriptional regulators OxyR (*dr0615*) and *Dr*RRA (*dr2418*), two *oxyR* type regulators that respond to peroxide stress, are essential for the regulation of *drdps1*. Both transcriptional regulators are repressors of *drdps1* but have no effect in the regulation of *drdps2* (*208-209*).

3.4.6 Mn/Fe ratio

Intracellular manganese in *D. radiodurans* cells has been proposed to be associated with cell protection against reactive oxygen species.

Leibowitz *et al.* in 1976 showed that *D. radiodurans* has 100 times more manganese then *E. coli* (*83*). Daly and co-authors have also reported that this bacterium has a high intracellular manganese concentration of 2 mM and can accumulate up to 22 mM when the growth medium was supplemented with 10 µM of manganese (*81*). Using electron paramagnetic resonance spectroscopy and X-ray-absorption near edge structure analysis, the predominant form of manganese in *D. radiodurans* was determined, as being Mn^{2+} and the Mn^{3+} form is practically absent (*69*). Using X-ray fluorescence it was possible to observe that manganese is distributed in the cell but with a regional intracellular concentration that was proposed to be related with phosphate granules (*69*). In contrast the intracellular iron concentration in this organism is lower when compared with radiation sensitive organisms (1.8-fold when compared with *E. coli* and 3.3-fold when compared with *S. oneidensis*) (*81*). This metal is mostly localized in the septum region between dividing cells (*69*).

The high intracellular manganese concentration and low iron concentration is reflected in an higher Mn/Fe ratio and the high ratio has been directly related with the capacity to survive in the presence of high ionizing radiation doses and desiccation conditions (*67, 81*). For instance, the radiation resistant organisms such as *D. radiodurans* and *K. radiotolerans* that have a high D_{10} values (D_{10} represents the irradiating dose required to reduce the population by 90%) of 16 and 2 kGy, also have a high Mn/Fe ratio of 0.24 and 0.087, respectively (*81-82*) while the radiation sensitive organisms such as *E. coli* and *S. oneidensis* that have a low D_{10} values (0.7 and 0.07 kGy) have a low Mn/Fe ratio of 0.0072 and 0.0005, respectively (Table 3.1) (*81*).

Table 3.1 - D_{10} survival values, intracellular manganese and iron concentrations and ratio of manganese/iron for radiation resistant organisms (*Deinococcus radiodurans*, *Deinococcus geothermalis*, *Enterococcus faecium*, and *Kineococcus radiotolerans*) and radiation sensitive organisms (*Escherichia coli* and *Shewanella oneidensis*). (ICP-MS: Inductively coupled plasma mass spectrometry).

Strain	D_{10} (kGy)	Total Mn: ICPMS/nmol Mn/mg protein	Total Fe: ICPMS/nmol Fe/mg Protein	Mn/Fe ratio	Reference
D. radiodurans	16	0.36	1.49	0.24	Daly *et al.*, 2004 (*81*)
D. geothermalis	10	0.78	1.7	0.46	Daly *et al.*, 2004 (*81*)
E. faecium	2.0	1.1	6.3	0.17	Daly *et al.*, 2004 (*81*)
K. radiotolerans	2.0	0.075	0.86	0.087	Bagwell *et al.*,2008(*82*)
E. coli	0.7	0.0197	2.72	0.0072	Daly *et al.,* 2004 (*81*)
S. oneidensis	0.07	0.0023	4.98	0.0005	Daly *et al.*, 2004 (*81*)

The role of the high intracellular manganese concentration has been associated with the presence of small manganese complexes (Chapter II) (*78, 89, 100*). It has been shown that the presence of manganese complexes in *D. radiodurans* are involved in the protection against ROS. To emphasize the presence of small complexes, Daly and co-authors showed that manganese is mostly attached to small molecules (less than 3 kDa) (*79*). Furthermore, they demonstrated that the ultrafiltrate obtained from *D. radiodurans* (protein-free cell extracts) has high amounts of manganese (5-fold higher), free amino acids (100-fold higher), nucleotides (35-fold higher) and orthophosphate (5-fold higher) than the ultrafiltrate from *E. coli* (*79*).

The enzymatic activity of endonuclease *Bam*HI in the presence of ultrafiltrate from *D. radiodurans* was preserved after submission to 17.5 kGy of IR or during 66 days of desiccation. A similar experience was done with the ultrafiltrate from the radiation sensitive bacteria *E. coli*, *Pseudomonas putida*, and *Thermus thermophilus*, but in this case the endonuclease *Bam*HI activity was not protected (*79*). Under these conditions high levels of protein oxidation was observed.

Addition of ultrafiltrate from *D. radiodurans* to *E. coli* and human lymphoblastoid Jurkat T cells during growth, protects the cells against 16 kGy of IR, preventing protein oxidation (*79*).

On the other hand, a low iron concentration could be important since iron is less available for promoting the production of ROS, for instance via Fenton and Haber-Weiss reactions (Chapter I, reactions 1.4 and 1.6).

3.4.7 Manganese and iron homeostasis

Iron and manganese are essential metals for many functions. However, when in excess, these elements are toxic to cells (Chapter II). The accumulation of high intracellular Mn^{2+} levels and low Fe^{2+} levels *in D. radiodurans* implies a regulatory system to maintain the Mn/Fe ratio (Table 3.1).

Manganese homeostasis in *D. radiodurans* can be regulated by three types of manganese-dependent transporters (Table 3.2): *Type 1*- Natural resistance-associated macrophage protein (Nramp); the main role of bacterial Nramp homologues is to transport manganese (*210*); in *D. radiodurans* it has been proposed to be responsible for the high manganese accumulation, and it was renamed MntH (*dr1709*) (*210-211*); *Type 2*- ABC-Mn^{2+} transporter (*dr2283*, *dr2284* and *dr2523*), involved in manganese uptake (*212*); *Type 3*- MntE pump *(dr1236)*, responsible for manganese efflux (*213*).

The *mntH* transporter gene is highly induced (4 to 6-fold) when *D. radiodurans* is submitted to 3 kGy of IR and desiccation (*119*), and is not present in radiation sensitive bacteria such as *S. oneidensis* (Scheme 3.2) (*68*). On the other hand, when *D. radiodurans* was submitted to high IR doses (15 kGy) a higher induction of *mntE* gene was observed (Scheme 3.2) (*214*).

Iron homeostasis can be maintained by iron-dependent transporters such as: ABC-heme transporter, ABC-Fe^{3+}-siderophore transporter, Fe^{2+} transporter protein, and ABC-Fe^{3+}-hydroxamate transporter (Table 3.2) (*210*). When *D. radiodurans* cells were submitted to 2 kGy of IR, several iron transporter genes have repressed, including heme transport system (*drb0014* and *drb0016*), Fe^{3+}-hydroxamate transporter (*drb0125*) and one iron chelator (*drb0124*) (*215*). However, in the presence of 15 kGy of IR the Fe^{3+}-siderophore transporter gene (*drb0121*) was up-regulated (Scheme 3.2) (*214*).

Table 3.2 – Several genes and respective proteins involved in metals influx or efflux.

Metal	Gene	Protein annotation
Manganese	*Dr1236*	Manganese efflux transport protein - mntE
	Dr1709	Manganese transport protein, H dependent - mntH
	Dr2283	ABC-Mn^{2+} transport system, permease component
	Dr2284	ABC-Mn^{2+} transport system, ATPase component
	Dr2523	ABC-Mn^{2+} transport system, periplasmic component
Iron	*Dr1219*	Fe^{2+} transport system protein B
	Dr1220	Fe^{2+} transport system protein A
	Dr2588	ABC - Fe^{3+}-hydroxamate transport system
	Dr2589	ABC-iron-siderophores-like
	Dr2590	ABC -cobalamin/Fe^{3+}-siderophores transport system, ATPase component
	Drb0014	ABC-heme transporter, periplasmic binding protein
	Drb0015	ABC-heme transporter, permease protein
	Drb0016	ABC-heme transport system, ATPase component
	Drb0121	ABC-cobalamin/Fe3+-siderophores transport system, ATPase component
	Drb0122/ Drb0123	ABC-iron-siderophores-like
	Dr0124	Iron-chelator utilization protein
	Drb0125	ABC-Fe^{3+}-hydroxamate transport system, periplasmic component

The above described manganese and iron transporters are regulated by Oxy (*dr0615*) (*208*), putative Mn-dependent transcriptional regulator, diphtheria toxin repressor (Dtx) (*dr2539*) (*211, 216*) and Ferric uptake regulator, a Mur regulator homolog (*dr0865*) (Scheme 3.2) (*212*).

The Oxy regulator is a transcriptional activator for the ABC-Fe^{3+}-hydroxamate transporter gene (*drb0125*), while for mntH (*dr1709*) it is a transcriptional repressor (*208*).

The DtxR regulator can be activated by Fe or Mn (*210*) and is a transcriptional repressor for mntH and ABC-Mn^{2+} transporter (*dr2283*) (*211*) or a transcriptional activator of iron transporter genes (*dr1219* and *drb0125*) (Scheme 3.2) (*216*).

The MurR homolog is a positive regulator of the *mntE* gene (*dr1236*) and a negative regulator of Mn transporter genes (*dr2283*, *dr2284* and *dr2523*). Moreover, it was shown that as expected a *mur* mutant accumulates high levels of manganese (Mn^{2+}), and in addition accumulates copper (Cu^{2+}) and zinc (Zn^{2+}), but not iron (Fe^{2+}). Despite the high amount of intracellular manganese, the *mur* mutant displayed a higher sensitivity to the addition of manganese or hydrogen peroxide when it was submitted to gamma and UV radiation.

These results demonstrated that manganese and iron are important for this bacterium. However the homeostasis of other metals should also be considered to be important for the cell (*212*).

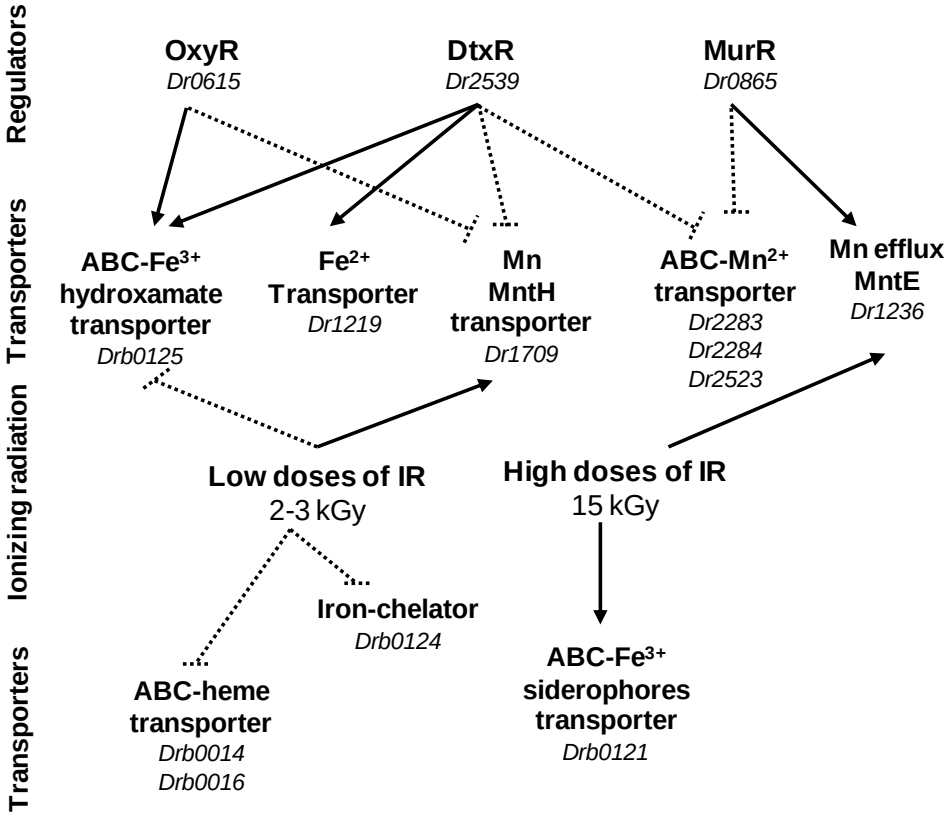

Scheme 3.2 – Schematic representation of different regulators (OxyR, DtxR and MurR) upon different doses of ionizing radiation (low and high) that can activate (solid line) or repress (dot line) different iron or manganese transporters.

3.5 Concluding remarks

D. radiodurans combines a diversity of physiological properties: the unusual cell wall with multilayers, the presence of high amounts of carotenoids in the membrane, the efficiency of DNA repair systems, the effectiveness of enzymatic ROS scavenging systems, the Mn^{2+} complexes with small molecules and low intracellular iron concentration. All these mechanisms are probably closely synchronized and regulated leading to cell protection (Fig. 3.8).

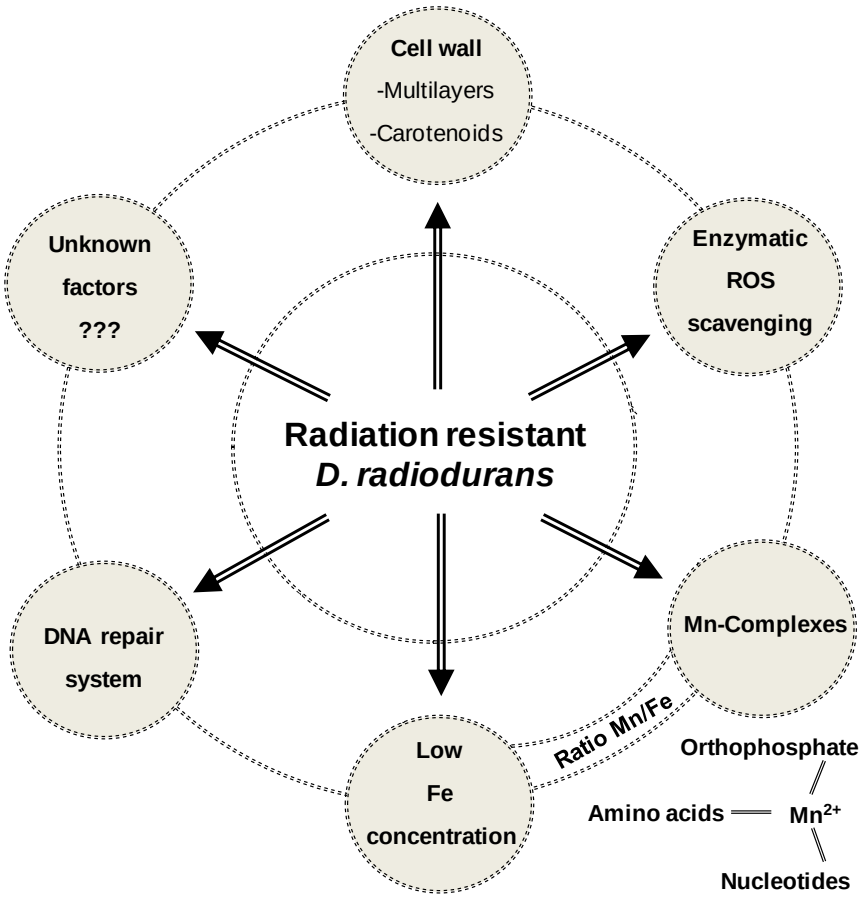

Figure 3.8 - Factors that could contribute to the high resistance of *D. radiodurans.*

CHAPTER IV

DNA binding Proteins from Starved conditions (Dps)

All the structures presented in this chapter were produced with PyMOL (*217-218*).

4.1 General features

DNA binding proteins from starved conditions (Dps) are prokaryotic proteins which have been found mainly in bacteria (*219-220*). Dps proteins belong to the Ferritin family that can be divided in three major sub-families: classical ferritins (Ftn), bacterioferritins (Bfr) containing a heme group, and Dps proteins (*65*). Classical Ftn are found in the three domains of life, and can be divided into Eukaryotic and Prokaryotic ferritins, while bacterioferritins and Dps are only present in Bacteria and Archaea (Fig. 4.1) (*65*).

Several bacteria encode for the three types of proteins, such as *E. coli* (*63, 221-222*), while other bacteria encode only for one or two types. For instance, in *Mycobacterium tuberculosis* a ferritin and a bacterioferritin are present (*223*), while in *D. radiodurans* Dps is the only sub-family present (*102*).

These sub-families are structurally and functionally related, and their main biological function is connected with their iron storage capacity (*65*). However, while ferritins and bacterioferritins have been proposed to be mostly involved in iron storage, Dps have also been associated with DNA protection.

E. coli Dps was the first of these proteins to be identified and it was observed to be highly expressed under starvation conditions and to be involved in the condensation of the nucleoid (*224*). Furthermore, this protein showed iron storage capacity *in vitro*. These two properties (DNA binding and iron storage) can contribute to the DNA protection observed *in vivo*. In fact, *E. coli dps* mutant exhibits higher sensitivity to oxidative DNA damage than the wild type strain (*225*).

The Dps nomenclature is ambiguous and in some cases the name attributed is related with the function that was initially identified. For instance, they appear described as: Dps-like peroxide resistance protein (Dpr) (*226-227*), neutrophil activating protein (NapA) (*228*), metalloregulation DNA-binding stress protein (MrgA) (*229*), amino acid hydrolase (HAA) (*230*) and antigen growth factor (Antigen TpF1) (Table 4.1) (*231*).

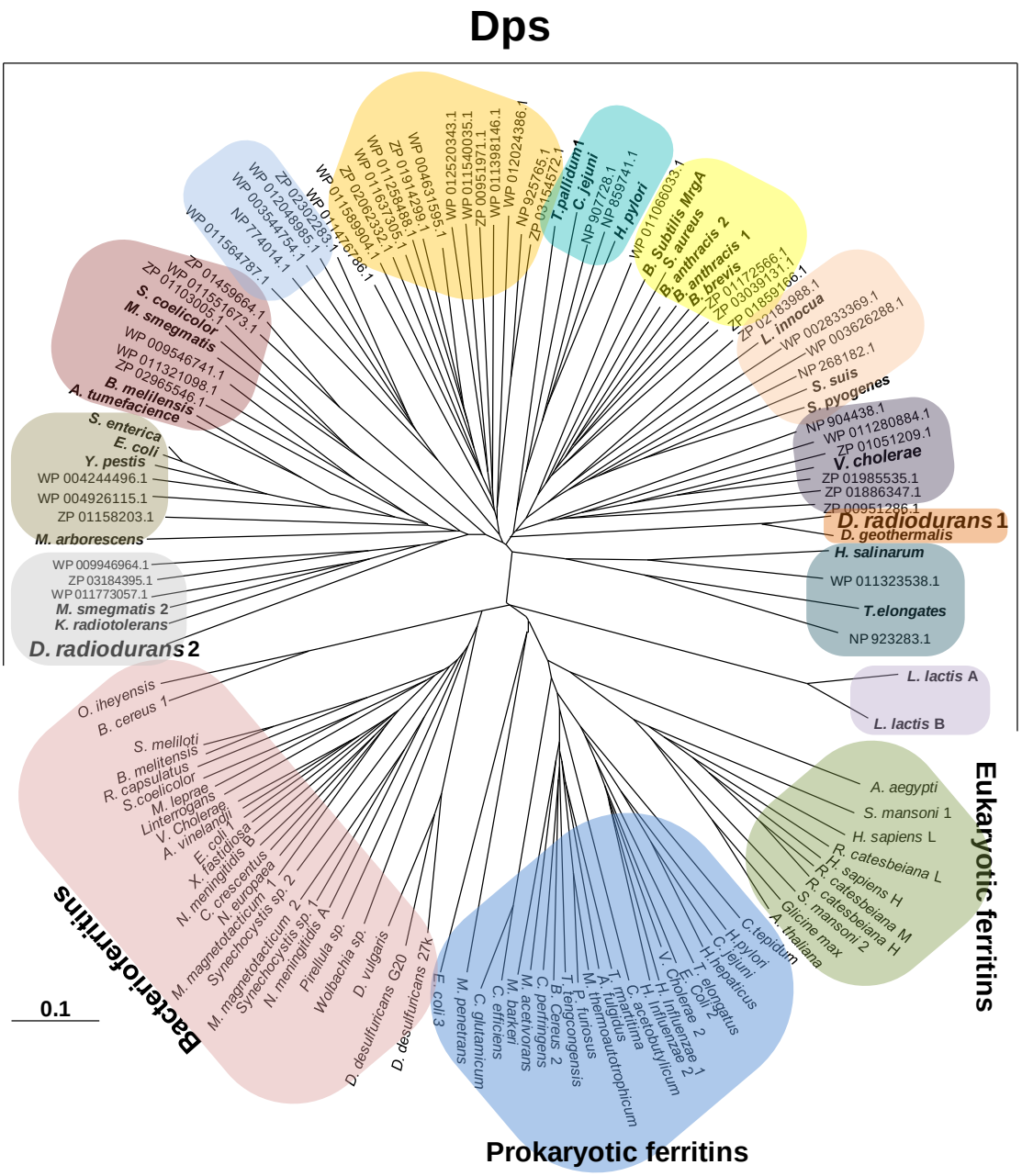

Figure 4.1 - Dendrogram of ferritin family members generated by amino acid sequences retrieved from the data banks (NCB accession number), using a BLAST search. The alignment and dendrogram were constructed using ClustalX 2.1.The tree was displayed with TreeView.

4.2 Structural characteristics

The crystal structure of *E. coli* Dps was determined in 1998 and it was the first protein structure of this family (*232*). Currently several Dps crystal structures have been published, including from pathogenic bacteria (*231, 233-235*) and Archaea (*236*) (Table 4.1).

All Dps structures present a conserved secondary, tertiary and quaternary structure (*203-204, 232, 236-238*). The monomer has a four helix bundle fold, in which the connection between helix B and C contains a loop with a short BC helix in the middle (Fig. 4.2) (*203-204, 232, 238-239*).

The Dps monomer assembles in a 12-mer quaternary structure, forming a spherical hollow dodecameric structure (*203-204, 232, 238*) contrary to ferritins and bacterioferritins proteins that assemble as 24-mers (*65, 222, 240*). The 12-mer assembly results in a 2-fold and a 3-fold symmetry axes, with 23-point-group symmetry (Fig. 4.2) (*203-204, 220*). The dodecameric structure of Dps contains eight 3-fold symmetry axes, that correspond to channels from the dodecamer surface to the internal hollow cavity. Four of these channels are located close to the N-terminal of the monomers and therefore are named “N-terminal channels” (Fig. 4.2, D), and are also found in the ferritin family of proteins. The other four channels are located near the C-terminal of the monomers, are known as “C-terminal channels” and are unique to Dps proteins (Fig. 4.2, E) (*203-204, 210*).

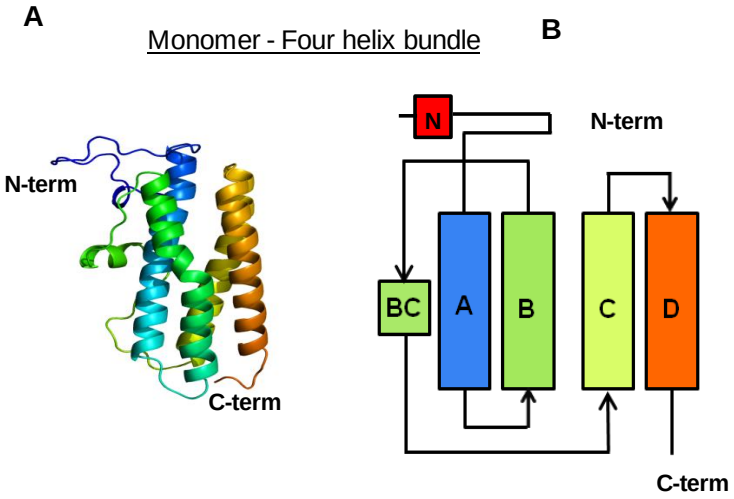

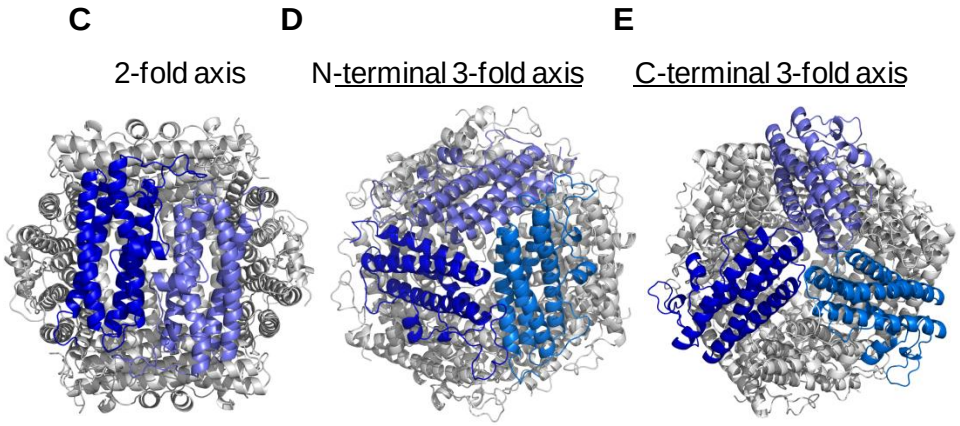

Figure 4.2 – Overall structure of Dps1 from *D. radiodurans*. **(A)** The four helix bundle monomer structure coloured from blue at the N-terminal to orange at the C-terminal (PDB accession code 2C2F). **(B)** Topology diagram of the monomer, showing the organization of the helix-bundle. **(C)** Dodecamer viewed along the two-fold axis. **(D)** Dodecamer viewed along the N-terminal three-fold axis. **(E)** *Dr*Dps1 dodecamer viewed along the C-terminal three-fold axis. Monomers are coloured in grey, except the monomers that form the presented axis that are in blue.

The spherical dodecamer has an external diameter of 80-90 Å and the internal hollow cavity has a diameter of 40-50 Å (*203-204, 220*). In this hollow cavity Dps can store up to 500 iron atoms (*65, 220*). However, it has been reported that some Dps may incorporate less iron, namely the Dps from *Trichodesmium erythraeum* that stores only 260 iron atoms/dodecamer (*64-65, 219-220, 241*). Dps as iron storage proteins have a ferroxidase center and each dodecamer contains twelve ferroxidase centers, related by a 2-fold non-crystallographic symmetry axis, separated by approximately 20 Å (Section 4.3.2, Fig. 4.5, A) (*203-204, 234, 242*).

Although all known Dps crystal structures are dodecameric, other oligomeric forms have been detected in solution: dimers, trimers, or hexamers, with changes in temperature, pH and salt concentration affecting the oligomerization states (*205, 243-244*).

The regions that are less conserved among Dps are the presence or not of N- or C-terminal tails. Frequently, these tails are not modeled in the crystal structures due to the lack of electron density, suggesting that these tails are flexible regions (*203-204, 245*). Nevertheless, in some crystal structures it was possible to observe several amino acid residues in the N- or C-terminal tails. *Lactococcus lactis* DpsB contains a N-terminal with 72 amino acids but in the crystal structure the first 53 amino acids

residues are not visible. The remaining 19 amino acids form a long alpha helix localized outside of the dodecamer surface (*245*).

The N-terminal tail of Dps1 from *D. radiodurans* has 54 amino acid residues in which the first 29 were not visible in the crystal structure. The remaining 25 amino acid residues are located at the dodecamer surface (*203, 246*).

The long N-terminal tail of Dps2 from *D. radiodurans* was also not observed in the corresponding crystal structure (*204*).

The structural properties of these tails, flexibility, localization at the protein surface and the presence of positively charged residues have been associated with the DNA-binding function (Section 4.4). In addition, these N- or C-terminal regions have also been associated with the stabilization of the dodecameric form in solution as showed in mutants without these regions. In the case of Dps from *M. smegmatis* the removal of eitheir N- or C-terminal tail leads to the loss of the dodecameric form, and the observation of lower oligomeric states was detected (*247*). When the C-terminal tail was removed from the Dps2 from *D. radiodurans*, the dodecameric form was no longer observed (*206*).

4.3 Iron storage capacity

The iron storage by Dps occurs in several steps (*63-64, 220*), which will be presented below.

4.3.1 Iron entry

The N-terminal channels have a length of approximately 10 Å and are funnel-shaped with a diameter decreasing from the external to the internal cavity, from around 10 Å to 3 Å, and are negatively charged (*203-204, 210*). The hydrophilicity of these pores is due to the presence of conserved carboxylate groups, 3-fold symmetry-related (Asp and Glu), forming three or four transient binding sites that could lead Fe^{2+} from the outside to the ferroxidase centre (Fig. 4.3), suggesting that iron entry occurs via the N-terminal channels (*203, 210, 230, 242, 244, 248*). This is supported by the presence of iron in this type of channels when the protein crystals were soaked with an iron solution. For example, in *D. radiodurans* Dps1 this channel, with a distance of 16 Å approximately, can be described as having three symmetry-layers of negatively charged residues, 3-fold symmetry-related, Glu_{173}-Asp_{172}-Asp_{181} (T1-T3) that could

lead Fe^{2+} from outside to inside of the cavity, directing the iron to the ferroxidase centre. The crystal structure showed one iron atom octahedrally coordinated by three related aspartate residues, Asp_{181}, and by three symmetry related water molecules (Fig. 4.3, A) (*203*). In the case of *M. arborescens* Dps crystal structure two iron-translocation sites were observed involving the three symmetry-related aspartates, E_{132} (T1), and three glutamines Q_{138} (T2) (Fig. 4.3, B). Unexpectedly, these iron atoms appear as a hexa-hydrated iron complex, instead of free iron. A putative third iron-translocation site, D_{139} (T3) can orient the iron from site T2 to the ferroxidase centre (Fig. 4.3, B) (*230*).

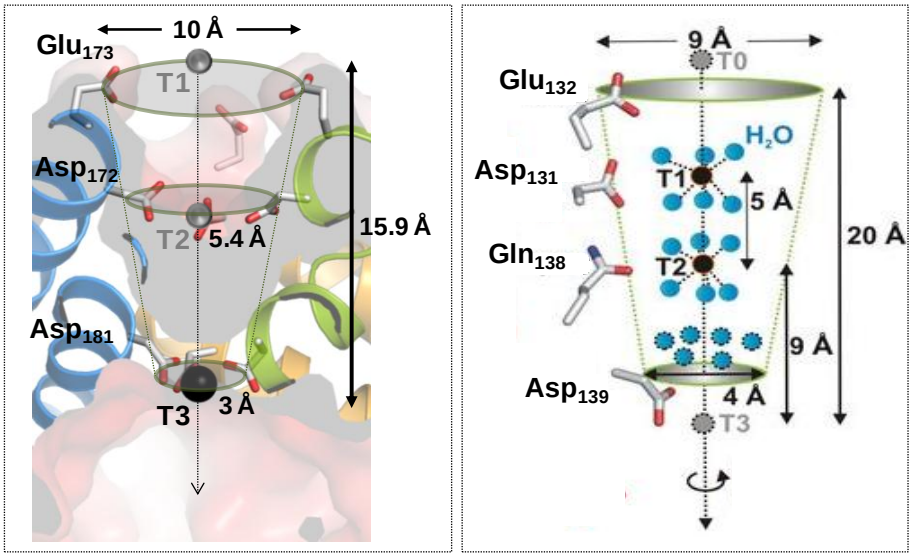

Figura 4.3 - N-terminal channel formed at 3-fold symmetry axis. **(A)** *Dr*Dps1 N-terminal channel is funnel-shaped from outside to inside with an diameter of 10Å - 5.4Å -3Å formed by three layers of negatively charged residues (Glu_{173}-Asp_{172}-Asp_{181}), from 3-fold symmetry-related (Green, blue and orange monomers). Residues involved in iron translocation are depicted in stick representation. Two putative iron sites (T1 and T2) are shown in grey and one iron site (T3) is shown as a black sphere, with a distance between T1-T3 of approximately 16 Å. The dot line along the 3-fold symmetry axis shows the iron direction from outside to inside (T1-T3). The electrostatic surface is represented in red and black. **(B)** *Ma*Dps N-terminal channel is funnel-shaped from outside to inside with an diameter of 9 Å to 4 Å, formed by four layers of amino acids residues (Glu_{132}-Asp_{131}-Gln_{138}-Asp_{181}). Residues involved in iron hexa-aquo cluster translocation are depicted in stick representation. Two iron hexa-aquo clusters (T1 and T2) are observed, diffusing from outside (with an diameter of 9 Å) to the inner cavity of the protein (with a diameter of 4 Å). A putative third iron site (T3) is shown in grey. Distances between the T1, T2 and T3 are shown, 5 Å and 9 Å, respectively. The dotted line along the 3-fold symmetry axis shows the iron direction from outside to inside (T0-T3). Figure adapted from (*203, 249*).

To support the importance of the N-terminal channels in iron entry, studies showed that modification of the channels properties reduced considerably the iron uptake. This was observed when the conserved channel aspartates, were substituted by phenylalanines, altering the chemical environment and reducing the internal diameter of the channel (*250*). Also, replacing the aspartates by asparagines, changing the electrostatic potential of the channel, decreased the rates of Fe^{2+} binding to the ferroxidase centers and of iron oxidation by hydrogen peroxide (*251*).

Besides these N-terminal 3-fold symmetry axis channels, in *Halobacterium salinarum* DpsA 12 channels were observed at the non-symmetrical interface of two subunits, where each channel ends close a ferroxidase centre (Fig. 4.4). In these channels three iron-translocation sites were observed (T1-T3), guiding the iron to the ferroxidase center (F1) (*236, 252*).

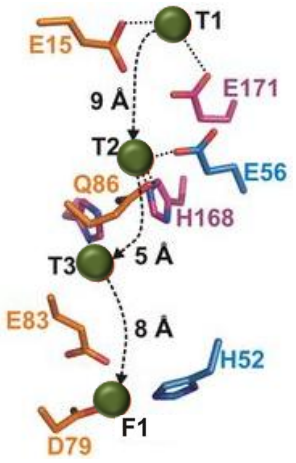

Figure 4.4 - Iron entry channel observed in *H. salinarum* DpsA crystal structure (pdb code: 1TJO). Residues involved in iron translocation are depicted in stick representation. Three iron ions (T1-T3) represented as green spheres, diffused from outside to the ferroxidase centre (F1). Distances between T1, T2, T3 and F1. Figure adapted from [21, 40].

4.3.2 Iron binding and oxidation at ferroxidation centre

In general, this protein family can oxidize Fe^{2+} to Fe^{3+} using preferentially H_2O_2 as oxidant, 100-2000 fold faster than using O_2 as oxidant (*63, 248, 253-254*). Nevertheless, there are some Dps in which the iron oxidation is faster in the presence of both oxidants, O_2 or H_2O_2 such as *Thermosynechococcus elongatus* DpsA or only in presence of O_2 as is case of the *B. anthracis* Dps1 (*254-255*). However, how the oxidation occurs in this case is not known.

Structural studies have contributed to understand the oxidation mechanism in this protein family. As mentioned, Dps crystal structures contain twelve ferroxidase

centers, related by a 2-fold non-crystallographic symmetry axis, at a distance of approximately 20 Å from each other (Fig. 4.5, A) (*203-204, 234, 242*). This catalytic site is the basis for Dps proteins to bind and oxidize Fe^{2+} to Fe^{3+}.

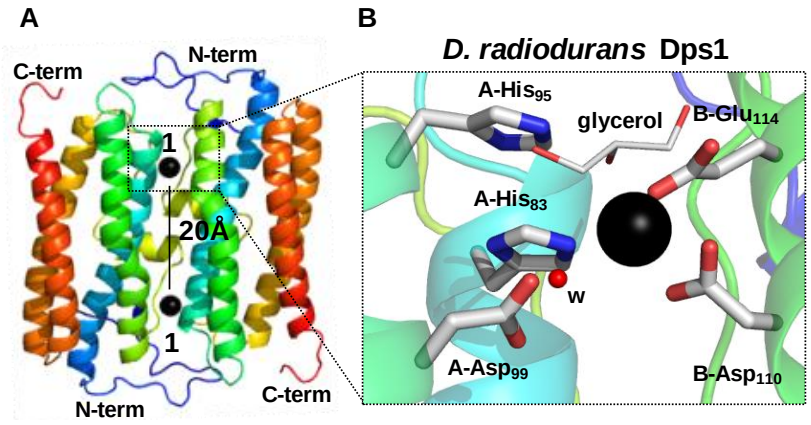

Figure 4.5 - Dimer interface viewed from the 2-fold axis of *D. radiodurans* Dps1 exhibiting the conserved mono-iron ferroxidase centre. **(A)** Dimer interface shows two mono-iron ferroxidase centres at an distance of 20 Å; represented as black spheres. **(B)** Zoomed-in view of the mono-iron ferroxidase centre, which is coordinated by three residues: His_{83} from subunit A, Asp_{110} (bidentate) and Glu_{114} (monodentate) from subunit B. Two non-protein ligands: water (w) and a glycerol molecule are also represented. PDB code: 2C2F. The waters are represented in red and labeled as "w". Residues from subunit A and B are prefixed with A- and B-, respectively.

The single iron atom in the ferroxidase center is coordinated by the following amino acids residues: one aspartate and one glutamate from one subunit and one histidine from the symmetry related monomer. Based on the several Dps crystal structures, one or two additional solvent molecules have been observed to be involved in the iron coordination. One of the solvent molecules forms a hydrogen bond with a conserved histidine, while the other solvent molecule (when present) is hydrogen-bonded with residues that can be aspartate, glutamine or glutamate (Fig. 4.5). The general binding motif can be represented as (**His**X_{11}HisX$_3$Asp/Gln/Glu)(**Asp**X_3**Glu**), where residues in bold correspond to the iron ligands, and in grey those that are involved in hydrogen bonds to the solvent molecules bound to the iron. The *H. salinarum* DpsA is an exception, with a binding motif (**His**X_{11}**His**)(**AspGlu**X_2**Glu**) (Fig. 4.6, E). The iron coordination observed in the different crystal structures so far known is either octahedral or tetrahedral (*203, 234, 242*).

In some cases, the presence of a second iron site (site 2) was observed close to the first iron atom (site 1). The distance from these two sites varies from 3 Å to 6 Å (Fig. 4.6) (*204, 210, 256*).

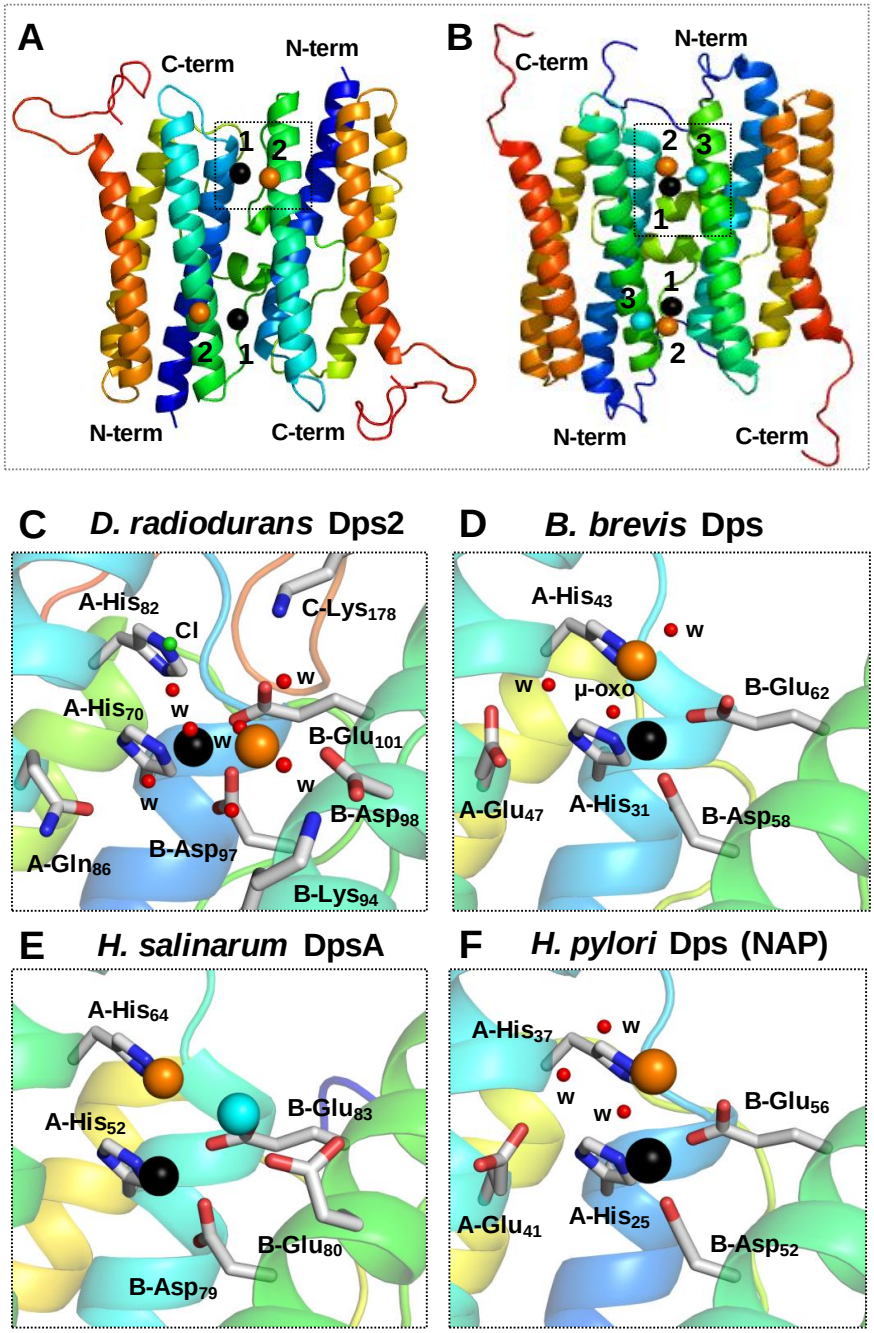

Figure 4.6 - Dimer interface viewed from the 2-fold axis of Dps exhibiting more than one metal

in the ferroxidase centre. The metal sites are represented as a black sphere (site1), orange sphere (site2) or cyan sphere (site3). **(A)** *D. radiodurans* Dps2 which contains two irons, site1 and site2 **(B)** *H. salinarum* Dps containing three irons (site1, site2 and site3). Zoomed-in view of the ferroxidase centre for **(C)** *D. radiodurans* Dps2 showing two irons (PDB code: 2C6R); **(D)** *B. brevis* Dps showing two irons (PDB code: 1N1Q); **(E)** *H. salinarum* Dps showing three irons (PDB code: 1TJO) and **(F)** *H. pylori* Dps (NAP) with two zincs (PDB code: 4EVB). The waters are represented in red and labeled as "w". The μ-oxo bridge in the panel D is represented in red and labeled as μ-oxo. Residues from subunit A and B are prefixed with A- and B-, respectively.

In the case of *D. radiodurans* Dps2 this second iron ion (site 2) is loosely coordinated by one amino acid residue, Asp_{98}, and via 5 water molecules, three of which form hydrogen-bonds with Lys_{94} (two hydrogen-bonds) and Lys_{178} (Fig. 4.6, C) (*204*).

In the *Bacillus brevis* Dps the second iron is coordinated via two water molecules that are hydrogen-bonded with Glu_{47} and His_{43} (Fig. 4.6, D). In addition one of the residues which coordinate the iron in site 1, Glu_{62}, is at a distance of 3.6 Å from the iron in site 2. Furthermore, in this *B. brevis* Dps structure a μ-oxo bridge was observed between the two irons (Fig. 4.6, D) (*256*).

In the case of *H. salinarum* DpsA, a third site (site 3) was also observed besides the second site (site 2) (Fig. 4.6, B and E). Both sites were proposed to be transiently occupied by iron, since they were only observed when the crystal was soaked during 30 min in an iron solution, while when the crystal was soaked for 120 min, only the site 1 was occupied by iron (*236*). These results and the loose coordination of the second and third iron atoms observed in the examples mentioned above, led to the suggestion that they represent intermediates during the iron incorporation mechanism (*204, 236*).

The presence of other metals has also been described in the ferroxidase centre when the crystals were incubated with divalent metals. For example, the *H. pylori* Dps (NAP) showed two sites (Site 1 and 2) occupied by zinc (Fig. 4.6, F) or cadmium forming a di-metal site in which the second metal site is also loosely coordinated (*210*).

4.3.3 Iron nucleation

The nucleation mechanism starts after migration of Fe^{3+} to the cavity of Dps, but how this occurs in Dps proteins is poorly understood (*63-64*). In classical ferritins it is known that the formation of the core occurs of several nucleation sites, formed by clusters of glutamate amino acids residues (*257-259*).

The iron migration to the nucleation sites and the nucleation process initiation in Dps proteins has been associated with the properties of the internal hollow cavity that is highly negatively charged due to existence of carboxylate residues, forming a perfect environment for iron storage similar to ferritins (*203-204, 236, 242*).The importance of this negatively charged cavity is evidenced in the crystal structure of *H. salinarum* DpsA. In this structure were observed two iron nucleation sites. One site is located close to the 2-fold symmetry axis (NI), where three iron peaks are observed (N11-N13) and due to the proximity of four amino acids, two Glu_{72} and two Glu_{75} symmetry-related, the iron nucleation core can be formed (Fig. 4.7).

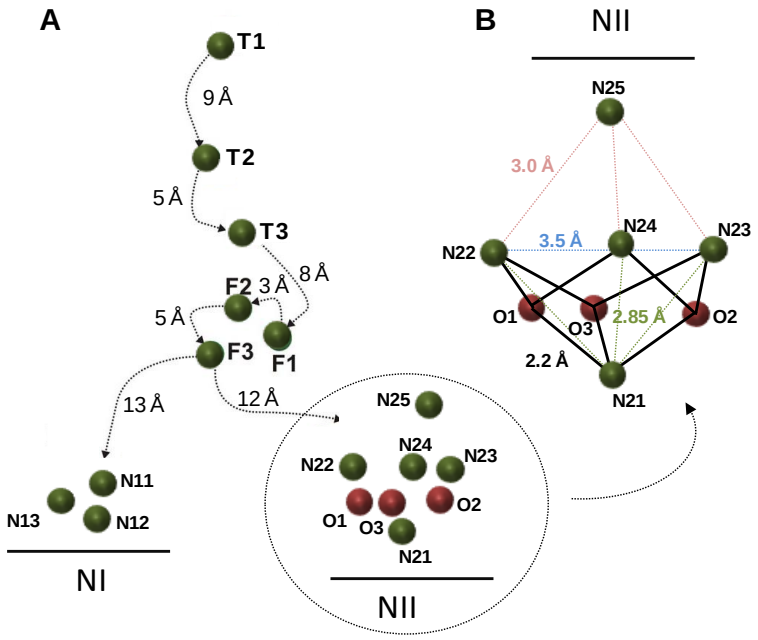

Figure 4.7 - Iron translocation, oxidation and storage pathway of *H. salinarum* DpsA. **(A)** Three translocation iron sites were observed (T1-T3) with a distance of 9 Å and 5 Å, respectively. T3 is close to the ferroxidase iron centre (F1), at a distance of 8 Å. In addition, close to the ferroxidase centre (F1), two iron sites (F2 and F3 sites) at a distance of 3 Å and 5 Å were observed and eight iron sites are occupied at a distance of 12-13 Å from F3 site. Three iron

peaks (N11-N13) were observed in nucleation site I (NI), five iron peaks and three oxygen atoms (O1-O3) were detected in the nucleation site II (NII). **(B)** Schematic view of the NII iron cluster, forming a distorted tetrahedron, appearing as an iron-oxide nanocluster. Symmetry equivalent distances between iron-iron and iron-oxygen atoms are marked, and the respective distances are given. The irons atoms are represented as green spheres and oxygen atoms as pink spheres. Figure adapted from (*249*).

The second iron nucleation site (NII) is coordinated by three symmetry Glu_{154}, where five iron peaks are observed (N21-N25) and three oxygens atoms (O1-O3) (Fig. 4.7, A). The translocation of iron between the ferroxidase iron centre and the nucleation sites, which are at a distance of *ca.* 12-13 Å, can be assisted by other negatively charged residues that are present in this DpsA, such as Glu_{158} and Glu_{161}, which are located at 6 Å from the ferroxidase centre and the nucleation sites (*236*).

4.3.4 Iron mineralization

Using kinetic studies of the Dps from *E. coli* or *L. innocua* it was proposed that the iron mineralization starts when iron accumulates in the nucleation sites as a ferric oxide hydroxide (Fe(O)OH) until *ca.* 500 iron atoms per Dps dodecamer are uptake (reaction 4.1), as observed for classical ferritins for up to 4500 iron atoms (*63-64*).

Reaction 4.1 $2Fe^{2+} + H_2O_2 + 2H_2O \longrightarrow 2Fe(O)OH + 4H^+$

Iron incorporation as hydrous ferric oxide core

However, other types of iron core have been described. For example, in the structure of *H. salinarum* DpsA the accumulation of five irons and three oxygens was observed in the core. These subsites are arranged as a distorted tetrahedron, forming an iron-oxide nanocluster, [4Fe-3O] cluster (Fig. 4.7, B) (*236*).

The incorporation of phosphate was observed in *T.* e*rythraeum* Dps, with an iron:phosphate (Fe:Pi) ratio of 4:1 (*241*). Phosphate incorporation has not been described for other Dps proteins, although both ferritins and bacterioferritins have the capacity to bind and incorporate phosphate; this incorporation depends on the presence of iron (*260-261*). In ferritins, it has been observed that the Fe:Pi incorporation ratio can vary from 2:1 to 20:1, forming a hydrated iron oxide-phosphate complex core $(Fe(O)OH)_8(FeO\text{-}OPO_3H_2)$ (*261-262*).

4.3.5 Iron release

In *in vitro* conditions, it was demonstrated that these proteins have the capacity to release iron by using reductants, namely sodium dithionite or a nicotinamide adenine dinucleotide / flavin mononucleotide mixture (NADH/FMN) (*251, 263-264*). However, the iron release mechanism is poorly understood. It has been suggested that it can occur via N- or C-terminal channels. Nevertheless, the C-terminal channels are in general blocked by hydrophobic residues. For example, the *T. elongatus* Dps contains three symmetrically related valines (Val_{157}), *D. radiodurans* Dps2 has phenylalanines (Phe_{198}) while *E. coli* Dps contain alanines (Ala_{57}) in the external surface of these channels (*203-204, 248*). However, they can act as an auxiliary route for iron passage, after some structural rearrangements, since iron in these channels has been observed in Dps structures (*203-204*). For example, in *D. radiodurans* Dps2, the C-terminal channel is defined by Asp_{87}-Glu_{83}-Tyr_{79}-Thr_{80}-Leu_{77}-Thr_{76}-Asp_{199}-Phe_{198} from the inside to the outside of the dodecamer. This C-terminal channel appears blocked by residue Phe_{198} avoiding the transit of cations along the channel. However an alternative route for cations was formed by residues Thr_{76}-Asp_{133}-Asp_{199}-Ile_{200} and one iron site was observed in this route (*204*).

In addition, it was observed that *T. erythraeum* Dps that stores iron and phosphate as aboved mentioned, is also capable of releasing phosphate as pyrophosphate or orthophosphate. The incorporated phosphate is bound at the surface of the iron core, and during the release process phosphate is the first to be released followed by iron (*261*).

In summary, considering the structural properties and functional kinetics studies in Dps, the iron storage mechanism has been proposed to occur in several steps: Fe^{2+} entry through N-terminal channels (Fig. 4.8, step 1) ; Fe^{2+} binding to the ferroxidase centre (Fig. 4.8, step 2); Fe^{2+} oxidation in the ferroxidase centre (Fig. 4.8, step 3); Fe^{3+} translocation to nucleation sites located inside the internal hollow sphere cavity (Fig. 4.8, step 4) where the mineralization starts (Fig. 4.8, step 5) (*63-64, 220*). Furthermore, the iron incorporated in the hollow cavity of Dps proteins can be reutilized during iron limitation (Fig. 4.8, step 6) and released by N- or C-terminal channels to the cytosol where it can be re-used (Fig. 4.8, step 7).

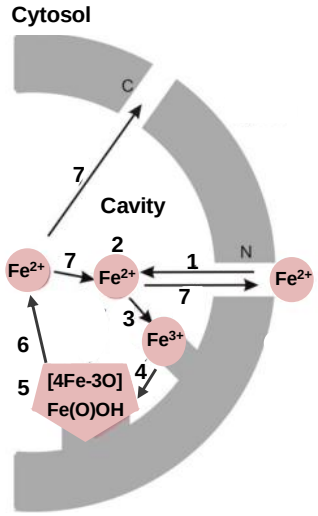

Figure 4.8 - A schematic representation of Dps hypothetical mechanism for iron storage into the internal hollow cavity and release. This mechanism can be divided into several steps. **Iron incorporation:** ***Step 1:*** Fe^{2+} entry by N-terminal channels, ***Step 2:*** Fe^{2+} binds to ferroxidase centre, ***Step 3:*** iron oxidization to Fe^{3+}, ***Step 4:*** Fe^{3+} moving to the nucleation site, ***Step 5:*** mineralization starts with the accumulation of oxyhydroxide core or 4-iron-3-oxo cluster at the nucleation sites. **Iron release: *Step 6:*** iron in Fe^{3+}(O)OH or [4Fe-3O] form is reduced to Fe^{2+}, ***Step 7:*** after reduction it can be transported to the external medium (e.g. cytosol) by N- or C- terminal channels. Figure adapted from Haikarainen *et. al*, 2010 (*220*).

4.4 DNA-binding ability

Despite the lack of any classical DNA-binding motifs, Dps proteins have N- or C-terminal tails which are not conserved but in some cases have been associated with the DNA-binding ability (*65, 219, 237, 247*). Structurally, these tails are flexible, localized outside the dodecamer sphere and contain positively charged amino acid residues which can contribute to the interaction with DNA (*203-204, 245*). Several studies have been performed demonstrating the vital importance of these tails for the binding to DNA, using mainly electrophoretic mobility shifts assays (EMSA) and atomic force microscopy (AFM) (*265-268*).

E. coli Dps has a long N-terminal tail with 22 amino acid residues, in which three lysines and one arginine (Lys_5, Lys_8 and Lys_{10} and Arg_{18}) are present (*232*). It was possible to observe that this Dps can bind and condense DNA forming Dps-DNA complexes, while a construct of this Dps lacking the N-terminal tail does not have the ability to promote DNA condensation and the DNA binding ability was strongly diminished (*265*).

Mycobacterium smegmatis Dps1 has a long C-terminal tail with 26 amino acid residues in which five of those are positively charged (Lys_{172}, Lys_{177}, Arg_{179}, Arg_{180} and Lsy_{181}), and it was demonstrated that these residues are essential for the binding to DNA (*247*).

D. radiodurans Dps1 has a long N-terminal tail which can be divided in two regions, of which have been shown to interact with DNA. The first region, (amino acid residues 1-29) contains seven positively charged residues (Lys_3, Lys_4, Lys_7, Lys_{13}, Lys_{15}, Lys_{16} and Arg_{27}). The second region (amino acid residues 30-54) contains a zinc binding site, and it was observed that in the absence of metal the DNA binding ability decreased. Furthermore, a positively charged Arg_{132} present in loop BC exposed at the external dodecamer surface was also proposed to contribute to the DNA-binding ability of this protein (*269-271*).

However, the ability to bind DNA is not limited to the presence of the positively charged regions, located at the N- or C-terminals. For example, the *Helicobacter pylori* Dps has positively charged amino acid residues located in the dodecamer surface that were proposed to bind to the negatively charged phosphate group from the DNA (*268*).

4.4.1 DNA packing

Characterization of the packing of Dps-DNA complexes has been addressed mostly by electron microscopy studies. Using this technique it was observed that Dps dodecamers form a 2-dimensional crystal with hexagonal packing (*272-273*). Addition of supercoiled DNA, linear double-stranded DNA or single-stranded RNA immediately leads to the formation of several tightly packed Dps-DNA and Dps-RNA co-crystals with three-dimensional morphology (*243, 272*). However, the addition of DNA/RNA does not disturb the Dps dodecamer hexagonal packing (*272-274*). These results suggest a model where DNA molecules can pack between the layers of Dps dodecamers (Fig. 4.9) (*273*). Under *in vivo* conditions the same type of DNA packing was observed for *E. coli* under starvation conditions, where the Dps protein is highly expressed when compared with other proteins (*272, 275*). This hexagonal DNA packing is no longer observed in the *E. coli dps* mutant, where DNA adopts a similar structure as observed in the exponential phase cells (*272-273*).

The different crystal packing observed for Dps dodecamers was used to suggest different models for the DNA-Dps complexes, in which DNA molecules are kept highly protected from the different stress conditions, conferring a physical DNA protection. *Bacillus brevis* Dps shows a similar multi-layered structure as mentioned, with an

hexagonal arrangement where DNA can be packed between hexagonal layers (Fig. 4.9, A) (*256*).

However, other studies suggested that DNA is included in holes formed between three adjacent Dps dodecamers with hexagonal packing, where the N-terminal tails are located (Fig. 4.9, B) (*232, 256*).

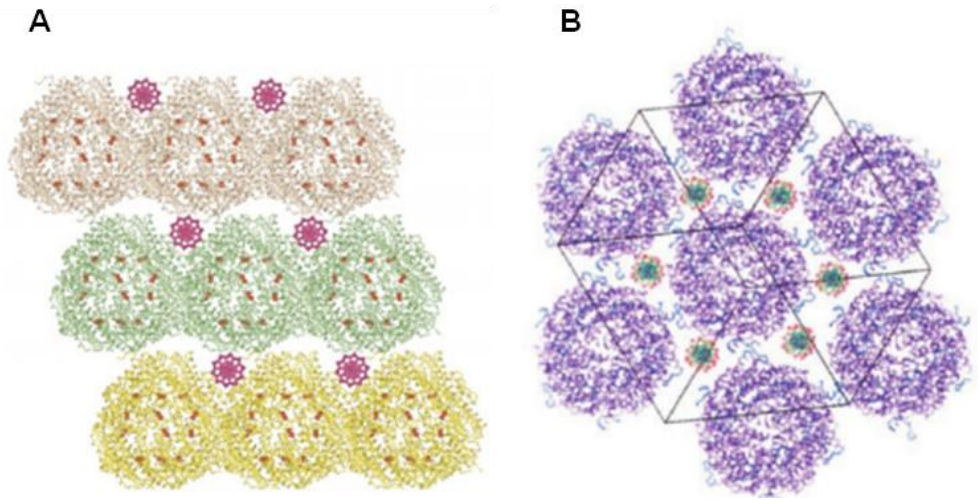

Figure 4.9 - Representation of two models for DNA-Dps complexes formation with hexagonal packing. **(A)** DNA molecules are accommodated in the holes between alternate layers of Dps dodecamers. DNA molecules are represented in pink colour and Dps dodecamer layers are represented in yellow, green and grey colours. **(B)** DNA molecules can pack in the holes formed by three dodecamers. DNA molecules are represented in green and the phosphate groups of the DNA are in pink; Dps dodecamers are coloured purple with their N-terminal tails in blue. The black line represents the cell unit from the crystal packing. Figure adapted from Ren *et. al*, 2003 (*256*) and Grant *et. al*, 1998 (*232*).

4.5 DNA protection

Dps proteins could have an important role on DNA protection from ROS by two mechanisms: iron storage and/or DNA binding [6].

DNA protection by Dps can occur only by its iron storage capacity. *M. smegmatis* Dps1 protein has ferroxidase activity and binds to DNA but does not promote its condensation, thus DNA-Dps complexes are not formed. In this case this protein shows the ability to protect DNA against ROS by its storage iron capacity but not against DNase, since it does not condense the DNA (*267*).

The importance of DNA-binding ability forming DNA-Dps complexes in the DNA protection mechanism is evident in the studies of the two *L. lactis* Dps which are not able to store iron, due to lack of a ferroxidase center and a negatively charged environment in the internal cavity. However, both Dps formed complexes with DNA which is enough to protect the DNA against ROS and methylation promoted damage (*245*).

As mentioned before, the *E. coli* Dps protein has the capacity to oxidize iron and to bind and condense DNA, conferring a high DNA protection by two mechanisms. The mechanism of DNA protection through iron storage using preferentially H_2O_2 as oxidant is a vital function of these proteins (*63-64, 253*). The simultaneous removal of Fe^{2+} and H_2O_2 leads to a strong inhibition of hydroxyl radical formation that could promote the damage of DNA molecules via Fenton reaction (reaction 1.4, Chapter I). Dps spin trapping experiments using an EMPO probe, that traps hydroxyl radicals yielding a specific electron paramagnetic resonance signal (EMPO-OH adduct) was used to demonstrated that in the presence of *E. coli* Dps the hydroxyl radical production was strongly decreased (*63*). Furthermore, in similar conditions, it was possible to observe using EMSA assays that upon addition of Dps the DNA is protected, while in its absence DNA was completely degraded (*63*).

DNA protection by *E. coli* Dps through its DNA binding capacity forming DNA-Dps complexes was observed using atomic force microscopy and EMSA (*265*). This capacity to form DNA-Dps complexes was also observed under *in vivo* conditions in the stationary phase in starvation conditions as mentioned in section 4.4.1 (*276*).

These two properties can confer higher capacity to protect DNA *in vitro* but also *in vivo*, since the *E. coli dps* mutant becomes more sensitive when compared with the wild type, mainly in the stationary phase under several conditions such as hydrogen peroxide, UV radiation, gamma radiation, iron and copper stresses (*276*).

4.6 Multifaceted functions of Dps proteins

Apart from the protection against oxidative stress, in the last decades it has been reported that Dps proteins are also involved on other functions, such as resistance against heat or cold shock (*276-277*), high-pressure stress (*278*), gamma or UV irradiation (*276*) and acid or base shock (*276, 279-280*). The participation of Dps in hydrolysis and synthesis of N-acylamino acids has been described (*230*). The

importance of Dps in antibiotic resistance such as streptomycin, nalidixic acid, norfloxacin and rifampicin was also reported. Moreover, it has been shown that Dps from several pathogenic bacteria can be involved in virulence (Table 4.1) (*281-282*). The pathogenic organisms lacking the *dps* gene have been shown to be hypersensitive to bactericidal antibiotics or less virulent (*228, 281, 283*). In patient sera with several gastric diseases caused by *H. pylori* specific antibodies for the Dps which is known as neutrophil activating protein (NAP) were found. In addition, it was shown that the NAP protein is crucial for the colonization of mice by of the bacterium, and when mice were vaccinated with *Hp*NAP, they became more resistant to *H. pylori* infections (*228, 284*).

Campylobacter jejuni Dps has also been found associated with the virulence of this organism. These studies indicated that Dps invades the host, and its virulence was associated with its ability to bind and damage the peripheral nerves under *in vivo* conditions (*285-286*). In patients with an axonal form of Guillain–Barré syndrome (GBS) caused by this bacterium the Dps and its specific antibodies were found in the serum (*285*). The Dps protein is also essential for biofilm formation and host colonization by *C. jejuni* (*283*).

Dps protein from *Listeria monocytogenes*, a food borne pathogen, is vital for the proliferation in the host. Moreover, the absence of this *dps* gene leads to a decrease in survival during starvation, oxidative stress or iron depletion conditions (*287*), probably inhibiting bacterial proliferation.

Another example of Dps involved in virulence is the glycosylated Dps from *Salmonella enterica* serovar Typhimurium (*288-289*). The glycosylation of this protein could be essential for the virulence of this bacterium since the glycosylation of diverse proteins has been associated with different functions, including adhesion and colonization of host cells (*289-290*). In addition, a Δ*dps* mutant of *Salmonella enterica* strain, became hypersensitive to bactericidal antibiotics (*281*).

In conclusion, Dps proteins from pathogenic organisms are involved mostly in biofilm formation, adhesion and colonization of host cells. It has been described that prokaryotic organisms have the competence to release proteins involved in the ROS detoxification to the extracellular space, including Dps proteins. The presence of Dps proteins during bacterial invasion could be essential for their protection against ROS, which are produced by phagocytic cells to kill invading bacteria (*291*).

4.7 More than one Dps in the same organism

The genomes of most known prokaryotes contain only one Dps encoding gene. However there are bacteria which contain two, three or four types of Dps (*102, 234, 255, 292-294*), at least one of which appears to have different oligomeric states in solution (*205, 243-245*).

M. smegmatis encodes for two Dps: Dps1 and Dps2. *In vitro*, Dps2 assembles in a stable dodecameric form, while in solution Dps1 has two oligomeric states: trimeric and dodecameric, which are regulated by temperature. The Dps1 dodecamer is the only oligomeric state that has the ability to bind and condense DNA, protecting the DNA against DNase; furthermore, it incorporates iron, protecting the DNA against ROS promoted degradation. The Dps1 trimer displays ferroxidase activity using O_2 as oxidant, similar to the ferroxidase activity found in the ferritin family (*243*). However, there is no information about these oligomeric states *in vivo*. In fact, the oxidation of Fe^{2+} to Fe^{3+} by the trimeric form, leads to a free Fe^{3+} in the cell, which will be consequently unavailable to be used by cell. Therefore, the role of this trimeric form in iron oxidation remains to be established *in vivo*. In addition, it was observed *in vivo* that both Dps1 and Dps2 bind to DNA forming different DNA-Dps complexes (*295*), thus probably conferring different levels of protection.

D. radiodurans also has two Dps; In solution, *Dr*Dps1 can vary its oligomeric state. Both the dimeric and the dodecameric form have DNA-binding ability but it has been reported that only the dimeric form was associated with DNA protection against ROS and DNase cleavage (*205*). On the other hand, *Dr*Dps2 was mainly associated with iron storage capacity as a dodecamer (*206*).

In *Bacillus anthracis,* Dps2 uses preferentially H_2O_2 as oxidant while Dps1 uses only O_2 (*254*). It can be speculated that under stress conditions, the bacterium would use mostly Dps2 to detoxify hydrogen peroxide and consequently incorporate iron, while in non-stress conditions the iron would be incorporated by Dps1 using oxygen as oxidant.

S*treptomyces coelicolor* contains three Dps: DpsA, DpsB and DpsC. It was observed that *in vitro* DpsB is a dimer, DpsC is a dodecamer while DpsA varies its oligomeric state between, dimer, hexamer and dodecamer in solution. As a dodecamer and hexamer, Dps can store iron using H_2O_2 as oxidant. However, no function was been attributed to the dimer form of DpsA or DpsB (*244*). *In vivo*, the

three Dps are proposed to be involved in the nucleoid condensation but are not induced in response to oxidative stress. In addition, DpsA is vital for the pre-spore compartment formation, after osmotic and heat stress during vegetative growth (*293, 296*). The multifaceted roles of DpsA may be related with its oligomeric states that changes under different conditions.

The cyanobacterium *Anabaena* PCC7120 contains four Dps proteins: Dps"all1173", Dps"all4145", Dps"all0458" and Dps"alr3808" (*297*). Two of these proteins, Dps"all1173" and Dps"all0458" are dodecamers, localized in the nucleoid region. Both have iron storage capacity and are able to protect DNA against H_2O_2 stress (*294, 297*). The *Anabaena dps"all0458"* mutant is more sensitive to cold stress, and under this condition an increase of the expression level of Dps"alr3808 was observed. However, it is important to mention that Dps"alr3808 is spread throughout the cell, while Dps"all0458" is localized in the nucleoid (*297*). These results suggested that more than one Dps are involved in the protection mechanism, contributing to the resistance of this organism under stress conditions. Furthermore, in this cyanobacterium, during growth supplemented with ammonia, several proteins involved in ROS detoxification are found in the extracellular space, including three Dps; Dps"all4145", Dps"all0458", Dps"alr3808" (*298*). This observation reinforces the idea that the translocation of Dps proteins to the extracellular medium is required as a protection mechanism against ROS observed in pathogenic bacteria, as described above and also in other organisms.

4.8 Concluding remarks

Dps proteins have a global role in the protection from oxidative damage but also are vital for other functions, depending on the organism and environmental conditions (Table 4.1). Furthermore, these Dps functions observed *in vivo* are very likely related with the central properties of Dps proteins observed *in vitro*, namely DNA-binding ability, ferroxidase activity and iron storage capacity.

Table 4.1 - Dps proteins from Bacteria and Archaea for which the crystal structure has been published. n.d. – not determined.

Organisms	Dps	PDB code	Ferroxidase activity	DNA binding	Other functions
Agrobacterium tumefaciens	Dps	1O9R	Yes (*266*)	No (*266*)	n.d.
Bacillus anthracis	Dps1	1JIG	Yes (*254*)	No	n.d.
Bacillus anthracis	Dps2	1JI5	Yes (*254*)	No	n.d.
Bacillus brevis	Dps	1N1Q	Yes (*299*)	Yes (*299*)	n.d.
Borrelia burgdorferi	NapA	2PYB	Yes (*300*)	n.d.	Involved in virulence (*300*)
Bacteroides fragilis	DpsL	2VZB	Yes (*301*)	No (*301*)	n.d.
Brucella melilensis;	Dps	3GE4	n.d.	n.d.	n.d
Bacillus subtilis	MrgA	2CHP	n.d.	Yes (*229*)	n.d.
Campylobacter jejuni	Dps	3KWO	Yes (*302*)	Yes (*303*)	Involved in biofilm formation and virulence (*283, 285-286*)
Deinococcus radiodurans	Dps1	2C2F	Yes (*205*)	Yes (*270*)	n.d.
Deinococcus radiodurans	Dps2	2C2J	Yes (*204*)	Yes (*206*)	n.d.
Escherichia coli	Dps	1DPS	Yes (*63*)	Yes (*224*)	Involved in multiple stress resistance (*276, 278, 304*)
Helicobacter pylori	NapA	1JI4	Yes (*210*)	Yes (*210*)	Involved in virulence (*233*)
Halobacterium salinarum	Dps	1TJO	Yes (*236*)	n.d.	n.d.
Kineococcus radiotolerans	Dps	4A25	Yes (*238*)	n.d.	n.d.
Lactococcus lactis	DpsA	1ZUJ	No (*245*)	Yes (*245*)	n.d.
Lactococcus lactis	DpsB	1ZS3	No (*245*)	Yes (*245*)	n.d.
Listeria innocua	Dps	1QGH	Yes (*64*)	No (*305*)	n.d.
Listeria monocytogenes	Dps	2IY4	Yes (*306*)	n.d.	Involved in multiple stress resistance and virulence (*307*)
Microbacterium arborescens	Dps	2YJJ	Yes (*230*)	No (*230*)	Hydrolysis and synthesys of N-acylamino acids (*308*)
Mycobacterium smegmatis	Dps1	1VEI	Yes (*309*)	Yes (*243*)	n.d.
Mycobacterium smegmatis	Dps2	2Z90	Yes (*292*)	Yes (*295*)	n.d.
Staphylococcus aureus	MrgA	2D5K	Yes (*310*)	Yes (*311*)	Involved in virulence (*312*)
Streptomyces coelicolor	DpsA	4CYA	Yes (*244*)	Yes (*293*)	Involved in pre-spore compartment, osmotic and heat stress resistance (*293*)
Streptomyces coelicolor	DpsC	4CYB	Yes (*244*)	Yes (*293*)	n.d.
Salmonella enterica	DpsL	3AK8	Yes (*239*)	n.d.	Involved in virulence (*281*)
Streptococcus pyogenes	Dpr	2WLA	Yes (*313*)	No	Involved in multiple stress resistance (*280*)
Sulfolobus solfataricus	DpsL	2CLB	Yes (*314*)	n.d.	n.d.
Streptococcus suis	Dpr	1UMN	Yes (*227*)	No (*250*)	n.d.
Thermosynechococcus elongates	Dps	2C41	Yes (*248*)	No (*248*)	n.d.
Thermosynechococcus elongates	DpsA	2VXX	Yes (*255*)	No(*255*)	n.d.
Treponema pallidum	TpF1	2FjC	Yes (*231*)	n.d.	Involved in virulence (*315*)
Vibrio cholerae	Dps	3IQ1	n.d.	n.d.	n.d.
Yersinia pestis	Dps	4DYU	n.d.	n.d.	n.d.

Part II
Experimental results

CHAPTER V

Dps from *Deinococcus radiodurans*: oligomeric forms of *Dr*Dps1 with distinct cellular functions and *Dr*Dps2 involved in metal storage

This chapter was published in the following paper:

Santos S. P., Mitchell E. P., Franquelim H. G., Castanho M. A., Abreu I. A., Romao C. V. (2015) Dps from *Deinococcus radiodurans:* oligomeric forms of Dps1 with distinct cellular functions and Dps2 involved in metal storage, *FEBS Journal*, 282 (22), 4307-27.

Santos S. P. participated in the manuscript preparation and was responsible for all the experimental work. AFM experiments were performed by Santos S. P. in collaboration with Franquelim H. G. and Castanho M. A..

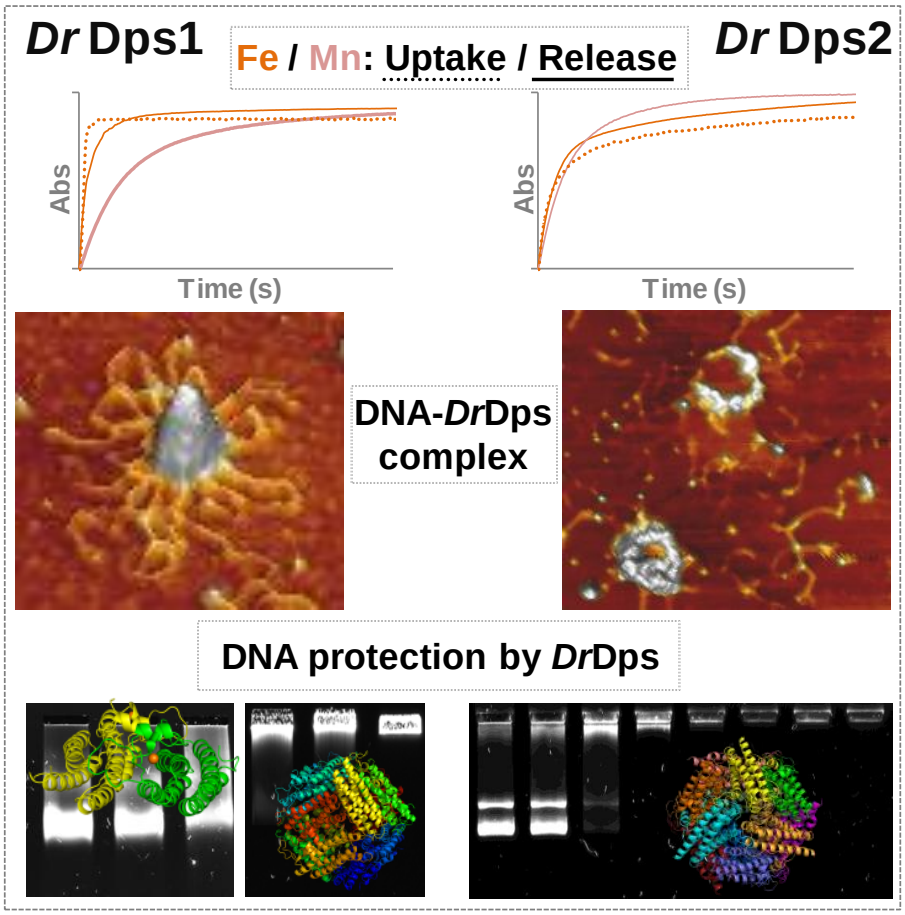

Highlights:

Dps from *Deinococcus radiodurans* (*Dr*Dps1 and *Dr*Dps2) are hollow spherical dodecamers. We addressed their involvement in the metal storage and DNA protection. Results showed that *Dr*Dps1 and *Dr*Dps2 can protect DNA, and both proteins are able to store and release iron and manganese. Furthermore, *Dr*Dps1 showed a structural dynamic plasticity with distinct cellular functions, from DNA protection to metal storage.

5.1 Abstract

The DNA-binding proteins from starved cells from *Deinococcus radiodurans*: *Dr*Dps1-*dr2263* and *Dr*Dps2-*drb0092* have a common overall structure of hollow spherical dodecamers. Their involvement in the homeostasis of intracellular metal and DNA protection were addressed.

Our results show that *Dr*Dps proteins are able to oxidize ferrous to ferric iron using both oxygen or hydrogen peroxide. The iron stored inside the hollow sphere cavity is fully released. Furthermore, these proteins are able to store and release manganese, suggesting they can play a role in manganese homeostasis as well. The interaction of *Dr*Dps with DNA was also addressed. Even though *Dr*Dps1 binds both linear and coiled DNA, *Dr*Dps2 preferentially binds to coiled DNA, forming different protein-DNA complexes, as clearly showed by atomic force microscopy. *Dr*Dps1 (dimer and dodecamer) and *Dr*Dps2 can protect DNA against reactive oxygen species, although the protection occurs at different Fe to protein ratios. The difference between *Dr*Dps could be the result of the *Dr*Dps1 higher iron oxidation rate in the presence of hydrogen peroxide and its higher affinity to bind DNA than *Dr*Dps2.

Using cellular extracts obtained from *D. radiodurans* cultures, we showed that *Dr*Dps1 oligomers observed in *in vitro* conditions are also presented *in vivo.* This indicates that *Dr*Dps1 has a structural dynamic plasticity that allows its oligomeric state to change between dimer, trimer and dodecamer. This in turn suggests the existence of a regulation mechanism that modulates the oligomer equilibrium and is dependent on growth stages and environmental conditions.

Keywords: Oxidative stress, DNA, manganese, oligomeric-state, ROS

5.2 Introduction

Deinococcus radiodurans is an aerobic gram-positive bacterium that survives exposure to several extreme conditions, such as high doses of radiation, desiccation and starvation (*100, 102, 316*). Under these conditions, the intracellular production of reactive oxygen species (ROS) is increased, which can be neutralized directly by several enzymatic systems, namely superoxide dismutases, catalases and peroxidases (*100, 146, 201, 317*). Additionally, the high manganese intracellular levels observed previously in *D. radiodurans* also have been proposed to contribute to the scavenging of ROS (*69, 81, 100*), but the molecular mechanisms involved in this process have yet to be clarified.

The Mn/Fe ratio is higher in *D. radiodurans* (Mn/Fe=0.24) than in the radiation sensitive bacteria *Escherichia coli* (Mn/Fe=0.0072) and *Shewanella oneidensis* (Mn/Fe=0.0005) (*68, 81*). Perhaps linked to this, *D. radiodurans* does not possess any genes encoding for ferritin (typically Fe-storage proteins), instead it contains two genes for DNA binding proteins from starved cells (Dps): *Dr*Dps1 (*dr2263*) and *Dr*Dps2 (*drB0092*). Dps have similar architecture and properties to iron-storage proteins, ferritins and bacterioferritins, but instead of a 24-mer structure they form dodecamers with a 23 symmetry (*65, 240, 318*). As bacterioferritins, Dps are also strictly prokaryotic proteins (*65, 219-220*). Dps have been mainly associated with oxidative stress response, being able to protect DNA under those conditions (*219-220, 319-320*). In addition to this, Dps proteins have been shown to be involved in the synthesis and hydrolysis of N-acyl amino acids (*230, 308*). They also have been described as a virulence factor (*321-324*) and as being associated with the axonal variant of Guillain-Barré syndrome (*325*).

E. coli Dps was the first protein of this family to be identified as being highly abundant in the stationary phase of starved cells (*224*). Later, it was reported that incubation of purified *E. coli* Dps results in self–aggregation in solution forming two-dimensional crystals. This was proposed to be the driving force for the formation of large Dps-DNA complexes during co-crystallisation (*272, 326*). The interaction between Dps and DNA occurs without any apparent DNA-sequence specificity. The Dps-DNA interaction has been proposed to be mediated by a variable number of positively charged amino acid residues, which can be present at the N-terminal (*245, 265, 292*), C-terminal tails (*247, 267*) or at the protein surface, as in the case of

Helicobacter pylori Dps (NAP) (*268*). Also, it was shown that DNA binding only occurs in the presence of Fe^{2+} or H_2O_2 for the *Campylobacter jejuni* Dps (*302-303*).

As iron-storage proteins, Dps can incorporate up to 500 iron atoms, preferentially using hydrogen peroxide as oxidant (*63, 220, 248, 274, 319*). The ferroxidase centers in most cases are located on the 2-fold axis, consisting of two mononuclear octahedral coordinated irons per dimer, separated by *ca.* 20 Å (*203-204, 210, 234, 256, 266*). A few examples are known in which a second iron was observed close to each ferroxidase center, suggesting a formation of a transient diiron site (*204, 256*). A Dps with a diiron site similar to bacterioferritins has been also reported (*327-328*).

Several organisms with more than one gene encoding for Dps have been identified, such as *Mycobacterium smegmatis*, *Bacillus anthracis, Thermosynechococcus elongatus, Streptomyces coelicolor* and *D. radiodurans* (*102, 243-244, 248, 254, 292*). Studies on these Dps suggest different cellular functions for each protein. In *B. anthracis* both Dps protect DNA from oxidative damage, however *Ba*Dps2 confers a higher DNA protection than *Ba*Dps1, and *Ba*Dps2 uses both oxygen and hydrogen peroxide to oxidize Fe^{2+}, whilst *Ba*Dps1 uses oxygen only (*254*). The *M. smegmatis* Dps have been proposed to promote different nucleoid organization: in conditions where *Ms*Dps1 is over-expressed, the DNA adopted a toroidal structure, whereas a coral reef structure was adopted when *Ms*Dps2 is over-expressed (*295*).

The Dps from *D. radiodurans*, *Dr*Dps1 and *Dr*Dps2, share 16% amino acid sequence identity. Their 3D-structure is similar to other Dps, consisting of dodecameric hollow spheres with a four-helix bundle conformation for each subunit (*203-204, 246*). When compared with other Dps, these proteins have a much longer N-terminal (54 and 72 amino acids for *Dr*Dps1 and *Dr*Dps2, respectively) before the four-helix bundle region. In this N-terminal region *Dr*Dps1 has a metal binding site, which has been proposed to be important for DNA binding (*269*); this protein is weakly associated with the nucleoid (*329*). The first 30 amino acid residues from *Dr*Dps2 are predicted to be a signal peptide (*204, 206, 330*). This protein was found to be localized in the cell periphery region (*206*); based on this and in the intracellular iron localization in *D. radiodurans* (*69*), it was suggested that this protein is associated mainly with iron storage (*206*).

Although some studies have been performed on both *Dr*Dps proteins (*203, 205-206, 246, 269*), several questions remain to be answered regarding their interaction

with DNA and their metal storage ability. Our work shows that *Dr*Dps2, and both dimeric and dodecameric forms of *Dr*Dps1 are able to protect the DNA against ROS at different Fe/12-mer *Dr*Dps ratios. Both proteins form distinct protein-DNA complexes. Also, it shows that *Dr*Dps1 has a higher DNA protection efficiency than *Dr*Dps2 and that its function is regulated by its oligomeric state. Additionally, iron and manganese storage and release are characterized. Our data also shows that *Dr*Dps are able to incorporate both iron and manganese when simultaneously submitted with both metals. However, manganese has been previously shown to inhibit the *Dr*Dps1 ferroxidase activity (*269*). Our *in vitro* data for both proteins is supported by studies on *D. radiodurans* extracts for both proteins and suggests that these proteins are involved in iron and manganese cellular homeostasis.

The present work characterizes *Dr*Dps-dependent cellular mechanisms which impact the protection of *D. radiodurans* against oxidative stress, and ultimately can be extrapolated to the resistance mechanisms against radiation.

5.3 Experimental procedures

5.3.1 Production, purification and oligomerization state of *Dr*Dps

*Dr*Dps1 and *Dr*Dps2 were expressed and purified as described previously (*203-204*). After purification the oligomerization state for each protein was determined by size exclusion chromatography (SEC) using a Superdex 200 column (10/300 GL, GE Healthcare) with 20 mM Tris-HCl pH 7.5, 150 mM NaCl buffer at 4 ºC. The column was previously calibrated using standard-proteins ranging from 14 to 660 kDa (GE Healthcare). To test *Dr*Dps1 oligomeric states the protein was analyzed at different temperatures (1 h at 4, 20, 37, 45 or 60 ºC), ionic strength (150 and 500 mM of NaCl), pH (6.5-8.0), and at different iron concentrations (100-500 Fe^{2+}/12-mer).

To test iron incorporation *Dr*Dps1 was incubated with iron and was analyzed on a 10 % native polyacrylamide gel electrophoresis (PAGE). Protein was stained using Bio-safe Coomassie (Bio-Rad); Fe^{2+} was detected as previously described (*250*); and Fe^{3+} was detected after staining with 20 % (v/v) of hydrochloric acid and 10 % (w/v) potassium ferrocyanide (*234*).

The effect of the presence of DNA on the *Dr*Dps1 oligomerization state was tested by SEC using the gel filtration buffer (pH 7.5) and 20 mM Bis-Tris pH 6.5, 150

mM NaCl. To test the presence of protein-DNA complexes, the eluted peaks were run in 1 % (w/v) agarose gel containing SYBR Safe DNA (Invitrogen), followed by detection using Fuji Fluorescent analyzer TLA-5100 (GE). Protein was detected using Bio-safe Coomassie (Bio-Rad).

5.3.2 Detection of *Dr*Dps protein levels in *D. radiodurans*

D. radiodurans cells were grown in M53 medium (500 mL) at 30 ºC. Four independent growths were performed and cells for analyses were collected at different time points. The effect of 50 mM hydrogen peroxide, 500 µM of ammonium iron (II) sulfate or 500 µM manganese (II) chloride were tested by adding these compounds to the media at a cell optical density (OD_{600nm}) of 0.3. Cells were then collected at different time points: 15 min (early exponential phase, OD_{600nm}=0.33), 2 hours (mid exponential phase OD_{600nm}=0.60), and 20 hours (stationary phase, OD_{600nm}=4.1). At each time point the cells were harvested at 11000 *g* and resuspended in 20 mM Tris–HCl pH 7.5, 150 mM NaCl, and disrupted in a French pressure cell at 15000 psi. Soluble fractions were obtained after centrifugation for 1 h at 20000 *g* at 4 ºC.

Soluble fractions were concentrated and protein concentration was determined by the Bradford method (Bio-Rad) (*331*). A total protein of 60 µg was loaded in 12 % PAGE. One gel was blotted into polyvinylidene fluoride membrane (Bio-Rad) for Western-blotting; and another gel was stained for DNA using SYBR Safe DNA (Invitrogen) and visualized using Fuji Fluorescent analyzer TLA-5100 (GE Healthcare). *Dr*Dps was detected using specific polyclonal antibodies against *Dr*Dps1 (AbDps1) or *Dr*Dps2 (AbDps2). The molecular mass of the different oligomeric forms was confirmed by 8 % Blue Native PAGE as previously described (*332*), using molecular markers with mass from 43 to 669 kDa, and followed by Western-blotting and detection using AbDps1 or AbDps2. The membranes were further incubated with secondary antibodies alkaline phosphatase are conjugated goat anti-rabbit IgG (Sigma Aldrich). Finally, the protein was revealed using a colorimetric detection with a solution 500X diluted of Nitrotetrazolium chloride and 5-Bromo-4-chloro-3-indolyl phosphate toluidine salt (NBT/BCIP stock solution 50X) for 5 min.

*Dr*Dps bands from the Western-blotting were quantified using ImageJ software. The data presented is from four independent samples.

The specificity for both *Dr*Dps antibodies was confirmed using *D. radiodurans* wild-type and the knockout mutants of both *Dr*Dps. The *Dr*Dps knockout mutants were previously described in (*333*).

5.3.3 Iron oxidation using O_2 or H_2O_2 as oxidants

Iron oxidation assays were performed in 50 mM MOPS pH 7.0, 150 mM NaCl, using O_2 or H_2O_2 as oxidants. The reactions were monitored at 310 nm on a UV-Visible spectrometer (UV-1603, Shimadzu) at 25 ºC with continuous stirring. Ammonium iron (II) sulfate solutions were prepared freshly and kept under argon. Controls were performed for each assay under the same conditions but without protein. Experiments were repeated three times for the conditions with 24-100 Fe^{2+} atoms/12-mer ratios and two times for the conditions above 200 Fe^{2+} atoms /12-mer ratios.

Iron oxidation rates by oxygen were determined under aerobic conditions using 0.5 µM of protein and different Fe^{2+} atoms /12-mer ratios (24 to 600). Iron oxidation rates by hydrogen peroxide were assayed under anaerobic conditions (argon) using two concentrations of hydrogen peroxide: 1 mM and 1 µM. The protein concentration used was 0.5 µM with the different Fe^{2+} atoms /12-mer ratios of 24, 50, 100 and/or 200. Experiments were repeated two times for conditions with 1 mM of hydrogen peroxide with 50-100 Fe^{2+} atoms /12-mer ratios and three times for the conditions with 1 µM of hydrogen peroxide with 50-200 Fe^{2+} atoms /12-mer ratios.

Iron oxidation rates by *Dr*Dps2 in the presence of DNA by O_2 or H_2O_2 were determined in the conditions described above, but using 1.0 µM of protein with 100 Fe^{2+} atoms /12-mer ratio. The protein was incubated in the presence of DNA 30 min before the addition of iron and the oxidant.

5.3.4 Iron and manganese incorporation

*Dr*Dps were incubated in 20 mM Tris-HCl pH 7.5, 150 mM NaCl under aerobic conditions with iron and/or manganese for 1 hour. A total of 1000 Fe^{2+} ions or 1000 Mn^{2+} ions were added per *Dr*Dps dodecamer. A total of 400 Fe^{2+} ions and 400 Mn^{2+} ions were added simultaneously per *Dr*Dps dodecamer. The samples were then

loaded on a column containing analytical grade Chelex 100 resin (Bio-Rad) to remove excess metals. The incorporated metals were then quantified by inductively coupled plasma atomic emission spectroscopy (ICP-AES) at REQUIMTE Laboratório de Análises (FCT, UNL). Two independent samples were prepared in identical conditions and measured.

5.3.5 Iron and manganese release

A total of 200 Fe^{2+} atoms/12-mer *Dr*Dps were added in a buffer containing 20 mM Tris-HCl pH 7.5, 150 mM NaCl at 25 ºC (*Dr*Dps used in the assay were in the dodecamer form). Samples were incubated under aerobic conditions for 1 hour and then were loaded on a column containing analytical grade Chelex 100 resin (Bio-Rad).

The Fe-release reaction contained 0.5 µM of *Dr*Dps-(Fe-loaded) in 50 mM MOPS pH 7.0, 150 mM NaCl under anaerobic conditions. Finally, 2.5 mM 2-2´bipyridyl and 2.5 mM sodium dithionite (as reducing agent) were added to the reaction. Time-dependent absorbance traces were recorded for 15 min at 520 nm indicative of the formation of Fe^{2+}-bipyridyl complex (UV-1603, Shimadzu).

For the manganese release experiments, *Dr*Dps were in the dodecamer form, a total of 500 Mn^{2+} atoms/12-mer *Dr*Dps were added in 20 mM Tris-HCl pH 7.5, 150 mM NaCl at 25 ºC and the samples were incubated for 1 h under aerobic conditions. Subsequently, the samples were passed through a Chelex 100 resin. The Mn-release reaction contained 0.01 µM of *Dr*Dps-(Mn-loaded) in 35 mM borate buffer pH 9.7 under anaerobic conditions. The oligomeric form was confirmed under these conditions to be the dodecameric form. Finally, 2 mM Triton X-100, 0.6 mM cetylpyridinium chloride (CP), 32 µM 9-phenyl-2,3,7-trihydroxy-6-fluorone (PF), and 2.5 mM sodium dithionite were added. The release of manganese was monitored at 591 nm for 15 min following the formation of the Mn^{2+}-PF-CP-TritonX-100 complex, and was quantified as previously described (*334*).

Iron and manganese release were quantified using calibration curves performed with different concentrations solutions of ammonium ferrous sulfate and manganese chloride.

Experiments were repeated three times each for the iron and manganese experiments.

5.3.6 Electrophoretic mobility shift assay (EMSA)

DNA-binding interaction studies were performed using 1 % (w/v) agarose gel at different pH values (6.5-8.0). The DNA used was: pUC19 supercoiled plasmid DNA (2686 bp), *D. radiodurans* genomic DNA and Gene Ruler Ladder Mix containing 21 linear fragments of DNA with different base pairs (bp), ranging from 100-10000 bp (Fermentas).

*Dr*Dps1 (0.2-5.5 µM) or *Dr*Dps2 (2.0-14 µM) dodecamers were incubated with 9 nM plasmid DNA or 10 ng/µL *D. radiodurans* genomic DNA for 15 min at room temperature in 40 mM Bis-Tris pH 6.5-7.0 or 40 mM Tris-HCl pH 7.5-8.0 plus 150 mM NaCl. Ladder Mix DNA (50 ng/µl) was incubated with *Dr*Dps with different concentrations of protein, between 2.5-11 µM, for 15 min at room temperature in 40 mM Bis-Tris pH 7.0, 150 mM NaCl.

After incubation, the reactions were stopped with 6x DNA Loading Dye and analysed in agarose gel containing SYBR Safe DNA (Invitrogen), using the running buffers according to pH: 40 mM Bis-Tris pH 6.5-7.0 or 89 mM Tris, 89 mM boric acid, 2.0 mM EDTA pH 7.5-8.0 at room temperature. The gel images were obtained using a Fuji Fluorescent analyzer TLA-5100 (GE Healthcare).

5.3.7 Atomic force microscopy (AFM)

Samples for analyses were prepared by incubating *Dr*Dps1 or *Dr*Dps2 (1-5 nM) with 1 nM plasmid DNA for 5 min, in 40 mM Bis-Tris pH 6.5 or 7.0. The samples were deposited onto freshly cleaved mica substrates, previously glued to a glass coverslip, in the presence of 15 mM $NiCl_2$. The samples were then incubated for 5 min to adhere to the mica, rinsed with Milli-Q water (Millipore) and finally air-dried. All operations were carried out at 23 ºC. AFM images were acquired using a JPK NanoWizard® II (Berlin, Germany) mounted on a Zeiss Axiovert 200 inverted microscope (Jena, Germany). Samples were scanned in intermittent contact mode (air) using uncoated silicon ACL cantilevers from Applied NanoStructure (Santa Clara, CA, USA), displaying a tip radius of 6 nm, resonance frequencies of 190 kHz and spring constant of 45 N/m. Images were acquired with a 512 × 512 resolution, 1-1.5 Hz scan rate and with a scan size of 2 or 4 µm. Data were analyzed using JPK image processing software v.3 and Gwyddion v.2.19.

5.3.8 DNA protection against hydroxyl radical formation and DNase cleavage

DNA protection from oxidative damage was assayed using 7 µM *Dr*Dps1 or *Dr*Dps2 incubated with 9 nM plasmid DNA in 40 mM Bis-Tris pH 7.0, 150 mM NaCl for 15 min. A ratio of 12 - 500 Fe atoms /12-mer *Dr*Dps plus 10 mM of H_2O_2 were added and the mixtures incubated for 5 min at room temperature. The reactions were then stopped with 6x DNA loading dye and then loaded into a 1 % (w/v) agarose gel.

The ability of *Dr*Dps to protect DNA from digestion by DNaseII cleavage was tested using 9 nM plasmid DNA incubated with 7, 14 or 20 µM of protein for 15 min. The reaction mixtures were incubated with 0.25 U DNaseII (Sigma-Aldrich) containing 1 mM $MgCl_2$ for 5 min at room temperature. The reactions were then stopped as described above. The gel images were obtained using a Fuji Fluorescent analyzer TLA-5100 (GE Healthcare).

5.4 Results

5.4.1 *Dr*Dps and their oligomerization state

The size-exclusion purification profile of *Dr*Dps1 in the buffer 20mM Tris-HCl pH 7.5, 150 mM NaCl at 4ºC indicates that the protein elutes in two different oligomeric states, which were identified as being mainly a trimer with a small contribution of the dodecamer.

Even though the *Dr*Dps1 trimer is the main form in the conditions mentioned above, the dodecamer is induced when the protein is incubated at temperatures from 20-60 ºC and by high salt concentrations (250-500 mM of NaCl) (Fig. 5.1, A-B). In the presence of iron, the dodecamer is also formed, and is able to store this metal, as confirmed by staining the native gel for iron detection (Fig. 5.1, C). Moreover the protein becomes also dodecameric when the pH decreases to 6.5 (Fig. 5.1, D), which in the presence of DNA forms *Dr*Dps1-DNA complexes, as observed by the appearance of a band of molecular mass higher than that of the *Dr*Dps1 dodecamer (Fig. 5.1, D*a*), and confirmed by EMSA (Fig. 5.1, D*b*, *c*).

Another *Dr*Dps1 lower oligomeric form was identified as corresponding to a dimer. This lower oligomeric form appears in the presence of DNA at pH 7.5, leading

to the formation of *Dr*Dps1-DNA complexes smaller than those observed at pH 6.5 (Fig. 5.1, D-E).

The molecular mass of the protein complexes was determined after an S-200 calibration curve, as described in the experimental procedures section, and the oligomeric states were inferred from the determined masses (Fig. 5.1, F).

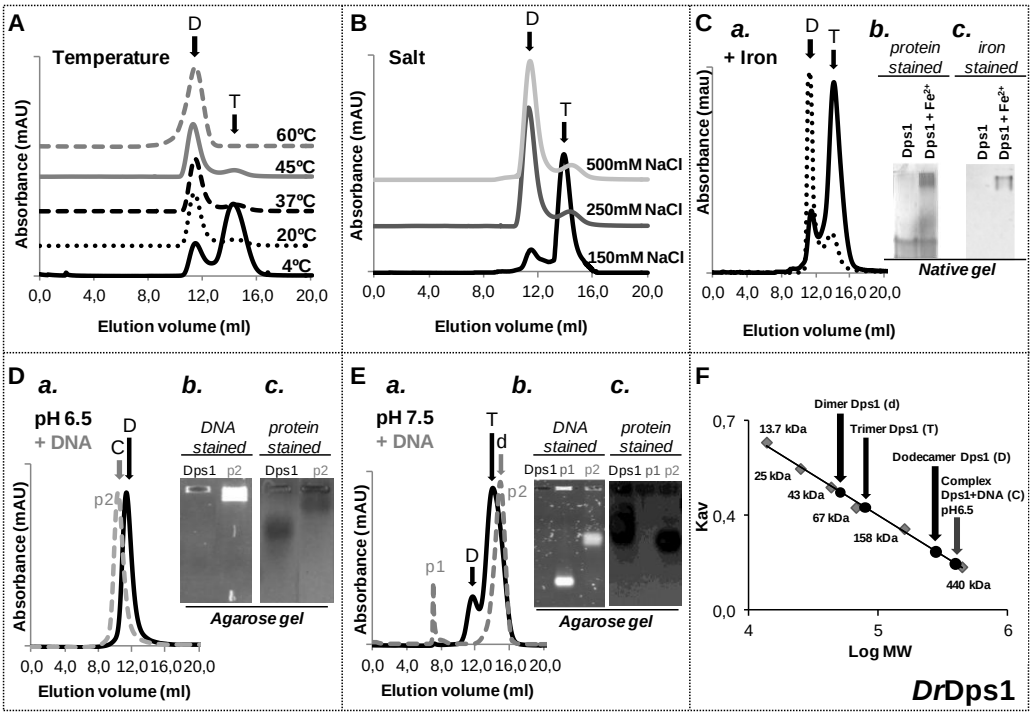

Figure 5.1 - Study of *Dr*Dps1 oligomerization state. **(A)** Effect of temperature on the oligomerization state of *Dr*Dps1, in 20 mM Tris-HCl pH 7.5, 150 mM NaCl. **(B)** Effect of the NaCl concentration on the oligomerization state of *Dr*Dps1, in 20 mM Tris-HCl pH 7.5. **(C)** Effect of the presence of iron, ***a.*** elution profile of recombinant *Dr*Dps1 (black line) and *Dr*Dps1 incubated with 100 Fe^{2+} atoms, for 60 min, at pH 7.5 (dotted line); ***b.*** **and** ***c.*** analysis of *Dr*Dps1 samples on 10 % PAGE, stained for protein (***b.***) and for iron (***c.***). **(D)** ***a.*** Elution profile of *Dr*Dps1 at pH 6.5 (black) and after incubation with plasmid DNA (dotted line); ***b.*** **and** ***c.*** agarose gel analyses of recombinant *Dr*Dps1 and peak fractions p2 (in the presence of DNA, forming the *Dr*Dps1-DNA complex), stained with SYBR Safe for DNA detection **(*b.*)**, or with Bio-safe Coomassie for protein detection **(*c.*)**. **(E)** ***a.*** Elution profiles of recombinant *Dr*Dps1 at pH 7.5 (black) and after incubation with plasmid DNA (dotted line); ***b.*** **and** ***c.*** agarose gel analyses of recombinant *Dr*Dps1 and peak fractions p1 and p2, stained with SYBR Safe for DNA detection **(*b.*)**, or with Bio-safe Coomassie for protein detection **(*c.*)**. **(F)** Size exclusion chromatography calibration curve; the different *Dr*Dps1 oligomeric forms are labeled as dimer (d), trimer (T), dodecamer (*D*) and as the complex *Dr*Dps1-DNA (C).

Although the dodecamer and dimer forms of *Dr*Dps1 were previously reported (*205, 270*), our data show that the oligomeric states interchanges between trimer to dodecamer and vice-versa upon variation of temperature, salt or pH; the dimer is only formed at pH 7.5 and in the presence of DNA.

The structures of the lower oligomeric forms of *Dr*Dps1 have not been determined. The dimer structure would correspond to the 2-fold axis dimer observed in the dodecamer structure. The trimer structure could be either the N-terminal trimer or the C-terminal trimer, based on the two types of 3-fold axes observed in the *Dr*Dps dodecamer structure. An analysis of the crystal structure of *Dr*Dps1 (*203*) using the server "Proteins, Interfaces, Structures and Assemblies" (*335*) suggests that the C-terminal trimer is the most probable assembly. Nevertheless, analysis of the number of hydrogen bonds between subunits for both types of trimers (N-terminal and C-terminal) using HBPLUS (*336*) indicates a similar number of hydrogen bonds: 30 hydrogen bonds from interacting residues for the N-terminal trimer versus 24 for the C-terminal trimer. This suggests that in solution, the trimer could be either the N- or the C- terminal trimers.

In order to address the presence of oligomeric forms in *Dr*Dps2, we tested the same conditions as previously shown for *Dr*Dps1. The *Dr*Dps2 oligomeric form is not affected by changes in temperature (between 4 to 60 ºC), NaCl concentration (150, 250, and 500 mM), pH, addition of iron (100-500 iron atoms/12-mer) or presence of DNA (Fig. 5.2). The iron incubation, confirmed that *Dr*Dps2 can store this metal (Fig. 5.2, D). Consequently, our results indicate that *Dr*Dps2 is a stable dodecamer in solution, confirming the previously reported data (*206*).

As mentioned for *Dr*Dps1, the molecular masses of *Dr*Dps2 complexes were determined after an S-200 calibration curve (Fig. 5.2, F).

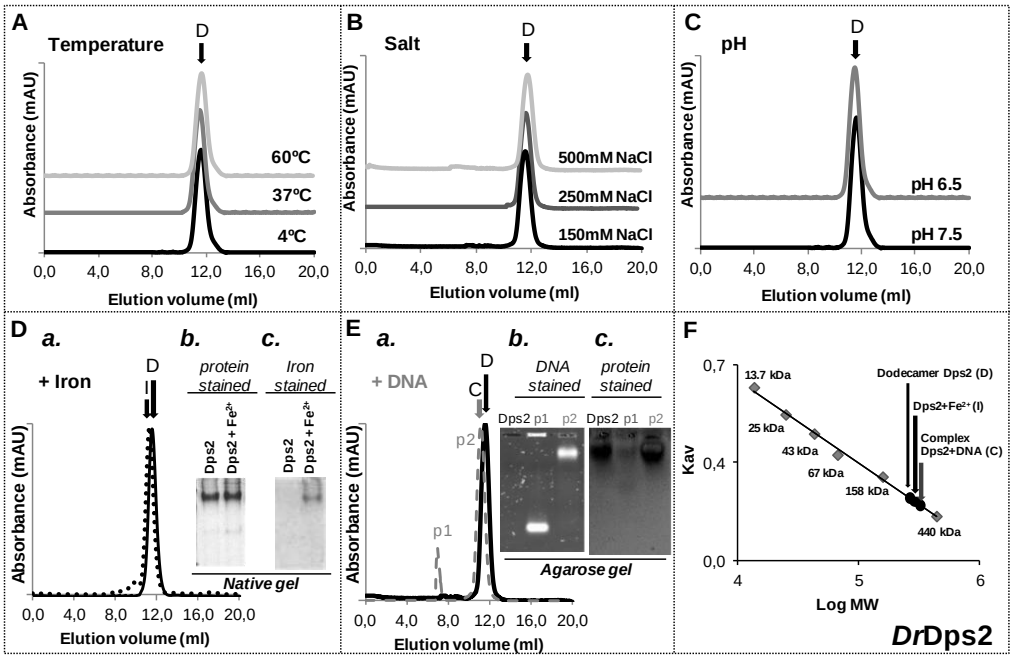

Figure 5.2 - Study of *Dr*Dps2 oligomerization state. **(A)** Effect of temperature on *Dr*Dps2, in 20 mM Tris-HCl pH 7.5, 150 mM NaCl. **(B)** Effect of NaCl concentration on *Dr*Dps2, in 20 mM Tris-HCl pH 7.5. **(C)** Effect of pH (pH 6.5 and 7.5). **(D)** Effect of the presence of iron, ***a.*** elution profile of recombinant *Dr*Dps2 (black line) and after incubation with 100 Fe^{2+} atoms, for 60 min, at pH 7.5 (dotted line); ***b.*** **and** ***c.*** analysis of recombinant *Dr*Dps2 and after incubation with iron, by 10 % PAGE, stained for protein (***b.***) and for iron (***c.***). **(E)** Incubation with DNA, ***a.*** elution profiles of recombinant *Dr*Dps2, at pH 7.5 (black) and after incubation with plasmid DNA (dotted line); ***b.*** and ***c.*** agarose gel analyses of recombinant *Dr*Dps2 and peak fractions p1 and p2, stained with SYBR Safe for DNA detection **(*b.*)**, or with Bio-safe Coomassie for protein detection **(*c.*)**. **(F)** Size exclusion chromatography calibration curve, the different *Dr*Dps2 oligomeric states detected are labeled dodecamer (*D*), complex *Dr*Dps2-DNA (C), and *Dr*Dps2 incorporated with iron (I).

5.4.2 *Dr*Dps expression profiles in *D. radiodurans*

In order to address the *in vivo* expression profile of *Dr*Dps and the presence of the lower *Dr*Dps1 oligomeric forms, both proteins were monitored during *D. radiodurans* growth when submitted to different conditions: control conditions, presence of manganese, iron or hydrogen peroxide (Fig. 5.3). *D. radiodurans* cell growths in the different conditions show that addition of hydrogen peroxide has an effect to slow down the growth, whereas the addition of manganese accelerates the cell growth after the mid-exponential phase (Fig. 5.3, A*a*). *Dr*Dps expression levels

were detected by Western-blotting using polyclonal antibodies specific for both proteins. The antibodies specificity for each *Dr*Dps was confirmed using the knockout mutants of *Dr*Dps (Fig. 5.3, A*b*).

Under the different conditions tested, *Dr*Dps1 expression profile is constant during the different growth stages, but a change in its oligomeric state was observed. Under control conditions and in the early exponential phase (OD_{600nm}= 0.3), *Dr*Dps1 is mainly dimeric. Still a small contribution of the trimeric form can be detected, which is no longer observed 15 min later (OD_{600nm}= 0.33, Fig. 5.3, B*a*). After addition of manganese and during the exponential growth phase, *Dr*Dps1 changes from dimeric to the trimeric form. When the stationary phase is reached, *Dr*Dps1 returns to its dimeric form (Fig. 5.3, B*b*). A similar effect, although to a lesser extent, is observed after the addition of hydrogen peroxide, since the dimeric form remains predominant during the exponential phase (Fig. 5.3, B*c*). Upon iron addition, the protein oligomeric form changed to dodecamer during the mid-exponential phase which was maintained in the stationary phase (Fig. 5.3, B*d*). The different oligomeric forms observed for *Dr*Dps1 under the different conditions were confirmed by Blue Native PAGE (Fig. 5.3, C*a*), as described in the experimental procedures section.

Our *in vitro* data, shows that *Dr*Dps1 oligomeric state is affected by temperature, revealing that at 30 ºC the protein is mostly a dodecamer (Fig. 5.1, A). Nevertheless, the data presented in Figure 5.3, B*a*, show that in control conditions *Dr*Dps1 is a dimer, suggesting that its oligomeric state in the cell is affected by other factors and not by temperature.

In order to confirm the presence of DNA associated with the *Dr*Dps1 dimer, trimer or dodecamer, a PAGE was performed under the same conditions as those shown in figure 5.3, B. The only band that was clearly associated with DNA corresponds to the dimer form of *Dr*Dps1 (Fig. 5.3, C*b*).

Under control growth conditions *Dr*Dps2 is mostly expressed in the mid-exponential phase, whereas in the stationary phase it is almost absent (Fig. 5.3, D). In the conditions where manganese and iron were added, a slight increase of the *Dr*Dps2 expression level during exponential growth is observed (Fig. 5.3, D*b*, *d*). The only condition is which the protein is more expressed in the stationary phase corresponds to the addition of hydrogen peroxide (Fig. 5.3, D*c*). *Dr*Dps2 remained a stable dodecamer under all of the tested conditions (Fig. 5.3, C*a*) as already observed by SEC (Fig. 5.2).

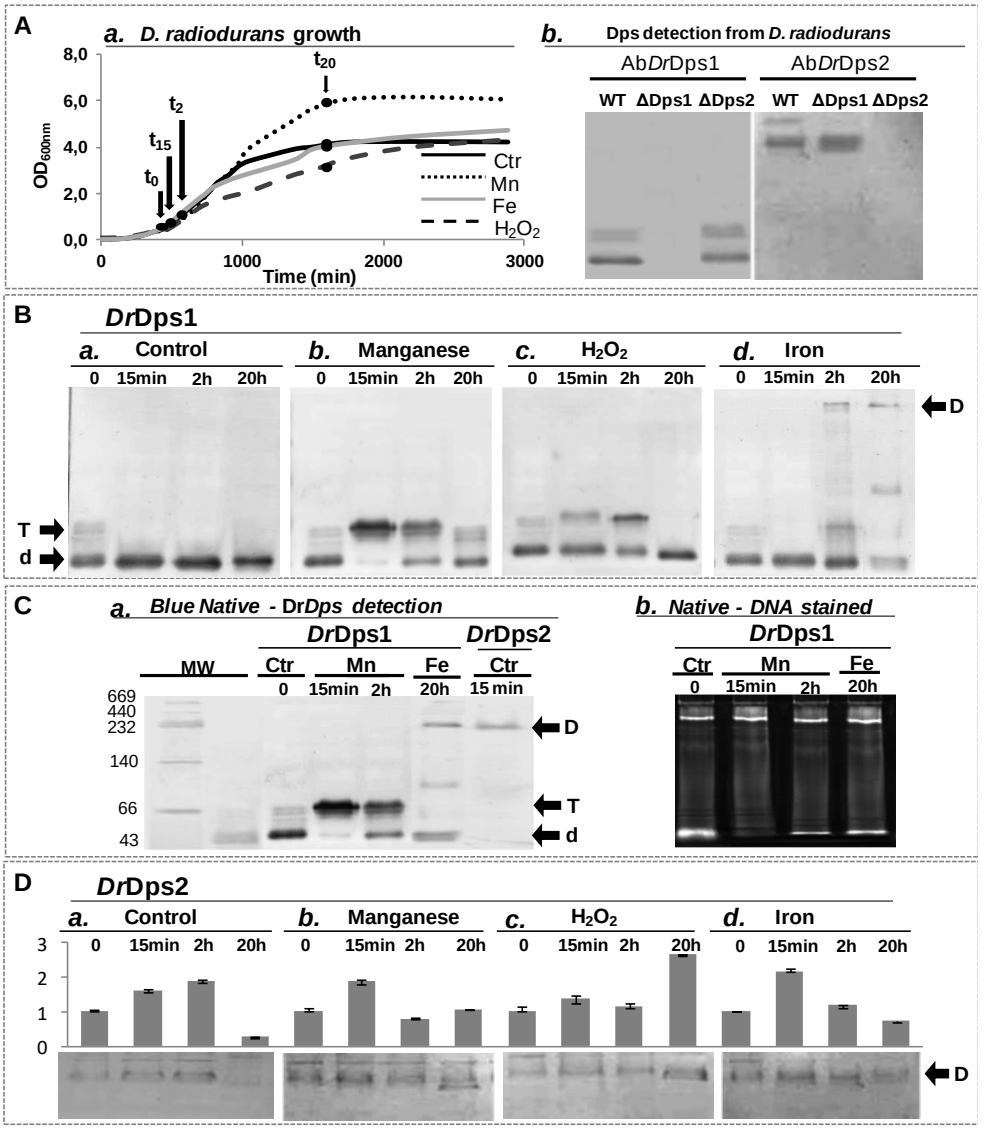

Figure 5.3 - Variation of *Dr*Dps1 and *Dr*Dps2 protein levels under different *D. radiodurans* growth conditions. **(A)** ***a.*** *D. radiodurans* cells grown in M53 medium with the addition, at an OD_{600nm} of 0.3 (time 0), of water (Control) (black line)**,** manganese chloride (dotted line)**,** hydrogen peroxide (dashed line) or iron (gray line); ***b.*** Detection of *Dr*Dps1 and *Dr*Dps2 in *D. radiodurans* cellular extracts, using *Dr*Dps1 and *Dr*Dps2 specific antibodies (Ab*Dr*Dps1 and Ab*Dr*Dps2, respectively), by western-blot analysis (native 12 % PAGE); WT- wild-type protein extracts, Δ*dps1* – *Dr*Dps1 knockout protein extracts, and Δ*dps2* – *Dr*Dps2 knockout protein extracts. **(B)** *Dr*Dps1 oligomeric state variation during *D. radiodurans* growth, in M53 supplemented as in **(A)**; time points analysed are t=0, 15min (early exponential phase, OD_{600nm}=0.33), 2h (mid exponential phase OD_{600nm}=0.6), and 20h (point 4, stationary phase, OD_{600nm}=4.1); analysis was done on western-blot in native conditions (12 % PAGE); labels are:

dimer (*d*), trimer (*T*) and dodecamer (*D*). **(C)** ***a.*** Western-blot analysis of blue native gel of soluble protein fractions from *D. radiodurans* cells, showing the molecular weights of the different oligomeric forms of *Dr*Dps1. Analyzed conditions are as in **(A)**. *Dr*Dps2 oligomeric state did not vary with growth conditions, thus a 15min control condition is showed. ***b.*** Native gel (12 % PAGE) of the same samples as in panel ***a.***, stained with SYBR Safe for DNA visualization. **(D)** *Dr*Dps2 detection in soluble protein fractions from *D. radiodurans* cells grown in M53 medium, using native-conditions western-blot analysis; bar-charts represent the quantification of the amount of *Dr*Dps2, using ImageJ. All lanes from PAGE were loaded with 60 µg of total protein.

5.4.3 Iron oxidation, incorporation and release

Iron incorporation in Dps occurs, as in ferritins, in a multistep process corresponding to ferrous entry, binding and oxidation at the ferroxidase center, followed by nucleation and mineral core growth inside the protein cavity (*63, 220*). The ability of *Dr*Dps to oxidize ferrous to ferric iron was measured under aerobic and anaerobic conditions using respectively, O_2 and H_2O_2 as the final electron acceptors, in order to correlate its iron oxidation kinetics with their structural differences at the ferroxidase center.

The *Dr*Dps iron storage capacity was determined using Inductively Coupled Plasma Atomic Emission Spectroscopy after the proteins were incubated with excess of iron (see experimental procedures section). This iron storage capacity was measured as 252 ± 27 Fe atoms/12-mer for *Dr*Dps1 and 398 ± 41 Fe atoms/12-mer for *Dr*Dps2. Even though both proteins store iron, *Dr*Dps1 has a lower iron storage limit, similar to the *Trichodesmium erythraeum* Dps (*241*), while iron storage capacity for *Dr*Dps2 is comparable to that generally described for Dps (*63, 220, 274*).

The iron oxidation by oxygen was measured in the presence of different Fe atoms/12-mer ratio. The oxidation profile for both proteins is different, it is clear that above 200 Fe atoms/12-mer *Dr*Dps2 shows a bi-phasic behavior for iron oxidation while for *Dr*Dps1 the presence of more than one phase for iron oxidation is not very pronounced (Fig. 5.4). The initial rate for iron oxidation versus the amount of Fe/12-mer is represented in figure 5.4 (Fig. 5.4, A,B *b*), instead of the maximum velocity, V_{max}. Since Dps, ferritin and bacterioferritins are not “real” enzymes, they are limited to the amount of metal that fit their cavity.

The initial iron oxidation rates observed for *Dr*Dps upon iron addition of 24 to 400 Fe atoms/12-mer increased from 0.8 ± 0.02 to 4.1 ± 0.06 µMmin^{-1} for *Dr*Dps1 (Fig. 5.4,

A) and from 1.2 ± 0.04 to 11.4 ± 0.04 µM min^{-1} for *Dr*Dps2 (Fig. 5.4, B). An additional increase in Fe atoms/12-mer ratio (500-600) led to almost no increase in the initial iron oxidation rate observed for *Dr*Dps1, suggesting that this protein had reached its maximum capacity for iron oxidation. Under the same conditions the initial iron oxidation rate of *Dr*Dps2 increased to 15.6 ± 0.02 µMmin^{-1}, reaching saturation for iron oxidation (Fig. 5.4, B).

Our results demonstrate that until 400 Fe atoms/12-mer *Dr*Dps2 has an initial iron oxidation rate *ca.* 2-fold higher than *Dr*Dps1. It is interesting to note that in the condition where 600 Fe/12-mer were added, *Dr*Dps2 reaches a saturation of iron oxidation in 10 min while *Dr*Dps1 during the same time is only able to oxidize around 40 % of the iron. This indicates that *Dr*Dps1 is much slower than *Dr*Dps2 for iron oxidation, although the difference of the initial iron oxidation rates is only about 2-fold higher for *Dr*Dps2.

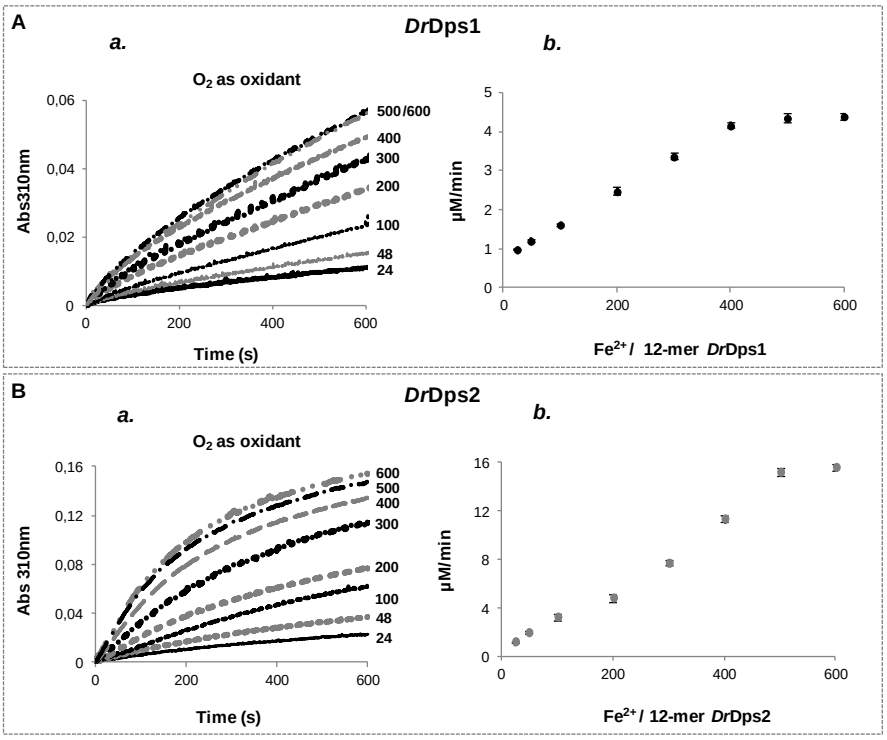

Figure 5.4 - Kinetics of Fe^{2+} oxidation by *Dr*Dps1 **(A)** and by *Dr*Dps2 **(B)** in the presence of oxygen. ***a.*** Iron oxidation profiles measured at 310 nm in the presence of different (24-600) ratios of Fe atoms per12-mer protein ***b.*** Dependency of initial iron oxidation rates with Fe atoms /12-mer protein ratios, for each *Dr*Dps.

Contrary to ferritins, which preferentially use O_2 for iron oxidation, most of the Dps so far studied can use hydrogen peroxide to oxidize the iron more efficiently than with oxygen. This can contribute to deplete intracellular hydrogen peroxide concentration avoiding putative Fenton chemistry that could lead to the formation of hydroxyl radicals (*63, 65, 237*).

The oxidation of iron in the presence of hydrogen peroxide was performed using two different concentrations of hydrogen peroxide. Our data shows that when 1 mM of hydrogen peroxide was used as the oxidizing agent, the initial iron oxidation rates for 50 and 100 Fe atoms/12-mer are respectively 534.0 ± 9.2 µM min^{-1} and 1030.3 ± 11.2 µM min^{-1} for *Dr*Dps1 and 276.9 ± 7.3 µM min^{-1} and 543.9 ± 9.6 µM min^{-1} for *Dr*Dps2. The initial iron oxidation rates is *ca.* 2-fold higher for *Dr*Dps1 than for *Dr*Dps2, but *Dr*Dps1 oxidizes totally the iron in the first 30 seconds, while *Dr*Dps2 is only able to oxidize the same amount of iron in 10 min (Fig. 5.5, A, B *a*). The iron oxidation rates under this condition are higher than those calculated with oxygen, corresponding to an increase of *ca.* 440 to 644-fold and 140 to 165-fold for *Dr*Dps1 and *Dr*Dps2, respectively upon addition of 50 and 100 Fe atoms/12-mer. In comparison, Dps from *E. coli* and *T. elongatus* show 100-fold and 2000-fold increase in iron oxidation rates with hydrogen peroxide *versus* oxygen, respectively (*63, 248, 319*).

When a lower concentration of hydrogen peroxide (1µM) was added, the iron oxidation is much slower than on the previous experiment. The iron oxidation is bi-phasic in the presence of 1µM of hydrogen peroxide and upon addition of 50-200 Fe atoms/12-mer (Fig. 5.5, A, B *b*). However, this bi-phasic profile is more evident for *Dr*Dps2, appearing after addition of 50 Fe atoms/12-mer, while for *Dr*Dps1 is only observable after the addition of 100 Fe atoms/12-mer. Under this condition (100 Fe/12-mer) there is an increase of 1.7 fold between phase 2 and phase 1 for *Dr*Dps2, while for *Dr*Dps1 is only 1.2 fold higher. At 200 Fe atoms/12-mer both proteins show two phases with similar iron oxidation rates: phase 1 (in the first 250 s) with initial iron oxidation rates of 22.7 ± 0.2 µM min^{-1} and 20.0 ± 0.2 µM min^{-1} for *Dr*Dps1 and *Dr*Dps2, respectively; phase 2, with initial iron oxidation rates of 49.0 ± 0.1 µM min^{-1} and 44.2 ± 0.1 µM min^{-1} for *Dr*Dps1 and *Dr*Dps2, respectively.

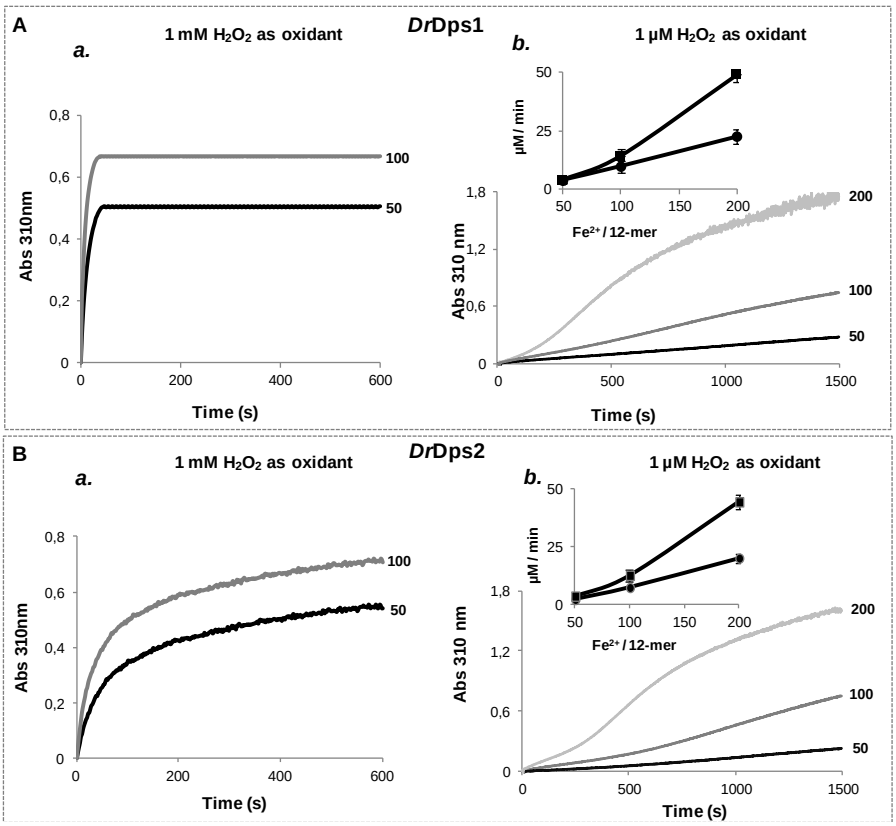

Figure 5.5 - Kinetics of Fe^{2+} oxidation by *Dr*Dps1 **(A)** and by *Dr*Dps2 **(B)** in the presence of hydrogen peroxide. ***a.*** Iron oxidation profiles of different Fe atoms/12-mer protein ratios (50-100), in the presence of 1 mM of hydrogen peroxide ***b.*** Iron oxidation profiles of different Fe atoms /12-mer ratio (50-200), in the presence of 1 µM of hydrogen peroxide, ***inset*** initial iron oxidation rates for each Fe atoms/12-mer ratios.

The ability of *Dr*Dps to release iron under reducing conditions was also analyzed. Iron release by *Dr*Dps1 is almost complete (90 %) after the first 50 seconds with an initial release rate of 512 ± 32 µM min^{-1} (Fig. 5.6, A). But for *Dr*Dps2 the iron release is bi-phasic: an initial phase (within the first 50 s) *Dr*Dps2 releases only 60 % of the iron incorporated with an initial release rate of 150 ± 21 µM min^{-1}; in a second slower phase that lasts up to 13 mins the remaining iron is fully released (Fig. 5.6, A). The difference on the iron release rates between the two *Dr*Dps, suggests that the mechanism for iron release of the two proteins is different. In the case of *Dr*Dps1 it is associated with the oligomeric change from the dodecamer form to the trimer (Fig. 5.6, B, lanes 1-3), releasing all iron immediately, represented schematically in figure 5.6 C,

while for *Dr*Dps2, the dodecamer state is maintained (Fig. 5.6, B, lanes 4-6) and the iron release would occur through the specific channels, showed schematically in figure 5.6 C.

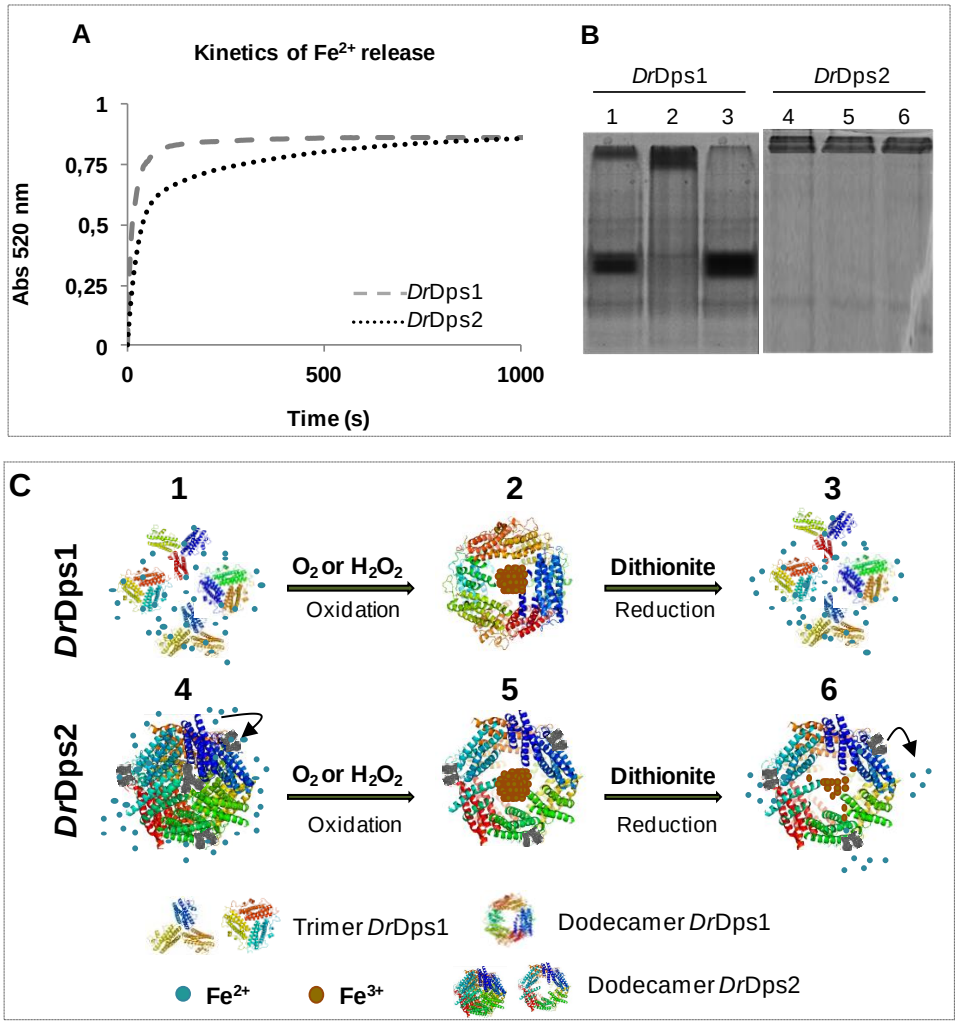

Figure 5.6 - Kinetics of iron release by *Dr*Dps1 (gray line) and *Dr*Dps2 (black line) **(A)**. Proteins at a concentration of 0.5 µM were incubated with 200 Fe atoms/12-mer, and iron release was monitored at 520 nm. **(B)** Analysis of recombinant *Dr*Dps1 or *Dr*Dps2 in the native state (lane 1, lane 4 respectively), incubated with 200 iron atoms (lane 2, lane 5), and incubated with iron followed by addition of the reducing agent- dithionite (lane3, lane 6). The native PAGE (12%) was stained for protein (Coomassie). **(C)** Schematic representation of the iron incorporation of *Dr*Dps1 (steps 1 to 2) or of *Dr*Dps2 (steps 4 to 5) and iron release of *Dr*Dps1 (steps 2 to 3) or *Dr*Dps2 (steps 5 to 6), based in results represented in Fig. 5.4, 5.5 and 5.6 A and B).

The difference in iron oxidation and incorporation between *Dr*Dps1 and *Dr*Dps2 may be explained by the different metal sites observed in their crystal structures determined in the iron soaked state (*203-204*) (Fig. 5.7, A). Both protein structures revealed a ferroxidase center located on the two-fold dimer axis. The iron is octahedrally coordinated by residues $His_{83/70}$ (from one subunit) and from the other subunit $Asp_{110/97}$ and $Glu_{114/101}$, and two non-residue ligands (amino acid numbering corresponds to *Dr*Dps1 and *Dr*Dps2, respectively) (*203-204*) (Fig. 5.7, A). However, in the *Dr*Dps2 crystal structure a second iron atom at a distance of *ca.* 6 Å from each ferroxidase iron center was found. This metal site has a loose octahedral coordination with five water molecules, one amino acid residue, Asp_{98} (OD1 at 2.4 Å), and Lys_{94} which is hydrogen bonded via a water molecule (Fe_2 ··· 2.5 Å ··· water ··· 2.4 Å ··· NZ Lys_{94}) (*204*). In *Dr*Dps1 the two amino acid residues, Asp_{98} and Lys_{94}, are structurally substituted by Glu_{111} and Pro_{107} (Fig. 5.7, A), suggesting that during the iron storage process this protein may not contain the second iron atom. This metal site could play a crucial role in the iron storage mechanism, probably by the formation of a transient di-iron center, and promoting higher iron oxidation rates using oxygen as oxidant, as observed in *Dr*Dps2.

Furthermore, an analysis of the electrostatic potential of the inner cavity molecular surface of the *Dr*Dps dodecamer reveals a predominance of negatively charged residues (Fig. 5.7, B, C), which is a suitable environment for iron storage. Nevertheless, it is interesting to note that *Dr*Dps2 presents a slightly more negatively-charged cavity when compared with *Dr*Dps1, which supports the different results from the iron oxidation and incorporation assays for the two proteins (Fig. 5.4 and 5.5). The highly negative electrostatic potential in the inner cavity observed for *Dr*Dps is comparable to the *Listeria innocua* Dps, a so-called “mini-ferritin”, and is higher than the *E. coli* Dps (*63, 305*) (Fig. 5.7, D). It is interesting to observe that a similar analysis performed for the *Lactococcus lactis* DpsA, which is a non-iron storage protein, reveals a completely different charge distribution inside the cavity (Fig. 5.7, D).

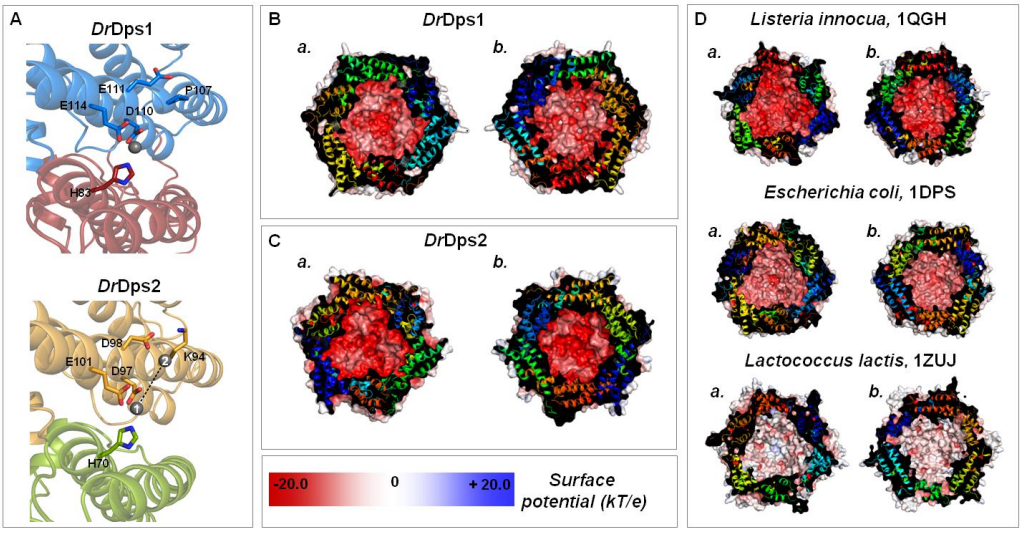

Figure 5.7 - (A) Intersubunit ferroxidase iron center of *Dr*Dps1 and *Dr*Dps2. The amino acid residues involved in the iron coordination are represented in different colors depending on the subunits to which they belong. For *Dr*Dps2 a second iron atom is present (labeled as "2"). **(B, C, D)** Electrostatic potential surfaces of *Dr*Dps1 **(B),** *Dr*Dps2 **(C)**, and Dps **(D)** from: *Listeria innocua* (pdb code 1QGH), *Escherichia coli* (pdb code 1DPS) and *Lactococcus lactis* (pdb code 1ZUJ). Two different orientations are represented: viewed from the 3-fold C-terminal axis **(*a*)** and from the 3-fold N-terminal axis **(*b*)**. Each monomer is represented in cartoon-view with a different colour. The electrostatic potentials were calculated with APBS (*337*) using a protein and solvent dielectric constants of 2.0 and 78.0, respectively; a temperature of 310 K; and an ionic strength of 0.15 M. The charge for each atom was calculated using PDB2PQR (*338*). PyMOL (*217-218*) was used as an interface to APBS, to analyse the electrostatic surfaces and produce the figures.

5.4.4 Manganese incorporation and release

It was previously reported that manganese inhibits the ferroxidase activity of *Dr*Dps1 at a Mn/Fe ratio of 0.2, which is similar to the ratio reported to exist inside the cell (*81, 269*). However the localization of these two metals, iron and manganese, is different: manganese is globally distributed in the cell while iron is localized closely to the region dividing cells (*69*). Therefore, inside the cell, *Dr*Dps can be in the presence of iron and/or manganese alone, depending on the localization of these metals and proteins. Thus the iron-independent storage and release of manganese was investigated.

*Dr*Dps1 incorporates 452 ± 84 Mn atoms/12-mer, while *Dr*Dps2 incorporates 583 ± 32 Mn atoms/12-mer. This corresponds, for both proteins, to a higher manganese capacity than for iron incorporation.

*Dr*Dps manganese release studies indicate that both proteins release 75 % of the total metal incorporated within the first 2 min of the release process, with similar initial rates (0.90 ± 0.14 µM min^{-1} and 1.1 ± 0.06 µM min^{-1} for *Dr*Dps1 and *Dr*Dps2, respectively). After this stage *Dr*Dps1 releases the remaining manganese, while *Dr*Dps2 only releases 85 % (Fig. 5.8). The residual manganese in *Dr*Dps2 could be located in the ferroxidase centers, thus inhibiting the ferroxidase activity, as previously reported for *Dr*Dps1 (*269*); or alternatively, manganese could form a di-metal Mn-Fe center, as proposed for the *Kineococcus radiotolerans* Dps, without affecting ferroxidase activity (*238*). In fact the two residues (His_{60} and Glu_{79}) proposed to be involved in the binding to site B of *K. radiotolerans* Dps are also structurally conserved in *Dr*Dps2 (His_{82} and Glu_{101}).

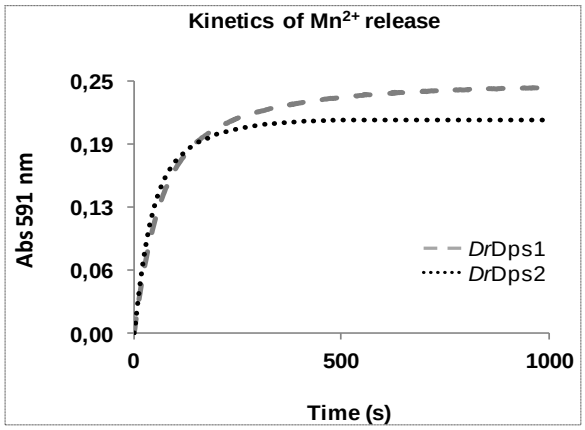

Figure 5.8 - Kinetics of manganese release by *Dr*Dps1 (gray line) and *Dr*Dps2 (black line). Proteins at a concentration of 0.01 µM were incubated with 500 Mn atoms/12 mer of protein, and manganese release was monitored at 591 nm.

Furthermore, it was investigated the *Dr*Dps metal storage when they were simultaneously submitted with both metals (Fe and Mn). It is interesting to note that *Dr*Dps1 incorporates similar amount of both metals, 114 ± 7 Mn/12-mer and 104 ± 9 Fe/12-mer. However it remains to be clarified the metal storage mechanism in a mixed metal environment, specially if we take into consideration the previous results that manganese inhibits the *DrD*ps1 ferroxidase activity (*269*). *Dr*Dps2 incorporates 142 ± 5 Mn/12-mer and 298 ± 11 Fe/12-mer, suggesting that this protein preferentially incorporates iron *versus* manganese.

5.4.5 DNA interaction

The interaction between *Dr*Dps and DNA was studied by EMSA using plasmid, genomic and linear DNA; and AFM was used to shed light on the structure of the Dps-plasmid DNA complexes.

*Dr*Dps1 induced a total DNA shift when 4.5 µM of protein was added to DNA, while for *Dr*Dps2 a partial DNA shift could only be observed with up to 8 µM of protein added. Above this concentration no further change was detected (Fig. 5.9, A, D). The difference in interaction between *Dr*Dps1 and *Dr*Dps2 with DNA is more evident when the proteins were incubated with *D. radiodurans* genomic DNA (Fig. 5.9, B, E). A *Dr*Dps1 concentration of 2.0 µM was enough to induce the formation of *Dr*Dps1-DNA complexes large enough not to enter in the agarose gel (Fig. 5.9, B). In contrast, for *Dr*Dps2, a 10 µM protein concentration was necessary to observe a small DNA shift (Fig. 5.9, E).

In order to understand the effect of DNA size and conformation on protein-DNA complex formation, assays using different linear DNA fragments of variable sizes (100-10000 bp) were performed. *Dr*Dps1 appears to bind preferentially larger DNA fragments (Fig. 5.9, C). This cannot exclude the fact that in the absence of larger DNA fragments *Dr*Dps1 would bind to smaller fragments as shown previously (*205, 270*). *Dr*Dps2 did not show any ability to bind linear DNA (Fig. 5.9, F) confirming the result mentioned earlier when the protein was incubated with plasmid DNA (Fig. 5.9, D).

Therefore, whilst *Dr*Dps1 binds to coiled and linear DNA, the most interesting point of the *Dr*Dps2-DNA interaction is that this protein binds mainly to supercoiled plasmid DNA.

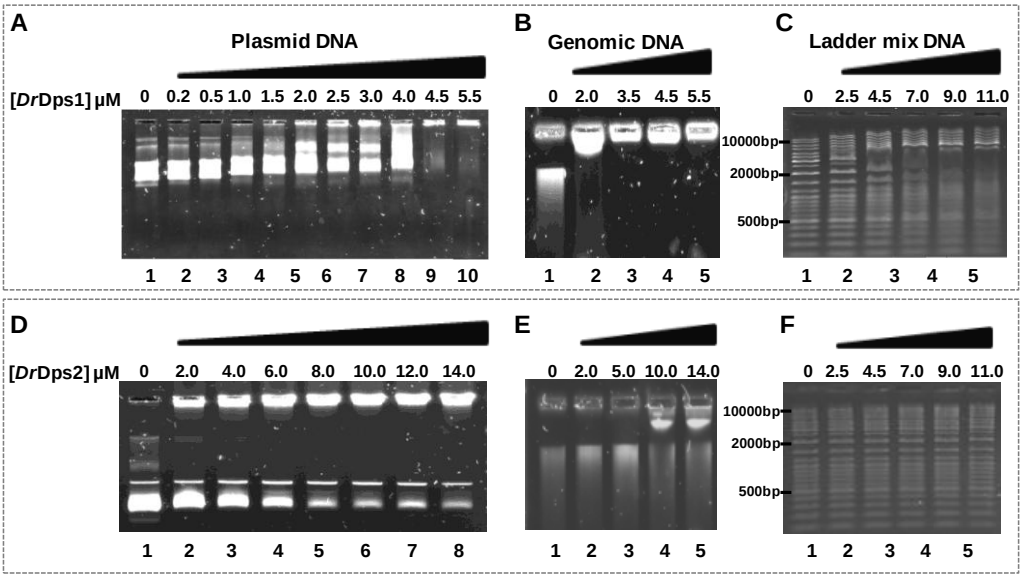

Figure 5.9 - Electrophoretic mobility shift assays for the binding of DNA to *Dr*Dps1 and *Dr*Dps2. Plasmid DNA incubated with *Dr*Dps1 **(A)** or *Dr*Dps2 **(D)** at pH 6.5; *lane 1*- plasmid DNA, *lane 2-10*, plasmid DNA incubated with *Dr*Dps1 (0.2 - 5.5 µM) or *Dr*Dps2 (2 - 14 µM). *D. radiodurans* genomic DNA incubated with *Dr*Dps1 **(B)** or *Dr*Dps2 **(E)** at pH 6.5; *lane 1*- genomic DNA, *lane 2–5*, in the presence of *Dr*Dps1 (2 – 5.5 µM) or *Dr*Dps2 (2 - 14 µM). Ladder Mix DNA incubated with *Dr*Dps1 **(C)** or *Dr*Dps2 **(F)** at pH 7.0; *lane 1*- ladder mix DNA ranging from 100 to 10000 bp, *lanes 2-5*, in the presence of *Dr*Dps1 (2.5 - 11 µM) or *Dr*Dps2 (2.5 - 11 µM).

Further evidence for the formation of *Dr*Dps-DNA complexes was obtained by AFM. The *Dr*Dps1-DNA complexes observed at pH 6.5 had a height within the range of 9 to 16 nm (*Dr*Dps1 height 8 nm and DNA height 1.5 nm) (Fig. 5.10, A, B, D). These complexes appear to contain plasmid DNA molecules looping out from a central aggregate that contains *Dr*Dps1 molecules (Fig. 5.10, D). This result showed that the DNA surrounds the protein, although previous studies have suggested that *Dr*Dps1 dodecameric form is not able to bend the DNA duplex (*270*). A similar structure complex was observed for Dps from *E. coli* and *H. pylori* NAP (*265, 268*). At pH 7.0 *Dr*Dps1 are sparsely distributed along the plasmid DNA (Fig. 5.10, E) suggesting the formation of smaller aggregates which is related to the different *Dr*Dps1 oligomerization states induced by pH, as described above (Fig. 5.1, D, E).

*Dr*Dps2 forms different protein-DNA complexes only 9 nm in height, suggesting that *Dr*Dps2 are surrounded by DNA but spread along the DNA with a toroidal morphology. The data indicates the formation of similar *Dr*Dps2-DNA complexes at pH

6.5-7.0 (Fig. 5.10, F-G). This type of protein-DNA complex structure was observed in the Dps1 from *M. smegmatis* (*295*), and DNA interaction studies of this protein indicate that the interaction is through its C-terminal region (*247*), which could be a similar case for *Dr*Dps2, which contains one lysine and two arginine residues (Lys_{204}, Arg_{209}, Arg_{211}), in this region.

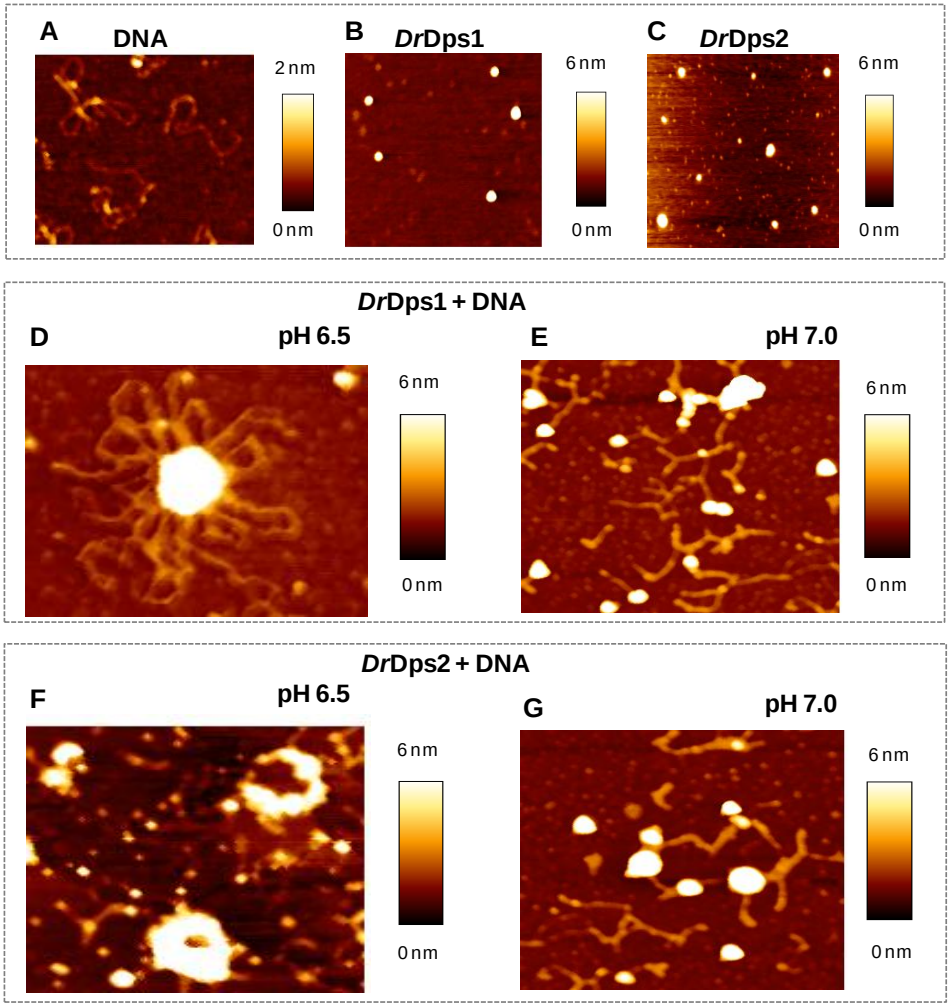

Figure 5.10 - Interaction of *Dr*Dps1 and *Dr*Dps2 with DNA observed by atomic force microscopy at pH 6.5 **(D, F)** or pH 7.0 **(E, G)**. **(A)** plasmid DNA, **(B)** *Dr*Dps1 without DNA, **(C)** *Dr*Dps2 without DNA. **(D, E)** *Dr*Dps1-DNA complexes at pH 6.5 **(D)** or pH 7.0 **(E)**. **(F, G)** *Dr*Dps2-DNA complexes at pH 6.5 **(F)** or pH 7.0 **(G)**.

5.4.6 DNA protection

In order to address the ability of *Dr*Dps to protect DNA, the proteins were incubated with DNA followed by the addition of iron and hydrogen peroxide to promote ROS formation. Without the presence of *Dr*Dps, a complete degradation of DNA was observed (Fig. 5.11, A-C, lane 3).

Previous studies on *Dr*Dps1 indicated that the dimer form of this protein protects DNA from ROS degradation, yet the dodecameric form did not confer any DNA protection under this condition (*205*). Our results on DNA protection show that both *Dr*Dps1 dimeric and dodecameric forms protect the DNA against ROS induced degradation (Fig. 5.11, A-B). It is interesting that the *Dr*Dps1 dimeric form is able to protect the DNA up to 200 Fe atoms/12-mer, above this value, a structural reorganization of the protein forming the dodecamer occurs, as observed in Fig. 5.11, A (bottom gel), and as shown by SEC (Fig. 5.1). Under this condition, there is no longer DNA protection. The *Dr*Dps1 dodecamer is able to protect DNA to above its iron storage capacity (500 Fe atoms/12-mer), as shown in Fig. 5.11, B, suggesting that DNA protection by *Dr*Dps1 could be due to its DNA interaction and to the fact that the protein-DNA complex formed is able to shield the DNA from degradation.

*Dr*Dps2 protects DNA only up to 100 Fe atoms/12-mer (Fig. 5.11, C), suggesting that the iron capacity of *Dr*Dps2 is affected by the presence of DNA. In fact, the iron oxidation rate by hydrogen peroxide in the presence of DNA is reduced (Fig. 5.11, D). The simple explanation is the possible blockage by DNA of the iron entry channels in *Dr*Dps2, or since *Dr*Dps2 binds to supercoiled plasmid DNA the observed effect could also be due to Fenton chemistry primarily occurring on the relaxed plasmid form.

The protection of DNA by *Dr*Dps1 from DNase I cleavage was previously described, in which higher concentrations of *Dr*Dps1 induce a higher DNA degradation (*205*), while *Dr*Dps2 was shown to confer protection to the DNA from DNase I cleavage (*206*). DNA protection from DNase II degradation by *Dr*Dps was analysed. *Dr*Dps-dependent DNA protection is observed at protein concentrations of 14 µM or 20 µM for *Dr*Dps1 and *Dr*Dps2, respectively. At lower protein concentrations, 7 µM (*Dr*Dps1) or 14 µM (*Dr*Dps2), a complete degradation of plasmid DNA was observed (Fig. 5.11, E). This suggests the existence of a Dps-dependent DNA protection mechanism, substantiated by the protein-DNA complex observed by AFM, that appears to shield the DNA from damage.

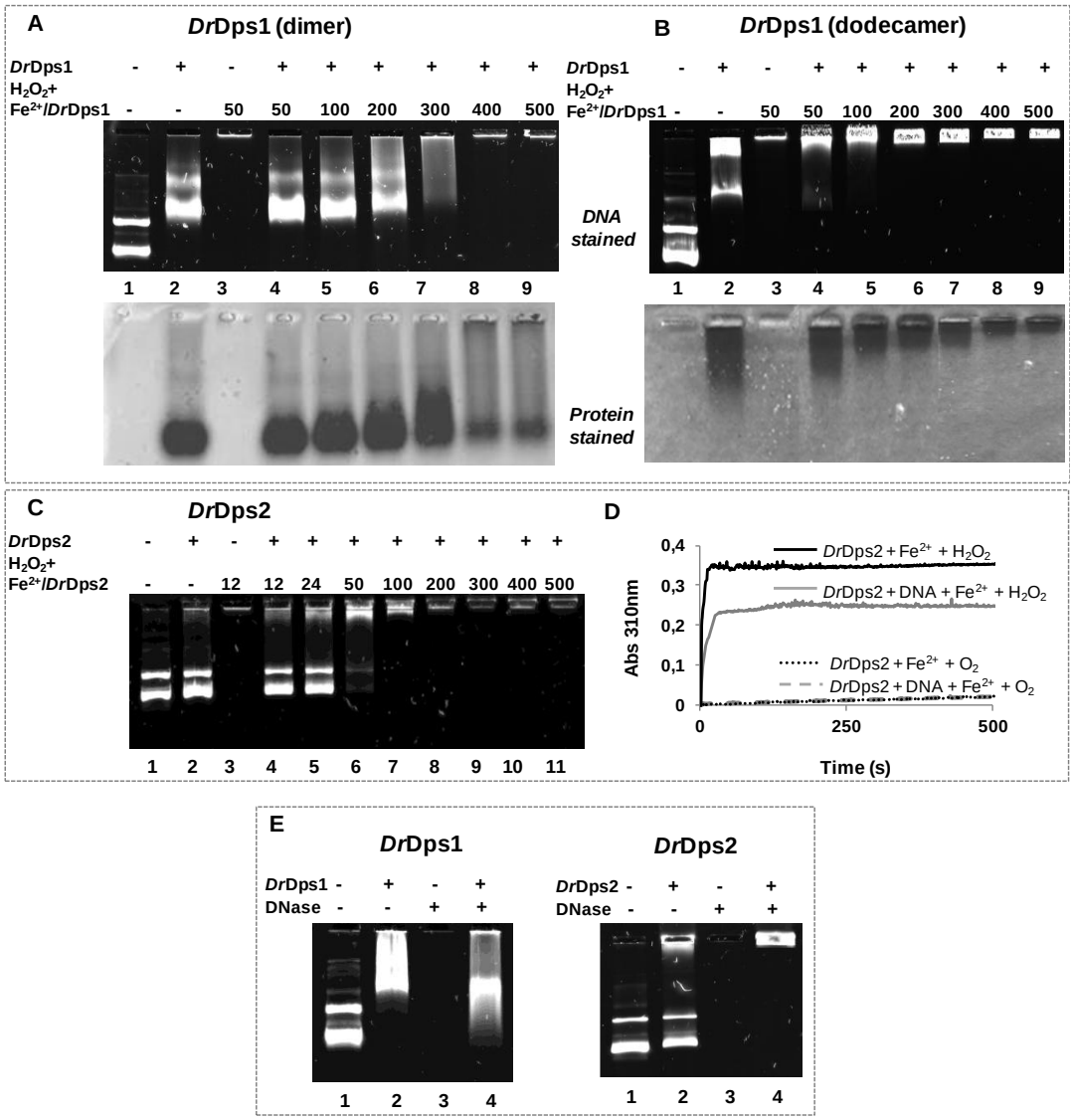

Figure 5.11 - Electrophoretic mobility shift assays showing protection of DNA by *Dr*Dps1 dimer **(A)**, *Dr*Dps1 dodecamer **(B)** and *Dr*Dps2 **(C)**, under oxidative stress conditions. *Lane 1*, plasmid DNA; *lane 2*, DNA incubated with protein; *lane 3*, DNA incubated with 10 mM of H_2O_2 and 12 **(C)** or 50 **(A, B)** atoms of Fe^{2+}; *lanes 4-11*, DNA incubated with *Dr*Dps1 **(A, B)** or *Dr*Dps2 **(C)**, followed by the addition of 1 mM of H_2O_2 and 12-500 Fe^{2+} atoms/12-mer *Dr*Dps. The top view is stained for DNA and the bottom view is stained for protein **(A, B)**. **(D)** Kinetics of Fe^{2+} oxidation by 1 µM of *Dr*Dps2 dodecamer in 20 mM MOPS pH 7.0, 150 mM NaCl. 100 Fe^{+2} atoms were added to *Dr*Dps2 using O_2 as oxidant (dotted line, black), plasmid DNA was incubated with *Dr*Dps2 for 30 min followed by of the addition of 100 Fe^{2+} atoms using O_2 as oxidant (dash line, gray), 100 Fe^{+2} atoms were added to *Dr*Dps2 using H_2O_2 as oxidant (solid line, black), plasmid DNA was incubated with *Dr*Dps2 for 30 min followed by the addition of 100 Fe^{2+} atoms using H_2O_2 as oxidant (solid line, gray). **(E)** DNA protection assay against DNase digestion by *Dr*Dps1 or *Dr*Dps2. *Lane 1*, plasmid DNA; *lane 2*, DNA incubated

with *Dr*Dps; *lane 3*, DNA in the presence of DNase; *lane 4*, DNA incubated with *Dr*Dps1 or *Dr*Dps2 and then treated with DNase.

5.5 Discussion

The study on *Dr*Dps shows that both proteins share a similar dodecameric structure (*203-204*), have ability to store metals (Fe and Mn), bind and protect DNA in *in vitro* conditions.

*Dr*Dps1 is constitutively expressed in *D. radiodurans* under control conditions throughout the different bacterial growth phases, which is in accordance to what was previously reported (*199, 333*). The effect of hydrogen peroxide addition to *D. radiodurans* cell growth was previously studied, and the authors claimed that the transcript of the *dps1* gene decreases when cells are exposed to this reagent (*208*). Nevertheless, a different study indicates that *dps1* promoter does not respond to the addition of hydrogen peroxide or iron (*206*). Our data indicates that *Dr*Dps1 remains constitutively expressed after the addition of hydrogen peroxide, iron or manganese (Fig. 5.3), in agreement with the study mentioned before (*206*).

*Dr*Dps1 presents different oligomeric forms depending on the *in vitro* conditions. The presence of different oligomeric states in other Dps also has been described in solution and has been associated with different functions (*205, 243, 267, 292*). For instance, the trimeric and dodecameric forms of Dps1 from *M. smegmatis* differ in their DNA binding properties. The trimer is unable to bind DNA and the dodecamer forms large crystalline arrays with DNA but both oligomeric forms protect the DNA against ROS (*243*). On the other hand a study on the *Dr*Dps1, shows that both oligomeric forms, dimer and dodecamer, bind to DNA (*205*). Nevertheless, the physiological relevance for the lower oligomeric states has not been clarified.

Our results show that the different *Dr*Dps1 oligomeric forms observed in *in vitro* conditions can also be identified in *D. radiodurans* extracts. Furthermore, it is interesting to observe that its oligomerization state changes during growth phases and is affected by the addition of different factors (manganese, iron and hydrogen peroxide) (Fig. 5.3). These results reinforce our *in vitro* data in which *Dr*Dps1 changes between dodecameric, trimer and dimer depending on the conditions (Fig. 5.1). *In vivo*, the conditions are determined by the environment and thus may not directly be

related to these *in vitro* conditions. Still, out data suggests that *in vivo Dr*Dps1 oligomeric forms and functional roles may adapt to environmental changes.

It is interesting to note that change in oligomerization is an essential property of heat shock proteins, which includes the formation of dimers and other different oligomers. In fact it has been proposed that the inter-conversation between the different forms may be related with their chaperone activity (*339-342*).

Based on our data, we propose the following model for the function of *Dr*Dps1. Under control conditions, *Dr*Dps1 is dimeric (Fig. 5.3, B *a*) and is associated with DNA (Fig. 5.3, C *b*), forming protein-DNA complexes similar to those observed by AFM (Fig. 5.10, E). This is also supported by a previous study in which *Dr*Dps1 immunolocalization under control conditions (similar to those used in our work) showed that this protein is weakly associated with the nucleoid (*207*). The *Dr*Dps1 dimer DNA interaction would probably occur through the N-terminal region which contains six lysines and one arginine residue with the motif $K_3K_4(x)_2K_7(x)_5K_{13}(x)K_{15}K_{16}(x)_{11}R_{28}$ and through the Arg_{132} which is located in the small BC helix, which is supported by previous deletion and mutation studies (*271*). However in this case it was proposed that the DNA interaction would occur with the dodecamer, but from our results we suggest that the interaction would be with the *Dr*Dps1 dimer.

The addition of manganese or hydrogen peroxide, to the cell growth medium, induces a structural conformation change towards the trimeric form which is no longer DNA bound (Fig. 5.3, C). This dissociation from the DNA is only possible due to the fact that the interaction between *Dr*Dps1 and the nucleoid is weak, as previously shown (*207*). Since the formation of the *Dr*Dps1 trimer is higher when manganese was added to the *D. radiodurans* cell growth compared with hydrogen peroxide (Fig. 5.3, B), we suggest that the trimer acts as a metal chaperone and is associated with the "antioxidant" manganese metabolite complexes which are proposed to be involved in *D. radiodurans* protection from oxidative stress (*84, 343*). Iron addition induces a gradual structural change towards dodecamer formation that is observed after mid-exponential and is more evident in the stationary phase. Under this condition the protein behaves as a typical iron storage protein with the ability to store iron. Our *in vitro* data shows that dodecamer *Dr*Dps1 is able to fully release the metal incorporated (Fig. 5.6), in a process associated with an oligomeric change. Furthermore, we can not rule out that under this condition the protein can also assume a role in manganese

storage, since *in vitro* *Dr*Dps1 incorporates the two metals (iron and manganese) in similar amounts when was submitted simultaneously to both metals.

Previous studies have indicated that *Dr*Dps2 was not detected in the nucleoid fractions (*207*) and immunolocalization of *Dr*Dps2 showed that this protein is localized at the cell periphery region (*206*). Based on this, it was proposed that this protein is involved on iron homeostasis (*206*). Our data shows that *Dr*Dps2 is a stable dodecamer in the different conditions tested *in vitro* (Fig. 5.2) and *in D. radiodurans* extracts (Fig. 5.3, D). In *D. radiodurans* soluble fractions, it was observed that *Dr*Dps2 is more expressed in the exponential phase, under control conditions and after the addition of manganese or iron, than in the stationary phase (Fig. 5.3, D). The protein is slightly more expressed after iron or manganese addition when compared to the control (Fig. 5.3, D). Our *in vitro* studies show that *Dr*Dps2 has higher iron oxidation rates under aerobic conditions and iron storage capacity than *Dr*Dps1 (Fig. 5.4), and also shows the ability to store manganese (Fig. 5.5). Furthermore, it is interesting that *Dr*Dps2 preferentially incorporates iron *versus* manganese, when submitted simultaneously to both metals. As a result, we consider that this protein is involved in intracellular metal storage, and could be more selective for iron depending on the cellular environment.

The hydrogen peroxide concentration in the cell has been estimated to be around 10^{-7} M in the exponential cell growth phase, which is well below the limit concentration estimated for toxicity (10^{-5} M) (*318, 344*). Therefore, under control cell growth conditions both *Dr*Dps would be able to oxidize the iron using hydrogen peroxide almost at the same oxidation rates, since the concentration of hydrogen peroxide is low. Whereas in an eventual oxidative stress burst, the intracellular hydrogen peroxide concentration increases, and in this condition *Dr*Dps1 becomes much more efficient for iron oxidation than *Dr*Dps2. The effect of ROS on *Dr*Dps promoter-activity has been described previously (*206*): the *dps1* promoter was not shown to respond to hydrogen peroxide addition, whilst *dps2* promoter activity increased under the same conditions in both the exponential and stationary phases. This is in agreement with our data, in which the addition of hydrogen peroxide does not induce a change in the *Dr*Dps1 expression levels, but a change in its oligomeric form is observed, dimer to trimer (Fig. 5.3). Under these conditions, *Dr*Dps1 trimer would be associated with manganese homeostasis and detoxification of ROS, whereas *Dr*Dps2 accumulates during the stationary phase of treated cells with hydrogen peroxide (Fig. 5.3), which

could be considered as a “typical Dps” response. Since, we have observed that *Dr*Dps2 expression level is higher in the stationary phase but we do not have any evidence for the formation of Dps-DNA two-dimensional crystals similar to those that have been described for the *E. coli* Dps (*272, 326*). Nevertheless, it is very interesting that our data show that the *Dr*Dps2-DNA interaction is specific for supercoiled DNA, forming a complex with toroidal morphology (Fig. 5.9-5.10). Since DNA packing in *D. radiodurans* adopts a toroidal morphology (*345-346*), *Dr*Dps2 could be part of this structure when hydrogen peroxide is present at certain concentrations, surrounding the DNA and forming a first protective barrier against different stress conditions.

Taken together, our results show that despite the conserved structural features of *Dr*Dps, they have different functions in the cell, and that these functions depend upon several intracellular factors such as metal availability and oxidative stress.

Further investigation into this family of proteins is required in order to fully elucidate their structural vs functional conservation inside cells.

5.6 Acknowledgements

This work was financed by Fundação para a Ciência e Tecnologia through the following Grants: PTDC/BIA-PRO/100365/2008 (C.V.R.), PTDC/QUI-BIQ/100007/2008 (I.A.A) and PEst-OE/EQB/LA0004/2011. S.P.S. is recipient of PhD Grant SFRH/BD/78870/2011. I.A.A and C.V.R. are recipient of the grants SFRH/BPD/78314/2011 and SFRH/BPD/94050/2013, respectively. We gratefully acknowledge Professor Emilia Chiancone and Dr. Pierpaolo Ceci from University of Rome, Italy for helping in EMSA initial studies. We thank Professor Suzanne Sommer from Institut de Génétique et Microbiologie (Paris, France) for kindly providing the *Dr*Dps knockout mutants.

CHAPTER VI

SAXS structural studies of Dps from *Deinococcus radiodurans* highlights the conformation of the mobile N-terminal tails

This chapter is part of the published paper:

Santos S. P, Cuypers M. G., Round A., Finet S., Narayanan T., Mitchell E. P., Romão C. V. (2016) SAXS structural studies of Dps from *Deinococcus radiodurans* highlights the conformation of the mobile N-terminal extensions, J. Mol. Biol. http://dx.doi.org/10.1016/j.jmb.2017.01.008

Santos S. P. participated in the manuscript preparation and was responsible for all the experimental work including SAXS data collection in BM29 beamline at ESRF, and data processing. The SAXS studies were performed in collaboration with Round A.. This work was complemented with the SAXS data collected in the ID02 beamline at ESRF in collaboration with Cuypers M.G., Finet S., and Narayanan T..

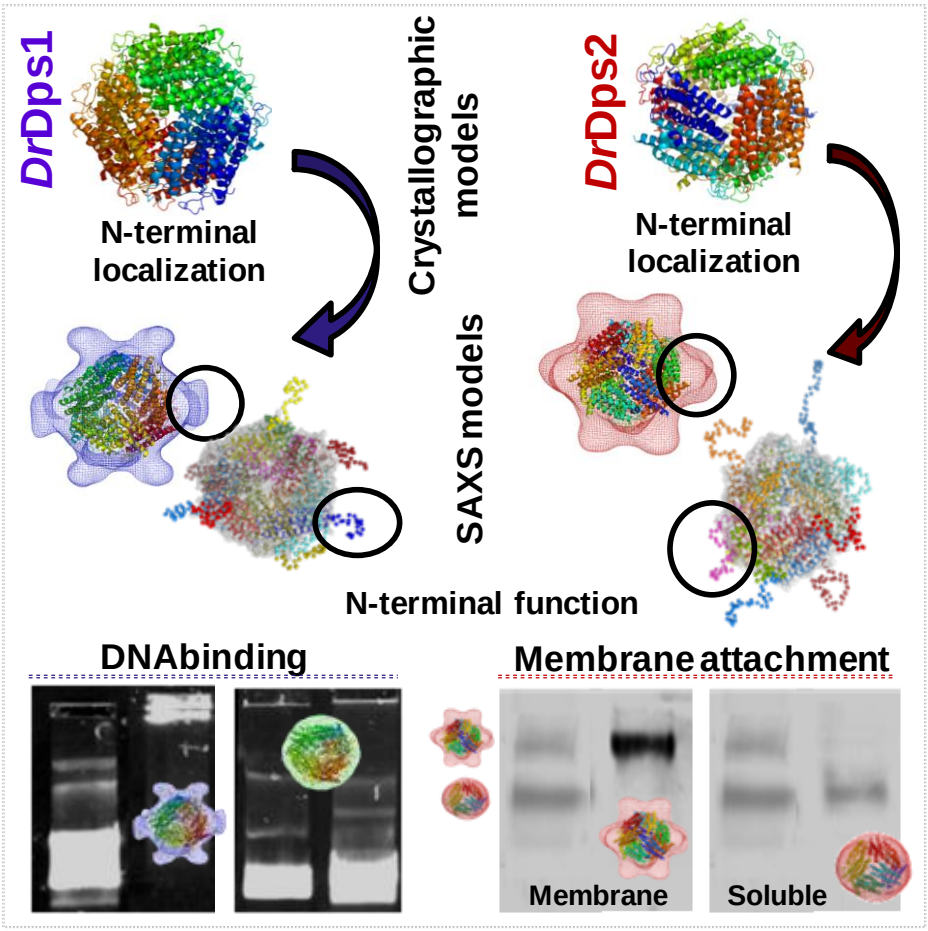

Highlights:

Location of the *Dr*Dps N-terminal tails protruding from the dodecamer spheres.

Function of the *Dr*Dps2 N-terminal tails and its association with the membrane.

6.1 Abstract

The radiation-resistant bacterium *Deinococcus radiodurans* contains two DNA-binding proteins from starved cells (Dps): *Dr*Dps1 (*Dr2263*) and *Dr*Dps2 (*Drb0092*). These are suggested to play a role in DNA interaction and manganese and iron storage. The proteins assemble as a conserved dodecameric structure with structurally uncharacterised N-terminal tails. In the case of *Dr*Dps1, these tails have been proposed to be involved in DNA interactions, while in *Dr*Dps2, their function has yet to be established.

The reported data reveal the relative position of the N-terminal tails to the dodecameric sphere in solution for both *Dr*Dps. The low-resolution small angle X-ray scattering (SAXS) results showed that the N-terminal tails protrude from the spherical shell of both proteins. The SAXS envelope of a truncated form of *Dr*Dps1 without the N-terminal tails appears as a dodecameric sphere, contrasting strongly with the protrusions observed in the full-length models.

The truncated and full-length versions of *Dr*Dps were also compared on the basis of their interaction with DNA to analyse functional roles of the N-terminal tails. *Dr*Dps1 N-terminal protrusions appear to be directly involved with DNA, whilst those from *Dr*Dps2 are indirectly associated with DNA binding. Furthermore, detection of *Dr*Dps2 in the *D. radiodurans* membrane fraction suggests that the N-terminus of the protein interacts with the membrane.

Keywords: DNA, metal, scattering, signal peptide, membrane

6.2 Introduction

*D*NA-binding *p*roteins from *s*tarved cells (Dps) belong to the ferritin family and have been identified only in prokaryotes. The function of these proteins has been associated mainly with iron storage and DNA protection against degradation promoted by reactive oxygen species (*219-220, 249*). The structure of these proteins is quite conserved. They are composed of 12 identical monomers, assembling together to form a roughly spherical dodecamer with 23 symmetry. This hollow shell has around 90 Å and 50 Å external and internal diameters, respectively. Each subunit is a four-helix bundle, as in ferritins, but contains a further short helix between helix B and C and lacks the fifth helix at the C-terminus, which is responsible for the 4-fold symmetry in ferritins (*219-220, 237, 240, 249*).

Although the dodecameric core is structurally conserved, the Dps family members have a variety of either shorter or longer tails of the amino acid chain at the N- or C-termini. These tails have been proposed to be involved in DNA interaction and condensation and are thought to be important for the DNA protection mechanism of Dps. For example, the Dps from *Escherichia coli* (*Ec*Dps) presents an N-terminal tail of 20 amino acid residues with four positively charged residues: three lysine residues (Lys_5, Lys_8, and Lys_{10}) and one arginine (Arg_{18}). Truncating the first 18 amino acid prevents DNA condensation (*265*). It has been therefore proposed that this region is implicated in DNA interaction. The model of *Ec*Dps resulting from elucidation of its crystal structure does not include the full N-terminus, suggesting a highly flexible region that could not be modeled (*232*). In the Dps from *Mycobacterium smegmatis* (*Ms*Dps1), the tail occurs at the C-terminus, which contains 26 amino acid residues. This region has three positively charged lysine residues (Lys_{172}, Lys_{177}, and Lys_{181}), which have also been suggested to be involved in DNA binding (*247*). Again, the crystal structure model of this protein does not include the tail; this disorder was suggested to be related with local flexibility (*309*). As for *Ec*Dps, the presence of the positively charged amino acid residues and the flexibility of this region could contribute to the interaction and condensation of DNA. On the other hand, for both Dps from *Lactococcus lactis*, which have an N-termini of 26 amino acid residues, it was possible to model this region in the corresponding crystal structures, since it forms a stable helix, and the deletion of this region in DpsA impairs DNA binding (*245*).

Interestingly, both Dps from *Deinococcus radiodurans* (*Dr*Dps) have longer N-terminal tails compared to any other Dps family members studied so far. Before the helix A of the four-helix bundle, *Dr*Dps1 and *Dr*Dps2 contain a total of 54 and 41 residues, respectively (Fig. 6.1).

The N-terminus of *Dr*Dps1 can be divided into two regions: a positively charged region (residues 1–29), which contains six lysine residues (Lys_3, Lys_4, Lys_7, Lys_{13}, Lys_{15}, and Lys_{16}) and one arginine (Arg_{28}) and has been proposed to be involved in the association with DNA (*270*). The second region (residues 30–55) contains a metal binding site with the motif $Asp_{36}X_2His_{39}X_{10}His_{50}X_4Glu_{55}$, which is located on the external surface of the dodecamer accessible to the solvent. The disruption of this metal site affects the dodecamer assembly and also reduces DNA binding ability (*269*), but its nature is not yet fully established, since different metals have been found to bind to this site, including zinc and cobalt (*347-348*).

*Dr*Dps2 contains a signal peptide with 30 amino acid residues, which makes this protein unique since the presence of a signal peptide has not been reported for other Dps homologues. It has been suggested that under *in vivo* conditions, this signal peptide directs *Dr*Dps2 to a non-cytoplasmic localization (*206*). This region is probably cleaved, and the mature protein has 41 amino acid residues before the start of the first helix (the amino acid residue numbering does not account for the signal peptide) (Fig. 6.1). The function of the N-terminal tail has yet to be addressed, but since it only harbours one positively charged residue, Arg_{33}, it is unlikely to be the DNA-binding region. However, at the C-terminus, this protein contains an tail of 24 amino acid residues, with three positively charged residues: one lysine and two arginines (Lys_{204}, Arg_{209}, and Arg_{211}). This C-terminal tail has been proposed to be involved in dodecamer formation. Although its role in DNA binding has not been addressed to date, the presence of positively charged residues in this region strongly hints that it could be involved in DNA interaction as in *Ms*Dps1.

As mentioned above, the N-terminal tail of *Dr*Dps1 is suggested to be involved in the interaction of *Dr*Dps with DNA, whilst in the case of *Dr*Dps2, the function remains unknown. However, a significant part of these N-terminal tails could not be modelled from the *Dr*Dps crystal structures obtained to date, probably due to protein degradation, disorder, or flexibility of these regions; *Dr*Dps1 lacks the first 29 amino acid residues, and *Dr*Dps2 crystal structure lacks the totality of its 41 residues (*347, 349*). It is crucial to determine the structural conformation and localisation relative to

the dodecamer sphere of these regions in solution. Solution small angle X-ray scattering (SAXS) is part of the suite of structural techniques available to explore the properties of biological macromolecules and provides unique, low-resolution conformational information, which sometimes cannot be obtained from other techniques (in this case, crystallography).

Therefore, solution scattering studies were performed on both *Dr*Dps, aiming to explore the structural conformation of these regions in solution. SAXS studies have been previously described for the Dps from *Porphyromonas gingivalis* (*350*), but only to characterise the spherical dodecamer shape. This current work describes the location and shape of the N-terminal flexible tails of *Dr*Dps proteins, which protrude outside from the dodecameric sphere. The aim was to obtain the *ab initio* shape from SAXS data and contribute to the unravelling of the function of these tails.

6.3 Experimental Procedures

6.3.1 Protein production and purification

*Dr*Dps1 was purified as previously described (*203*). *Dr*Dps1 truncated protein lacking the 50 N-terminal amino acids residues (*Dr*Dps1t$_{\Delta 1-50}$) was obtained from the *in situ* cleavage of *E. coli* extract with recombinant *Dr*Dps1. The protocol for protein expression and purification was performed at room temperature using the same procedures described for *Dr*Dps1. Sample purity was judged by SDS-PAGE and Western blotting analysis as described in Ref. (*351*), which confirmed that the protein was 100% cleaved to yield *Dr*Dps1t$_{\Delta 1-50}$. In order to determine the starting amino acid sequence, the N-terminal sequencing was made for *Dr*Dps1t$_{\Delta 1-50}$. This was done first using SDS-PAGE followed by Western blotting (semi-dry system, BioRad) using polyvinylidene fluoride membrane (PVDF). Before loading the samples into 15% SDS-PAGE, the gel was submited to a pre-run with a running buffer [1.5% (wt/vol) Tris, 7.2% (wt/vol) glycine, and 0.5% (wt/vol) SDS at pH 8.3] with 40 μM of glutathione for 2 h at 100 V. Subsequently, the running buffer was removed, and a new running buffer was added, containing an extra 3% (vol/vol) of thioglycolic acid. The sample was applied to the gel and the run was performed at 150 V at room temperature. Then, the gel was washed in the blotting running buffer [10% (vol/vol) methanol and 10 mM

CAPS at pH 11]. PVDF membrane was activated in 100% methanol for 30 s and washed with water and then with the blotting running buffer for 15 min. The sample transfer was done for 30 min at 15 V at room temperature. After the transfer, the PVDF membrane was stained with Coomassie brilliant blue R-250 (BioRad) followed by washing with water and 50% (vol/vol) methanol. The N-terminal amino acid residue sequence was determined by Edman reaction using Procise 491 HT Protein Sequencer (Applied Biosystems). These data were provided by the Analytical Laboratory, Analytical Services Unit from Instituto de Tecnologia Química e Biológica António Xavier, Universidade Nova de Lisboa.

*Dr*Dps2 was purified as previously described (*204*). A truncated construct lacking the 39 N-terminal amino acid residues (*Dr*Dps2t$_{\Delta 1-39}$) was cloned into a plasmid pET151/D-TOPO (Gateway system, Invitrogen) with His-Tag and Tobacco Etch Virus (TEV) cleavage site at the N-terminus. The resulting plasmid was transformed into *E. coli* BL21 (DE3) Star, and overexpression was obtained by growing cells at 37 °C in LB with 100 µg/ml ampicillin until an optical density at 600 nm of 0.6. The cells were induced with 0.5 mM of IPTG, which were grown for 4 h at 37 °C. The cells were collected by centrifugation at 16,000 *g* for 20 min at 4 °C, resuspended in lysis buffer [20% (wt/vol) sucrose, 50 mM Tris-HCl (pH 8.0), 100 mM NaCl, 1 mM $MgCl_2$, 0.1 mg/ml lysozyme, and 20 µg/ml DNase], and broken in a French pressure cell at 35,000 psi.

The protein expressed was found in inclusion bodies, which were collected by centrifugation at 11,000 *g* for 15 min at 4 °C. The inclusion bodies were refolded using the previously reported procedure (*203*). The renaturated sample was loaded in 5-ml HisTrap HP column [1.5 ml/min, 20 mM Tris-HCl (pH 7.5), 250 mM NaCl, 2.5% glycerol, 1 mM PMSF, and 10-500 mM Imidazole]. The *Dr*Dp2t$_{\Delta 1-39}$ sample was eluted at 100-300 mM imidazole, and it was immediately dialysed against 20 mM Tris-HCl (pH 7.5), 150 mM NaCl, 2.5% glycerol, and 1 mM PMSF. His-Tag was cleaved by an overnight incubation at 4 °C with TEV protease. Finally, the sample was loaded on the 5-ml HisTrap HP column (GE) using the same buffers as described above. The protein was eluted in flow-through, and its purity was judged by SDS-PAGE analysis.

The oligomerisation state for all proteins, after purification, was resolved by SEC using a Superdex 200 10/300 GL (GE Healthcare) column equilibrated with 20 mM Tris–HCl (pH 7.5) and 150 mM NaCl buffer. The column was previously calibrated using the standard's proteins ranging 14–660 kDa (GE Healthcare).

All samples, *Dr*Dps1, *Dr*Dps1t$_{\Delta 1-50}$, *Dr*Dps2, and *Dr*Dps2t$_{\Delta 1-39}$ used in experiments were dialyzed in 20 mM Tris–HCl (pH 7.5) plus 150 mM NaCl buffer and concentrated to 10 mg/ml.

6.3.2 ESRF beamline BM29: SAXS setup, data collection for *Dr*Dps1, *Dr*Dps1t$_{\Delta 1-50}$ and *Dr*Dps2

SAXS data were collected at the ESRF BioSAXS beamline BM29 (*352*). An online HPLC system (Viscotek GPCmax, Malvern Instruments) was used (*353*) coupled directly to the BM29 sample changer (*354*) exposure unit inlet valve. Independently, three *Dr*Dps1, two *Dr*Dps1t$_{\Delta 1-50}$, and two *Dr*Dps2 samples were loaded into vials and automatically injected onto the SEC, Superdex 200 10/300 GL (GE Healthcare), equilibrated with 20 mM Tris–HCl (pH 7.5) and 150 mM NaCl buffer at room temperature *via* an integrated syringe system.

SAXS data were collected using X-rays of wavelength of 0.9919 Å and a sample-to-detector distance of 2.81 m corresponding to q ranges of 0.08–4.5 nm^{-1} (Table 6.1). About 1500 (1 frame s^{-1}) frames were collected for each sample, where q is the magnitude of the scattering vector given by $q = 4\pi/\lambda \sin(\theta)$, with 2θ the scattering angle. All data processing of each sample was performed automatically using the *EDNA* online data analysis (*355*) pipeline using tools from the EMBL-HH *ATSAS* 2.5.1 (*356*), generating radially integrated, calibrated, and normalised one-dimensional profiles for each frame. All frames were compared with the initial frame, and matching frames were merged to create the reference buffer. Any subsequent frames, which differed from the reference buffer, were subtracted and then processed within the *EDNA* pipeline. The invariants calculated by the *ATSAS* tool (*AUTORG*) were used to select a subset of frames from the peak scattering intensity. Frames with a consistent radius of gyration (R_g) from the peak scattering intensity were automatically merged to yield a single averaged frame corresponding to the scattering of an individual SEC-purified species. The peaks of interest were reprocessed manually to maximise the signal-to-noise ratio. Individually, the frames (approximately 60 for *Dr*Dps1, 40 for *Dr*Dps1t$_{\Delta 1-50}$, and 45 for *Dr*Dps2) corresponding to the highest protein concentration were merged and used for all further data processing and model fitting. A Kratky plot was used to confirm the fold of the all proteins samples.

6.3.3 Data processing for *Dr*Dps1, *Dr*Dps1t$_{\Delta 1\text{-}50}$ and *Dr*Dps2

The radius of gyration was computed from the slope of the Guinier plot of the profile (*349*) using PRIMUS (ATSAS) (*357*) represented by this equation: I (q) = I(0) exp [− ($q^2R_g^2$)/3], and this equation is valid when the momentum transfer (q) is near zero or when q.R_g < 1.3 (*347*). Curve fitting was carried out to determine the value of the maximal particle size (D_{max}) by calculating the pair distance distribution function [*P(r)*] for an arbitrary monodispersive system model using GNOM (*358*). Also, R_g and Porod volume were obtained by *P(r)* function using the GNOM program that is included in *ATSAS* 2.5.1 suite (*358*). The *P(r)* function was obtained only for the *q* values < 2 nm^{-1}.

Theoretical scattering curves were calculated from structures of *Dr*Dps1 or *Dr*Dps2 (PDB codes 2C2U and 2C2J) and compared with the experimental data SAXS using CRYSOL (*359*). The *ab initio* shapes were obtained from the SAXS data for each sample using GASBOR program (*360*) and EOM (*361*), first without structural information from the crystal structure, applying no symmetry (point group 1), then imposing the crystal structure point group symmetry (P23) of the *Dr*Dps dodecameric particles and the total protein residues expected per monomer (207 for *Dr*Dps1, 158 for *Dr*Dps1t$_{\Delta 1-50}$, and 211 for *Dr*Dps2).

6.3.4 SAXS model shape representation

For each *Dr*Dps (*Dr*Dps1, *Dr*Dps1t$_{\Delta 1-50}$, and *Dr*Dps2), a total of 10 *ab initio* reconstructed models obtained with GASBOR were matched by DAMAVER (*362*) program package (based on the program SUPCOMB) (*363*). The models were obtained only from the *q* range < 2 nm^{-1}. Low-resolution electron density maps of the molecular envelopes were computed with PDB2VOL and converted to CCP4 format with MAP2MAP (both programs are part of the SITUS (v2.5) program package (*348, 364-368*). Docking of the X-ray crystal structures with the SAXS maps was performed using Colacor (SITUS v2.5) and by manual translation and rotation. The shape reconstruction is contoured at 1 sigma and represented by density mesh using PYMOL (*217-218*).

6.3.5 Electrophoretic mobility shift assay (EMSA)

*Dr*Dps1t$_{\Delta 1–50}$ (2–25 μM) or *Dr*Dps2t$_{\Delta 1–39}$ (0.5–8 μM) was incubated with 9 nM pUC19 supercoiled plasmid DNA for 15 min at room temperature in 40 mM Bis-Tris (pH 6.5) plus 150 mM NaCl buffer. DNA-binding interaction studies were performed as previously described (*351*).

6.3.6 Detection of *Dr*Dps2 in *D. radiodurans*

D. radiodurans cells were grown in M53 medium (500 mL) at 30 °C, as previously described (*351*). Cells were collected at mid-exponential phase (OD_{600nm} = 0.60) and were then harvested at 11000 *g* and resuspended in 20 mM Tris–HCl (pH 7.5) plus 150 mM NaCl. Cells were disrupted in a French pressure cell at 15000 psi. Membrane and soluble fractions were obtained after ultracentrifugation for 1 h at 186000 *g* and at 4 °C. After protein concentration using 3-kDa protein concentrator (Amicon), the protein was quantified using the modified Biuret method (*369*) for the membrane fraction, and the soluble fraction was quantified by Bradford method (Bio-Rad) (*331*). A total protein of 60 μg was loaded in 12% PAGE, and *Dr*Dps2 was detected by Western blot analysis as previously described (*351*). The data presented are from three independent samples.

6.3.7 Accession numbers

The scattering data collected in BM29 beamline are deposited in the Small Angle Scattering Biological Data Bank (SASBDB) (*370*), with the following accession codes (Table 6.1): SASDBG7 (*Dr*Dps1), SASDBF7 (*Dr*Dps2), and SASDBH7 (*Dr*Dps1t$_{\Delta 1–50}$).

6.4 Results

6.4.1 SAXS data from *Dr*Dps using on-line chromatography

SAXS data were measured at the ESRF (Grenoble, France) BioSAXS beamline, BM29 (*352*), using an online size-exclusion chromatography (SEC) column coupled with the standard experimental setup (*354*). Full-length *Dr*Dps1 and *Dr*Dps2 and their truncated constructs were analysed in order to confirm the data analysis and

interpretations obtained from the full-length proteins. The *Dr*Dps1 truncated form lacks the first 50 amino acid residues (*Dr*Dps1t$_{\Delta 1-50}$), while the *Dr*Dps2 truncated form (*Dr*Dps2t$_{\Delta 1-39}$) lacks the initial 39 amino acid residues (numbering does not take in consideration the 30 residues from the signal peptide; Fig. 6.1).

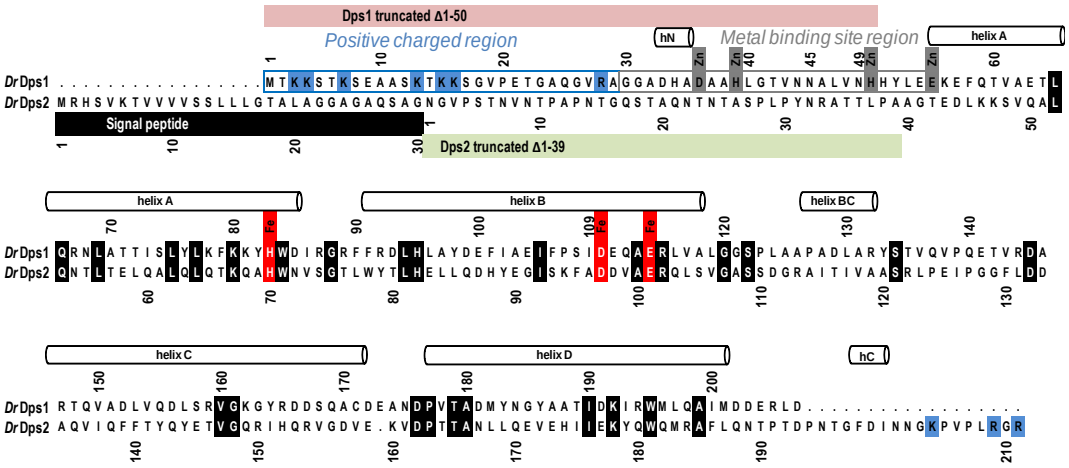

Figure 6.1 - Structural alignment of Dps1 and Dps2 from *D. radiodurans*. *Dr*Dps secondary structure is shown above the alignment, in which the hN represents a helix present in the N-terminal region of *Dr*Dps1, and the hC represents a helix present in the C-terminal region of *Dr*Dps2. The strictly conserved amino acids are represented as black boxes, ferroxidase ligands are represented as red boxes, zinc metal ligands are represented in grey boxes, and positive charged residues present in the N- or C-termini are represented as blue boxes. For *Dr*Dps1, the N-terminal region that was truncated is represented in pink. The two regions from these N-terminal tails, the positively charged region and metal binding site region, are represented in blue and grey, respectively. For *Dr*Dps2, the signal peptide is represented in black, and the truncated region is shown in green.

Analysis of the elution profile obtained from the SEC indicates that *Dr*Dps1 elutes as two oligomeric forms, corresponding to dodecamer and trimer, and *Dr*Dps2 elutes as a stable dodecamer, as previously described (*351*). The truncated form *Dr*Dps1t$_{\Delta 1-50}$ presented a similar elution profile as the full-length protein. *Dr*Dps2t$_{\Delta 1-39}$ showed the presence of several oligomeric states; however, the dodecameric assembly was only present in small quantities, making it impossible to determine a structural model for this oligomeric state. Therefore, the samples carried forward for in-depth analysis were *Dr*Dps1, *Dr*Dps1t$_{\Delta 1-50}$, and *Dr*Dps2, using SAXS data obtained from the dodecamer fraction.

Analysis of the Krakty plot indicates that the three proteins, *Dr*Dps1, *Dr*Dps1t$_{\Delta 1\text{-}50}$ and *Dr*Dps2, were correctly folded (Fig. 6.2).

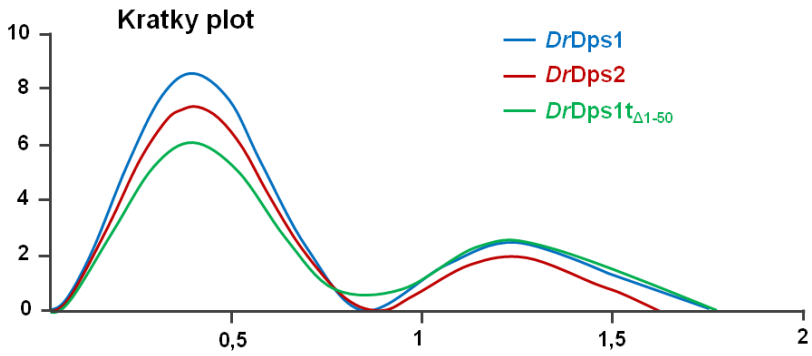

Figure 6.2 - Kratky plot profile of *Dr*Dps1 (blue line), *Dr*Dps1t$_{\Delta 1\text{-}50}$ (green line) and *Dr*Dps2 (red line).

Furthermore the three proteins show similar SAXS scattering profiles with typical features for a spherical particle (Fig. 6.3, A). The Guinier plots of each scattering profile provide a linear fit for a monodisperse solution (Fig. 6.3, B), and the radius of gyration (R_g) was calculated from this approximation. The value of R_g is similar for both *Dr*Dps1 and *Dr*Dps2, 4.15 nm and 4.25 nm, respectively, whilst the value for *Dr*Dps1t$_{\Delta 1\text{–}50}$ is smaller at 3.88 nm (Table 6.1).

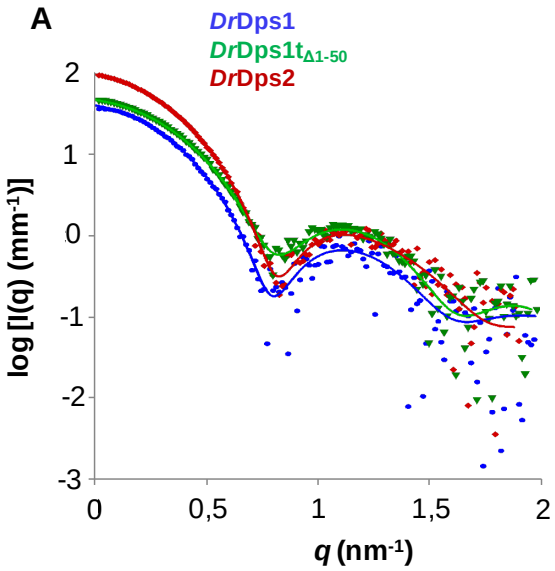

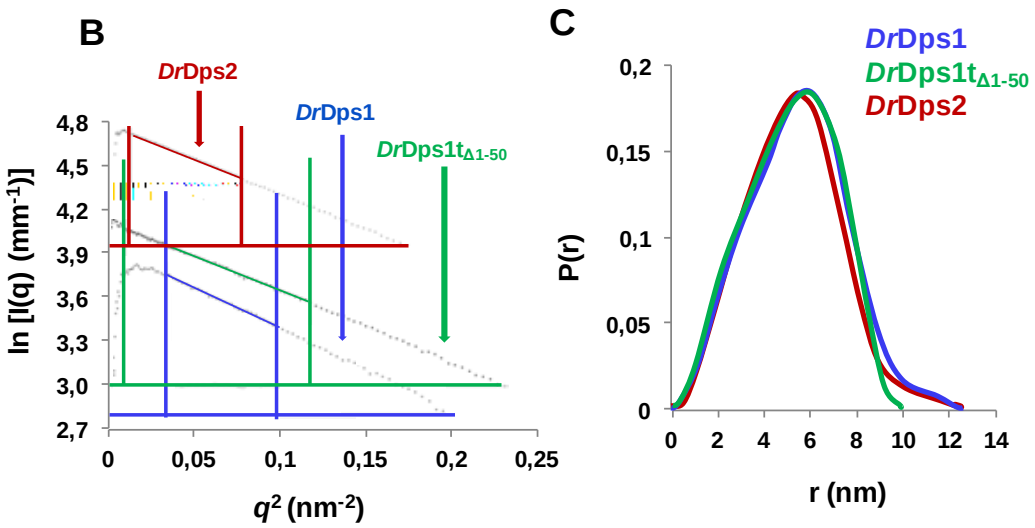

Figure 6.3 - SAXS profile of *Dr*Dps1, *Dr*Dps1t$_{\Delta 1–50}$, and *Dr*Dps2. **(A)** Experimental (dotted line) and calculated (solid line) scattering curves. **(B)** Guinier plot and linear fit (solid line) to the data for the Guinier region, q_{max}*Rg < 1.3. **(C)** *P(r)* profile. In all panels, *Dr*Dps1 is represented in blue, *Dr*Dps1t $_{\Delta 1–50}$ in green, and *Dr*Dps2 in red.

Based on the pair distance distribution function [*P(r)*] determined by the indirect Fourier transform from the scattering profile curves using GNOM (*358*), it was possible to determine the molecular mass for each sample and compare it with the calculated theoretical molecular mass determined from the known sequences (Table 6.1). The *P(r)* was determined using the data of the *q* range < 2 nm^{-1}, since above *q* > 2 nm^{-1}, the data contain significant noise (Fig. 6.3, A). The *P(r)* profile of both *Dr*Dps1 and *Dr*Dps1t$_{\Delta 1–50}$ showed a single maximum at a radius (r) of ~ 5.5 nm with a shoulder at around 2.2 nm, while *Dr*Dps2 showed a single maximum at ~ 5.0 nm with a less pronounced shoulder at ~ 2.0 nm (Fig. 6.3, C). These profiles are characteristic of a spherical shape with a hollow core (*371*). The value of 5.5–5.0 nm corresponds to the external radius of the proteins, while the value of 2.0–2.2 nm corresponds to the internal radius. The values are consistent with the crystal structures, in which the external radius for both proteins is approximately 4.5 nm and the internal radius is around 2.0 nm. Furthermore, the *P(r)* profiles for the two full-length proteins present an extended tail with maximal particle size (D_{max}) of 12.75 nm and 12.74 nm for *Dr*Dps1 and *Dr*Dps2, respectively, probably related to the presence of the long N-

terminal tails in these two proteins (Fig. 6.3, C). This feature is notably absent from the *P(r)* profile for *Dr*Dps1t$_{\Delta 1-50}$, which has a D_{max} of 10.00 nm (Fig. 6.3, C).

The R_g values determined using the *P(r)* are similar to those determined using the Guinier approximation, which demonstrates consistency on the results (Table 6.1). Moreover, the D_{max} obtained for *Dr*Dps1t$_{\Delta 1-50}$ is similar to the diameter obtained in the crystal structure, which is approximately 9 nm (*203*).

Table 6.1 - Data collection and scattering-derived parameters from the *Dr*Dps1, *Dr*Dps1t$_{\Delta 1-50}$, and *Dr*Dps2 using the SEC coupled to the SAXS detector.

	***Dr*Dps1**	***Dr*Dps1t$_{\Delta 1-50}$**	***Dr*Dps2**
Data collection parameters			
Beamline	BM29, ESRF		
Beam geometry	700 x 700 micrometres		
Wavelength (Å)	0.9919		
q range (nm^{-1})	0.08 – 4.5 nm^{-1}		
Exposure time (sec)	1		
Structural parameters			
$I(0)$ (from Guinier)	50.55	52.25	123.88
R_g (nm) (from Guinier)	4.15	3.88	4.25
$I(0)$ (cm^{-1}) (from $P(r)$)	50.75	52.14	121.90
R_g (nm) (from $P(r)$)	4.14	3.83	4.17
D_{max} (nm) (from $P(r)$)	12.75	10.00	12.74
Porod volume estimate (nm^3) (+/- 10%) (from $P(r)$)	447.74	290.96	497.67
R_g (nm) (from EOM)	4.14	3.70	4.88
D_{max} (nm) (EOM)	14.16	10.50	18.84
Porod volume estimate (nm^3) (EOM)	436.85	339.46	445.08
Molecular-mass estimation			
Molecular mass M_r (from Porod volume) (+/- 10%) (kDa)	263.4+/-16	171.1+/-21	292.7+/-23
Molecular mass M_r (from EOM) (kDa)	257.0	200.7	261.7
Calculated dodecamer M_r from sequence (kDa)	276.2	216.4	279.9
CRYSOL (χ^2)			
Experimental scattering data	12.82	10.24	21.44
EOM scattering data (EOM)	0.64	--	0.32
Model (χ^2)			
GASBOR	11.0	14.6	3.03
EOM	11.90	--	12.39
Software			
Primary data reduction (circular averaging)	PRIMUS		
Data processing	PRIMUS		
Ab initio analysis	GASBOR, DAMMIN and EOM		
Computation of pdb model intensities	CRYSOL		
Three-dimensional graphics representation	PyMOL		
Accession Codes (SASBDB)	SASDBG7	SASDBH7	SASDBF7

6.4.2 *Dr*Dps SAXS *ab initio* derived molecular envelopes

Molecular envelopes for each protein were obtained by *ab initio* modelling using the programs DAMMIN and GASBOR (dummy atoms: 5858 ± 51 for *Dr*Dps1, 5895 ± 32 for *Dr*Dps1t$_{\Delta 1-50}$, 5858 ± 14 for *Dr*Dps2) using default parameters and imposing P23 symmetry, consistent with the symmetry observed for the oligomer in solution, that is, the dodecameric hollow sphere with 23 symmetry. The knowledge of the oligomer symmetry is critical, as trials using P1 symmetry did not sufficiently restrain the modelling and did not yield an interpretable model. The q range used to generate the models was $q < 2$ nm^{-1}. The results using both programs were identical, and only the models obtained with GASBOR are presented. A total of 10 *ab initio* reconstructed models were averaged and filtered to obtain the final model for each sample. The normalised spatial discrepancy value of a set of GASBOR models for *Dr*Dps1, *Dr*Dps1t$_{\Delta 1-50}$, and *Dr*Dps2 were 0.77 ± 0.043, 0.90 ± 0.10, and 0.87 ± 0.08, respectively (Fig. 6.4, A1, B1, and C), with final χ^2 values against corrected data of 11.0, 10.6, and 3.0 for *Dr*Dps1, *Dr*Dps1t$_{\Delta 1-50}$, and *Dr*Dps2, respectively (Table 6.1).

The crystal structure of *Dr*Dps docks well into the SAXS molecular envelope generated from the corresponding experimental scattering data. However, the SAXS envelopes determined for *Dr*Dps1 and *Dr*Dps2 present extra areas protruding from the sphere (Fig. 6.4, A1 and B1), which are attributed to the N-terminal regions and were not observed in the crystal structure. Importantly, these protrusions are not observed in the SAXS envelope corresponding to *Dr*Dps1t$_{\Delta 1-50}$, consistent with the absence of the first 50 amino acid residues in this protein construct. The crystal structure of *Dr*Dps1 docks into the spherical envelope of *Dr*Dps1t$_{\Delta 1-50}$ (Fig. 6.4, C). The models obtained for *Dr*Dps1, *Dr*Dps2, and *Dr*Dps1t$_{\Delta 1-50}$ are superimposed in the central region of the dodecamer, but the extra areas protruding the sphere are only observed in the full-length proteins, *Dr*Dps1 and *Dr*Dps2.

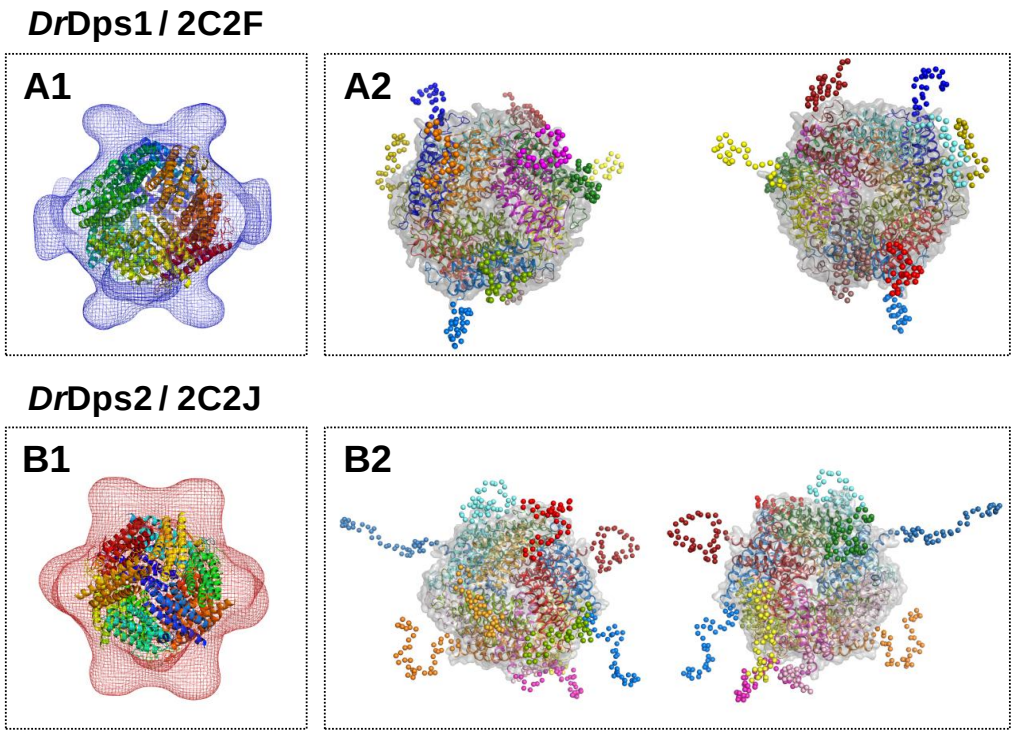

Figure 6.4 - *Dr*Dps *ab initio* models superimposed with the corresponding crystal structures. **(A1** and **B1)** *Ab initio* shape generated by DAMAVER from GASBOR models for **(A1)** *Dr*Dps1 and **(B1)** *Dr*Dps2, represented as blue mesh and red mesh, respectively. **(A2** and **B2)** Molecular envelope obtained by using EOM for **(A2)** *Dr*Dps1 and for **(B2)** *Dr*Dps2, represented through the 3-fold N-terminus (left) and 3-fold C-terminus (right). **(C)** *Ab initio* shape generated by DAMAVER from GASBOR models for *Dr*Dps1t$_{\Delta 1-50}$ represented as green mesh. *Dr*Dps crystal structures are represented in cartoon with each monomer in a different colour.

The N-terminal regions from Dps are known to be flexible regions but in the sense that they change conformation upon different conditions; for this reason, it has not been possible to structurally characterise these regions by X-ray crystallography where they were disordered, perhaps due to crystal packing. The low-resolution models obtained show in solution that these regions protrude from the dodecamer sphere as observed in both models obtained from GASBOR/DAMMIN for *Dr*Dps1 and *Dr*Dps2. These models correspond to the average shape attributed to the N-terminal regions that could not be observed in the crystal structure.

It is important to mention that using GNOM program followed by GASBOR/DAMMIN to obtain the final *ab initio* models from scattering curves of a flexible sample may lead to some possible errors. This is due to the over-background adjustment of the scattering curve, since GNOM tries to force intensity decay to q^{-4} (globular shape) using a constant (*358*). Thus, analysis using only GNOM should be taken with caution. In order to complement our studies, molecular envelopes for each protein were obtained using ensemble optimisation method (EOM), an approach that was developed to characterise protein mobility (*361*) (described below).

6.4.3 EOM to flexible systems

The results showed that by using EOM, it generates specific structural assemblies of the N-terminal tails demonstrating that these regions have a high degree of mobility, in which the 12 individual regions protruding from the dodecamer hollow sphere have different conformations (Fig. 6.4, A2 and B2).

The different parameters were also obtained using EOM, namely R_g, D_{max}, and molecular mass estimation (Table 6.1). The R_g determined for *Dr*Dps1, *Dr*Dps1t$_{\Delta 1-50}$, and *Dr*Dps2 are similar to those obtained from Guinier plots and *P(r)*. However, the D_{max} obtained using EOM for both *Dr*Dps1 and *Dr*Dps2 is higher than those determined by *P(r)*, 14.16 and 18.84, respectively, in contrast to those for *Dr*Dps1t$_{\Delta 1-50}$ (D_{max} = 10.50; Table 6.1). The D_{max} difference corresponds to the different conformations of the N-terminal tail observed in the models generated by EOM, showing 12 individual regions protruding from the dodecamer hollow sphere (Fig. 6.4, A2 and B2). The estimation of the molecular mass for each protein is similar to the theoretical molecular mass (Table 6.1).

6.4.4 Comparison of SAXS scattering curves and crystal structure models

The comparison of scattering experimental data for the full-length *Dr*Dps proteins with the corresponding crystal structure curves using CRYSOL gives a fit (χ^2 value) of 12.8 and 21.4 for *Dr*Dps1 and *Dr*Dps2, respectively (Table 6.1). Similar χ^2 values were obtained using the program FoXS (*372*). These high χ^2 values are associated

with structural differences between the crystal structure and the proteins in solution, which could be related to the presence of the N-terminal regions. The χ^2 value for *Dr*Dps1t$_{\Delta 1-50}$ at 10.2 is lower when compared with the *Dr*Dps1 crystal structure (modelled without the 29 residues).

Further comparison with a truncated model of *Dr*Dps1, the deletion of the total region of the N-terminus (residues 30–50) in the crystal structure, yields an even lower χ^2 of 9.7. The decrease from 10.2 to 9.7 is due to the fact that the crystal structure lacks the first 29 residues, while the truncated model used to obtain the SAXS envelope lacks 50 residues. Moreover, the scattering curves obtained from the crystal structures were compared using CRYSOL with the scattering curves of each *Dr*Dps generated by EOM (fit for the best ensemble). In this case, the χ^2 values obtained are lower than those presented above, 0.64 and 0.32 for *Dr*Dps1 and *Dr*Dps2, respectively (Fig. 6.5).

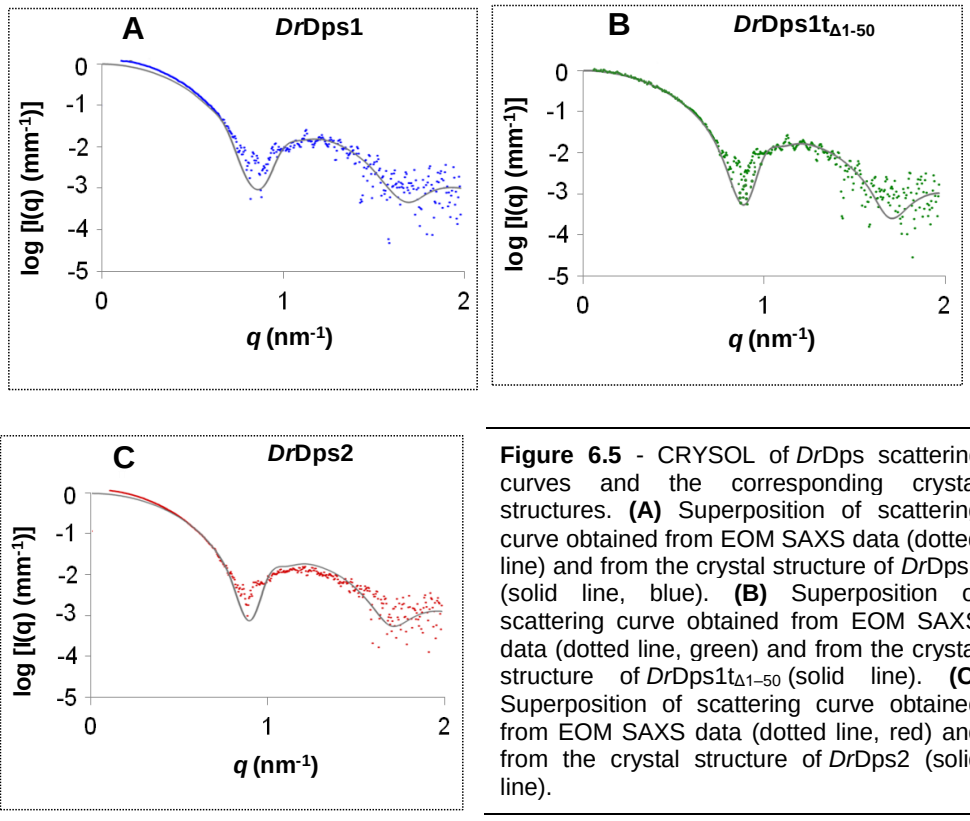

Figure 6.5 - CRYSOL of *Dr*Dps scattering curves and the corresponding crystal structures. **(A)** Superposition of scattering curve obtained from EOM SAXS data (dotted line) and from the crystal structure of *Dr*Dps1 (solid line, blue). **(B)** Superposition of scattering curve obtained from EOM SAXS data (dotted line, green) and from the crystal structure of *Dr*Dps1t$_{\Delta 1-50}$ (solid line). **(C)** Superposition of scattering curve obtained from EOM SAXS data (dotted line, red) and from the crystal structure of *Dr*Dps2 (solid line).

6.4.5 The function of the N-termini

In order to address the role of the *Dr*Dps N-terminal regions with respect to DNA, the truncated forms of *Dr*Dps, *Dr*Dps1t$_{\Delta 1–50}$, and *Dr*Dps2t$_{\Delta 1–39}$ were incubated with DNA in the same conditions as described previously for the full-length proteins (*351*). The result shows that there was no observable DNA gel migration shift in the presence of *Dr*Dps1t$_{\Delta 1–50}$ up to a concentration of 25 µM (Fig. 6.6, A), compared to only 4 µM of full-length protein that has been previously shown to induce a shift (*351*). This indicates that the absence of the N-terminal protrusions compromises the interaction with the DNA, which is in accordance with previous results (*270*).

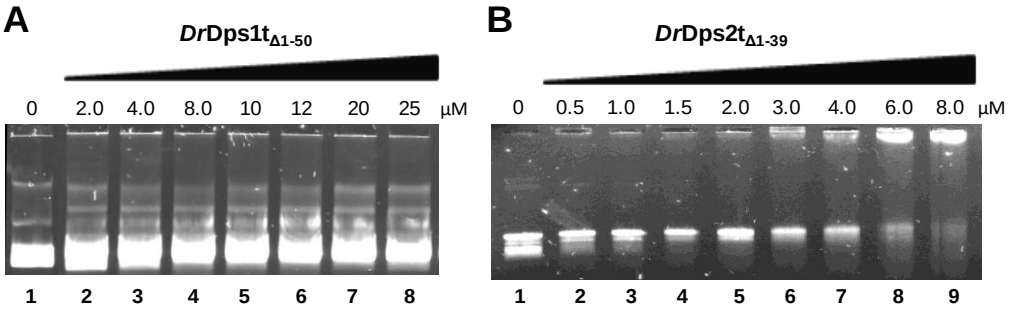

Figure 6.6 - Plasmid DNA binding **(A)** *Dr*Dps1t$_{\Delta 1–50}$ protein or **(B)** *Dr*Dps2t$_{\Delta 1–39}$ at pH 6.5 using agarose gel electrophoresis. Plasmid DNA alone (lane1) or increasing the concentration of *Dr*Dps1t$_{\Delta 1–50}$ (2–25 µM) or *Dr*Dps2t$_{\Delta 1–39}$ (0.5–8 µM) incubated with plasmid DNA (lanes 2–9).

In contrast, in the case of *Dr*Dps2t$_{\Delta 1–39}$, the addition of 8 µM of protein induced a DNA gel migration shift. *Dr*Dps2 and DNA have been previously shown to interact and form *Dr*Dps–DNA complexes only with the supercoiled form of the plasmid DNA (*351*). Here, we show that *Dr*Dps2t$_{\Delta 1–39}$ is able to shift all the forms of plasmid DNA, being no longer selective for the type of DNA and suggesting that the N-terminal region plays a key role in this selection event (Fig. 6.6, B).

The genomic sequence encoding for *Dr*Dps2 contains a signal peptide (*204, 206*), which suggests that this protein could interact with the membrane. Therefore, the N-terminal function in association with the cell membrane was investigated. *D. radiodurans* bacteria were grown in M53 medium, and *Dr*Dps2 was detected by Western blotting, as previously described (*351*). The protein was detected in both membrane and soluble fractions but with different molecular masses (Fig. 6.7),

suggesting that the form present in the membrane corresponds to the full-length *Dr*Dps2 (without the signal peptide) while the one in the soluble fraction contains the N-terminus cleaved. These data suggest that the N-terminal tail, with most of the residues containing polar but uncharged side chains, would have a further role in an interaction with the membrane.

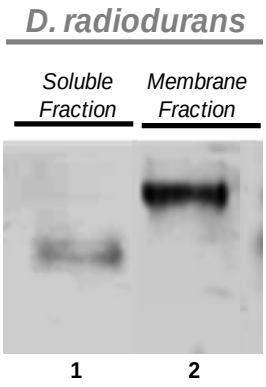

Figure 6.7 - Western blotting detection of *Dr*Dps2 in soluble and membrane fractions from *D. radiodurans* cells. Lane 1 - soluble fraction; lane 2 - membrane fraction.

6.5 Discussion

6.5.1 *Dr*Dps SAXS data

Dps from *D. radiodurans* have long N-terminal tails before the first helix from the four-helix bundle, which were not modelled in the crystal structures determined to date (Fig. 6.1). These regions are predicted to have a coiled structure, being very flexible, appear disordered in the crystal, and therefore not modeled (*203-204, 246*). The structure of these regions was therefore addressed using *Dr*Dps in solution in order to understand if they are fully disordered or form some level of stable organisation that could be visualised. In the present work, the low-resolution molecular envelopes of the N-terminal tails of *Dr*Dps and their relative position with respect to the protein shell were elucidated by SAXS.

The *ab initio Dr*Dps SAXS envelopes generated by the program GASBOR/EOM match the dimensions of the protein dodecameric spheres previously determined by protein crystallography. Besides the central dense core, the reported model envelopes harbour extra electron density areas (related by enforced P23 symmetry) distributed

around the sphere surface. In order to confirm this interpretation, the SAXS envelope model of a *Dr*Dps truncated construct lacking 50 N-terminal residues (*Dr*Dps1t$_{\Delta 1-50}$) was analysed and only showed a spherical particle without any protruding regions (Fig. 6.4, C). Furthermore, the scattering parameters determined from this shorter protein, R_g and D_{max}, are in agreement with those obtained from the crystal structures.

Two types of models were generated for both *Dr*Dps, a static molecular envelope produced from GASBOR/DAMMIN representing the average scattering, and a flexible model obtained from EOM (Fig. 6.4). The different models are consistent on the central core, which show a hollow dodecameric sphere. The major difference is observed on the N-terminal tails arrangement; in the static model, 12 symmetric regions protruded from the dodecamer sphere, whereas in the flexible model, the N-terminal regions that protruded from the central sphere correspond to individual asymmetric tails with different conformations. Although the low-resolution static model contains important structural information, an ensemble method such as EOM represents a good approach to determine the different conformations that exist in solution.

6.5.2 *Dr*Dps and its N-terminal tail

Both the N- and C-terminal tails have been reported to be involved in the interactions between Dps and DNA. This interaction has been proposed to occur through a flexible tail rich in positively charged residues such as described in the cases of *Ec*Dps and *Ms*Dps1 (*247, 265*). Flexibility of the N-terminal regions has been one of the factors that contribute to the interaction with DNA; however, in solution and without the presence of DNA, these regions are not disordered but instead present an organised structure as observed by the average scattering shapes obtained from the GASBOR molecular envelopes. To complement our studies, we applied EOM. Different conformations were obtained for the different N-terminal tails, indicating that these regions may adopt different conformations, which could be important for promoting DNA binding.

The first 30 amino acid residues of *Dr*Dps1 contain a total of seven positively charged residues: six lysines (Lys_3, Lys_4, Lys_7, Lys_{13}, Lys_{15}, and Lys_{16}) and one arginine (Arg_{28}; Fig. 6.1). DNA interaction studies of a *Dr*Dps1 truncated form without

the first 55 amino acid residues (*270*) and our comparative data with *Dr*Dps1 show that this region is involved in DNA binding, since the truncated forms have less affinity for DNA (Fig. 6.6, A) compared to the full-length protein (*205, 351*). This truncated form, which retains the dodecamer form, could still interact with the DNA by the positively charged residue Arg_{132} located at the surface of the protein as previously proposed (*269*). Nevertheless, the affinity for the DNA in this case is much lower than for the full-length protein, as observed in Fig. 6.6, A.

The N-terminal tail of *Dr*Dps2 comprises 41 amino acid residues before the first helix from the four-helix bundle (*204*). The SAXS model envelopes indicate that in solution, the N-terminal tails can form 12 individual extra protrusions outside of the hollow sphere (Fig. 6.4, B). The secondary structure prediction using the PSIPRED (*373*) server based on the amino acid sequence for this region gives almost wholly coil, suggesting conformational flexibility. Since each region contains six proline residues, the structural flexibility of polypeptide regions would be reduced, which may be important to accommodate the N-terminus into the structures observed in the SAXS envelope, forming the structural arrangements observed in the GASBOR molecular envelope corresponding to the average scattering shapes of these regions obtained in solution. DNA interaction studies using the *Dr*Dps2t$_{\Delta 1-39}$ indicate that this truncated form binds to all the plasmid DNA forms (Fig. 6.6, B). This result differs from the full-length *Dr*Dps2, which only binds to the supercoiled form from the plasmid DNA (*351*). The first 41 N-terminal amino acids only contain one positively charged residue (Arg_{33}), most of which (49% out of 41 residues) are polar with uncharged side chains (3 × Ser, 8 × Thr, 2 × Gln, and 7 × Asn), and finally, 46% are non-polar with aliphatic side chains (6 × Pro, 6 × Ala, 3 × Gly, 2 × Val, and 2 × Leu). Based on this, it can be suggested that although this N-terminal region is not directly involved in DNA interactions, it could presumably guide the DNA to bind either to the positively charged residues located at the protein surface (Lys_{46}, Lys_{47}, Arg_{122}, and Arg_{149}) or to the positively charged residues (Lys_{204}, Arg_{209}, and Arg_{211}) located at the C-terminal region (Fig. 6.1). The absence of the N-terminal tail would expose these positively charged regions located at the protein surface, thereby favouring *Dr*Dps2 propensity to interact with DNA (Fig. 6.6).

Analysis of the cell extracts of *D. radiodurans* shows that *Dr*Dps2 is present in membrane and soluble fractions (Fig. 6.7), although under the tested conditions, most of the protein is present in the membrane fraction. This is in agreement with previous

results, which showed the localisation of this protein as being close to the membrane region (*206*). When comparing the two forms present in the soluble and membrane fractions, we suggest that the form present in the soluble fraction would correspond to the N-terminal tail-free protein (form observed in the crystal structure), while the form observed in the membrane fraction would be the full-length. Therefore, the N-terminus would allow an interaction with the membrane, indicating that the two forms of *Dr*Dps2 (full-length and truncated forms) are present in *D. radiodurans* but with distinct physiological roles.

6.6 Conclusion

We present results from the SAXS experiments performed on both *Dr*Dps that show for the first time that both proteins exist in solution with a definable particle size corresponding to dodecameric spheres with protruding N-terminal regions. The SAXS envelope determined for *Dr*Dps1 shows 12 N-terminal protrusions pointing outside of the sphere, and the model generated for the *Dr*Dps1 truncated form (*Dr*Dps1t$_{\Delta 1-50}$) shows that the protein maintains its spherical dodecameric shape but without the protruding tails, demonstrating that these protrusions observed for the full-length protein are from the N-terminal regions. The truncation of the first 50 amino acid residues of the N-terminal region of *Dr*Dps1 almost abolishes the interaction with DNA, indicating that these tails protruding from the dodecameric sphere are essential for stabilising the protein–DNA complex.

*Dr*Dps2 SAXS data show that the N-terminal tails are organised as 12 individual tails and these tails are crucial for maintaining the dodecamer protein structure. The N-terminal protrusions in *Dr*Dps2 are probably involved in the interaction with DNA by hooking DNA close to the positively charged residues located at the surface or the C-terminal part of the protein. However, these protrusions can also be important for interacting with the membrane: the presence of a signal peptide directs *Dr*Dps2 to the membrane region, and then, the interaction with the membrane would be maintained through the N-terminal tails. Nevertheless, the interaction between *Dr*Dps2 and the membrane needs to be further investigated.

This study takes advantage of the complementarity of both crystal X-ray diffraction and protein structure analysis in solution by SAXS to provide a complete characterisation of *Dr*Dps biomolecular structures under native conditions.

6.7 Acknowledgements

This work was supported by the European Synchrotron Radiation Facility (ESRF, Grenoble, France) from data collection material and equipment, and by the Fundação para a Ciência e Tecnologia grants PTDC/BIA-PRO/100365/2008 and PTDC/QUI-BIQ/100007/2008. This work was further supported by MOSTMICRO (LISBOA-01-0145-FEDER-007660) Research Unit co-funded by FCT, through national funds, and by FEDER under the PT2020 Partnership Agreement. S.P.S. and C.V.R. acknowledge the FCT grants SFRH/BD/78870/2011 and SFRH/BPD/94050/2013, respectively.

CHAPTER VII

How does *Deinococcus radiodurans* cope with stress? *Dr*Dps as a missing link between manganese and protection

This chapter is in preparation to be published:

Santos S.P., Yang Y., Rosa M., Rodrigues M., . De La Tour C. B., Sommer S., Teixeira M., Carrondo Maria A., Cloetens P., Abreu I. A., and V. Romão C.V. Cross-talk between Dps in *Deinococcus radiodurans* triggers Mn distribution, in preparation.

Santos S. P. was responsible for most of the experimental work with exception of X-ray fluorescence imaging data collection and processing, construction of the *D. radiodurans dps* delected mutants, and the *D. radiodurans* GFP-*dps* constructs. X-ray fluorescence imaging data collection and processing were done by Santos S.P., Abreu I. A., Yang Y., Cloetens P., and Bohic S. and Romão C.V. in ID16A – Nano-imaging beamline at ESRF. The *D. radiodurans dps* delected mutants and the GFP-*dps* constructs were performed by De La Tour C. B., and Sommer S.. RT-PCR assays were executed Santos S. P. in collaboration with Rosa M.G., Rodrigues M.A.A., and Abreu I. A.

Nano-imaging at ID16 accepts first users

X-ray fluorescence imaging - 3D

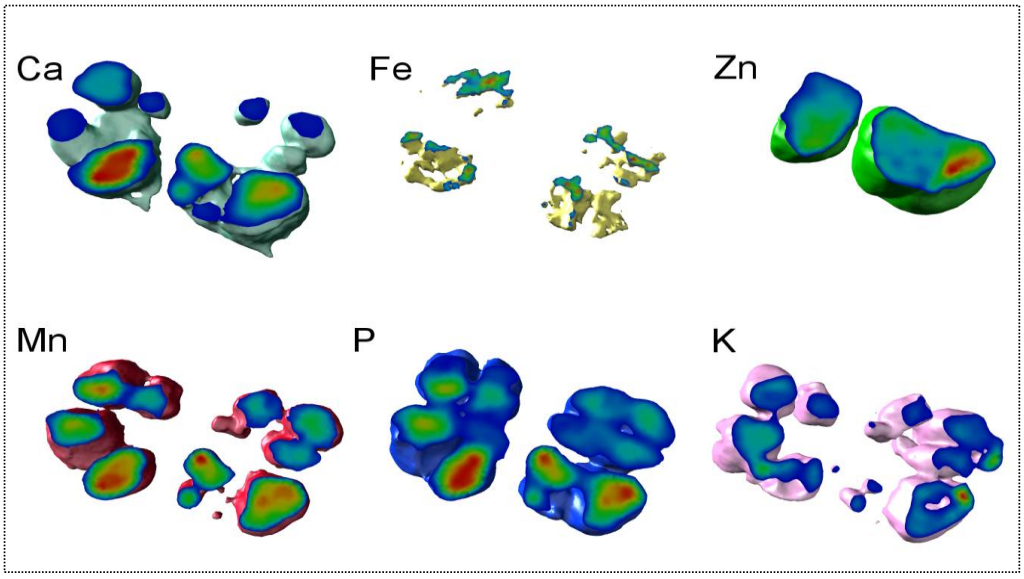

7.1 Abstract

Deinococcus radiodurans is the most highly resistant organism to radiation known to date. It has been proposed that manganese plays a crucial role as a protection mechanism, forming complexes with small molecules, such as phosphate (Mn^{2+}-Pi). Nevertheless, several questions remain to be answered related with the molecular mechanisms of these small complexes Mn^{2+}-Pi, namely if *Dr*Dps proteins are involved on manganese homeostasis.

These questions were addressed by studying *D. radiodurans* wild-type strain and *dps* knockout mutants. Metal distribution was determined at nano-resolution by X-ray fluorescence imaging. In control condition was observed that manganese, phosphate and calcium are concentrated in phosphate granules sub-structures, which upon stress conditions, are re-distributed inside the cell. Furthermore, manganese and phosphate are co-localized, probably in the form of Mn^{2+}-Pi complexes, being available for protection under oxidative stress conditions. It is interesting that these elements are not concentrated in the granules in *dps1* knockout mutant, but rather homogenously distributed in the cell, which may explain the high resistance of this strain to the exposure to oxidative stress. This suggests that *Dr*Dps1 is involved in the incorporation of these elements to the granules. Moreover, cell division is highly affected in the *dps2* knockout mutant, mainly in stress conditions, but also manganese-phosphate content in the granules is decreased. These dual functions of *Dr*Dps2 are regulated by the different oligomeric states of *Dr*Dps1.

Our results demonstrate distinct roles of *Dr*Dps, namely in phosphate granules build up, manganese trafficking and cell division, being both of them essential for the survival of this bacterium under stress conditions.

Keywords: phosphate granules, oxidative stress, metal, X-ray fluorescence

7.2 Introduction

Deinococcus radiodurans is an aerobic, red-pigmented, mesophilic and gram positive coccus (*100*). As a gram positive it has a peptidoglycan layer, but by electron microscopy it was observed that this organism contains an unusual cell wall with multilayers, including outer membranes, that are characteristic of gram negative bacteria (*153-154*). In this organism were detected circular or oval electron-dense phosphate granules with a darker margin, observed in the centre of each cell (*165*). These sub-structures were visualized mostly in the exponential phase, while in the stationary phase it was observed similar structures but were empty suggesting that granules are present but without phosphate molecules (*167*).

D. radiodurans as a radioresistant bacterium has been the focus of several studies in order to understand the mechanisms underlying its resistance. Over the years, several proposals have been arisen to explain the protection mechanisms, like: high levels of carotenoids in the membrane region, efficiency of DNA repair systems, effective enzymatic ROS scavenging systems, such as superoxide dismutase and catalase enzymes and non-enzymatic ROS scavenging systems (*100*). The non-enzymatic ROS scavenging system relies on the high intracellular manganese concentration and is currently the most accepted proposal, in which this metal plays a crucial role protecting proteins against oxidation (*69, 79*).

In this organism has been demonstrated that the ratio between manganese and iron concentration is higher (ratio Mn/Fe of 0.24) than those of sensitive radiation organisms. However these studies were limited to two sensitive radiation bacteria: *E. coli* (ratio Mn/Fe of 0.0072) and *Shewanella oneidensis* (ratio Mn/Fe of 0.0005) (*81*). During cell growth, it was proposed that the level of manganese does not change. In the exponential phase manganese was suggested to be mostly associated with small molecules such as fructose-1,6-biphosphate, nucleic acids and phosphate molecules, including orthophosphate, pyrophosphate and polyphosphate. Therefore, when manganese can forms complexes with these small molecules have the ability to detoxify ROS (*71, 75, 78*). In the stationary phase, most of the manganese present in the cell is proposed to be associated with proteins, such as MnSOD (*374-375*), suggesting that proteins could also play an important role in the intracellular protection of *D. radiodurans.*

Previous studies using X-ray fluorescence imaging showed that manganese is distributed inside the cell, but with a higher regional intracellular concentration associated with the electron-dense phosphate granules, while iron was found mostly in the septum region (*69*). However, the resolution of these data was at the µm scale and the cells analysed were only in control conditions and at the early exponential phase (*69*). Therefore further studies using X-ray fluorescence imaging at nano-resolution scale, under control and stress conditions, were essential to acquire knowledge on the metal homeostasis in *D. radiodurans* and correlate to its resistance mechanisms, which were performed under this work.

D. radiodurans has two Dps proteins (*Dr*Dps1-*dr2263* and *Dr*Dps2-*drb0092*) and both have been associated with the manganese homeostasis, since in *in vitro* conditions both proteins showed the ability to store and release manganese. In order to correlate the protection mechanisms of *D. radiodurans* with manganese and *Dr*Dps, we have conduct X-ray fluorescence imaging studies that allowed to localize metals inside the cell. Furthermore, these studies were complemented, with cellular location of *Dr*Dps determined by fluorescence microscopy. All these results show that both *Dr*Dps have dual functions, which are associated with cell protection and metals homeostasis.

7.3 Experimental procedures

7.3.1 GFP-*dps1* and GFP-*dps2* bacterial strains and transformation

D. radiodurans strains expressing *Dr*Dps proteins fused to GFP-tag were constructed by the tripartite ligation method (*376*). Plasmid pFAP246 was the source for the cassette containing the GFP-tag and the resistance gene to chloramphenicol (*377*). The genetic structure and the purity of the resulted tagged genes were verified by PCR and sequence analysis. Strains expressing tagged proteins were grown with aeration in TGY2x at 30°C. Media were supplemented with chloramphenicol (3.5 µg/ml final concentration).

D. radiodurans Δ*dps1*, Δ*dps2* and Δ*dps1*Δ*dps2* strains were described previously (*333*).

7.3.2 *Deinococcus radiodurans* growths

D. radiodurans cells wild-type, Δ*dps1*, Δ*dps2*, Δ*dps1*Δ*dps2,* GFP-*dps1 and* GFP-*dps2* strains were grown in M53 medium at 30 ºC. Four independent growths were performed and cells were collected at different time points. The effect of different compounds were tested, namely: 0.5 mM manganese (II) chloride, 0.5 mM ammonium iron (II) sulfate, 50 mM hydrogen peroxide, 1 mM methyl viologen and 0.5 mM manganese (II) chloride followed by the addition of 1 mM methyl viologen, 2 hours after. These compounds were added to the media at an optical density (OD_{600nm}) of 0.3. A control (water addition) growth was performed and followed simultaneously.

Cells were collected at different time points: 0 (before adding any compound – OD=0.3), 15 min (early exponential phase), 2 hours (mid exponential phase), and 20 hours (stationary phase) after adding the different compounds.

The viability of the cells during the growth was assessed using 10 µg/ml propidium-iodide dye. The cells were visualized on a Leica DM RA2 microscope.

7.3.3 RNA isolation and RT-PCR

For total RNA extraction, 4 ml of *D. radiodurans* cells were collected from point 0, 15 min and 2 h for the following strains: wild type, Δ*dps1*, Δ*dps2* and Δ*dps1*Δ*dps2,* by 5 min centrifugation at 11000 *g*, and 4 ºC. The pellets were resuspended in 100µl of water containing 45 mg/ml lysozyme and 4 mg/ml of proteinase K, and incubated at 37°C for 45 min. After incubation, 350 µl of the lysis solution (Rnaspin Mini RNA Isolation kit - GE-Healthcare) and 1 % (w/v) of β-mercaptoethanol were added and mixed by vortexing. Total RNA was extracted using Rnaspin Mini RNA Isolation kit followed by spectrophotometric and gel quantification using ImageJ software.

cDNA was synthesized from DNase-treated RNA (2 µg) with Transcriptor High Fidelity cDNA Synthesis Kit (Roche) following the manufacturer's protocol.

Random hexamer primers were used for synthesis (Table 7.1). cDNA products were standardized for semiquantitative RT-PCR using AAAA primers as reference. Cycle numbers were optimized for each template using cDNA from controls to assure that the amplification reaction was tested in the exponential phase. Transcripts normalization was performed using cDNA concentrations.

NCBI Primer BLAST available online was used for the primer design (https://www.ncbi.nlm.nih.gov/tools/primer-blast/). Primers for four target genes of *D. radiodurans* used in RT-PCR are shown in Table 7.1.

pfkA (ATP-dependent 6-phosphofructokinase) gene was used as a marker of oxidative stress.

The data presented is from two biological and three experimental replicate experiments.

Table 7.1 - Sequences of the primers used in the RT-PCR.

Name	Gene ID	Primers (Forward **- F** / Reserse **- R**)	Product size (bp)
dps1	*dr2263*	**(F)** TCGTCAACCACCACTACCTG **(R)** GGAGCATCCAGCGAATCTTG	453
dps2	*drb0092*	**(F)** CACTACGAGGGCATCAGCAA **(R)** TTGATGTCGAAGCCGGTGTT	341
mnsod	*dr1279*	**(F)** CACACCAAGCATCACCAGAC **(R)** GCGTCTTCGFCTTCTGCTT	293
pfkA	*dr0635*	**(F)** GTACCCGATGGTGTGGTCAG **(R)** CAACCTGACATGGCCTACCC	453

7.3.4 Sample preparation for Western blotting assay, catalase and superoxide dismutase activity

Cells of *D. radiodurans* wild-type, Δ*dps1*, Δ*dps2* and Δ*dps1*Δ*dps2* strains were harvested at 11000 *g* and resuspended in 20 mM Tris–HCl pH 7.5, 150 mM NaCl and disrupted in a French pressure cell at 15000 psi (for each time point). The cellular extracts were centrifuged for 1 h at 18000 *g* and 4 ºC. Each cellular extract was concentrated and protein concentration determined by the Bradford method (Bio-Rad) (*331*).

7.3.4.1 Western blotting assay

A total protein of 60 µg was loaded in 12 % PAGE, after the gel was blotted into polyvinylidene fluoride membrane (Bio-Rad) and *Dr*Dps were detected using specific

polyclonal antibodies against *Dr*Dps1 (AbDps1) or *Dr*Dps2 (AbDps2). Protein bands were revealed using a colorimetric detection as previously described in chapter V. *Dr*Dps bands from the Western-blotting were quantified using ImageJ software. The data presented is from four independent samples.

7.3.4.2 Mobility shift detection of phosphorylated proteins - Mn^{2+}-Phos-tag Western blotting

The samples analysed correspond to wild-type strain in manganese and control conditions from time point at 2 hours. Cellular extract containing 60 µg of total protein was centrifuged at 18000 *g*, and the supernatant was injected into 12 % PAGE. Two gels were simultaneously performed, without (control) and containing a 10 mM $MnCl_2$ and 5 mM Phos-tag AAL-107 solution (Wako Chemicals USA, Inc.) in the revolving gel. These two solutions lead to the formation of a di-nuclear metal complex (1,3-bis[bis(pyridin-2-ylmethyl)amino]propan-2-olato di-manganese (II) complex - Mn^{2+}-Phos-tag) acting as a selective phosphate-binding tag molecule (*378*). After, the *Dr*Dps1 protein bands were detected by Western-Blot, as previously described in chapter V.

7.3.4.3 *Dr*Dps2 detection from soluble and membrane fractions

Cellular extracts from *D. radiodurans* wild-type and Δ*dps1* strains in control conditions and after manganese addition at time point of 2 h were ultracentrifuged at 180000 *g*, 4ºC.

Recombinant *Dr*Dps1 trimeric form was added to cellular extract of point 2 h in control and in manganese conditions for *D. radiodurans* Δ*dps1* strain and incubated 1 h, followed also by ultracentrifuged at 180000 *g*, 4ºC.

Soluble and membrane fractions were quantified using Bradford (Bio-Rad) (*331*) and modified Biuret method (*369*), respectively. A total of 30 µg of protein of each condition was loaded on a 10 % PAGE, and the *Dr*Dps2 protein bands were detected by Western-Blotting, as previously described in chapter V. Data presented are from three independent samples.

7.3.4.4 Interaction between *Dr*Dps1 and *Dr*Dps2

Both *Dr*Dps (30 µg of recombinant *Dr*Dps1 trimeric form and 30 µg of recombinant *Dr*Dps2) were incubated during 1 hour, in 20 mM Tris-HCl pH 7.5, plus 150 mM NaCl at room temperature. Recombinant pure proteins were used as a control (30 µg of *Dr*Dps1 trimeric form and *Dr*Dps2). The different samples were loaded on a 12 % PAGE.

7.3.4.5 Superoxide dismutase activity assay

Superoxide dismutase activity was determined using the activity gel assay based on the inhibition of Nitro Blue Tetrazolium (NBT) reduction by $O^{\bullet -}_2$ under light (*379-380*).

Cellular extracts, containing 9 µg of total protein were separated electrophoretically in PAGE (12 %), immediately after the gel was incubated during 20 min in a 2 % (w/v) NBT solution, and washed in water to remove the excess of NBT. The gel was then incubated during 15 min in a solution 100 x diluted of TEMED-riboflavin-potassium phosphate solution (28 mM TEMED, 2.8 mM riboflavin, 36 mM potassium phosphate pH 7.8). Afterwards the gel was exposed to light until the appearance of white bands, indicating the presence of superoxide dismutase activity.

MnSOD activity inhibition was performed by the addition of 2 or 4 % SDS to the sample and incubation at 37 ºC during 30 min to 2 hours (*381*).

CuZnSOD activity inhibition was performed by the addition of 10 mM KCN to NBT solution (*380, 382*).

MnSOD from *Arabidopsis thaliana* and CuZnSOD from bovine erythrocytes were used as control.

7.3.4.6 Catalase activity assay

Catalase activity was determined using gel polyacrylamide assay (*383*). The method is based on the ferricyanide-negative stain which consists on the removal of peroxide by the protein not allowing the reduction of potassium ferricyanide to potassium ferrocyanide, that reacts with ferric chloride forming a Prussian blue precipitate.

Cellular extracts containing 9 µg of total protein were separated electrophoretically on a 10 % PAGE. Afterwards the gel was washed 3 x 15 min with water to remove interfering buffer salts and then immersed in a solution of 5 mM H_2O_2. The gel was gently stirred for 2 min and then rinsed with water. A freshly prepared solution of 2 % (w/v) potassium ferricyanide ($K_3[Fe(CN)_6]$) and 2 %(w/v) iron chloride ($FeCl_3 \bullet 6H_2O$) were added. After the appearance of white bands the gel was washed with water.

7.3.5 *Dr*Dps1 and *Dr*Dps2 immunolocalization

D. radiodurans cells GFP-*dps1* and GFP-*dps2* strains in control, manganese and methyl viologen conditions were collected by centrifugation (11000 *g*, 1 min) from time point 0 (OD=0.3) and 2 hours. Cells were resuspended in phosphate buffer saline (PBS) and fixed with 3.7 % paraformaldehyde, and stained with 2 µg/ml of 4,6-diamidino-2-phenylindole dihydrochloride (DAPI - Invitrogen), and 10 µg/ml of *N*-(3-Triethylammoniumpropyl)-4-(6-(4-(Diethylamino) Phenyl) Hexatrienyl) Pyridinium Dibromide (FM4-64 - Invitrogen). DAPI is a dye that stains nucleoid DNA with blue colour (wavelenghts of excitation/emission - 350/470 nm), and FM 4-64 is a dye that stains membranes with red colour (excitation/emission - 515/640 nm). FITC filter (fluorescein-isothiocyanate-excitation/emission 495/517 nm) was used to visualize GFP-tag constructs.
Cells were visualized on a Leica DM RA2 microscope and the images were captured with a charged-coupled device (CCD) camara. The images were further processed using iImageJ software.

7.3.6 X-ray fluorescence imaging

An aliquot of 1 ml from a growth of *D. radiodurans* cells wild type, Δ*dps1*, Δ*dps2* and Δ*dps1*Δ*dps2* strains in control and methyl viologen conditions were collected at time point 2 hours. Cells were fixed using 3.7 % paraformaldehyde for 15 min at room temperature followed by 30 min in ice, then washed 2 times in PBS and stored frozen at -20ºC.

Cells were afterwards resuspended in 25 µl of water, and then 1 µl was added to a Si3N4 membrane (Silson Ltd) with size of 1.5 mm × 1.5 mm, thickness of 500 nm. Cells were air dried and then mounted in the cell support.

Correlative imaging of both X-ray phase contrast and X-ray fluorescence was performed on the same sample to investigate its morphology and elemental content. Experiments were performed under vacuum at room temperature on the Nano-Imaging beamline ID16A at the European Synchrotron Radiation Facility (ESRF, Grenoble). The multilayer coated fixed curvature Kirkpatrick-Baez (KB) focusing mirror system (*384*) provides the nanofocus (~30 nm) and a very high flux of $4.1x10^{11}$ ph/s from the broad bandpass (1%) at 17 keV. X-ray phase contrast imaging was firstly performed by recording magnified Fresnel projection images with an equivalent pixel size of 15 nm. Quantitative phase maps were retrieved (*385*) and converted to areal density (µg/mm^2) in all figures. X-ray fluorescence (XRF) measurements were performed subsequently with a step size of 40 nm or 50 nm and a dwell time of 50 ms (*386*). The summed spectrum recorded with a 6-element silicon drift detector was fitted with the freely available software PyMca (*387*). The absolute calibration to the elemental areal density (ng/mm^2) was determined by a thin film standard (AXO Dresden GmbH).

7.4 Results

7.4.1 *Deinococcus radiodurans* growth

In order to correlate the presence of metals, such as iron and manganese with the capacity to survive to high doses of oxidative stress and with the role of manganese as protection mechanism, different compounds were added to the growth of *D. radiodurans* wild-type in the early exponential phase (OD_{600nm}= 0.3). The compounds tested were iron, manganese, hydrogen peroxide and methyl viologen. Methyl viologen is routinely used as an effector in oxidative stress research, damaging the cell indirectly by $O_2^{\bullet -}$ production, through its redox cycling (*5*).

The presence of iron did not affect cell growth while addition of manganese (Mn) allowed cells grow for longer, starting later the stationary phase when compared with the control condition. Cell growth rate is affected after adding hydrogen peroxide or methyl viologen which induced an oxidative stress burst in the cells (Fig. 7.1, A).

However, methyl viologen produces a higher impact than hydrogen peroxide, cells enter in a lag phase and only start to recover after 28 hours. Upon these conditions (H_2O_2 and Mv) the cells are viable as those from the control conditions.

Manganese has been proposed to have a crucial role in the protection mechanism of macromolecules against its oxidation in *D. radiodurans* (*69*). In order to address this question, this metal was added prior to methyl viologen (Mn/Mv) addition. The cell growth curve showed similar profile when compared with the control condition (Fig. 7.1, A). This indicates that the extra addition of manganese protects the cell from the oxidative stress burst promoted by methyl viologen.

In order to understand the function of both Dps from *D. radiodurans*, three different knockout mutants were analysed: two single knockout mutants (Δ*dps1* and Δ*dps2*) and one double knockout mutant (Δ*dps1*Δ*dps2*). The tested cell growth conditions were the same as those described above for the wild-type strain (Fig. 7.1, B-D).

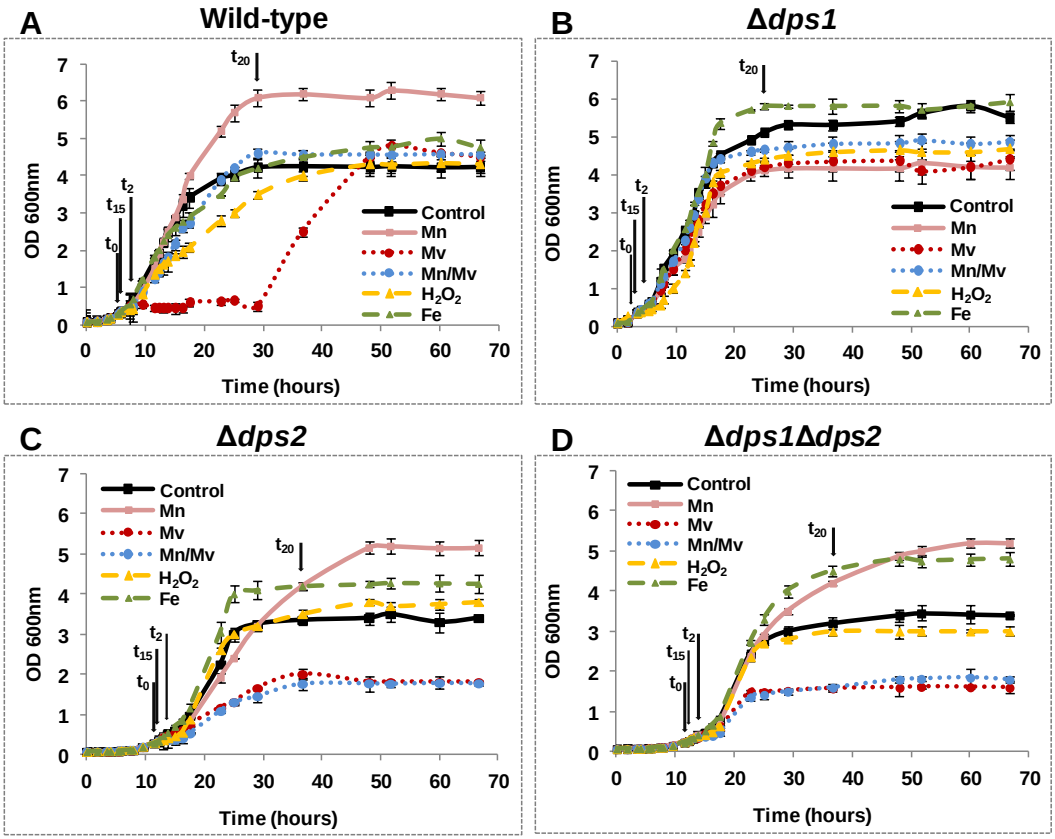

Figure 7.1 - *D. radiodurans* cells submitted to different conditions. Growth curves of *D. radiodurans*

cells strains: **(A)** wild-type, **(B)** Δ*dps1,* **(C)** Δ*dps2,* **(D)** Δ*dps1*Δ*dps2*, grown in M53 medium with the addition at time 0 (OD=0.3) of water (Control condition, black line)**,** manganese (Mn, pink line), iron (Fe, green line), hydrogen peroxide (H_2O_2, yellow line), methyl viologen (Mv, red line), and manganese followed by the addition of methyl viologen (Mn/Mv, blue line). The time points analysed are represented by the arrows and correspond to time 0, 15min (early exponential phase), 2h (mid exponential phase), and 20h (stationary phase).

D. radiodurans cells Δ*dps1* strain entered 2 times faster in the exponential phase when compared with wild-type cells. However, the major difference observed is that addition of any compounds mentioned above, did not affect the cell growth rate, including methyl viologen or manganese (Fig. 7.1, B).

For Δ*dps2* and Δ*dps1*Δ*dps2* cell strains, the lag phases are around two times longer when compared with *D. radiodurans* wild-type cells (Fig. 7.1, C and D). In these cases, addition of methyl viologen strongly affects the cell growth rate, cells enter in lag phase, and even 70 hours after are not able to recover as occurs for the wild-type cells submitted to the same conditions (Fig. 7.1, A). Addition of manganese prior to methyl viologen show similar cell growth profile when compared with addition of only methyl viologen. Thus, prior addition of manganese to *D. radiodurans* Δ*dps2* or Δ*dps1*Δ*dps2* cell strains does not protect cells, as occurs for the wild-type cells (Fig. 7.1, A).

These results showed that *D. radiodurans* cells without *Dr*Dps1 are able to sustain an oxidative stress burst. In contrast, in the absence of *Dr*Dps2, cells are not able to recover from a burst of oxidative stress even upon external manganese addition.

7.4.2 Cellular localization of elements at nano-resolution level

Localization of the different elements in *D. radiodurans* cells was performed using X-ray fluorescence imaging, which contributed to understand how manganese is involved in the protection mechanisms against oxidative stress. *D. radiodurans* cells analyzed were: wild-type, Δ*dps1*, Δ*dps2,* and Δ*dps1*Δ*dps2* strains grown under control and methyl viologen conditions collected at time point of 2 hours (Fig. 7.2).

It has been described that this bacterium can form single of pair cells but it appears frequently as tetrads (*100-101*). Our phase contrast results showed that *D.*

radiodurans cells are grouped in tetrads or in tetrads of tetrads (an example of one tetrad is highlighted with a black circle in Figure 7.2, A1).

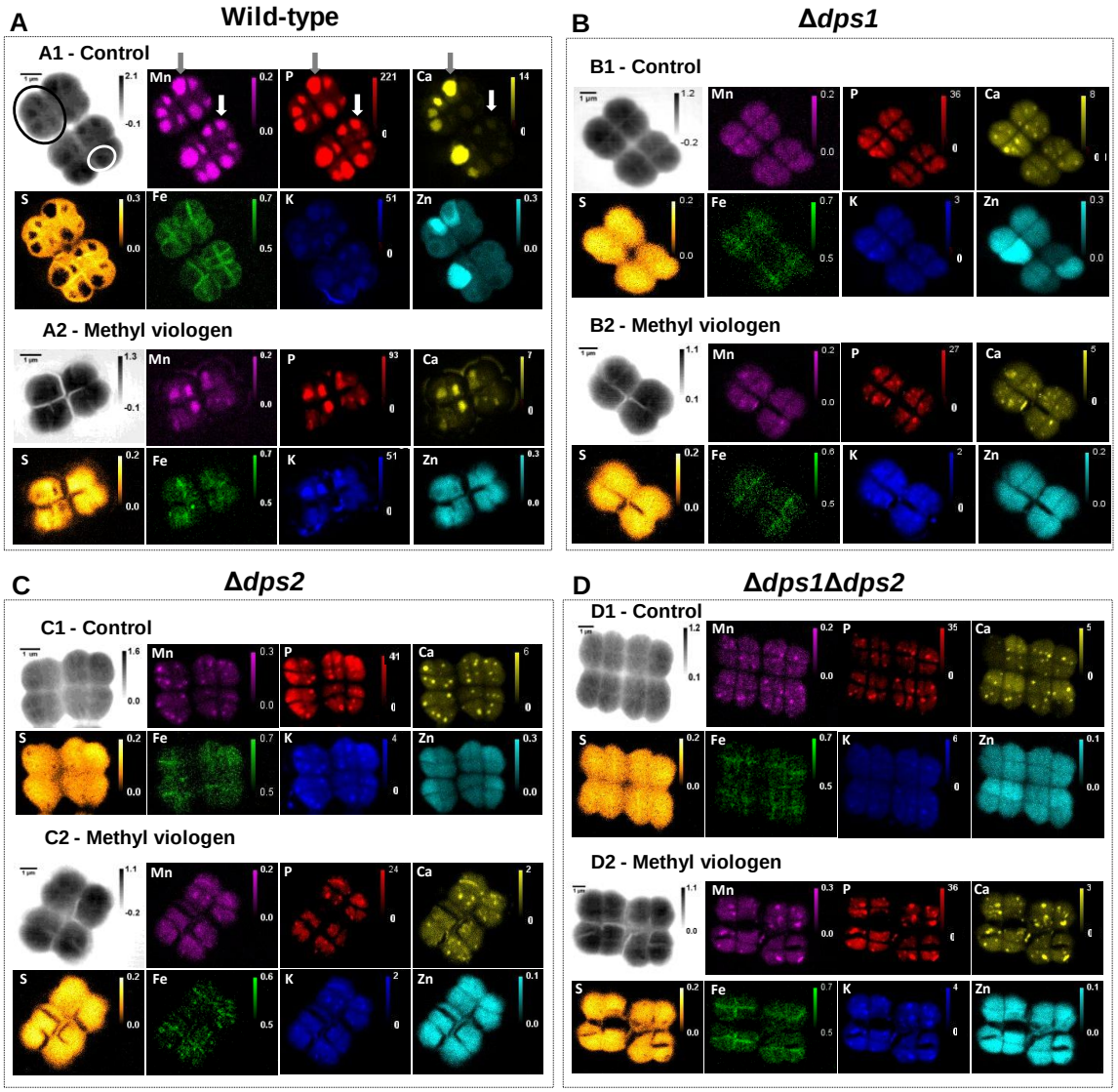

Figure 7.2 – Elements localization in *D. radiodurans* cells, using X-ray fluorescence imaging. Elements mapping in *D. radiodurans* **(A)** wild-type, **(B)** Δ*dps1,* **(C)** Δ*dps2* and **(D)** Δ*dps1*Δ*dps2* strains. The samples analysed were *D. radiodurans* cells in control (1) and methyl viologen (Mv - 2) conditions at time point 2 hours. Black circle represents a tetrad, and white circle represents a phosphate granule. Gray arrow shows a granule rich in phosphorus, manganese and calcium, and white arrow shows a granule rich only in phosphorus and manganese elements.

Each cell contains one circular dark region which corresponds to the electron-dense phosphate granules that were previously described in *D. radiodurans* cells (Fig. 7.2, A1, white circle) (*165, 167*). It has been reported that the composition of phosphate granules can vary between organisms, from polyphosphates, pyrophosphates, lipids, to proteins and different metals (*170, 173, 175-177*), as described in chapter III.

D. radiodurans wild-type cells grown under control conditions, showed an homogeneous distribution of sulphur, except in the region corresponding to phosphate granules, indicating that these granules are a compartmental region (Fig. 7.2, A1). On the other hand, our results showed that calcium, manganese and phosphorus elements are co-localized in this compartmental region. Most of the observed granules are rich on both manganese and phosphorus elements, while in the case of calcium it was observed a higher variation between different granules (Fig. 7.2, A1, grey and white arrows). It has been reported that manganese can form complexes with phosphate molecules, being able to detoxify ROS. Since manganese and phosphorus are co-localized in all the tested conditions suggest that in this bacterium, manganese II (Mn^{2+}) and phosphate (Pi) are present as complexes in Mn^{2+}-Pi form.

The granules also contain potassium, which could be involved in the phosphate uptake to these sub-structures, since it was observed that potassium uptake and phosphate are dependent from each other, as described in *E. coli* (*38-39*). This element is also distributed in the cytosol and membrane region, which could be essential to define a membrane potential value together with sodium and chloride anions (*22, 27*).

Iron cellular localization shows that this metal is mostly concentrated in the septum region, which could be required during cell division. Zinc on the other hand is homogeneously distributed. However, it is interesting to note that some cells have higher amount of zinc than others, probably due to a difference in cell division, where zinc is proposed to have a functional role, for instances in zinc-finger proteins (*55*).

In *D. radiodurans* wild-type cells strain under oxidative stress conditions, promoted by addition of methyl viologen, phosphorus, manganese and calcium are distributed in the cytosol and close to the membrane, presenting a lower concentration in the phosphate granules (Fig. 7.2, A2).

Under these conditions, iron is less concentrated in the septum region while zinc is homogeneously distributed, and no difference between cells was observed, which

could be due to the fact that these cells are in lag phase as observed in the cell growth curves (Fig. 7.1, A).

Similar X-ray fluorescence imaging studies were performed for *D. radiodurans* Δ*dps1* strain cells in control and stress conditions (Fig. 7.2, B). Manganese and phosphorus are homogeneously spread on both control and stress conditions contrarily to the wild-type strain (Fig. 7.2, A). These results suggest that *Dr*Dps1 could be involved in the building up of the granules with manganese and phosphorus elements. Thus, in absence of *Dr*Dps1, there is no difference between control and stress conditions, showing that manganese, and phosphorus are globally distributed inside the cell.

Under the same conditions a concentrated region of calcium was detected, suggesting that the calcium is stored in the granules. Therefore, the mechanism associated with the storage of calcium is distinct from elements, like manganese and phosphorous.

This explains the results obtained on the cell growth curves of Δ*dps1* strain, in which addition of methyl viologen did not affect the cell growth (Fig. 7.1, B), indicating that Mn^{2+}-Pi complexes are already distributed in the cell, ready to detoxify ROS, generated by the addition of methyl viologen.

On the knockout mutants, Δ*dps2* and Δ*dps1*Δ*dps2* strains cells, the build up of granules was also affected and small circular like-granules were identified containing small amounts of manganese, phosphorus and calcium (Fig. 7.2, C and D). Moreover, more than one phosphate like-granule per cell were observed, contrasting with one large phosphate granule detected in the wild-type cells (Fig. 7.1, A1). It is important to refer that under stress conditions the septum region is compromised on both Δ*dps2* and Δ*dps1*Δ*dps2*, affecting the cellular division which occurs in a disordered manner (Fig. 7.2, C2 and D2). As mentioned in chapter III, it has been described that cell division in *D. radiodurans* is an orderly process, where tetrads are generated by the formation of two septa in opposite sides perpendicularly to the cell wall forming two cells and then the two new septa start to form before the last two are finished in another plane (*100-101*). These results support the cell growth curves obtained for these two knockout mutants under stress condition. After methyl viologen addition the cell growth enters in a long lag phase, and even 70 hours after the stress, cells are not able to recover (Fig. 7.1, C and D).

Localization of iron and zinc is similar in the three different *dps* knockout mutants; iron appears more concentrated in the septum region and zinc homogenously spread in cells (Fig. 7.2, B, C and D), as occurs for the wild-type cells under control conditions (Fig. 7.2, A1). Furthermore, intracellular phosphorus and potassium levels decrease on the three *dps* knockout mutants when compared with the wild-type strain (Fig. 7.2).

7.4.3 *Dr*Dps1 protein expression levels

D. radiodurans wild-type and Δ*dps2* strains were analysed for protein expression profile of *Dr*Dps1 (Fig. 7.3, A-B). The samples were obtained from growths under different conditions: control, hydrogen peroxide, iron, manganese, methyl viologen and manganese followed by methyl viologen.

*Dr*Dps1 is mainly in the dimeric form, with a small contribution of a trimeric form in the early exponential phase under control conditions of *D. radiodurans* wild-type strain. Afterwards, *Dr*Dps1 changes only to the dimer state, in the exponential and stationary phases (Fig. 7.3, A). This dimeric state is associated with DNA, as reported before (Fig. 5.3, Cb, Chapter V).

However, *Dr*Dps1 oligomeric state changes to trimer after addition of different compounds mentioned above (Fig. 7.3, A). One exception is when iron was added, which induced the formation of *Dr*Dps1 dodecamer. Comparing these results, *Dr*Dps1 trimeric form is more pronounced when manganese and/or methyl viologen was added to the cell growth. It is interesting to note that in the condition where manganese was added prior to methyl viologen, the trimeric form of *Dr*Dps1 still remains after 20 hours of growth, contrarily to the other conditions in which *Dr*Dps1 dimeric form is the only oligomeric form present at this time point. Moreover, *Dr*Dps1 total expression level increased approximately 3-fold in this condition while in the others remained approximately constant (Fig 7.3, A).

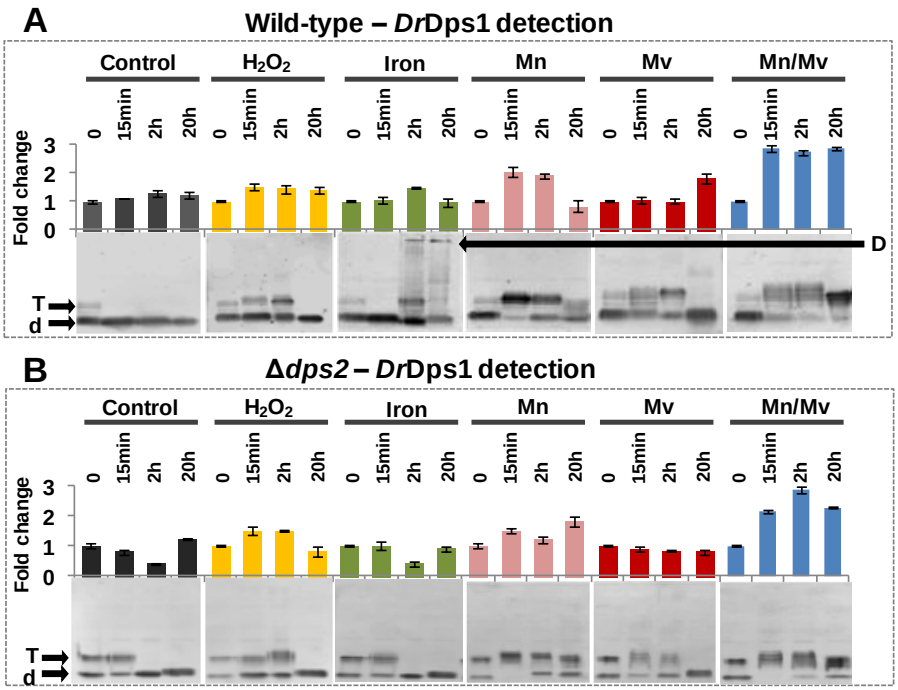

Figure 7.3 - Detection of Dps1 in *D. radiodurans* cellular extracts by Western-blot analysis. **(A)** *Dr*Dps1 detection in wild-type and **(B)** Δ*dps2* cellular extract. The conditions analysed were the following: control, H_2O_2, iron, manganese (Mn), methyl viologen (Mv) and manganese followed by the addition of methyl viologen (Mn/Mv). The time points analysed were t=0, 15min, 2h and 20h. Labels are: dimer (*d*), trimer (*T*) and dodecamer (*D*). Bar-charts represent the quantification of the amount of the total *Dr*Dps1 using ImageJ from four independent samples.

The *Dr*Dps1 oligomeric change between dimer and trimer was also observed in all tested conditions of Δ*dps2* strains (Fig. 7.3, B). Thus absence of *Dr*Dps2 does not affect the formation of these two *Dr*Dps1 oligomeric states. However, this is not the case when iron was added to the growth, since in the Δ*dps2* strains iron does not induce the formation of *Dr*Dps1 dodecamer. This suggests that the formation of *Dr*Dps1 dodecamer is dependent of *Dr*Dps2.

7.4.4 *Dr*Dps1 regulated by post-translational modification

The mechanism by which *Dr*Dps1 changes its oligomeric state between dimeric and trimeric is not known (Fig. 5.3, B and 7.3, Chapters V and VII). In order to address if the oligomeric states modification of *Dr*Dps1 is associated with a post-translational

modification, namely phosphorylation, cellular extracts before (dimeric form) and after addition of manganese (mainly trimeric form) were analysed (Fig. 7.4). Phosphorylation is known as one of the major post-translational modifications which regulate the structure and consequently the function of several proteins (*22*).

Samples were loaded in a 10 % PAGE without or containing a Mn^{2+}-Phos-tag complex that specifically binds to phosphorylated proteins and retards the protein migration in the gel (Fig. 7.4). The results showed that the presence of the Mn^{2+}-Phos-tag complex did not alter the *Dr*Dps1 dimer form migration profile. However, the profile of *Dr*Dps1 trimer was modified in the presence of the Mn^{2+}-Phos-tag complex, appearing other bands that migrated less in the gel. These results showed that *Dr*Dps1 trimer is phosphorylated.

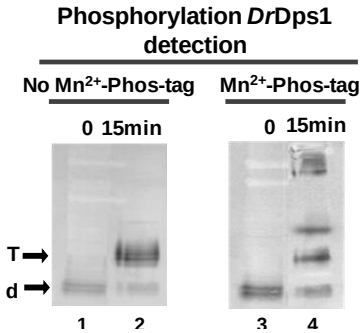

Figure 7.4 - Phosphorylated *Dr*Dps1 detection in *D. radiodurans* wild-type cellular extracts by Western-blot analysis. Cellular extracts of the manganese condition at time 0 and 15 min were loaded in PAGE without (lane 1-2) or containing 10 mM $MnCl_2$ and 5 mM Phos-tag AAL-107 forming an Mn^{2+}-Phos-tag complex (lane 3-4) which bind specifically phosphorylated proteins. Labels are: dimer (*d*), trimer (*T*).

7.4.5 *Dr*Dps2 protein expression level

*Dr*Dps2 protein expression level was analysed in *D. radiodurans* wild-type and in Δ*dps1* cells strains in all conditions describe above. *Dr*Dps2 expression levels increase approximately 1.5 to 1.9 fold in exponential phase in control conditions when compared with early exponential phase. However, in stationary phase the expression levels decrease 3.5-fold, when compared with the early exponential phase (Fig. 7.5, A).

When metals, iron or manganese were added to the cell growth it was observed only a slight increase in *Dr*Dps2 expression level, when compared with the control condition (Fig. 7.5, A).

Under stress conditions, *Dr*Dps2 expression level increase approximately 10-fold in the stationary phase when compared with the stationary phase in the control

condition (Fig. 7.5, A), suggesting that *Dr*Dps2 is essential in the protection against ROS.

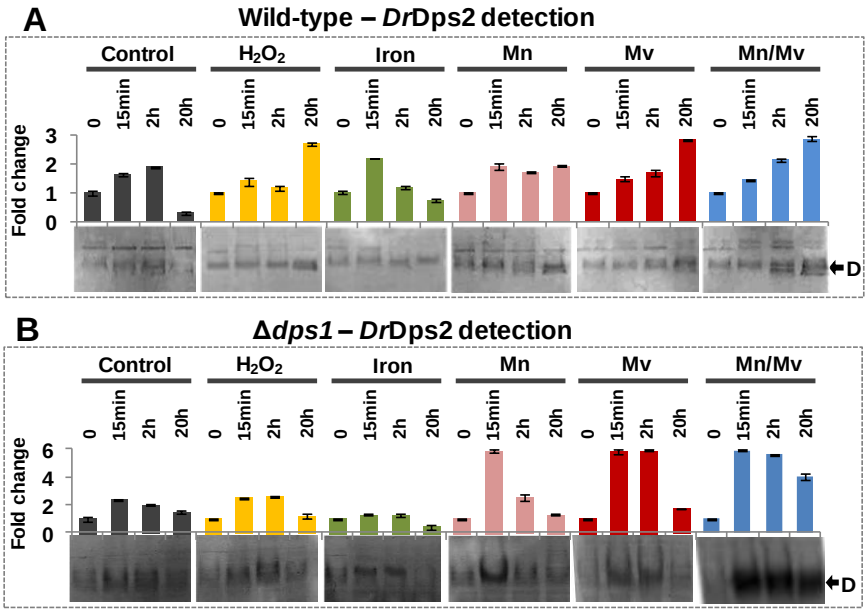

Figure 7.5 - Detection of Dps2 in *D. radiodurans* cellular extracts by Western-blot analysis. *Dr*Dps2 detection in **(A)** wild-type and **(B)** Δ*dps1* cellular extract. The conditions analysed were the following: control, H_2O_2, iron, manganese (Mn), methyl viologen (Mv) and manganese followed by the addition of methyl viologen (Mn/Mv). The time points analysed were t=0, 15min, 2h and 20h. Label is dodecamer (*D*). Bar-charts represent the quantification of the total amount of *Dr*Dps2 using ImageJ from four independent samples.

For Δ*dps1* strain (Fig. 7.5, B), it was observed that *Dr*Dps2 expression levels increased approximately 3-fold in the manganese, methyl viologen and manganese/methyl viologen conditions when compared with control conditions, but also comparing with the wild-type strain, for each corresponding time point and conditions (Fig. 7.5, A). Furthermore, it is interesting to mention that these conditions are those in which *Dr*Dps1 appears mostly as a trimer in the wild-type strain (Fig. 7.3, A). These results suggest that *Dr*Dps1 as a trimer would be involved on the regulation of *Dr*Dps2 expression.

7.4.6 *Dr*Dps2 in cytosol depends of *Dr*Dps1

*Dr*Dps2 contains a signal peptide and it has been observed that this protein is mostly localized close to the membrane region (*206*). Therefore, the presence of

*Dr*Dps2 in both soluble and membrane fractions was investigated in *D. radiodurans* wild-type (Fig. 7.6, A) and Δ*dps1* strains (Fig. 7.6, B). In *D. radiodurans* wild-type cells, under control conditions, *Dr*Dps2 was mostly found in the membrane, 3-fold higher when compared with the soluble fraction. However, the presence of *Dr*Dps2 increases 2.5-fold in the soluble fraction after addition of manganese, while in the membrane fraction it decreased slightly, 0.5-fold (Fig. 7.6, A).

It is interesting to observe that the form found in the membrane fraction has a higher molecular mass (*Dr*Dps2$_M$), than the one present in the soluble fraction (*Dr*Dps2$_C$) (Fig. 7.6, A).

Moreover, after manganese addition to the cell growth, the *Dr*Dps2 detected in the soluble fraction presents a higher molecular mass than in control conditions (Fig. 7.6, A). This difference maybe due to the storage of manganese by *Dr*Dps2 by its cytosolic form.

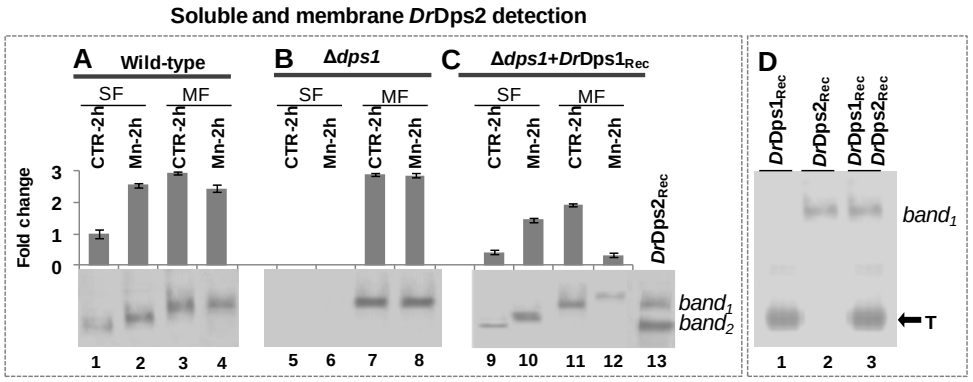

Figure 7.6 - *Dr*Dps2 detection in soluble and membrane fractions in *D. radiodurans* **(A)** wild-type and **(B)** Δ*dps1* strains. The soluble (SF, lane 1, 2, 5, and 6) and membrane (MF, lane 3, 4, 7 and 8) fractions were isolated from control (CTR) and manganese (Mn) conditions at time 2h. **(C)** *Dr*Dps1 recombinant pure protein (*Dr*Dps1$_{Rec}$) was added to cellular extract of Δ*dps1* and after incubation for 1 hour, the soluble (lane 9 and 10) and membrane fractions (lane 11 and 12) were obtained and loaded in PAGE. Bar-charts represent the quantification of the amount of the total *Dr*Dps2 using ImageJ from four independent samples. *Dr*Dps2 recombinant (*Dr*Dps2$_{rec}$ - lane 13), in which *band$_1$* corresponds to the *Dr*Dps2 dodecamer without signal peptide (279 kDa), and *band$_2$* corresponds to *Dr*Dps2 dodecamer without N-terminal tails (232 kDa). **(D)** Cleavage of *Dr*Dps2 N-terminal tails in *in vitro* conditions by *Dr*Dps1. Recombinant *Dr*Dps1 as a trimer (lane 1), recombinant full length *Dr*Dps2 (lane 2, *band$_1$*), recombinant *Dr*Dps1 trimeric form incubated during 1 hour with recombinant full length *Dr*Dps2 (lane 3). Label is: Trimer *Dr*Dps1 (T).

Recombinant full length *Dr*Dps2 kept for longer periods at 4ºC, cleaves the N-terminal tail leading to a truncated form of the protein (Fig. 7.6, lane 13). These two forms are comparable in terms of molecular mass detected in PAGE conditions with those observed in the soluble and membrane fractions isolated from *D. radiodurans* cell. This suggests that *Dr*Dps2$_M$ form corresponds to the full length protein, while the *Dr*Dps2$_C$ form has cleaved its N-terminal tails (Fig. 5.3 C and 7.3, Chapters V and VII).

*Dr*Dps2 protein was only detected in the membrane fraction obtained from Δ*dps1* cells strain, in control and manganese conditions (Fig. 7.6, B), thus, indicating that the presence of *Dr*Dps2$_C$ depends on *Dr*Dps1. To corroborate this, recombinant *Dr*Dps1 protein as a trimer was added to the cellular extract of *D. radiodurans* Δ*dps1* strain. Analysis of both soluble and membrane fractions shows that *Dr*Dps2 was detected in both fractions after addition of recombinant *Dr*Dps1 (Fig. 7.6, C). However, addition of recombinant *Dr*Dps1 as a trimer to the full length recombinant *Dr*Dps2 does not lead to the N-terminal tail truncation under in *in vitro* conditions (Fig. 7.6, D). Thus, cleavage of the *Dr*Dps2 N-terminal tails, and therefore the presence of this protein in the cytosol occur indirectly through *Dr*Dps1.

7.4.7 Immunofluorescence localization of *Dr*Dps1 and *Dr*Dps2

Cells analyzed by fluorescence microscopy were obtained from *D. radiodurans* GFP-*dps1* or GFP-*dps2* strains, at time point of 2 hours in control, manganese and methyl viologen conditions (Fig. 7.7). The cells expressing GFP-*dps1* or GFP-*dps2* proteins presented similar growth rates as *D. radiodurans* wild-type cells under those conditions, indicating that the tagged proteins were functional.

The results showed that *Dr*Dps1 in control conditions was found uniformly distributed throughout the DNA suggesting a co-localization with this structure (Fig. 7.7, A). Addition of manganese or methyl viologen, changes the localization of *Dr*Dps1, appearing diffused in the cell. However in some cells, it was possible to observe that the protein is concentrated in a specific circular region (Fig. 7.7, B and C). This region is similar to those observed by X-ray fluorescence imaging as being phosphate granules (Fig. 7.2). This suggests that *Dr*Dps1 co-localizes with phosphate granules, under manganese and methyl viologen conditions.

*Dr*Dps2 cellular localization changes upon addition of different compounds (Fig. 7.7, D-F). In control conditions was observed that *Dr*Dps2 is mostly present in the

septum membrane region (Fig. 7.7, D). After manganese or methyl viologen addition the protein is dispersed in the cytosol, though remaining a part close to the membrane (Fig. 7.7, E and F). These results are in agreement with the data presented in Fig 7.6, A, where it is shown that in control conditions the protein is mostly present in the membrane fraction while after manganese addition *Dr*Dps2 was detected on both membrane and soluble fractions.

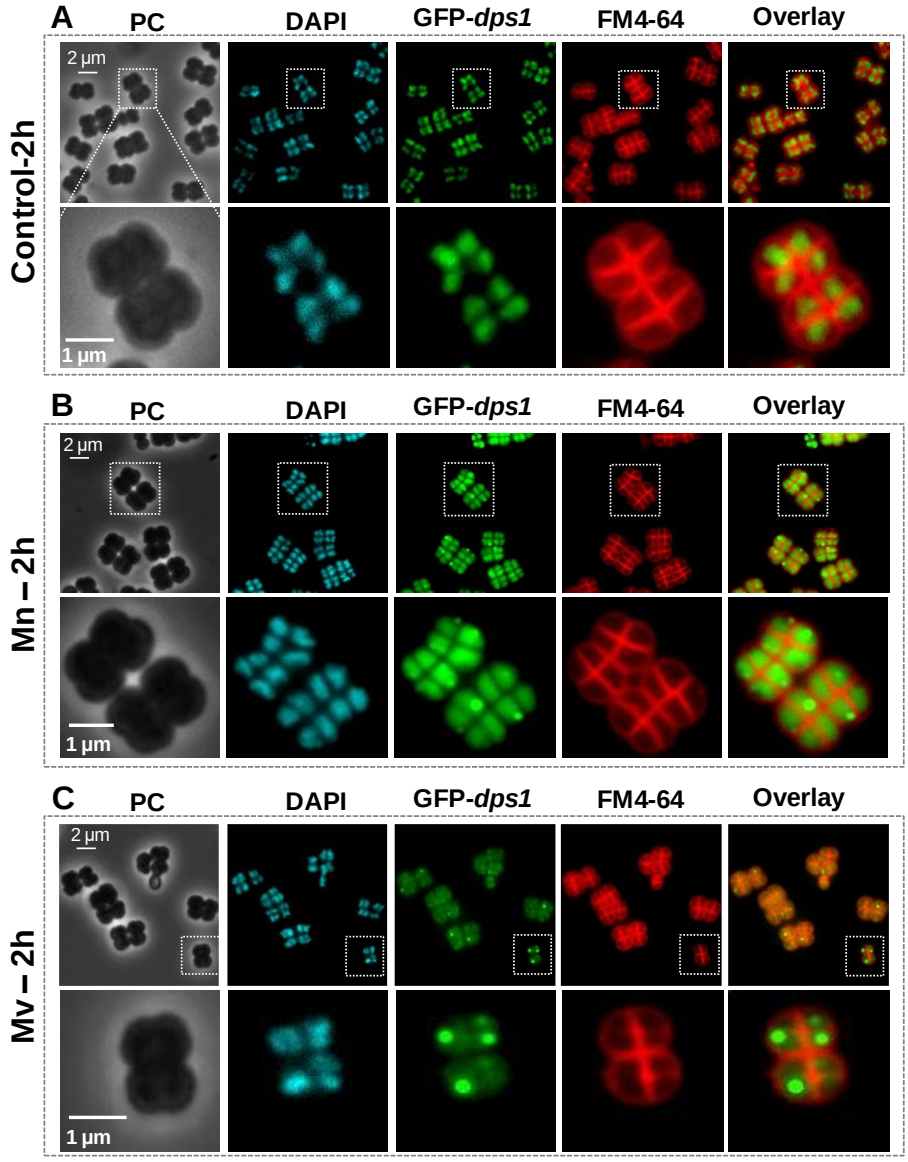

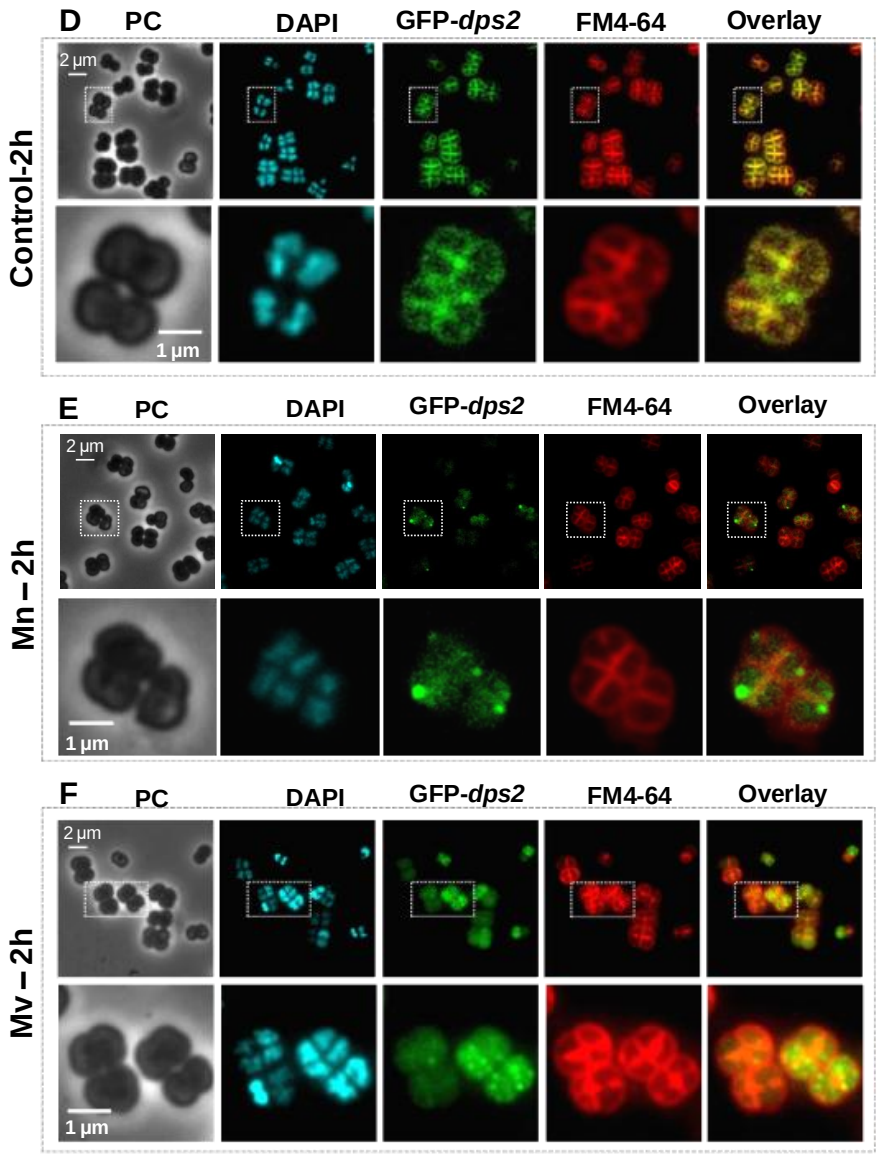

Figure 7.7 - *D. radiodurans* Dps cellular localization using fluorescence microscopy. **(A-C)** GFP-*dps1* cellular localization. **(D-F)** GFP-*dps2* cellular localization. The samples analysed were *D. radiodurans* cells in control **(A and D)**, manganese (Mn) **(B and E)** and methyl viologen (Mv) **(C and F)** conditions at 2 hours. The cell images are represented in phase contrast (PC), stained for DNA using DAPI (blue), green fluorescence for GFP-*dps* constructs, and the membranes stained with FM4-64 (red). The overlay corresponds to GFP-*dps* with the membrane fluorescence. The white squares correspond to the amplified region.

7.4.8 MnSOD activity from *D. radiodurans*

In order to understand the role of superoxide dismutase enzymes as a protection mechanism against oxidative stress in *D. radiodurans*, SOD activity was detected in cellular of extracts *D. radiodurans* wild-type, Δ*dps1*, Δ*dps2,* and Δ*dps1*Δ*dps2* cells strains in the conditions mentioned above (Fig. 7.8).

SOD activity was detected, showing three activity bands, in all conditions tested in the exponential phase (Fig. 7.8, bands a-c). In the stationary phase was observed the presence of at least two SOD activity bands, depending on the condition. However, in the condition where the cell growth was supplemented with manganese, the three bands of SOD activity were observed in both the exponential and stationary phases (Fig. 7.8).

It is interesting to observe that in *D. radiodurans* wild-type, Δ*dps2,* and Δ*dps1*Δ*dps2* cells strains in the stationary phase of Mn/Mv condition, was observed a new SOD band that migrates more in the gel (band d), which has not been reported until now. This SOD band was also observed for all conditions tested in stationary phase of the Δ*dps1* strain (Fig. 7.8, B).

D. radiodurans genome encodes for four superoxide dismutases: two CuZnSOD (*dr1546 and drA0202*), one MnSOD (*dr1279*) and a fourth predicted SOD still of unknown type *dr0644* (*102*).

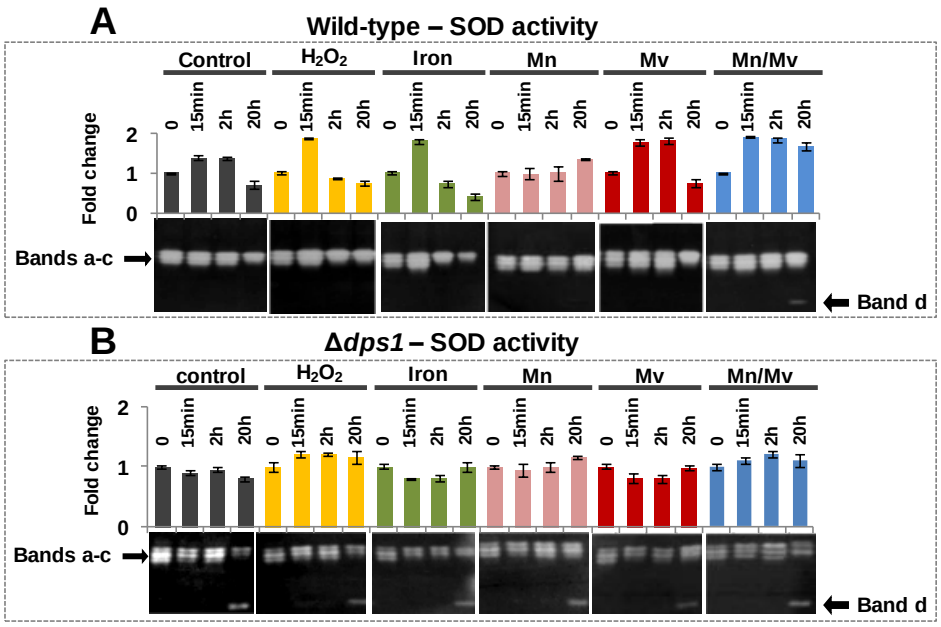

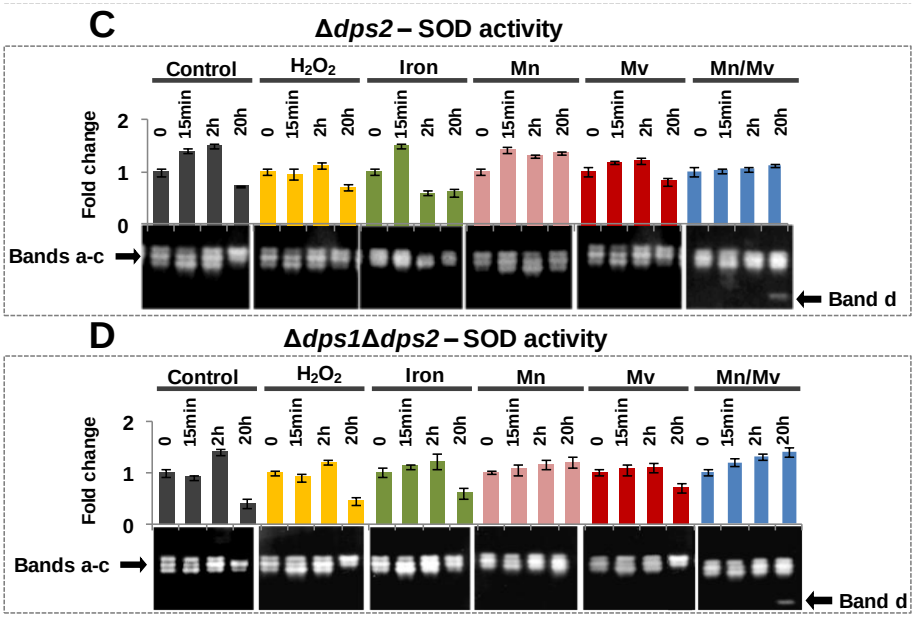

Figure 7.8 - *D. radiodurans* SOD activity. Total SOD activities in *D. radiodurans* cellular extracts **(A)** wild-type, **(B)** Δ*dps1*, **(C)** Δ*dps2* and **(D)** Δ*dps1*Δ*dps2* strains. The conditions analysed were the following: control (black colour), hydrogen peroxide (yellow colour), iron (green colour), manganese (Mn, pink colour), methyl viologen (Mv, red colour), and manganese followed by the addition of methyl viologen (Mn/Mv, blue colour). The time points analysed were t=0, 15min, 2h and 20h. Bar-charts represent the quantification of the amount of the total SOD activity, using ImageJ from four independent samples. Labels are MnSOD isoforms (Bands a-d).

In order to confirm if the three bands (bands a-c) and the new band (band d) correspond to MnSOD or CuZnSOD enzymes, inhibitions of the SOD band activities were performed (Fig. 7.9). Addition of 2-4 % of SDS is used to inhibit MnSOD activity while potassium cyanide is used to inhibit CuZnSOD activity (*381*).

The presence of KCN did not inhibit any SOD activity band, with the exception of CuZnSOD commercial enzyme used as control. On the other hand SDS strongly compromised the SOD activity bands (a-d) present in *D. radiodurans* extract as well as the MnSOD from *Arabidopsis thaliana* used as control which was completely abolished. Since it was still detected a residual activity with 2% of SDS, the percentage of SDS was increased up to 4 % (Fig. 7.9). Under this condition, the SOD activity from the four bands (a-d) was almost abolished. These results suggest that the SOD activity bands a-d corresponds to MnSOD protein, but probably corresponding to different isoforms. These different isoforms could be involved in the cell protection being dependent on the manganese and the new band could be essential to protect

the cell under stress conditions in stationary phase. The higher resistance observed in the Δ*dps1* cell growth curves upon addition of methyl viologen, could also be related with this new MnSOD isoform (Fig. 7.1, B).

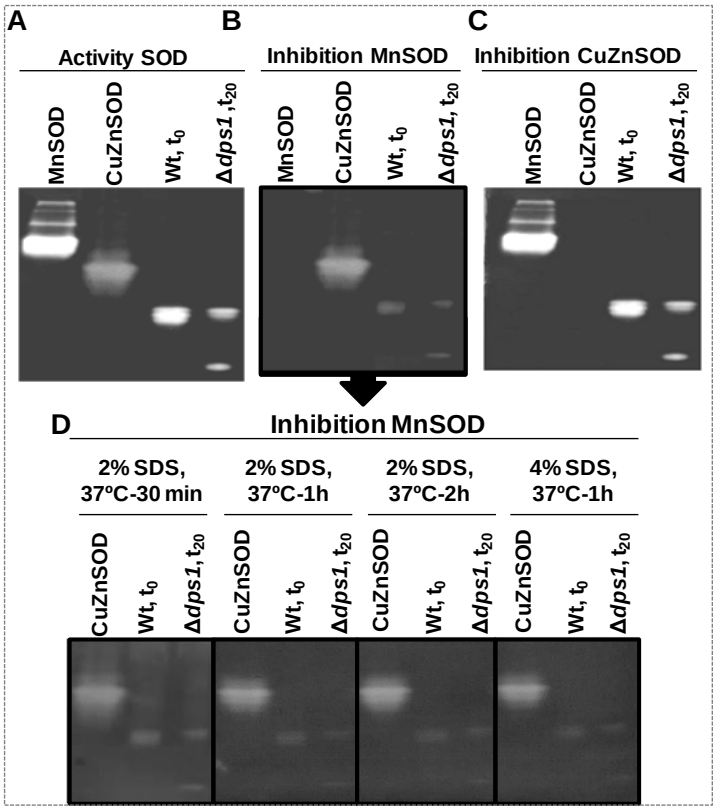

Figure 7.9 – *D. radiodurans* SOD activity inhibitions. **(A)** SOD activity was performed in point 0 for the wild-type strain and in point 20 hours for the Δ*dps1* strain. **(B)** Inhibition of MnSOD activity using 2 % of SDS, incubated 30 min at 37 ºC. **(C)** Inhibition of CuZnSOD activity using potassium cyanide. **(D)** Inhibition of MnSOD activity using different SDS percentage (2-4 %) and different incubation times (30 min - 2 hours). MnSOD and CuZnSOD enzymes were used as control.

7.4.9 Catalase activity from *D. radiodurans*

D. radiodurans genome encodes for three heme containing catalases, KatA, KatB and KatC (*dr1998, dra0259, and dra0146,* respectively) (*102*). However, experimentally it was observed activity only for two catalases based on studies of knockout mutants for the three catalases. KatA (*DR1998*) showed two activity bands, while KatB (*DRA0259*) showed only one band in native acrylamide gel, and no activity band was attributed to KatC (*202*).

Our data showed similar results, where three bands were detected in exponential phase in control conditions. Based in the data previously presented by Jeong et al. (*202*), band 1 corresponds to KatB and bands 2 and 3 corresponds to KatA (Fig. 7.10, A). In *D. radiodurans* wild-type cells in stationary phase, a different catalase activity band was observed, in all conditions tested (Fig. 7.10, Ba, band 4). This new band could corresponds to KatC, which may be essential to detoxify ROS in the stationary phase. After addition of hydrogen peroxide and iron catalase activity increases, in the stationary phase (Fig. 7.10, Ba), when compared with the other conditions.

The total catalase activity in the Δ*dps1* strain, under control conditions, is identical to the wild-type cells (Fig. 7.10, A). On the other hand, catalase activity levels on the knockout mutants Δ*dps2* and Δ*dps1*Δ*dps2* are similar between them, but approximately 2.5-fold lower when compared with the total activity detected for the wild-type under control conditions. This lower activity could contribute for the damage observed in these two strains under stress conditions, decreasing the cell protection. Furthermore in these two knockouts mutants, the catalase activity is not affect by the addition of different compounds, being similar to the control conditions for the different knockout mutants (Fig. 7.10, Bb, Bc, and Bd).

It is interesting to note that band 4 does not appear for any *dps* knockout mutant, under any conditions ((Fig. 7.10, B).

These results demonstrated that KatA is present at higher levels in *D. radiodurans* cells in all growth phases, suggesting an important role in ROS detoxification. Nevertheless, both KatB and KatC are also involved, being essential in stress conditions.

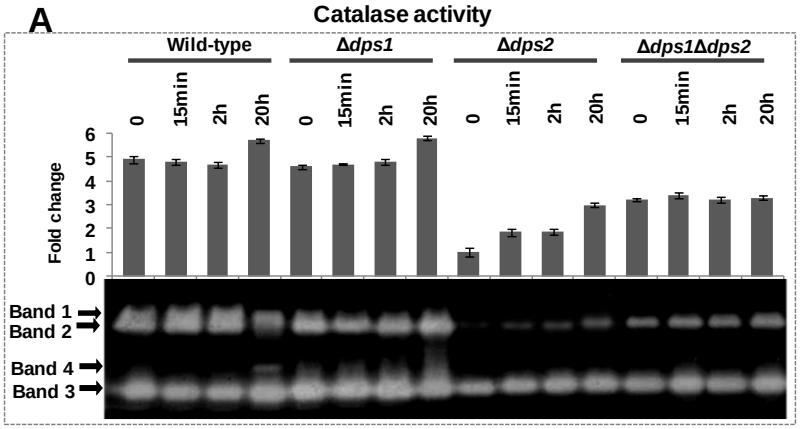

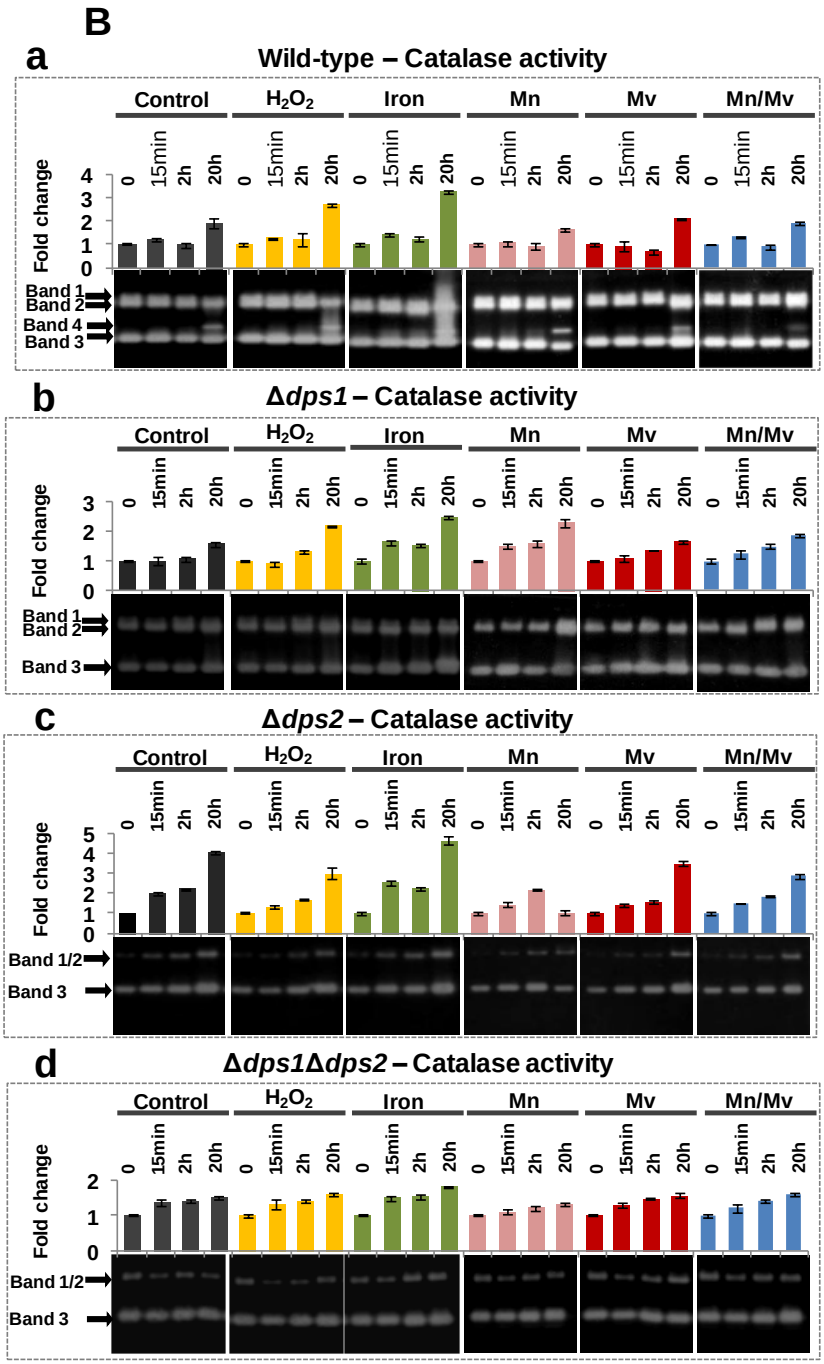

Figure 7.10 - *D. radiodurans* catalase activity levels. **(A)** Total catalase activities in *D. radiodurans* wild-type, Δ*dps1*, Δ*dps2* and Δ*dps1*Δ*dps2* strains in control conditions. **(B)** Total catalase activities in *D. radiodurans* cellular extracts wild-type **(Ba)**, Δ*dps1* **(Bb)**, Δ*dps2* **(Bc)** and Δ*dps1*Δ*dps2* **(Bd)** strains. The time points analysed were t=0, 15min, 2h and 20h. The conditions analysed were the following: Control (black colour), hydrogen peroxide (yellow

colour), iron (green colour), manganese (Mn, pink colour), methyl viologen (Mv, red colour), manganese followed by the addition of methyl viologen (Mn/Mv, blue colour). Bar-charts represent the quantification of the amount of catalase activity, using ImageJ from four independent samples. Labels are KatB (band 1) KatA (bands 2-3), and a new band could corresponds to KatC.

7.4.10 *dps1*, *dps2* and *Mnsod* genes expression levels

In order to correlate the gene expression levels of *dps1*, *dps2* and *Mnsod* with the protein expression level presented above and to understand the link between protection mechanisms associated with manganese, RT-PCR assays were performed. *dps1*, *dps2* and *Mnsod* genes expression level were analysed in *D. radiodurans* wild-type, Δ*dps1*, Δ*dps2* and Δ*dps1*Δ*dps2* cells strains submitted to different conditions (Fig. 7.11).

The three genes expression levels were strongly repressed in wild-type strain under manganese conditions when compared with control conditions. However in the knockout mutants this effect was not observed, suggesting that the protection through manganese is dependent on both *Dr*Dps (Fig 7.11).

Under stress conditions (Mv and Mn/Mv) *dps1* expression increases in the wild-type strain whereas in the *dps1* knockout mutant an increase of *dps2* gene was observed (Fig. 7.11, A).

Regarding the expression level of *mnsod*, it is identical on the different conditions for the three *dps* knockout mutants (Fig. 7.11, B).

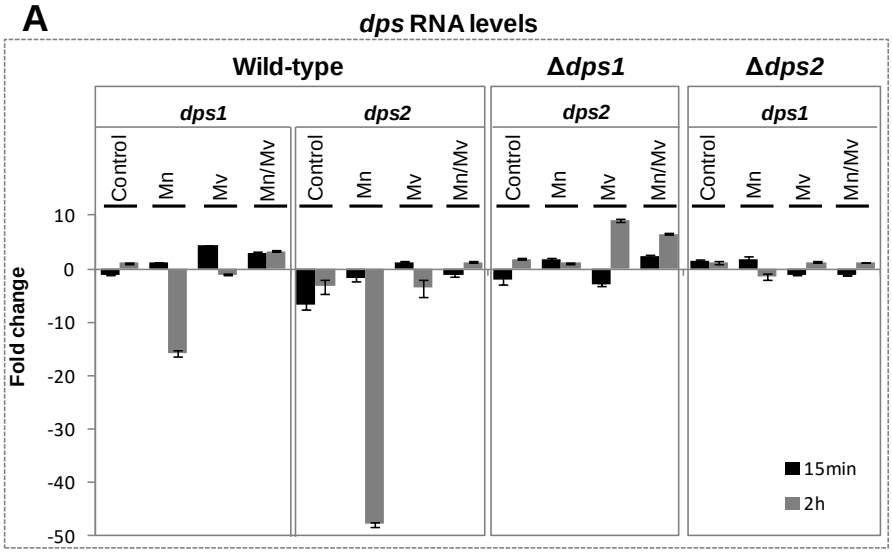

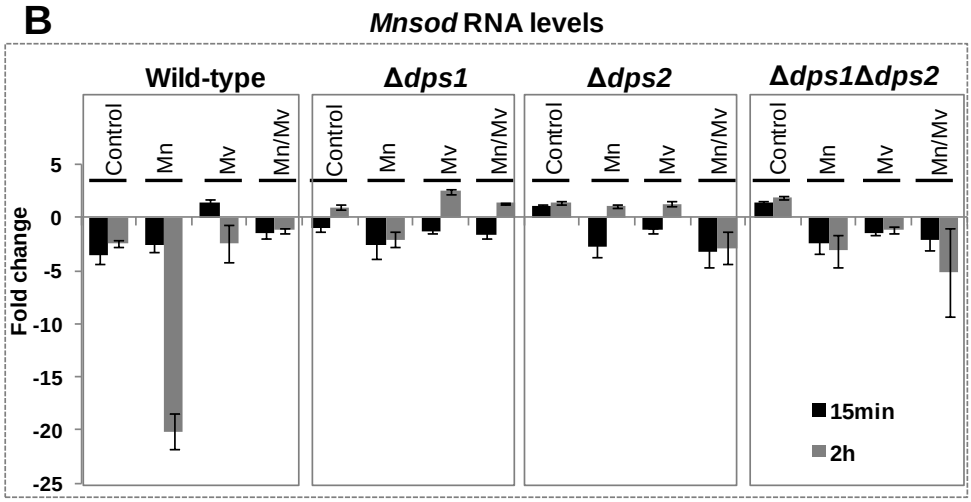

Figure 7.11 - RT-PCR for *dps1*, *dps2* and *Mnsod* genes in *D. radiodurans.* **(A)** *dps1* and *dps2* genes expression levels in wild-type, Δ*dps1* and Δ*dps2* strains. **(B)** *Mnsod* gene levels in *D. radiodurans* wild-type, Δ*dps1*, Δ*dps2* and Δ*dps1*Δ*dps2* strains. The conditions analysed were the following: control, manganese (Mn), methyl viologen (Mv), manganese followed by the addition of methyl viologen (Mn/Mv). The time points analysed were 0, 15 min and 2 hours. The point 0 was used to normalize the points 15 min (black bar) and 2 hours (gray bar). Bar-charts represent the RNA quantification, using ImageJ from six independent samples.

7.5 Discussion

7.5.1 Phosphate granules

Deinococcus radiodurans is a bacterium which survives to the presence of extreme conditions, such as: ionizing and UV radiation, desiccation and H_2O_2 (*67, 118-120, 122*). This survival has been associated with the high intracellular manganese concentration, which forms complexes with small molecules such as phosphate leading to protein protection against ROS (*69, 134*).

Under control conditions *D. radiodurans* contains an intracellular compartmental region, rich in phosphorus, manganese, and calcium (Fig. 7.2, A1). This region coincides with the phosphate granules that were identified as electron-dense phosphate granules by electron microscopy in several studies (*165*) and which are

described in chapter III. Daly and co-authors observed that manganese was concentrated in a specific region also suggesting a co-localization of this metal with phosphate granules. However this study was performed at low resolution and many questions remained to be understood (*67, 69*), which was accomplished with our work.

Under oxidative stress conditions promoted by the addition of methyl viologen, the localization of calcium, manganese, and phosphorus changes: instead of being stored in the granules they are mostly distributed in the cell (Fig. 7.2, A2). These results suggest that this organism has a protection mechanism based in the distribution of manganese, calcium and phosphorus. In control conditions the granules act as a reservoir for these elements, which could be important to control the nutrient levels maintaining the cell energy, as occurs for other bacteria as referred in chapter III. For example in wild-type cells manganese addition induces cells to enter later in the stationary phase, therefore constituting a crucial mechanism to maintain cell homeostasis. Under stress conditions these elements are delivered to the cytosol and membrane region, conferring protection to the cell.

The function of each element needs to be further investigated. However based on our results the mechanism that regulates the storage of calcium storage in phosphate granules is different from those associated with manganese and phosphorus. Calcium could act as an intracellular signaling messenger, being released from the granules, activating proteins such as kinases dependent of calcium, as reported in Eukaryotic but also in Prokaryotic organisms, described in chapter II (*44*), while manganese and phosphorus in the form of Mn^{2+}-Pi complexes are available to scavenger ROS.

7.5.2 *Dr*Dps implicated in manganese homeostasis

The role of *Dr*Dps in manganese homeostasis in *D. radiodurans* was addressed in this thesis.

In *in vivo* conditions, the presence of manganese strongly represses both *dps* genes (Fig. 7.11, A), although the protein expression levels are slightly increased for both *Dr*Dps (Fig. 7.3, A and 7.5, A). Moreover, under this condition *Dr*Dps1 changes its oligomeric state from dimer to trimer and the cytosolic form of *DrDps2* is increased *versus* the membrane form when compared with control conditions (Fig. 7.6, A). These results in *D. radiodurans* suggest a link between *Dr*Dps and manganese, which is stored in the phosphate granules.

7.5.2.1 Mn^{2+}-Pi complexes regulated by *Dr*Dps1

The oligomeric state of *Dr*Dps1 is regulated by phosphorylation and is related with its cellular localization. As a dimer is co-localized with DNA, while as a trimer which is phosphorylated is disperse in the cytosol, although a co-localization with phosphate granules was also observed.

The phosphorylation could be triggered by signaling process involving calcium ions, decreasing the interaction between *Dr*Dps1 and DNA and consequently its delocalization from the nucleoid to the cytosol and phosphate granules.

The function of *Dr*Dps1 was further studied with knockout mutants. In the absence of *dps1* (Δ*dps1* strain) the presence of manganese and phosphorus in granules is compromised, appearing distributed in the cell and being identical in control or stress conditions.

These results suggest that *Dr*Dps1 regulates the homeostasis of manganese and phosphorus, affecting directly or indirectly the levels of these elements in the granules. Since the oligomeric state and cellular localization of *Dr*Dps1 is identical in the conditions where manganese or methyl viologen were added, the mechanism for regulation would involve the storage or distribution of Mn^{2+}-Pi complexes. Under extra addition of manganese *Dr*Dps1 would regulate the storage of Mn^{2+}-Pi complexes into granules while under stress conditions would allow the release of these two elements from the granules.

7.5.2.2 *Dr*Dps2 dual function: involved in Mn^{2+}-Pi complexes trafficking and in cell protection

It has been reported that *Dr*Dps2 protein has a signal peptide (*204*), and thus it was suggested that this protein could be exported to the membrane region. In *D. radiodurans* wild-type cells in control conditions, *Dr*Dps2 is localized mainly in the membrane region during exponential phase (Fig. 7.7, D). This result is corroborated by our Western blot assays, in which *Dr*Dps2 was detected mostly in membrane fraction, 3-fold higher when compared with the level present in the cytosol (Fig. 7.6, A). These two forms, membrane (*Dr*$Dps2_M$) and cytosolic (*Dr*$Dps2_C$) have different molecular masses. Our data suggest that *Dr*$Dps2_M$ has the N-terminal tails while

*Dr*Dps2$_C$ form has the N-terminal tails cleaved. It is important to mention that *Dr*Dps2$_C$ form is dependent on *Dr*Dps1 as a trimer, the phosphorylated form. In Δ*dps1* cell strain *Dr*Dps2 appears only in the membrane faction, but after addition of recombinant *Dr*Dps1 as a trimer to cell extract it was possible to detect the cytosolic form of *Dr*Dps2 (Fig. 7.6).

These two different cellular localizations and the two forms, with and without the N-terminal tail, suggest a dual function for *Dr*Dps2.

Our results showed that *Dr*Dps2$_C$ form presents a higher molecular mass when extra manganese was added to the cell growth as compared with the control conditions, indicating that this protein in the cytosolic form incorporates manganese. This is supported by *in vitro* studies, in which was observed that *Dr*Dps2 has the capacity to incorporate manganese (Chapter V). However whether in these conditions *Dr*Dps2 also incorporates phosphate needs to be further investigated, nevertheless the incorporation of phosphate in the presence of iron by a Dps was been already reported (*241*).

The function of *Dr*Dps2$_C$ was complemented by studies in knockout mutant strains. In Δ*dps2* the storage of manganese and phosphate in phosphate granules is strongly compromised, these elements are globally distributed in cytosol when compared with control conditions (Fig. 7.2), thus suggesting that *Dr*Dps2 is involved in storage of Mn^{2+}-Pi complexes into phosphate granules. Since addition of manganese or methyl viologen to the cell growth leads to an increase of *Dr*Dps2$_C$ form, this protein is suggested to be involved in the Mn^{2+}-Pi complexes trafficking in the cell. Under manganese conditions, the Mn^{2+}-Pi complexes are incorporated into *Dr*Dps2$_C$ and delivered to the phosphate granules, while under stress conditions the protein would be involved in the trafficking of theses complexes from the granules to the cytosol and membrane. These complexes in the cytosol and membrane are then available to scavenge ROS and therefore protecting the membrane and soluble proteins against oxidation, as demonstrated by Daly, *et al.* (*79*).

*Dr*Dps2$_M$ form protects the membrane region and consequently contributing for the cell division. This function was elucidated using *dps* knockout mutants. In both Δ*dps2* and Δ*dsp1*Δ*dps2* the initial growth rate is affected, which is 2-times slower when compared with the wild-type strain under control conditions (Fig. 7.1). Under stress conditions the septum structure was damaged and the cell division was affected occurring in a disordered manner (Fig. 7.2). The higher protection against oxidative

stress observed for the Δ*dps1* strain, in the methyl viologen condition could be related with the fact that in this mutant, *Dr*Dps2 is only present in the membrane region (Fig. 7.1, B and 7.6, B). Furthermore under stress conditions in the wild-type strain there is an increase of *Dr*Dps2 expression levels only in the stationary phase, while in the Δ*dps1* cell strain the *Dr*Dps2 expression level immediately increase after the stress addition (in the first 15 min), conferring a higher protection to the cell.

7.5.3 Iron homeostasis involve both *Dr*Dps

Some members belonging to the Dps family have been described as iron storage proteins (*63-64*). In fact, in *in vitro* conditions was observed that both *Dr*Dps have a role in iron storage. *Dr*Dps1 in solution appear mainly as a trimer, but changes its oligomeric to dodecamer after iron addition, showing capacity to incorporate approximately 250 iron atoms per dodecamer. On the other hand *Dr*Dps2 as a stable dodecamer has a higher capacity to incorporate iron, 400 atoms per dodecamer. The function of *Dr*Dps in iron homeostasis is elucidated in this thesis, however many questions remains to be answered and complementary studies are needed.

In *in vivo* condition, the presence of iron also induces a changed of *Dr*Dps1 oligomeric state, from dimer to dodecamer with a trimer as intermediate while the *Dr*Dps2 expression levels increased slightly.

The data obtained from the knockout mutants showed that in Δ*dps2* strain *Dr*Dps1 dodecamer formation does not occur, suggesting that this dodecamer form is dependent of *Dr*Dps2 (Fig. 7.3, B).

These results suggest that *Dr*Dps2 incorporates and transport iron through the cell as a cytosolic form in a mechanism similar to that described above for manganese, from the membrane to the cytosolic region but in that case iron is delivered to *Dr*Dps1, inducing dodecamer formation, acting thus as a typical iron storage protein.

7.5.4 Enzymatic ROS scavenging systems; SODs and catalases

As suggested by our work the non-enzymatic system, Mn^{2+}-Pi complexes, has been demonstrated as being the most important protection mechanism against ROS. However it should be noted that other mechanisms can contribute for cell protection,

such as enzymatic ROS scavenging systems. *D. radiodurans* contains three catalases and four superoxide dismutase enzymes. Our work demonstrated that KatA, KatB and different MnSOD isoforms are constitutively expressed, contributing for ROS detoxification. Moreover these two families of proteins become more important in stationary phase, where the catalase activity levels increased and a new catalase band appears that could be KatC. However from our data it was not observed a major change in the SOD activity during the growth but a new isoform of MnSOD was detected, which is dependent on the manganese availability. In fact, it has been previously reported that most manganese available in the cell in the stationary phase is associated with proteins, mainly with MnSOD, instead of being associated with phosphate.

Thus, these results showed that different protection systems work simultaneously to promote the high protection observed in this bacterium, and that manganese is the essential factor, forming Mn^{2+}-Pi complexes or associated to proteins, both the systems contributing for ROS detoxification.

Part III

General discussion and conclusion

CHAPTER VIII

General discussion and conclusion

The work presented in this thesis was centered on the studies of two Dps (*Dr*Dps1-*dr2263* and *Dr*Dps2-*drb0092*) from *Deinococcus radiodurans*, a radiation resistant organism. The results allowed us to elucidate about the function of *Dr*Dps and correlate it with the protection mechanisms against oxidative stress of this bacterium, which ultimately can be extrapolated to those that occur upon exposure to radiation.

8.1 Dps from *D. radiodurans in vitro* conditions

It has been observed that *in vitro* conditions, Dps family members have the ability to protect the cell against ROS by their capacity to incorporate Fe^{2+} and to bind/condense DNA (*63-64, 219, 237, 247*). This was also observed for both Dps from *D. radiodurans* (Chapter V).

*Dr*Dps have the ability to bind Fe^{2+} at the ferroxidase centre, which under oxidizing conditions (oxygen or hydrogen peroxide) is oxidized to Fe^{3+}, being incorporated into the *Dr*Dps hollow cavity. *Dr*Dps2 incorporates approximately 400 Fe atoms/12-mer while *Dr*Dps1 only incorporates around 250 Fe atoms/12-mer. Under reducing conditions the incorporated iron is released from the protein cavity (Chapter V).

Manganese incorporation by *Dr*Dps was also addressed, and our results showed that both proteins have capacity to incorporate manganese. *Dr*Dps1 incorporates approximately 500 Mn atoms/12-mer whereas *Dr*Dps2 stores about 600 Mn atoms/12-mer (Chapter V).

*Dr*Dps-DNA interaction was assessed by EMSA and AFM, and our data shows that both *Dr*Dps have the ability to bind DNA and form protein-DNA complexes. *Dr*Dps1 binds to both linear and supercoiled forms of the DNA, showing a protein/DNA ratio of 500 and *Dr*Dps2 binds only to DNA in the supercoiled form with a protein/DNA ratio of 1500. The protein-DNA complexes formed with *Dr*Dps are quite distinct as observed by AFM. In the *Dr*Dps1-DNA complex, DNA is looping out from a central aggregate, whereas in the *Dr*Dps2-DNA complex the protein is spread along the DNA forming a toroidal morphology (Chapter V).

Interaction between Dps and DNA is proposed to occur mainly through positively charged amino acid residues present at N- or C-terminal tails, as it has been demonstrated previously for several Dps proteins (*219, 245, 247, 265*). From previous

work (*270*) and also from our work, *Dr*Dps1 binds to DNA through the positively amino acid residues present at the N-terminal region, that are solvent exposed as observed by our SAXS analysis. Truncation of this region almost abolished the interaction with DNA (Chapter VI). However, as previously suggested, the positively charged residues located at the protein surface may also contribute for the interaction with DNA, namely residue Arg_{132} (*270*).

The N-terminal regions of *Dr*Dps2, also protrude from the dodecamer as observed from our SAXS studies, but this region contains only one positively charged residue, Arg_{33}. When this region was removed the protein still binds to DNA; in fact 8 µM of protein is enough to form large complexes of protein-DNA contrasting with 14 µM for the full length protein (Chapter V and VI). The interaction with DNA occurs probably through the C-terminal region since it contains three positively charged residues (Lys_{204}, Arg_{209} and Arg_{211}). However, it cannot be excluded that the positively charged amino acid residues located at the protein surface, namely Lys_{46}, Lys_{47}, Arg_{122}, Arg_{149}, may also be involved in the interaction with DNA, a similar situation as reported for the Dps (NAP) from *H. pylori* (*268*). As mentioned above, truncation of the N-terminal region of *Dr*Dps2 increases the affinity of the protein for DNA. Moreover the protein is able to interact with both linear and supercoiled forms of DNA, contrasting with the full-length protein which only binds to the supercoiled form. This suggests that the N-terminal region would be involved in selecting the type of DNA conformation. This selection mechanism could be important for the function of *Dr*Dps2 *in vivo*.

The differences between *Dr*Dps on their properties on iron storage and DNA interaction consequently leads to distinct effects on DNA protection, in which *Dr*Dps1 protects DNA more efficiently than *Dr*Dps2. Both proteins showed the ability to protect DNA in the presence of hydroxyl radical formed by addition of hydrogen peroxide and iron, however at different ratios of Fe atom /12-mer, 500 Fe atoms/12-mer and 50 Fe atoms/12-mer, for *Dr*Dps1 and *Dr*Dps2, respectively. This result contrasts with the iron storage capacity determined for both proteins, 270 Fe atoms/12-mer and 500 Fe atoms/12-mer, for *Dr*Dps1 and *Dr*Dps2, respectively. Thus, this suggests that the mechanism by which DNA is protected by *Dr*Dps1 occurs due to both iron storage and DNA binding, in which the large complexes formed between *Dr*Dps1-DNA allow the protection of DNA. On contrary, the DNA protection by *Dr*Dps2, is mostly due to its DNA binding ability, since iron oxidation is decreased when *Dr*Dps2-DNA complex is formed (Chapter V).

8.2 Dps structural alignment

In addition to the common *in vitro* functions of Dps proteins, the two proteins from *D. radiodurans* also have a conserved tertiary and quaternary overall structure: twelve monomers, each with a four-helix bundle arrangement, form a hollow dodecameric sphere (*203-204, 246*). In order to understand if both Dps from *D. radiodurans* are significantly homologous with those from other organisms, a structural alignment based on all Dps crystal structures available in PBD database was performed (Fig. 8.1). Furthermore, this analysis allows to establish a correlation between the function and the structures of Dps.

Dps proteins from pathogenic bacteria are grouped together in the red cluster. Most of these Dps have been proposed to be associated with the virulence of the pathogen, as in the case of the Dps (NAP) from *H. pylori*.

Most of the proteins that cluster in the orange group are associated with iron storage capacity, for example the Dps from *L. innocua* which is known as the mini-ferritin. Also in this group Dps involved in virulence of the pathogens are included, such as Dps from *S. aureus* and *S. pyogenes.*

The purple group can be divided into two sub-groups, the one that contains the proteins from *Lactococcus* sp., which bind to DNA but are not able to store iron, since they lack the conserved ligands that are involved in the ferroxidase activity and the hollow cavity is not negatively charged. The other two proteins are known as Dps-like proteins (*S. solfataricus* and *B. fragilis*), and present only the ferroxidase activity.

The yellow group clusters only three proteins. The common properties between them are their ferroxidase activity.

Dps from *E. coli*, which was the first protein to be identified from the Dps-family, has both ferroxidase activity and is able to interact and protect DNA, clusters in the green group with other Dps that have similar characteristics such as those from *M. smegmatis* and *S. coelicolor*. However this group is quite heterogeneous, since it contains Dps proteins from pathogenic organisms, such as *Y. pestis* and *S. enterica*, that have been associated with virulence. *Dr*Dps2 belongs to this group and presents identity of about 25% with the Dps from *M. smegmatis* and *K. radiotolerans*. On the other hand, *Dr*Dps1 shows to be unique among those that have been structurally characterized (Fig. 8.1).

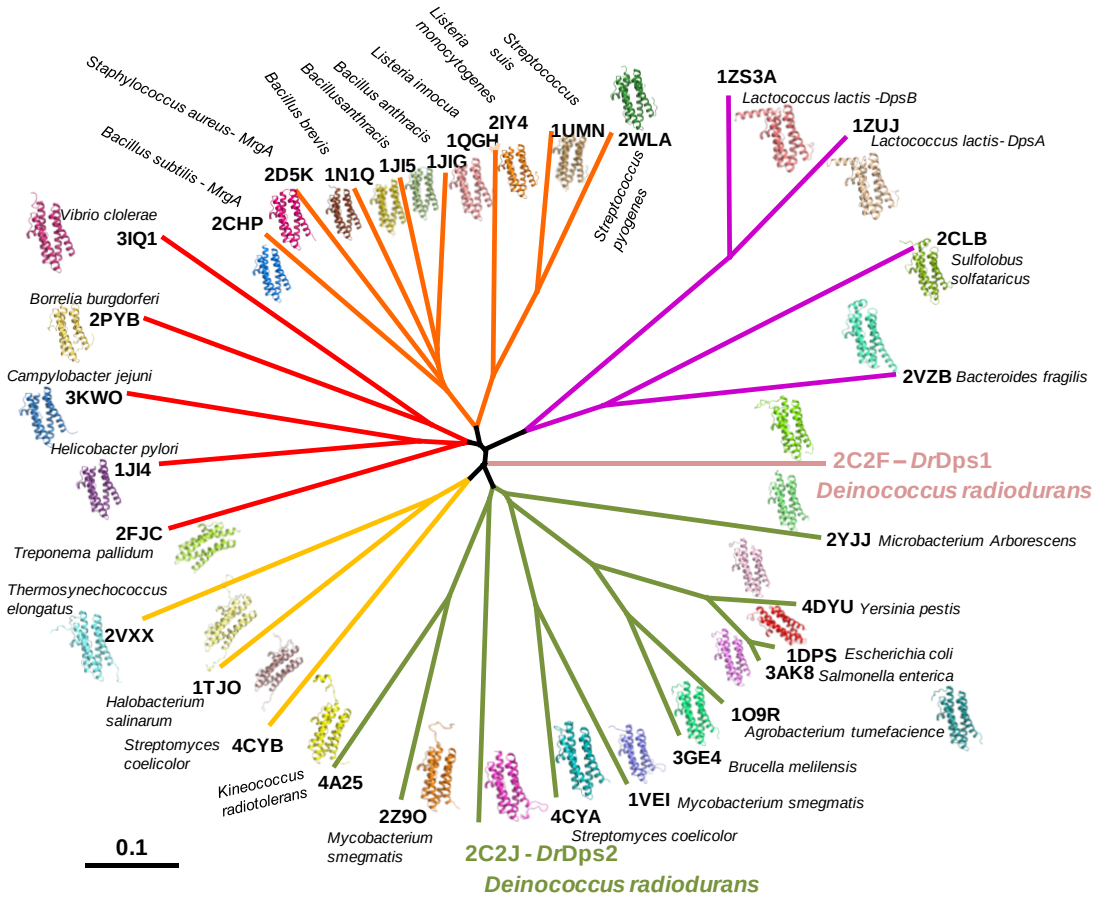

Figure 8.1 – Dendrogram based on the 3D structural superpositions of the available Dps structures. The structural alignment was constructed using Modeller (*388*), the dendogram was built using ClustalX 2.1 (*389*) and displayed with TreeView (*390*). PDB code 2C2F, in pink colour corresponds to *Dr*Dps1 while the PDB code 2C2J, in green colour corresponds to *Dr*Dps2.

8.3 Dps from *Deinococcus* species

D. radiodurans is so far known as the organism with the higher D_{10} value; D_{10}=16 (Table 8.1). In order to elucidate if the protection mechanism present in *D. radiodurans* in which *Dr*Dps are involved are common to other radiation resistant *Deinococcus* sp. or if is unique of this bacterium an analysis for the presence of homologous *Dr*Dps1 and *Dr*Dps2 was performed.

Table 8.1 – Dps in *Deinococcus* sp. Each *dps* of *Deinococcus* sp. was obtained using the data banks (NCB accession number) including a BLAST search of in-progress genomes. The alignment was constructed using ClustalX 2.1 (*389*)and the percentage of identity was calculated using the Genedoc program (*391*). Pink corresponds to Dps genes from *Deinococcus* sp. homologous to *Dr*Dps1 (gene *dr2263*) with values higher than 50 % identity, while the green correspond to Dps genes from *Deinococcus* sp. homologous with *Dr*Dps2 (gene *drb0092*). The blue corresponds to Dps from *Deinococcus* sp. with identity values lower than 50 % for both *Dr*Dps.

		Identity		D_{10} (kGy)	
***D. radiodurans* (Dr)**	**Dps gene**	***dr2263***	***drb0092***	**16**	Daly,2004 [1]
***D. radiodurans* (Dr)**	***dr2263***	--	14 %		
D. gobiensis **(Dgo)**	***Dgo_ca0262*** ***Dgo_ca0741***	60 % 15 %	11 % 84 %	15 kGy *	Yuan, 2009[2]
D. geothermalis **(Dgeo)**	***Dgeo_0281***	71 %	16 %	10	Daly,2004 [1]
D. phoenicis **(Deiph)**	***Deiph_dps***	69 %	16 %	> 8	Vaishampayan, 2014 [3]
D. grandis **(Deigr)**	***Deigr_1029***	55 %	12 %	10	Shashidhar, 2006 [4]
D. deserti **(Deide)**	***Deide_2120***	76 %	16 %	15 kGy *	Groot, 2005 [5]
D. maricopensis **(Deima)**	***Deima_3048***	55 %	16 %	> 10	Pukall, 2011 [6]
D. proteolyticus **(Deipr)**	***Deipr_0748***	63 %	14 %	15 kGy *	Copeland, 2012 [7]
D. swuensis **(Deis)**	***Deis_dps***	69 %	14 %	> 5	Kim, 2015 [8]
D.puniceus **(Deipu)**	***Deipu_dps***	71 %	15 %	12 kGy *	Lee, 2015 [9]
D. apachensis **(Dapa)**	***Dapa1_dps*** ***Dapa2_dps***	73 % 21 %	15 % 13 %	10 kGy *	Rainey, 2005 [10]
D. peraridilitoris **(Deipe)**	***Deipe_0824***	52 %	12 %	10 kGy *	Rainey, 2007 [11]
D. pimensis **(Deip)**	***Deipi1_dps*** ***Deip2_dps***	51 % 21 %	13 % 13 %	10 kGy *	Rainey, 2005 [10]
D. misasensis **(Dmis)**	***Dmis_dps***	20 %	19 %	2.3 kGy *	Asker, 2008 [12]

* For these organisms the D_{10} was not determined; instead it was observed that they are resistant to the specified value of ionizing radiation.

Sequence identifiers to Dps gene: *D. radiodurans* (*dr2263,* gi|15807254; *drb0092,* gi|6460837); *D. gobiensis* (*dgo_ca0262,* gi|379998999; *dgo_ca0741*, gi|504497049)*; D. geothermalis* (*dgeo_0281*, gi|499848695); *D. phoenicis* (*deiph_dps,* gi|736325612); *D. grandis* (*deigr_1029*, gi|960505187); *D. deserti* (*deide_2120,* gi|226319148); *D. maricopensis* (*deima_3048,* gi|503323519); *D. proteolyticus* (*deipr_0748,* gi|503379853); *D. swuensis*

(*deis_dps,* gi|746726275); *D. puniceus* (*deipu_dps*, gi|1028461677); *D. apachensis* (*dapa1_dps,* gi|518417535; *dapa2_dps*, gi|916362679; *D. peraridilitoris* (*deipe_0824,* gi|505047607); *D. pimensis* (*deip1_dps*, gi|653295748); *Deip2_dps* gi|653301829); *D. misasensis* (*dmis_dps*, gi|736315553).

From thirteen analyzed genomes that belong to *Deinococcus* sp. (Fig. 8.2) most contain a Dps homologous to *Dr*Dps1 sharing high identity of more than 50% (Fig. 8.2 and Table 8.1), suggesting that this Dps1-type protein is common in *Deinococcus* sp. and could contribute for the higher radiation resistant mechanism observed in these species. On the other hand, homologous proteins to *Dr*Dps2 are not present in most of the genomes analyzed (Fig. 8.2, Table 8.1). One exception is the bacterium *D. gobiensis* that contains both homologous protein to *Dr*Dps1 and *Dr*Dps2, with identities of 60% and 84%, respectively (Table 8.1). This suggests that the protection mechanism against oxidative stress, in *D. gobiensis* would be similar to that in *D. radiodurans* and the Dps proteins could contribute for this protection.

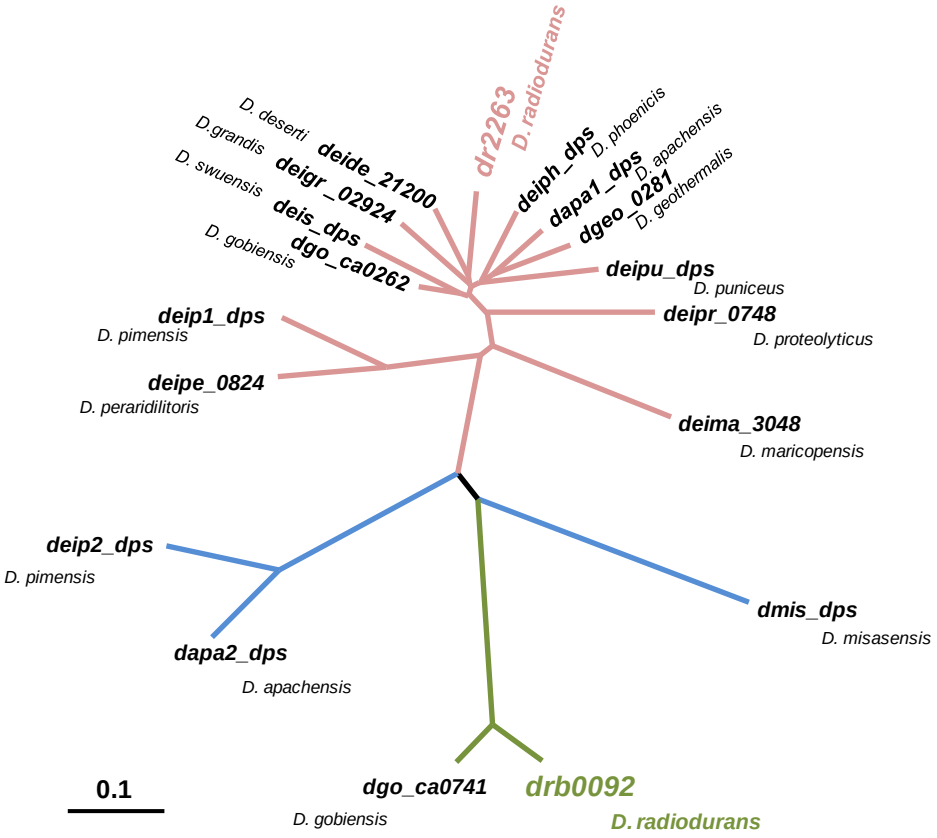

Figure 8.2 - Dendrogram of Dps from *Deinococcus* sp. displayed with TreeView. The sequence

alignment was constructed using ClustalX 2.1 (*389*) and the dendrogram is displayed with TreeView (*390*). The sequences were obtained using the data banks (NCIB accession number) including a BLAST search of in-progress genomes. The colour code is the same as in table 8.1.

This analysis together with the one presented in Fig. 8.1, shows that *Dr*Dps1 is unique to radiation resistant organisms, (Fig. 8.3) from *Deinococcus* sp. while *Dr*Dps2 presents identity with other typical Dps, for instance Dps from *E. coli* and *K. radiotolerans* (Fig. 8.3). This suggests that the *Dr*Dps1 protein could be one common key for high radiation resistance observed in *Deinococcus* sp., while *Dr*Dps2 could help in protection as a metal storage protein.

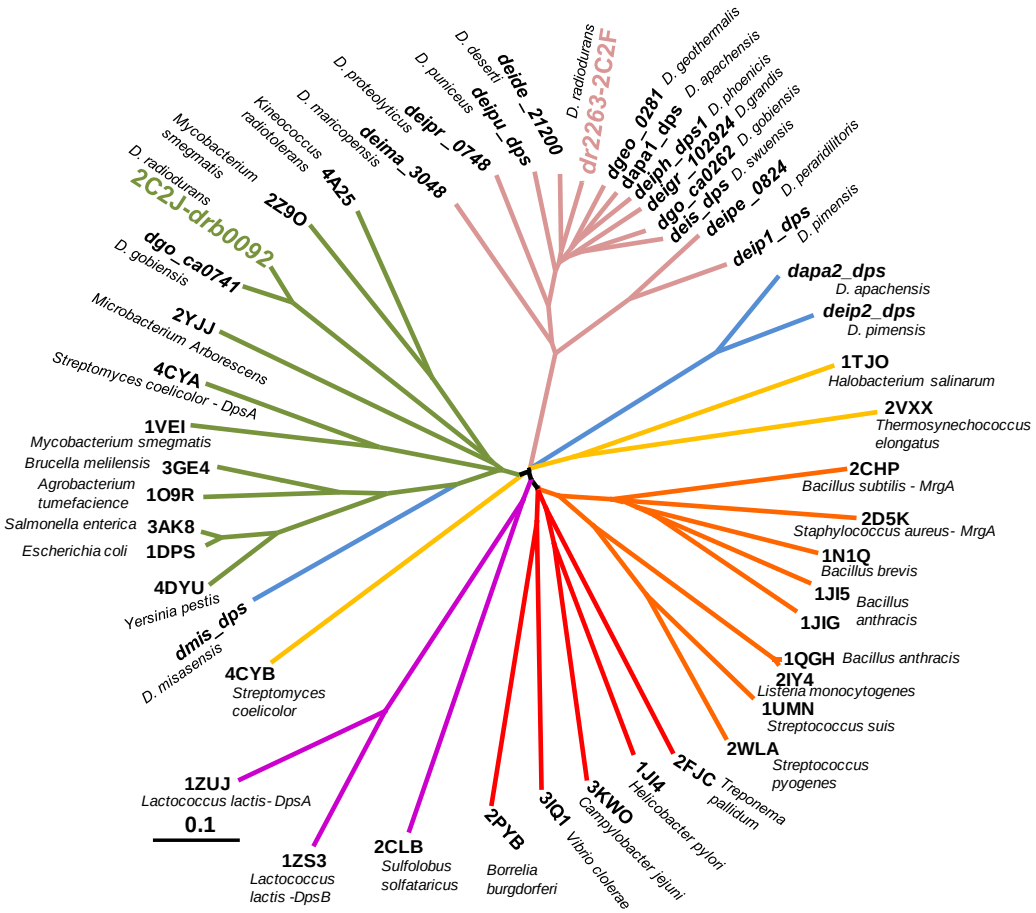

Figure 8.3 - Dendrogram of Dps from *Deinococcus* sp. and Dps in which the crystal structures have been determined. The dendrogram was constructed using profile alignment in

ClustalX 2.1 (*389*) of the structural alignment presented in Fig. 8.1 with the sequence alignment of Dps from *Deinococcus* sp. presented in Fig. 8.2. The dendrogram is displayed with TreeView (*390*). The colour code is the same as in Fig. 8.1 and Fig. 8.2.

8.4 *Dr*Dps and its oligomeric states

Crystal structures of Dps family members show that these proteins form dodecamers in the crystal lattice, although in solution other oligomeric states have been described such as dimers, trimers and hexamers. However, the function of each oligomer has not been extensively studied. For example, it is known that *M. smegmatis* contains two Dps, and it was demonstrated that in *in vitro conditions* Dps1 has two oligomeric states, trimer and dodecamer. The dodecamer form was proposed to bind/condense DNA, incorporate iron, and protect DNA against ROS and DNase, while the trimer form showed a ferroxidase activity using O_2 as oxidant, similar to the ferroxidase activity found in the ferritin family (*243*). However, the physiological relevance of the different oligomeric states has not been addressed.

The bacterium S*. coelicolor* contains three Dps: DpsA, DpsB and DpsC. DpsA changes its oligomeric state between, dimer, hexamer and dodecamer while DpsB appears only as a dimer. DpsA as hexamer and dodecamer stores iron, however no function is known for the dimer form of DpsA and DpsB. Although these proteins *in vivo* conditions are proposed to be involved in nucleoid condensation and pre-spore compartment formation (*244, 293*), the different oligomeric states have not been associated with any of these biological functions.

The two Dps from *D. radiodurans* have distinct behaviors in solution (Chapter V and VII). *Dr*Dps1 changes its oligomeric state between low molecular mass forms, namely dimer and trimer, to a high-molecular mass dodecamer form. These oligomeric states were identified *in vitro and in vivo* conditions. *Dr*Dps1 dimeric form was detected in cell extracts obtained under control conditions, and being associated with DNA. Addition of manganese or methyl viologen induced a change in the oligomeric state of *Dr*Dps1 and the trimeric form is more pronounced than the dimeric form. *Dr*Dps1 dodecamer state was obtained by iron addition to the cell growth. These different oligomeric states are proposed to be related with distinct functions of *Dr*Dps1 inside the cell upon stress response (Section 8.5).

*Dr*Dps2 behaves as a stable dodecamer under all tested *in vitro* and *in vivo* conditions. However, it is quite interesting that this protein contains a signal peptide, which has not been reported until now for any other Dps protein (*206*). Although the function of this signal peptide has not been clarified, the data now obtained from analysis of cell extracts, detects *Dr*Dps2 in both soluble and membrane fractions, but showing different molecular masses. The form present in the membrane (*Dr*Dps2$_M$) has a higher molecular mass, and could correspond to the full length protein (with N-terminal tail) while the form present in the soluble fraction (*Dr*Dps2$_C$) has a lower molecular mass and was suggested to correspond to the *Dr*Dps2 without N-terminal tail (Chapter VI and VII). Thus, *Dr*Dps2 in *D. radiodurans* cells is detected in two forms, associated with the membrane in which the signal peptide would be involved and a soluble form present in the cytosol.

8.5 Protection mechanism *in D. radiodurans*

8.5.1 Regulation by post-translational modification

The protection mechanisms of *D. radiodurans* which are associated with manganese are regulated by post-translational modifications (Chapter VII). Addition of external compounds to the cell growth that induce an oxidative stress condition, namely methyl viologen, leads to a physiological distribution of elements such as phosphate, calcium or manganese, which are released from the granules to the cytosol and membrane region. The cellular distribution of calcium could promote a signaling pathway cascade, activating other proteins such as kinases, which are then associated with the phosphorylation of different targets (*42*). One of those is *Dr*Dps1 which is phosphorylated as a trimer (Chapter VII).

The knowledge about kinases is not very extensive in *D. radiodurans*. The most studied kinase is the restricted to radiation pyrroloquinoline quinone (PQQ) inducible protein kinase (RqkA) (*dr2518*). This is a membrane protein, which has a kinase domain similar to eukaryotic type serine/threonine protein kinases (eSTPK) at the N-terminus and at the C-terminus contains a putative PQQ interacting domain. This protein responds to oxidative stress and DNA damage, and it has been shown to phosphorylate two proteins involved in DNA repair: PprA and RecA (*392-393*). Since RqkA has both functional and structural domains similar to eSTPK, it is suggested that

the phosphorylation site motif of recognition is similar to eSTPKs. Besides the proteins mentioned above (PprA, RecA), other proteins from *D. radiodurans* have putative phosphomotifs for RqkA (*392, 394*). One of these identified proteins was *Dr*Dps1, and the putative phosphomotif is D_{145}AR**T**QVADLV (*392*), in which Thr_{148} is localized in helix C, accessible from the external surface.

Furthermore *Dr*Dps1 has a long N-terminal tail that is rich in serine and threonine amino acids residues (Fig. 8.4, green amino acids). These residues are close in the sequence to the positively charged residues that are proposed to be involved with the negatively charged phosphate backbone of the DNA (Fig. 8.4, blue amino acids): **Thr_2**, Lys_3, Lys_4, **Ser_5**, **Thr_6**, Lys_7, **Ser_8**, X_{9-11}, **Ser_{12}**, Lys_{13}, **Thr_{14}**, Lys_{15}, Lys_{16}, **Ser_{17}**, X_{18-21}, **Thr_{22}**, X_{23-27}, Arg_{28} (*270-271, 351*).

An analysis of the predicted phosphorylation sites in *Dr*Dps1 protein using computational prediction of kinase-specific phosphorylation sites (GPS 2.0 software or Net-Phos 3.1) showed that these serines and threonines are the amino acids residues with a high score for phosphorylation. However a few serines, threonines and one tyrosine residues also showed higher scores, namely Thr_{60}, Ser_{108}, Ser_{122}, Tyr_{133}, Ser_{134}, Thr_{142}, and Ser_{168} (Fig. 8.4, green colour). Four of these amino acids residues, Ser_{122}, Tyr_{133}, Ser_{134}, Thr_{142}, are located in loop BC close to Arg_{132} which is also proposed to be involved in DNA binding (Fig. 8.4, yellow colour) (*270-271*). This suggests a link between the interaction with DNA and the phosphorylation. Under certain conditions the chemical modification by phosphorylation would occur, and the interaction between *Dr*Dps1 and DNA is decreased. Consequently, this induces a conformational change at structural level of *Dr*Dps1, from dimer to trimer, altering then its localization and function which will be discussed below.

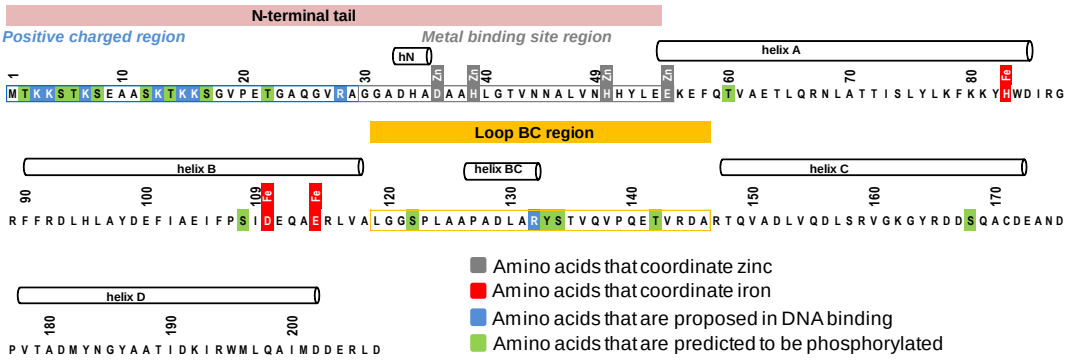

Figure 8.4 - *Dr*Dps1 primary and secondary protein sequence. Amino acids with high score to

phosphorylation are shown in green colour. Most of these residues are present in the positively charged region from the N-terminal tail (pink colour), and from loop BC region (yellow colour).

8.5.2 *Dr*Dps1 as a Mn^{2+}-dependent metal sensor protein

*Dr*Dps1 contains at the N-terminal tail a metal site with the binding motif **Asp**$_{36}$X$_2$**His**$_{39}$X$_{10}$**His**$_{50}$X$_4$**Glu**$_{55}$. This metal site has been proposed to be essential for dodecamer oligomerization and DNA interaction [11, 24]. In fact, it has been described that the metal site assists the interaction between *Dr*Dps1 and DNA, through the positively charged residues present at the N-terminal by inducing a proper orientation of the N-terminal (*203, 395*). Different metals, such as zinc and cobalt have been observed to bind to this site [11-12], but the nature of this metal site needs to be further investigated.

This N-terminal metal site is structurally homologous to metal sites present in other proteins, namely the metalloregulatory transcriptional repressors belonging to the SmtB family, where the zinc site is a metal sensor (*396-397*). Also, it is interesting to note that solute-binding proteins, SitA, PsaA, and MntC present structurally similar metal sites. These proteins are components of ABC membrane transporters that play a crucial role in metal ion uptake, selecting the metal required by the cell. Both zinc and manganese metals were observed to bind the metal site in the SitA protein (PDB codes: 3ZTT and 1PSZ, **His**$_{64}$X$_{73}$**His**$_{137}$X$_{66}$**Glu**$_{203}$X$_{75}$**Asp**$_{278}$) (*398*). However, zinc binding is irreversible, while manganese binding is reversible, suggesting that in *in vivo* this protein regulates manganese levels instead of zinc (*399*). Two other examples containing similar metal sites but with manganese, are proteins involved on the regulation of manganese, namely PsaA (PDB code: 4OXQ and 4OXR, **His**$_{66}$X$_{73}$**His**$_{139}$X$_{66}$**Glu**$_{205}$X$_{75}$**Asp**$_{280}$) and MntC (PDB code: 4K3V, **His**$_{50}$X$_{73}$**His**$_{123}$X$_{66}$**Glu**$_{189}$X$_{75}$**Asp**$_{264}$) (*400-402*).

Taking in consideration the structural homology between these metal centres, we propose that in *in vivo* the metal site at the N-terminal tail of *Dr*Dps1 may function as a Mn^{2+}-dependent metal sensor protein regulating the intracellular manganese level in cytosol and granules, responding to stress conditions.

8.5.3 The role of *Dr*Dps in metals homeostasis

It has been observed that Mn^{2+} complexed with orthophosphate or pyrophosphate has the ability to scavenge superoxide anion, $O_2^{\bullet -}$ (Chapter II, reactions 2.13-2.16) (*71, 75-76*).

In *D. radiodurans* cells it has been demonstrated that intracellular Mn^{2+} in the exponential phase, under control and gamma radiation conditions binds to phosphate groups (90-95 %), including 52 % of fructose-1,6-biphosphate, 24 % of nucleic acids and 20 % of other phosphates such as orthophosphate, pyrophosphate and polyphosphate (*374*). Furthermore, these complexes with manganese and small molecules have been proposed to be the main protection mechanism occurring in *D. radiodurans.* However one of the questions that remains to be answered is how does regulation of this protection mechanism occurs.

The work presented here correlates both *Dr*Dps with metal homeostasis in *D. radiodurans* and the protection mechanism against ROS, associated with intracellular manganese and phosphate. The evidence that both *Dr*Dps are essential for manganese homeostasis is demonstrated by X-ray fluorescence imaging results. In the knockouts mutants (Δ*dps1,* Δ*dps2* and Δ*dps1*Δ*dps2*), the manganese and phosphate storage into phosphate granules are strongly compromised, and most of the elements are dispersed in the cell instead of being stored in granules as occurs in the wild-type strain (Fig. 8.5).

Furthermore, our results showed that manganese homeostasis is regulated by a process that involves *Dr*Dps1 as dimer and trimer, regulating the *Dr*Dps2 levels in the cytosolic (*Dr*Dps2$_C$) and membrane (*Dr*Dps2$_M$) regions. *Dr*Dps1 dimeric form is associated with DNA, and is regulated by post-translation phosphorylation modification leading to the trimeric form which was observed to be distributed in the cytosol and co-localized with the phosphate granules. Although the function of the dimeric form is not yet understood, the trimeric form affects the concentration of Mn^{2+}-Pi complexes present in the granules, regulating a process that leads to an increase of *Dr*Dps2$_C$ form (Fig. 8.5, A).

*Dr*Dps2$_C$ is suggested to incorporate Mn^{2+}-Pi complexes, since the molecular mass of this form is slightly higher when extra manganese was added. Then this protein would deliver the complexes to the granules, contributing for the storage of the complexes. Under oxidative stress conditions the Mn^{2+}-Pi complexes would be

incorporated into *Dr*Dps2$_C$ and its trafficking occurs from the granules to the cytosol, and membrane region (Fig. 8.5, A).

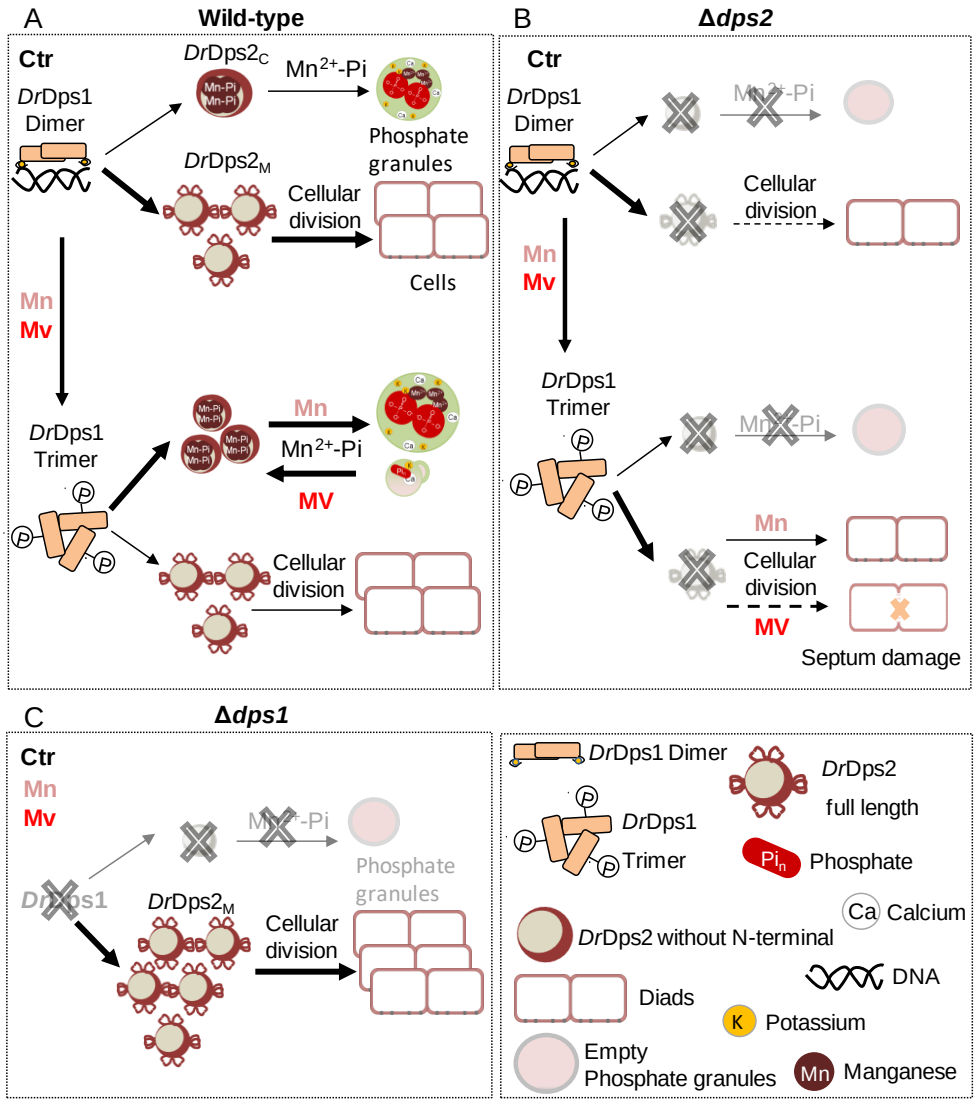

Figure 8.5 - Schematic representation of the possible role for both *Dr*Dps from *D. radiodurans* in manganese-phosphate (Mn^{2+}-Pi) complexes homeostasis and in cell division. **(A)** Wild-type cell strain, in control (Ctr), manganese (Mn) and methyl viologen (Mv) conditions. Under control conditions, *Dr*Dps1 dimer is bound to DNA while under manganese or methyl viologen conditions it changes to trimer. *Dr*Dps2 appears as a cytosolic form (*Dr*Dps2$_C$), without N-terminals tails, but most of *Dr*Dps2 is present in the membrane, attached through N-terminal tails (*Dr*Dps2$_M$). *Dr*Dps2$_C$ form is involved in Mn^{2+}-Pi complexes trafficking from membrane to granules, under control and manganese conditions, or from granules to cytosol, and membrane region under methyl viologen conditions, where the granules appear with less amount of Mn^{2+}-Pi complexes or

empty. *Dr*Dps2$_M$ form affects the cell division. **(B)** Δ*dps2* cell strain, the granules are Mn^{2+}-Pi complexes empty and the septum region is damaged. **(C)** Δ*dps1* cell strain, *Dr*Dps2$_C$ form depends on *Dr*Dps1 and the granules are empty while *Dr*Dps2$_M$ form is involved in the increase of the cell division.

*Dr*Dps2$_M$ is a predominant form when *Dr*Dps1 is a dimer and becomes even the only form present in the absence of *Dr*Dps1. The results on the knockouts mutants showed that *Dr*Dps2$_M$ form affects cell division, protecting the septum formation in stress conditions. Under control conditions, the initial growth rate diminished 2-fold for the Δ*dps2* and Δ*dps1*Δ*dps2* and under stress conditions the septum region appears damaged in these knockouts mutants (Fig. 8.5, B).

On the other hand in the *dps1* knockouts mutants the initial rate growth is 2-times faster and addition of methyl viologen does not affect the growth, suggesting that *Dr*Dps2 present only in the membrane efficiently protects it (Fig. 8.5, C). In addition in this knockout mutant strain the Mn^{2+}-Pi complexes are homogenously distributed in the cell and available for protein protection against the degradation promoted by ROS.

The dodecamer form of *Dr*Dps1 detected in cell extracts after addition of iron to the cell growth, suggests that this protein may also function as a typical iron storage protein (Fig. 8.6, A). Moreover it was observed that the dodecamer formation is dependent on *Dr*Dps2, since in the *dps2* knockout mutant the formation of *Dr*Dps1 dodecamer does not occur (Fig. 8.6, B). These results suggest that *Dr*Dps2$_C$ form is involved in metal trafficking from the membrane to the cytosolic region, where iron can then be delivered to and stored by *Dr*Dps1 (Fig. 8.6, A).

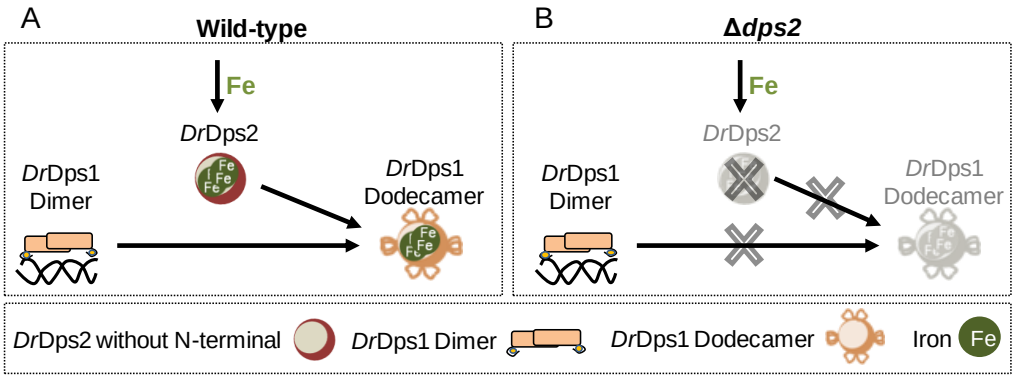

Figure 8.6 – Role of both *Dr*Dps from *D. radiodurans* in iron homeostasis. **(A)** Wild-type cell strain, under control conditions *Dr*Dps1 is bound to DNA as a dimer while under iron conditions it changes to dodecamer. The dodecamer formation is dependent on *Dr*Dps2 cytosolic form that can assist the trafficking of iron from the membrane region to the cytosol and then iron is

delivered and incorporated by *Dr*Dps1 as dodecamer. **(B)** Δ*dps2* cell strain, *Dr*Dps1 dodecamer formation is dependent on *Dr*Dps2$_C$.

8.5.4 The function of *Dr*Dps in the oxidative stress protection mechanism of *D. radiodurans*

Based on all the studies presented in this thesis we propose a model for the protection response mechanism of *D. radiodurans* submitted to a burst of oxidative stress, involving both *Dr*Dps and the small Mn^{2+}-Pi complexes.

Under control conditions, elements, such as calcium, manganese and phosphate are stored in the granules (Fig. 8.7, A). X-ray fluorescence imaging of *D. radiodurans* cells shows that manganese and phosphate are co-localized, suggesting that this two elements form Mn^{2+}-Pi complexes. *Dr*Dps1 is mostly detected in the form of a dimer and is associated with DNA while *Dr*Dps2 is predominately associated with the membrane in the septum region assisting the cell division but there is a small part of *Dr*Dps2 observed in the cytosol (Fig. 8.7, A).

Under an external stimulus that generates a condition of oxidative stress to the cells that in our studies was induced by methyl viologen, the response mechanism involves the delocalization of metals from the granules, namely the distribution of calcium and Mn^{2+}-Pi complexes (Fig. 8.7, B).

Calcium release can be associated with the activation of signaling pathways involving kinases, which could be important for the activation of post-translational-modifications, such as the phosphorylation of *Dr*Dps1, changing its oligomeric state from dimer to trimer. Its localization is altered from the nucleoid region to the cytosol and phosphate granules region. Under these conditions, Mn^{2+}-Pi complexes are released from the granules (Fig. 8.7, B, Step 1).

As mentioned above, as part of the dual function of *Dr*Dps2, *Dr*Dps2$_M$ is cleaved in the N-terminal tails by a mechanism which involves indirectly *Dr*Dps1, them *Dr*Dps2$_C$ incorporate Mn^{2+}-Pi complexes and distribute these complexes through the cytosol, septum and membrane regions (Fig. 8.7, B, Steps 2.1, 2.2, and 2.3). The release to the membrane and septum regions can be assisted via Mn-transporters such as MntE pump *(dr1236)*, responsible for manganese efflux (*213*) or by *Dr*Dps2$_M$ (Fig. 8.7, B, Steps 2.4 and 2.5). The Mn^{2+}-Pi complexes released and distributed in the cell are involved in the detoxification of ROS produced during the oxidative stress,

leading to the protection proteins, such as *Dr*Dps2$_M$. In this case *Dr*Dps2$_M$ that remains in the membrane can contribute to the cell division by protecting the septum during cell division.

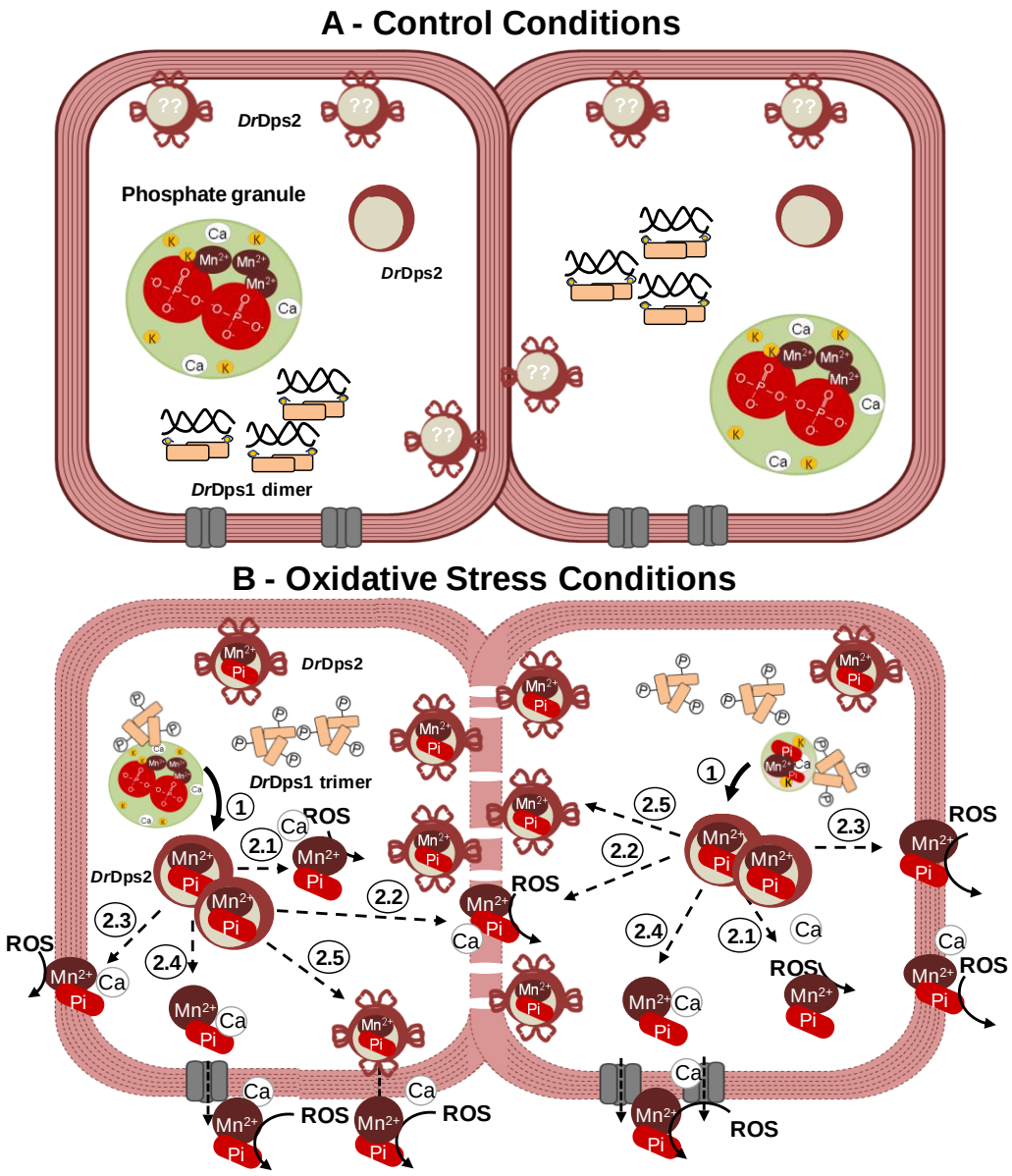

Figure 8.7 – Proposed model for the protection mechanism of D. radiodurans, under oxidative stress conditions, linking DrDps1 and DrDps2 cellular function with manganese homeostasis. (A) Under control conditions, mostly DrDps2 is attached to the membrane through the N-terminal tail, but also in the cytosol, without N-terminal tails. DrDps1 is bound to DNA. Phosphate (Pi), manganese (Mn2+), potassium (K) and calcium (Ca) are store in a granule

which is highly rich in these elements. (B) Under oxidative stress conditions, DrDps1 is phosphorylated and changes its oligomeric state from dimer to trimer and the translocation occurs to the granules and cytosol. DrDps1 as a trimer regulates manganese and phosphate release as Mn2+-Pi complexes (Step1) and DrDps2 would incorporate Mn2+-Pi complexes which are delivered to the cytosol (Step 2.1), septum (Step 2.2) and membrane regions (step 2.3). The release of the Mn2+-Pi complexes to the membrane and septum regions can be assisted via Mn-transporters (Step 2.4) or DrDps2 (Step 2.5), to be used as a first protection barrier against ROS.

8.6 Conclusion

The current thesis aimed to understand the mechanisms of protection against oxidative stress of the radiation resistant bacterium *Deinococcus radiodurans*. The focus of our work was to study the two DNA binding proteins from starved conditions: *Dr*Dps1 (*dr2263*) and *Dr*Dps2 (*drb0092*).

These two proteins are structurally conserved with other Dps, being composed of twelve monomers in the crystal form, and each monomer presents a four-helix bundle structure. Besides this structural conservation, a comparison of all the Dps crystal structures shows that *Dr*Dps1 is unique among the known Dps structures, while *Dr*Dps2 presents some 25 % structural identity with Dps from *M. smegmatis* and *K. radiotolerans*. However a survey for Dps-like sequences in *Deinococcus* sp. known so far reveals that *Dr*Dps1 is mostly conserved (93 %) while *Dr*Dps2 is only present in 14% among *Deinococcus* sp. analysed. This suggests that most *Deinococcus* sp. have a similar mechanism protection against radiation, which involves *Dr*Dps1.

With the work developed during this thesis, we proposed a model for the role of both *Dr*Dps and its association with the homeostasis of Mn^{2+}-Pi complexes contributing to the intracellular protection against oxidative stress.

Under control conditions *Dr*Dps1 is in its dimeric form associated with DNA, while *Dr*Dps2 is mostly associated with the membrane and manganese is stored in the phosphate granules together with other ions namely, phosphate and calcium. After stress addition it is initiated a cascade of signals in which the different elements are released from the granules. Under these conditions, the function of *Dr*Dps1 is regulated by post-translational modification, namely phosphorylation, inducing a change in the oligomeric form from dimer to trimer coupled with a change in its cellular localization. *Dr*Dps1 in trimeric form regulates the intracellular distribution of the Mn^{2+}-

Pi complexes, so that they will be used for the detoxification of reactive oxygen species protecting the cell against the degradation promoted by these species.

*Dr*Dps2 has a dual function: when present in the cytosol, lacks the N-terminal tails, functioning as a typical metal storage protein. In fact; it can assist the incorporation of Mn^{2+}-Pi complexes and subsequently distribute these complexes, from the granules to the cytosol and membrane region. The protein associated with the membrane through its N-terminal tail helps cell division, but is also suggested to be essential to confer more protection being involved in the Mn^{2+}-phosphate complexes transport to the membrane, forming the first protection barrier against oxidative stress with ability to scavenge ROS, protecting then the cell.

Nevertheless it is important to note that other protection mechanisms from *D. radiodurans* should not be ignored, since they also contribute for the cell protection preserving the proteins from the effects of oxidation. For instance, enzymatic ROS scavenging systems such as catalase and MnSOD. These proteins are involved in cell protection mainly in the stationary phase, where the catalase activity levels increase and a new isoform of MnSOD appears depending on the availability of manganese. Therefore, all these factors work synergistically contributing for a common protection mechanism against oxidative stress.

Although we have addressed the effect of methyl viologen to promote a condition of oxidative stress, the *Dr*Dps dependent cellular mechanisms involved in the protection of *D. radiodurans* against these oxidative stress conditions can be ultimately extrapolated to the resistance mechanisms against radiation.

In conclusion, the current work contributes for unrevealing the cellular molecular mechanisms involved in the protection of *D. radiodurans* after exposure to radiation.

9 References

1. Nyska, A., and Kohen, R. (2002) Oxidation of biological systems: Oxidative stress phenomena, antioxidants, redox reactions, and methods for their quantification, *Toxicol Pathol 30*, 620-650.

2. Schieber, M., and Chandel, N. S. (2014) ROS Function in Redox Signaling and Oxidative Stress, *Current Biology 24*, R453-R462.

3. Ray, P. D., Huang, B. W., and Tsuji, Y. (2012) Reactive oxygen species (ROS) homeostasis and redox regulation in cellular signaling, *Cell Signal 24*, 981-990.

4. Ayala, A., Munoz, M. F., and Arguelles, S. (2014) Lipid peroxidation: production, metabolism, and signaling mechanisms of malondialdehyde and 4-hydroxy-2-nonenal, *Oxid Med Cell Longev 2014*, 360438.

5. Cabiscol, E., Tamarit, J., and Ros, J. (2000) Oxidative stress in bacteria and protein damage by reactive oxygen species, *Int Microbiol 3*, 3-8.

6. Dixon, S. J., and Stockwell, B. R. (2014) The role of iron and reactive oxygen species in cell death, *Nat Chem Biol 10*, 9-17.

7. Auten, R. L., and Davis, J. M. (2009) Oxygen toxicity and reactive oxygen species: the devil is in the details, *Pediatr Res 66*, 121-127.

8. Lee, J., Koo, N., and Min, D. B. (2004) Reactive Oxygen Species, Aging, and Antioxidative Nutraceuticals, *Compr Rev Food Sci Food Saf 3*, 21-33.

9. Valentine, J. S., Wertz, D. L., Lyons, T. J., Liou, L. L., Goto, J. J., and Gralla, E. B. (1998) The dark side of dioxygen biochemistry, *Curr Opin Chem Biol 2*, 253-262.

10. Keyer, K., Gort, A. S., and Imlay, J. A. (1995) Superoxide and the production of oxidative DNA damage, *J Bacteriol 177*, 6782-6790.

11. Imlay, J. A. (2003) Pathways of oxidative damage, *Annu Rev Microbiol 57*, 395-418.

12. Branchaud, B. P. (1999) Free radicals as a result of dioxygen metabolism, *Met Ions Biol Syst 36*, 79-102.

13. Davies, M. J. (2003) Singlet oxygen-mediated damage to proteins and its consequences, *Biochem Biophys Res Commun 305*, 761-770.

14. D'Autreaux, B., and Toledano, M. B. (2007) ROS as signalling molecules: mechanisms that generate specificity in ROS homeostasis, *Nat Rev Mol Cell Biol 8*, 813-824.

15. Sharma, P., Jha, A. B., Dubey, R. S., and Pessarakli, M. (2012) Reactive Oxygen Species, Oxidative Damage, and Antioxidative Defense Mechanism in Plants under Stressful Conditions, *J Botany 2012*, 26.

16. Landrum, J. T. (2013) Reactive Oxygen and Nitrogen Species in Biological Systems: Reactions and Regulation by Carotenoids, *Humana Press Carotenoids and Human Health (Book)*, 57-102.

17. McCord, J., Crapo, J., and Fridovich, I. (1977) Superoxide dismutase assays: A review of methodology. Superoxide and superoxide dismutases, *Academic London 1*, 11-17.

18. Sawyer, D. T. (1991) Oxygen Chemistry, *Oxford University Press New York*.

19. Dickinson, B. C., and Chang, C. J. (2011) Chemistry and biology of reactive oxygen species in signaling or stress responses, *Nat Chem Biol 7*, 504-511.

20. Halliwell, B., Gutteridge, J. M. C. . (1989) Free Radicals in Biology and Medicine, *Oxford University Press, Oxford, UK*.

21. Kehrer, J. P. (2000) The Haber-Weiss reaction and mechanisms of toxicity, *Toxicology 149*, 43-50.

22. Crichton, R. R. (2008) Biological inorganic chemistry, An introduction, *Elsevier*.

23. Romão, C. V., Vicente, J. B., Borges, P. T., Frazão, C., and Teixeira, M. (2016) The dual function of flavodiiron proteins: oxygen and/or nitric oxide reductases, *J Biol Inorg Chem 21*, 39-52.

24. Zamocky, M., Furtmuller, P. G., and Obinger, C. (2008) Evolution of catalases from bacteria to humans, *Antioxid Redox Signal 10*, 1527-1548.

25. Fischer, W. W., Hemp, J., and Valentine, J. S. (2016) How did life survive Earth's great oxygenation?, *Curr Opin Chem Biol 31*, 166-178.

26. Gray, M. J., and Jakob, U. (2015) Oxidative stress protection by polyphosphate-new roles for an old player, *Curr Opin Microbiol 24*, 1-6.

27. Fraústo da Silva, J. J. R., Silva, J. A. L.,. (2011) Os elementos químicos e a vida, *IST Press*.

28. Fraústo da Silva, J. J. R., Williams, R. J. P. (1991) The biological chemistry of the elements, *Oxford University press*.

29. Riordan, J. F. (1977) The role of metals in enzyme activity, *Ann Clin Lab Sci 7*, 119-129.

30. Srivastava, P., and Kowshik, M. (2013) Mechanisms of metal resistance and homeostasis in haloarchaea, *Archaea 2013*, 732864.

31. Averill, B. A., Eldredge, Patricia. (2012) Principles of general chemistry V.1.0, *Books*, 1-3033.

32. Bruins, M. R., Kapil, S., and Oehme, F. W. (2000) Microbial resistance to metals in the environment, *Ecotox Environ Safe 45*, 198-207.

33. Nies, D. H. (1999) Microbial heavy-metal resistance, *Appl Microbiol Biotechnol 51*, 730-750.

34. Lisher, J. P., and Giedroc, D. P. (2013) Manganese acquisition and homeostasis at the host-pathogen interface, *Front Cell Infect Mi 3*, 1-15.

35. Zhen, M. F., E. Jacobsen; David, P. Giedroc. (2009) Metal Transporters and Metal Sensors: How Coordination Chemistry Controls Bacterial Metal Homeostasis, *Chem Rev 109(10)*, 4644–4681.

36. Palmer, B. F. (2015) Regulation of Potassium Homeostasis, *Clin J Am Soc Nephrol 10*, 1050-1060.

37. Epstein, R. J. (2003) Human Molecular Biology An Introduction to the Molecular Basis of Health and Disease, *Cambridge, University Press*.

38. Weiden, P. L., Epstein, W., and Schultz, S. G. (1967) Cation transport in *Escherichia coli*. VII - Potassium requirement for phosphate uptake, *J Gen Physiol 50*, 1641-1661.

39. Damadian, R. (1967) Abnormal phosphorus metabolism in a potassium transport mutant of *Escherichia coli*, *Biochim Biophys Acta 135*, 378-380.

40. Gilliland, G. L. T., Alexey (2006) Structural Calcium (Trypsin, Subtilisin), *Handbook Metalloproteins Part 9. Calcium*, 1-13.

41. Bertini, I., Gray, Harry, Stiefel, Edward I., Valentine, Joan (2007) Biological Inorganic Chemistry: Structure and Reactivity, *University Science Books*, 1-739.

42. Clapham, D. E. (2007) Calcium signaling, *Cell 131*, 1047-1058.

43. Herbaud, M. L., Guiseppi, A., Denizot, F., Haiech, J., and Kilhoffer, M. C. (1998) Calcium signalling in *Bacillus subtilis*, *Bba-Mol Cell Res 1448*, 212-226.

44. Dominguez, D. C. (2004) Calcium signalling in bacteria, *Molecular Microbiology 54*, 291-297.

45. Torrecilla, I., Leganes, F., Bonilla, I., and Fernandez-Pinas, E. (2001) Calcium transients in response to salinity and osmotic stress in the nitrogen-fixing cyanobacterium *Anabaena* sp PCC7120, expressing cytosolic apoaequorin, *Plant Cell Environ 24*, 641-648.

46. Torrecilla, I., Leganes, F., Bonilla, I., and Fernandez-Pinas, F. (2000) Use of recombinant aequorin to study calcium homeostasis and monitor calcium transients in response to heat and cold shock in cyanobacterial, *Plant Physiol 123*, 161-175.

47. Jones, H. E., Holland, I. B., Baker, H. L., and Campbell, A. K. (1999) Slow changes in cytosolic free Ca^{2+} in *Escherichia coli* highlight two putative influx mechanisms in response to changes in extracellular calcium, *Cell Calcium 25*, 265-274.

48. Williams, R. J. P. (1987) The Biochemistry of Zinc, *Polyhedron 6*, 61-69.

49. McCall, K. A., Huang, C. C., and Fierke, C. A. (2000) Function and mechanism of zinc metalloenzymes, *J Nutr 130*, 1437s-1446s.

50. Chang, R. (2005) Physical Chemistry for the Biosciences, *University Science Books*, 1-677.

51. Roux, C., Bhatt, F., Foret, J., de Courcy, B., Gresh, N., Piquemal, J. P., Jeffery, C. J., and Salmon, L. (2011) The reaction mechanism of type I phosphomannose isomerases: new information from inhibition and polarizable molecular mechanics studies, *Proteins 79*, 203-220.

52. Landro, J. A., and Schimmel, P. (1993) Metal-binding site in a class I tRNA synthetase localized to a cysteine cluster inserted into nucleotide-binding fold, *P Natl Acad Sci USA 90*, 2261-2265.

53. Ma, L., Tibbitts, T. T., and Kantrowitz, E. R. (1995) *Escherichia coli* Alkaline-Phosphatase X-Ray Structural Studies of a Mutant Enzyme (His-412-]Asn) at One of the Catalytically Important Zinc-Binding Sites, *Protein Sci 4*, 1498-1506.

54. Vallee, B. L., and Auld, D. S. (1993) Cocatalytic zinc motifs in enzyme catalysis, *P Natl Acad Sci USA 90*, 2715-2718.

55. Laity, J. H., Lee, B. M., and Wright, P. E. (2001) Zinc finger proteins: new insights into structural and functional diversity, *Curr Opin Struc Biol 11*, 39-46.

56. Rakhit, R., and Chakrabartty, A. (2006) Structure, folding, and misfolding of Cu,Zn superoxide dismutase in amyotrophic lateral sclerosis, *Biochim Biophys Acta 1762*, 1025-1037.

57. Dolphin, D., Forman, A., Borg, D. C., Fajer, J., and Felton, R. H. (1971) Compounds I of Catalase and Horse Radish Peroxidase - Pi-Cation Radicals, *P Natl Acad Sci USA 68*, 614-&.

58. Groves, J. T., Haushalter, R. C., Nakamura, M., Nemo, T. E., and Evans, B. J. (1981) High-Valent Iron-Porphyrin Complexes Related to Peroxidase and Cytochrome-P-450, *J Am Chem Soc 103*, 2884-2886.

59. Miller, A. F. (2012) Superoxide dismutases: ancient enzymes and new insights, *FEBS Lett 586*, 585-595.

60. Andrews, S. C., Robinson, A. K., and Rodriguez-Quinones, F. (2003) Bacterial iron homeostasis, *FEMS Microbiol Rev 27*, 215-237.

61. Cammack, R., and Cooper, C. E. (1993) Electron paramagnetic resonance spectroscopy of iron complexes and iron-containing proteins, In *Methods Enzymol, Academic Press*, pp 353-384.

62. Schwertmann, U. (1991) Solubility and dissolution of iron oxides, *Plant Soil 130*, 1-25.

63. Zhao, G., Ceci, P., Ilari, A., Giangiacomo, L., Laue, T. M., Chiancone, E., and Chasteen, N. D. (2002) Iron and hydrogen peroxide detoxification properties of DNA-binding protein from starved cells. A ferritin-like DNA-binding protein of Escherichia coli, *J Biol Chem 277*, 27689-27696.

64. Su, M., Cavallo, S., Stefanini, S., Chiancone, E., and Chasteen, N. D. (2005) The so-called Listeria innocua ferritin is a Dps protein. Iron incorporation, detoxification, and DNA protection properties, *Biochemistry 44*, 5572-5578.

65. Andrews, S. C. (2010) The Ferritin-like superfamily: Evolution of the biological iron storeman from a rubrerythrin-like ancestor, *Bioch Biophys Acta 1800*, 691-705.

66. Roehm, K.-H. (2001) Electron Carriers: Proteins and Cofactors in Oxidative Phosphorylation, In *eLS*, John Wiley & Sons, Ltd.

67. Daly, M. J. (2009) A new perspective on radiation resistance based on *Deinococcus radiodurans*, *Nat Rev Microbiol 7*, 237-245.

68. Ghosal, D., Omelchenko, M. V., Gaidamakova, E. K., Matrosova, V. Y., Vasilenko, A., Venkateswaran, A., Zhai, M., Kostandarithes, H. M., Brim, H., Makarova, K. S., Wackett, L. P., Fredrickson, J. K., and Daly, M. J. (2005) How radiation kills cells: survival of *Deinococcus radiodurans* and *Shewanella oneidensis* under oxidative stress, *FEMS Microbiol Rev 29*, 361-375.

69. Daly, M. J., Gaidamakova, E. K., Matrosova, V. Y., Vasilenko, A., Zhai, M., Leapman, R. D., Lai, B., Ravel, B., Li, S. M. W., Kemner, K. M., and Fredrickson, J. K. (2007) Protein oxidation implicated as the primary determinant of bacterial radioresistance, *Plos Biol 5*, 769-779.

70. Barynin, V. V., Whittaker, M. M., Antonyuk, S. V., Lamzin, V. S., Harrison, P. M., Artymiuk, P. J., and Whittaker, J. W. (2001) Crystal structure of manganese catalase from *Lactobacillus plantarum*, *Structure 9*, 725-738.

71. Barnese, K., Gralla, E. B., Valentine, J. S., and Cabelli, D. E. (2012) Biologically relevant mechanism for catalytic superoxide removal by simple manganese compounds, *P Natl Acad Sci USA 109*, 6892-6897.

72. Zhang, H., Ishige, K., and Kornberg, A. (2002) A polyphosphate kinase (PPK2) widely conserved in bacteria, *P Natl Acad Sci USA 99*, 16678-16683.

73. Jensen, A. N., and Jensen, L. T. (2015) CHAPTER 1 Manganese Transport, Trafficking and Function in Invertebrates, In *Manganese in Health and Disease*, pp 1-33, RSC Adv.

74. Leopoldini, M., Russo, N., and Toscano, M. (2009) Determination of the Catalytic Pathway of a Manganese Arginase Enzyme Through Density Functional Investigation, *Chem Eur J 15*, 8026-8036.

75. Archibald, F. S., and Fridovich, I. (1982) The scavenging of superoxide radical by manganous complexes: *In vitro*, *Arch Biochem Biophys 214*, 452-463.

76. Gray, B., and Carmichael, A. J. (1992) Kinetics of Superoxide Scavenging by Dismutase Enzymes and Manganese Mimics Determined by Electron-Spin-Resonance, *Biochem J 281*, 795-802.

77. McNaughton, R. L., Reddi, A. R., Clement, M. H., Sharma, A., Barnese, K., Rosenfeld, L., Gralla, E. B., Valentine, J. S., Culotta, V. C., and Hoffman, B. M. (2010) Probing *in vivo* Mn^{2+} speciation and oxidative stress resistance in yeast cells with electron-nuclear double resonance spectroscopy, *P Natl Acad Sci USA 107*, 15335-15339.

78. Berlett, B. S., Chock, P. B., Yim, M. B., and Stadtman, E. R. (1990) Manganese(II) catalyzes the bicarbonate-dependent oxidation of amino acids by hydrogen peroxide and the amino acid-facilitated dismutation of hydrogen peroxide, *P Natl Acad Sci USA 87*, 389-393.

79. Daly, M. J., Gaidamakova, E. K., Matrosova, V. Y., Kiang, J. G., Fukumoto, R., Lee, D. Y., Wehr, N. B., Viteri, G. A., Berlett, B. S., and Levine, R. L. (2010) Small-molecule antioxidant proteome-shields in *Deinococcus radiodurans*, *Plos One 5*, e12570.

80. Archibald, F. S., and Fridovich, I. (1981) Manganese and defenses against oxygen toxicity in *Lactobacillus plantarum*, *J Bacteriol 145*, 442-451.

81. Daly, M. J., Gaidamakova, E. K., Matrosova, V. Y., Vasilenko, A., Zhai, M., Venkateswaran, A., Hess, M., Omelchenko, M. V., Kostandarithes, H. M., Makarova, K. S., Wackett, L. P., Fredrickson, J. K., and Ghosal, D. (2004) Accumulation of Mn(II) in, *Deinococcus radiodurans* facilitates gamma-radiation resistance, *Science 306*, 1025-1028.

82. Bagwell, C. E., Milliken, C. E., Ghoshroy, S., and Blom, D. A. (2008) Intracellular copper accumulation enhances the growth of *Kineococcus radiotolerans* during chronic irradiation, *Appl Environ Microbiol 74*, 1376-1384.

83. Leibowitz, P. J., Schwartzberg, L. S., and Bruce, A. K. (1976) The *in vivo* association of manganese with the chromosome of *Micrococcus radiodurans*, *Photochem Photobiol 23*, 45-50.

84. Culotta, V. C., and Daly, M. J. (2013) Manganese complexes: diverse metabolic routes to oxidative stress resistance in prokaryotes and yeast, *Antioxid Redox Signal 19*, 933-944.

85. Archibald, F. S., and Fridovich, I. (1981) Manganese, superoxide dismutase, and oxygen tolerance in some lactic acid bacteria, *J Bacteriol 146*, 928-936.

86. Archibald, F. S., and Fridovich, I. (1982) Investigations of the state of the manganese in *Lactobacillus plantarum*, *Arch Biochem Biophys 215*, 589-596.

87. Rao, N. N., Gomez-Garcia, M. R., and Kornberg, A. (2009) Inorganic polyphosphate: essential for growth and survival, *Annu Rev Biochem 78*, 605-647.

88. Akiyama, M., Crooke, E., and Kornberg, A. (1993) An exopolyphosphatase of *Escherichia coli*. The enzyme and its *ppx* gene in a polyphosphate operon, *J Biol Chem 268*, 633-639.

89. Barnese, K., Gralla, E. B., Cabelli, D. E., and Valentine, J. S. (2008) Manganous phosphate acts as a superoxide dismutase, *J Am Chem Soc 130*, 4604-4606.

90. Wanner, B. C. (1996) In *Escherichia coli* and *Salmonella*: Cellular and Molecular Biology, *ASM Press: Washington D.C., 1*, 1357-1381.

91. Al-Maghrebi, M., Fridovich, I., and Benov, L. (2002) Manganese supplementation relieves the phenotypic deficits seen in superoxide-dismutase-null *Escherichia coli*, *Arch Biochem Biophys 402*, 104-109.

92. Inaoka, T., Matsumura, Y., and Tsuchido, T. (1999) SodA and manganese are essential for resistance to oxidative stress in growing and sporulating cells of *Bacillus subtilis*, *J Bacteriol 181*, 1939-1943.

93. Sanchez, R. J., Srinivasan, C., Munroe, W. H., Wallace, M. A., Martins, J., Kao, T. Y., Le, K., Gralla, E. B., and Valentine, J. S. (2005) Exogenous manganous ion at millimolar levels rescues all known dioxygen-sensitive phenotypes of yeast lacking CuZnSOD, *J Biol Inorg Chem 10*, 913-923.

94. Reddi, A. R., and Culotta, V. C. (2011) Regulation of manganese antioxidants by nutrient sensing pathways in *Saccharomyces cerevisiae*, *Genetics 189*, 1261-1270.

95. Aguirre, J. D., and Culotta, V. C. (2012) Battles with iron: manganese in oxidative stress protection, *J Biol Chem 287*, 13541-13548.

96. Swinnen, E., Wanke, V., Roosen, J., Smets, B., Dubouloz, F., Pedruzzi, I., Cameroni, E., De Virgilio, C., and Winderickx, J. (2006) Rim15 and the crossroads of nutrient signalling pathways in *Saccharomyces cerevisiae*, *Cell Div 1*, 3.

97. Cunningham, K. W. (2011) Acidic calcium stores of *Saccharomyces cerevisiae*, *Cell Calcium 50*, 129-138.

98. Anderson, A. W., Nordan, H. C., Cain, R. F., Parrish, G., and Duggan, D. (1956) Studies on a Radio-Resistant *Micrococcus*, Isolation, Morphology, Cultural Characteristics, and Resistance to Gamma Radiation, *Food Technol-Chicago 10*, 575-578.

99. Stackebrandt, E., and Woese, C. R. (1981) Towards a phylogeny of the actinomycetes and related organisms, *Curr Microbiol 5*, 197-202.

100. Slade, D., and Radman, M. (2011) Oxidative Stress Resistance in *Deinococcus radiodurans*, *Microbiol Mol Biol Rev 75*, 133-191.

101. Murray, R. G., Hall, M., and Thompson, B. G. (1983) Cell division in *Deinococcus radiodurans* and a method for displaying septa, *Can J Microbiol 29*, 1412-1423.

102. White, O., Eisen, J. A., Heidelberg, J. F., Hickey, E. K., Peterson, J. D., Dodson, R. J., Haft, D. H., Gwinn, M. L., Nelson, W. C., Richardson, D. L., Moffat, K. S., Qin, H., Jiang, L., Pamphile, W., Crosby, M., Shen, M., Vamathevan, J. J., Lam, P., McDonald, L., Utterback, T., Zalewski, C., Makarova, K. S., Aravind, L., Daly, M. J., Minton, K. W., Fleischmann, R. D., Ketchum, K. A., Nelson, K. E., Salzberg, S., Smith, H. O., Venter, J. C., and Fraser, C. M. (1999) Genome sequence of the radioresistant bacterium *Deinococcus radiodurans* R1, *Science 286*, 1571-1577.

103. Thornley, M. J. (1963) Radiation Resistance among Bacteria, *J Appl Bacteriol 26*, 334-345.

104. Asker, D., Awad, T. S., Beppu, T., and Ueda, K. (2008) *Deinococcus misasensis* and *Deinococcus roseus*, novel members of the genus *Deinococcus*, isolated from a radioactive site in Japan, *Syst Appl Microbiol 31*, 43-49.

105. de Groot, A., Chapon, V., Servant, P., Christen, R., Saux, M. F., Sommer, S., and Heulin, T. (2005) *Deinococcus deserti* sp. nov., a gamma-radiation-tolerant bacterium isolated from the Sahara Desert, *Int J Syst Evol Microbiol 55*, 2441-2446.

106. Ferreira, A. C., Nobre, M. F., Rainey, F. A., Silva, M. T., Wait, R., Burghardt, J., Chung, A. P., and da Costa, M. S. (1997) *Deinococcus geothermalis* sp. nov. and *Deinococcus murrayi* sp. nov., two extremely radiation-resistant and slightly thermophilic species from hot springs, *Int J Syst Bacteriol 47*, 939-947.

107. Rainey, F. A., Ray, K., Ferreira, M., Gatz, B. Z., Nobre, M. F., Bagaley, D., Rash, B. A., Park, M. J., Earl, A. M., Shank, N. C., Small, A. M., Henk, M. C., Battista, J. R., Kampfer, P., and da Costa, M. S. (2005) Extensive diversity of ionizing-radiation-resistant bacteria recovered from Sonoran Desert soil and description of nine new species of the genus *Deinococcus* obtained from a single soil sample, *Appl Environ Microbiol 71*, 5225-5235.

108. Lai, W. A., Kampfer, P., Arun, A. B., Shen, F. T., Huber, B., Rekha, P. D., and Young, C. C. (2006) *Deinococcus ficus* sp nov., isolated from the rhizosphere of Ficus religiosa L., *Int J Syst Evol Microbiol 56*, 787-791.

109. Jolivet, E., Corre, E., L'Haridon, S., Forterre, P., and Prieur, D. (2004) *Thermococcus marinus* sp. nov. and *Thermococcus radiotolerans* sp. nov., two hyperthermophilic archaea from deep-sea hydrothermal vents that resist ionizing radiation, *Extremophiles 8*, 219-227.

110. Jolivet, E., L'Haridon, S., Corre, E., Forterre, P., and Prieur, D. (2003) *Thermococcus gammatolerans* sp nov., a hyperthermophilic archaeon from a deep-sea hydrothermal vent that resists ionizing radiation, *Int J Syst Evol Microbiol 53*, 847-851.

111. Kottemann, M., Kish, A., Iloanusi, C., Bjork, S., and DiRuggiero, J. (2005) Physiological responses of the halophilic archaeon *Halobacterium* sp strain NRC1 to desiccation and gamma irradiation, *Extremophiles 9*, 219-227.

112. Williams, E., Lowe, T. M., Savas, J., and Diruggiero, J. (2007) Microarray analysis of the hyperthermophilic archaeon *Pyrococcus furiosus* exposed to gamma irradiation, *Extremophiles 11*, 19-29.

113. Phillips, R. W., Wiegel, J., Berry, C. J., Fliermans, C., Peacock, A. D., White, D. C., and Shimkets, L. J. (2002) *Kineococcus radiotolerans* sp nov., a radiation-resistant, Gram-positive bacterium, *Int J Syst Evol Microbiol 52*, 933-938.

114. Billi, D., Friedmann, E. I., Hofer, K. G., Caiola, M. G., and Ocampo-Friedmann, R. (2000) Ionizing-radiation resistance in the desiccation-tolerant cyanobacterium *Chroococcidiopsis*, *Appl Environ Microb 66*, 1489-1492.

115. Nishimura, Y., Ino, T., and Iizuka, H. (1988) *Acinetobacter-Radioresistens* Sp-Nov Isolated from Cotton and Soil, *Int J Syst Bacteriol 38*, 209-211.

116. Gladyshev, E., and Meselson, M. (2008) Extreme resistance of *Bdelloid rotifers* to ionizing radiation, *P Natl Acad Sci USA 105*, 5139-5144.

117. Leaper, S., Resnick, M. A., and Holliday, R. (1980) Repair of Double-Strand Breaks and Lethal Damage in DNA of Ustilago-Maydis, *Genet Res 35*, 291-307.

118. Battista, J. R., Earl, A. M., and Park, M. J. (1999) Why is *Deinococcus radiodurans* so resistant to ionizing radiation?, *Trends Microbiol 7*, 362-365.

119. Tanaka, M., Earl, A. M., Howell, H. A., Park, M. J., Eisen, J. A., Peterson, S. N., and Battista, J. R. (2004) Analysis of *Deinococcus radiodurans*'s transcriptional response to ionizing radiation and desiccation reveals novel proteins that contribute to extreme radioresistance, *Genetics 168*, 21-33.

120. Mattimore, V., and Battista, J. R. (1996) Radioresistance of *Deinococcus radiodurans*: functions necessary to survive ionizing radiation are also necessary to survive prolonged desiccation, *J Bacteriol 178*, 633-637.

121. Selvam, K., Duncan, J. R., Tanaka, M., and Battista, J. R. (2013) DdrA, DdrD, and PprA: Components of UV and Mitomycin C Resistance in *Deinococcus radiodurans R1*, *Plos One 8*, e69007.

122. Wang, P., and Schellhorn, H. E. (1995) Induction of Resistance to Hydrogen-Peroxide and Radiation in *Deinococcus Radiodurans*, *Can J Microbiol 41*, 170-176.

123. (2000) Radiation safety fundamentals workbook, *University of California, Santa Cruz 4rd ed*.

124. (1989) Harmful effects of ultraviolet radiation. Council on Scientific Affairs, *JAMA 262*, 380-384.

125. Mothersill, C., and Seymour, C. (2001) Radiation-induced bystander effects: past history and future directions, *Radiat Res 155*, 759-767.

126. Azzam, E. I., Jay-Gerin, J. P., and Pain, D. (2012) Ionizing radiation-induced metabolic oxidative stress and prolonged cell injury, *Cancer Letters 327*, 48-60.

127. Hattori, Y., Nishigori, C., Tanaka, T., Uchida, K., Nikaido, O., Osawa, T., Hiai, H., Imamura, S., and Toyokuni, S. (1996) 8-Hydroxy-2'-Deoxyguanosine Is Increased in Epidermal Cells of Hairless Mice after Chronic Ultraviolet B Exposure, *J Invest Dermatol 107*, 733-737.

128. Zhang, X., Rosenstein, B. S., Wang, Y., Lebwohl, M., and Wei, H. (1997) Identification of Possible Reactive Oxygen Species Involved in Ultraviolet Radiation-Induced Oxidative DNA Damage, *Free Radic Biol Med 23*, 980-985.

129. Zhang, L., Yang, Q., Luo, X., Fang, C., Zhang, Q., and Tang, Y. (2007) Knockout of *crtB* or *crtI* gene blocks the carotenoid biosynthetic pathway in *Deinococcus radiodurans* R1 and influences its resistance to oxidative DNA-damaging agents due to change of free radicals scavenging ability, *Arch Microbiol 188*, 411-419.

130. Jurkiewicz, B. A., and Buettner, G. R. (1994) Ultraviolet light-induced free radical formation in skin: an electron paramagnetic resonance study, *Photochem Photobiol 59*, 1-4.

131. Jurkiewicz, B. A., and Buettner, G. R. (1996) EPR detection of free radicals in UV-irradiated skin: mouse versus human, *Photochem Photobiol 64*, 918-922.

132. Krisko, A., and Radman, M. (2010) Protein damage and death by radiation in *Escherichia coli* and *Deinococcus radiodurans*, *P Natl Acad Sci USA 107*, 14373-14377.

133. Bosshard, F., Riedel, K., Schneider, T., Geiser, C., Bucheli, M., and Egli, T. (2010) Protein oxidation and aggregation in UVA-irradiated *Escherichia coli* cells as signs of accelerated cellular senescence, *Environ Microbiol 12*, 2931-2945.

134. Fredrickson, J. K., Li, S. M., Gaidamakova, E. K., Matrosova, V. Y., Zhai, M., Sulloway, H. M., Scholten, J. C., Brown, M. G., Balkwill, D. L., and Daly, M. J. (2008) Protein oxidation: key to bacterial desiccation resistance?, *ISME J 2*, 393-403.

135. Potts, M. (1994) Desiccation tolerance of prokaryotes, *Microbiol Rev 58*, 755-805.

136. Minton, K. W. (1994) DNA repair in the extremely radioresistant bacterium *Deinococcus radiodurans*, *Mol Microbiol 13*, 9-15.

137. Zahradka, K., Slade, D., Bailone, A., Sommer, S., Averbeck, D., Petranovic, M., Lindner, A. B., and Radman, M. (2006) Reassembly of shattered chromosomes in *Deinococcus radiodurans*, *Nature 443*, 569-573.

138. Lin, J., Qi, R., Aston, C., Jing, J., Anantharaman, T. S., Mishra, B., White, O., Daly, M. J., Minton, K. W., Venter, J. C., and Schwartz, D. C. (1999) Whole-genome shotgun optical mapping of *Deinococcus radiodurans*, *Science 285*, 1558-1562.

139. Daly, M. J. (2012) Death by protein damage in irradiated cells, *DNA Repair (Amst) 11*, 12-21.

140. Ulmer, K. M., Gomez, R. F., and Sinskey, A. J. (1979) Ionizing radiation damage to the folded chromosome of *Escherichia coli K-12*: sedimentation properties of irradiated nucleoids and chromosomal deoxyribonucleic acid, *J Bacteriol 138*, 475-485.

141. Cox, M. M., Keck, J. L., and Battista, J. R. (2010) Rising from the Ashes: DNA Repair in *Deinococcus radiodurans*, *PLoS Genet 6*, e1000815.

142. Schlesinger, D. J. (2007) Role of RecA in DNA damage repair in *Deinococcus radiodurans*, *FEMS Microbiol Lett 274*, 342-347.

143. Bentchikou, E., Servant, P., Coste, G., and Sommer, S. (2010) A major role of the RecFOR pathway in DNA double-strand-break repair through ESDSA in *Deinococcus radiodurans*, *PLoS Genet 6*, e1000774.

144. Xu, G., Wang, L., Chen, H., Lu, H., Ying, N., Tian, B., and Hua, Y. (2008) RecO is essential for DNA damage repair in *Deinococcus radiodurans*, *J Bacteriol 190*, 2624-2628.

145. Blattner, F. R., Plunkett, G., 3rd, Bloch, C. A., Perna, N. T., Burland, V., Riley, M., Collado-Vides, J., Glasner, J. D., Rode, C. K., Mayhew, G. F., Gregor, J., Davis, N. W., Kirkpatrick, H. A., Goeden, M. A., Rose, D. J., Mau, B., and Shao, Y. (1997) The complete genome sequence of *Escherichia coli K-12*, *Science 277*, 1453-1462.

146. Makarova, K. S., Aravind, L., Wolf, Y. I., Tatusov, R. L., Minton, K. W., Koonin, E. V., and Daly, M. J. (2001) Genome of the extremely radiation-resistant bacterium *Deinococcus radiodurans* viewed from the perspective of comparative genomics, *Microbiol Mol Biol Rev 65*, 44-79.

147. Heidelberg, J. F., Paulsen, I. T., Nelson, K. E., Gaidos, E. J., Nelson, W. C., Read, T. D., Eisen, J. A., Seshadri, R., Ward, N., Methe, B., Clayton, R. A., Meyer, T., Tsapin, A., Scott, J., Beanan, M., Brinkac, L., Daugherty, S., DeBoy, R. T., Dodson, R. J., Durkin, A. S., Haft, D. H., Kolonay, J. F., Madupu, R., Peterson, J. D., Umayam, L. A., White, O., Wolf, A. M., Vamathevan, J., Weidman, J., Impraim, M., Lee, K., Berry, K., Lee, C., Mueller, J., Khouri, H., Gill, J., Utterback, T. R., McDonald, L. A., Feldblyum, T. V., Smith, H. O., Venter, J. C., Nealson, K. H., and Fraser, C. M. (2002) Genome sequence of the dissimilatory metal ion-reducing bacterium *Shewanella oneidensis*, *Nat Biotechnol 20*, 1118-1123.

148. Gutman, P. D., Fuchs, P., and Minton, K. W. (1994) Restoration of the DNA damage resistance of *Deinococcus radiodurans* DNA polymerase mutants by *Escherichia coli DNA polymerase I* and Klenow fragment, *Mutat Res 314*, 87-97.

149. Hansen, M. T. (1978) Multiplicity of genome equivalents in the radiation-resistant bacterium *Micrococcus radiodurans*, *J Bacteriol 134*, 71-75.

150. Krasin, F., and Hutchinson, F. (1977) Repair of DNA double-strand breaks in *Escherichia coli*, which requires recA function and the presence of a duplicate genome, *J Mol Biol 116*, 81-98.

151. Englander, J., Klein, E., Brumfeld, V., Sharma, A. K., Doherty, A. J., and Minsky, A. (2004) DNA toroids: framework for DNA repair in *Deinococcus radiodurans* and in germinating bacterial spores, *J Bacteriol 186*, 5973-5977.

152. Sukhi, S. S., Shashidhar, R., Kumar, S. A., and Bandekar, J. R. (2009) Radiation resistance of *Deinococcus radiodurans R1* with respect to growth phase, *FEMS Microbiol Lett 297*, 49-53.

153. Glauert, A. M., and Thornley, M. J. (1969) The topography of the bacterial cell wall, *Annu Rev Microbiol 23*, 159-198.

154. Work, E., and Griffith.H. (1968) Morphology and Chemistry of Cell Walls of *Micrococcus Radiodurans*, *J Bacteriol 95*, 641-&.

155. Rothfuss, H., Lara, J. C., Schmid, A. K., and Lidstrom, M. E. (2006) Involvement of the S-layer proteins Hpi and SlpA in the maintenance of cell envelope integrity in *Deinococcus radiodurans R1*, *Microbiology 152*, 2779-2787.

156. Baumeister, W., and Kubler, O. (1978) Topographic study of the cell surface of *Micrococcus radiodurans*, *P Natl Acad Sci USA 75*, 5525-5528.

157. Kubler, O., and Baumeister, W. (1978) The structure of a periodic cell wall component (HPI-layer of *Micrococcus radiodurans*), *Cytobiologie 17*, 1-9.

158. Anderson, R., and Hansen, K. (1985) Structure of a novel phosphoglycolipid from *Deinococcus radiodurans*, *J Biol Chem 260*, 12219-12223.

159. Tian, B., Xu, Z., Sun, Z., Lin, J., and Hua, Y. (2007) Evaluation of the antioxidant effects of carotenoids from *Deinococcus radiodurans* through targeted mutagenesis, chemiluminescence, and DNA damage analyses, *Biochim Biophys Acta 1770*, 902-911.

160. Luan, H., Meng, N., Fu, J., Chen, X., Xu, X., Feng, Q., Jiang, H., Dai, J., Yuan, X., Lu, Y., Roberts, A. A., Luo, X., Chen, M., Xu, S., Li, J., Hamilton, C. J., Fang, C., and Wang, J. (2014) Genome-wide transcriptome and antioxidant analyses on gamma-irradiated phases of *Deinococcus radiodurans R1*, *Plos One 9*, e85649.

161. Mitchel, R. E. J. (1975) Origin of Cell-Surface Proteins Released from *Micrococcus radiodurans* by Ionizing-Radiation, *Radiat Res 64*, 380-387.

162. Mitchel, R. E. J. (1976) Ionizing-Radiation Damage in *Micrococcus radiodurans* Cell-Wall - Release of Polysaccharide, *Radiat Res 66*, 158-169.

163. Gentner, N. E., and Mitchel, R. E. J. (1975) Ionizing Radiation-Induced Release of a Cell-Surface Nuclease from *Micrococcus-Radiodurans*, *Radiat Res 61*, 204-215.

164. Li, M. F., Sun, H. X., Feng, Q., Lu, H. M., Zhao, Y., Zhang, H., Xu, X., Jiao, J. D., Wang, L. Y., and Hua, Y. J. (2013) Extracellular dGMP Enhances *Deinococcus radiodurans* Tolerance to Oxidative Stress, *Plos One 8*, e54420.

165. Thornley, M. J., Horne, R. W., and Glauert, A. M. (1965) The fine structure of *Micrococcus radiodurans*, *Arch Mikrobiol 51*, 267-289.

166. Comolli, L. R., Kundmann, M., and Downing, K. H. (2006) Characterization of intact subcellular bodies in whole bacteria by cryo-electron tomography and spectroscopic imaging, *J Microsc 223*, 40-52.

167. Eltsov, M., and Dubochet, J. (2005) Fine structure of the *Deinococcus radiodurans* nucleoid revealed by cryoelectron microscopy of vitreous sections, *J Bacteriol 187*, 8047-8054.

168. Docampo, R., de Souza, W., Miranda, K., Rohloff, P., and Moreno, S. N. (2005) Acidocalcisomes - conserved from bacteria to man, *Nat Rev Microbiol 3*, 251-261.

169. Ruiz, F. A., Lea, C. R., Oldfield, E., and Docampo, R. (2004) Human platelet dense granules contain polyphosphate and are similar to acidocalcisomes of bacteria and unicellular eukaryotes, *J Biol Chem 279*, 44250-44257.

170. Ramos, I. B., Miranda, K., Pace, D. A., Verbist, K. C., Lin, F. Y., Zhang, Y., Oldfield, E., Machado, E. A., De Souza, W., and Docampo, R. (2010) Calcium- and polyphosphate-containing acidic granules of sea urchin eggs are similar to acidocalcisomes, but are not the targets for NAADP, *Biochem J 429*, 485-495.

171. Kornberg, A. (1999) Inorganic polyphosphate: a molecule of many functions, *Prog Mol Subcell Biol 23*, 1-18.

172. Docampo, R., Ulrich, P., and Moreno, S. N. (2010) Evolution of acidocalcisomes and their role in polyphosphate storage and osmoregulation in eukaryotic microbes, *Philos Trans R Soc Lond B Biol Sci 365*, 775-784.

173. Seufferheld, M., Vieira, M. C., Ruiz, F. A., Rodrigues, C. O., Moreno, S. N., and Docampo, R. (2003) Identification of organelles in bacteria similar to acidocalcisomes of unicellular eukaryotes, *J Biol Chem 278*, 29971-29978.

174. Seufferheld, M., Lea, C. R., Vieira, M., Oldfield, E., and Docampo, R. (2004) The $H(^{+})$-pyrophosphatase of *Rhodospirillum rubrum* is predominantly located in polyphosphate-rich acidocalcisomes, *J Biol Chem 279*, 51193-51202.

175. Friedber.I, and Avigad, G. (1968) Structures Containing Polyphosphate in *Micrococcus Lysodeikticus*, *J Bacteriol 96*, 544-&.

176. Fang, J., Ruiz, F. A., Docampo, M., Luo, S., Rodrigues, J. C., Motta, L. S., Rohloff, P., and Docampo, R. (2007) Overexpression of a Zn^{2+}-sensitive soluble exopolyphosphatase from *Trypanosoma cruzi* depletes polyphosphate and affects osmoregulation, *J Biol Chem 282*, 32501-32510.

177. Lemercier, G., Espiau, B., Ruiz, F. A., Vieira, M., Luo, S., Baltz, T., Docampo, R., and Bakalara, N. (2004) A pyrophosphatase regulating polyphosphate metabolism in acidocalcisomes is essential for *Trypanosoma brucei* virulence in mice, *J Biol Chem 279*, 3420-3425.

178. Zhang, H., Gomez-Garcia, M. R., Shi, X., Rao, N. N., and Kornberg, A. (2007) Polyphosphate kinase 1, a conserved bacterial enzyme, in a eukaryote, *Dictyostelium discoideum*, with a role in cytokinesis, *P Natl Acad Sci USA 104*, 16486-16491.

179. Lu, H.-G., Zhong, L., de Souza, W., Benchimol, M., Moreno, S., and Docampo, R. (1998) Ca^{2+} Content and Expression of an Acidocalcisomal Calcium Pump Are Elevated in Intracellular Forms of *Trypanosoma cruzi*, *Mol Cell Biol 18*, 2309-2323.

180. Scott, D. A., and Docampo, R. (2000) Characterization of isolated acidocalcisomes of *Trypanosoma cruzi*, *J Biol Chem 275*, 24215-24221.

181. Vercesi, A. E., and Docampo, R. (1996) Sodium-proton exchange stimulates Ca^{2+} release from acidocalcisomes of *Trypanosoma brucei*, *Biochem J 315*, 265-270.

182. Vercesi, A. E., Grijalba, M. T., and Docampo, R. (1997) Inhibition of Ca^{2+} release from *Trypanosoma brucei* acidocalcisomes by 3,5-dibutyl-4-hydroxytoluene: role of the Na^{+}/H^{+} exchanger, *Biochem J 328*, 479-482.

183. Montalvetti, A., Rohloff, P., and Docampo, R. (2004) A functional aquaporin co-localizes with the vacuolar proton pyrophosphatase to acidocalcisomes and the contractile vacuole complex of *Trypanosoma cruzi*, *J Biol Chem 279*, 38673-38682.

184. Tinsley, C. R., and Gotschlich, E. C. (1995) Cloning and characterization of the meningococcal polyphosphate kinase gene: production of polyphosphate synthesis mutants, *Infect Immun 63*, 1624-1630.

185. Ayraud, S., Janvier, B., Labigne, A., Ecobichon, C., Burucoa, C., and Fauchere, J. L. (2005) Polyphosphate kinase: a new colonization factor of *Helicobacter pylori*, *FEMS Microbiol Lett 243*, 45-50.

186. Rangarajan, E. S., Nadeau, G., Li, Y., Wagner, J., Hung, M. N., Schrag, J. D., Cygler, M., and Matte, A. (2006) The structure of the exopolyphosphatase (PPX) from *Escherichia coli* O157:H7 suggests a binding mode for long polyphosphate chains, *J Mol Biol 359*, 1249-1260.

187. Lindner, S. N., Knebel, S., Wesseling, H., Schoberth, S. M., and Wendisch, V. F. (2009) Exopolyphosphatases PPX1 and PPX2 from *Corynebacterium glutamicum*, *Appl Environ Microbiol 75*, 3161-3170.

188. van Veen, H. W. (1997) Phosphate transport in prokaryotes: molecules, mediators and mechanisms, *Antonie Van Leeuwenhoek 72*, 299-315.

189. Fuhs, G. W., and Chen, M. (1975) Microbiological basis of phosphate removal in the activated sludge process for the treatment of wastewater, *Microb Ecol 2*, 119-138.

190. Ahn, K., and Kornberg, A. (1990) Polyphosphate kinase from *Escherichia coli*. Purification and demonstration of a phosphoenzyme intermediate, *J Biol Chem 265*, 11734-11739.

191. van Veen, H. W., Abee, T., Kortstee, G. J., Pereira, H., Konings, W. N., and Zehnder, A. J. (1994) Generation of a proton motive force by the excretion of metal-phosphate in the polyphosphate-accumulating *Acinetobacter johnsonii* strain 210A, *J Biol Chem 269*, 29509-29514.

192. Rao, N. N., and Kornberg, A. (1996) Inorganic polyphosphate supports resistance and survival of stationary-phase *Escherichia coli*, *J Bacteriol 178*, 1394-1400.

193. Baxter, M., and Jensen, T. (1980) Uptake of Magnesium, Strontium, Barium, and Manganese by *Plectonema-Boryanum* (Cyanophyceae) with Special Reference to Polyphosphate Bodies, *Protoplasma 104*, 81-89.

194. Ogawa, N., Tzeng, C. M., Fraley, C. D., and Kornberg, A. (2000) Inorganic polyphosphate in *Vibrio cholerae*: genetic, biochemical, and physiologic features, *J Bacteriol 182*, 6687-6693.

195. Alvarez, S., and Jerez, C. A. (2004) Copper ions stimulate polyphosphate degradation and phosphate efflux in *Acidithiobacillus ferrooxidans*, *Appl Environ Microbiol 70*, 5177-5182.

196. Tinsley, C. R., Manjula, B. N., and Gotschlich, E. C. (1993) Purification and characterization of polyphosphate kinase from *Neisseria meningitidis*
Infect Immun 61, 3703-3710.

197. Miller, A. F. (2004) Superoxide dismutases: active sites that save, but a protein that kills, *Curr Opin Chem Biol 8*, 162-168.

198. Chou, F. I., and Tan, S. T. (1990) Manganese(II) induces cell division and increases in superoxide dismutase and catalase activities in an aging *Deinococcal* culture, *J Bacteriol 172*, 2029-2035.

199. Lipton, M. S., Pasa-Tolic, L., Anderson, G. A., Anderson, D. J., Auberry, D. L., Battista, J. R., Daly, M. J., Fredrickson, J., Hixson, K. K., Kostandarithes, H., Masselon, C., Markillie, L. M., Moore, R. J., Romine, M. F., Shen, Y., Stritmatter, E., Tolic, N., Udseth, H. R., Venkateswaran, A., Wong, K. K., Zhao, R., and Smith, R. D. (2002) Global analysis of the *Deinococcus radiodurans* proteome by using accurate mass tags, *Proc Natl Acad Sci U S A 99*, 11049-11054.

200. Abreu, I. A., Hearn, A., An, H., Nick, H. S., Silverman, D. N., and Cabelli, D. E. (2008) The kinetic mechanism of manganese-containing superoxide dismutase from *Deinococcus radiodurans*: a specialized enzyme for the elimination of high superoxide concentrations, *Biochemistry 47*, 2350-2356.

201. Markillie, L. M., Varnum, S. M., Hradecky, P., and Wong, K. K. (1999) Targeted mutagenesis by duplication insertion in the radioresistant bacterium *Deinococcus radiodurans*: Radiation sensitivities of catalase (katA) and superoxide dismutase (sodA) mutants, *J Bacteriol 181*, 666-669.

202. Jeong, S. W., Jung, J. H., Kim, M. K., Seo, H. S., Lim, H. M., and Lim, S. (2016) The three catalases in *Deinococcus radiodurans*: Only two show catalase activity, *Biochem Biophys Res Commun 469*, 443-448.

203. Romao, C. V., Mitchell, E. P., and McSweeney, S. (2006) The crystal structure of Deinococcus radiodurans Dps protein (DR2263) reveals the presence of a novel metal centre in the N terminus, *J Biol Inorg Chem 11*, 891-902.

204. Cuypers, M. G., Mitchell, E. P., Romão, C. V., and McSweeney, S. M. (2007) The crystal structure of the Dps2 from *Deinococcus radiodurans* reveals an unusual pore profile with a non-specific metal binding site, *J Mol Biol 371*, 787-799.

205. Grove, A., and Wilkinson, S. P. (2005) Differential DNA binding and protection by dimeric and dodecameric forms of the ferritin homolog Dps from *Deinococcus radiodurans*, *J Mol Biol 347*, 495-508.

206. Reon, B. J., Nguyen, K. H., Bhattacharyya, G., and Grove, A. (2012) Functional comparison of *Deinococcus radiodurans* Dps proteins suggests distinct *in vivo* roles, *Biochem J 447*, 381-391.

207. Toueille, M., Mirabella, B., Guerin, P., Bouthier de la Tour, C., Boisnard, S., Nguyen, H. H., Blanchard, L., Servant, P., de Groot, A., Sommer, S., and Armengaud, J. (2012) A comparative proteomic approach to better define *Deinococcus* nucleoid specificities, *J Proteomics 75*, 2588-2600.

208. Chen, H., Xu, G. Z., Zhao, Y., Tian, B., Lu, H. M., Yu, X. M., Xu, Z. J., Ying, N. J., Hu, S. N., and Hua, Y. J. (2008) A Novel OxyR Sensor and Regulator of Hydrogen Peroxide Stress with One Cysteine Residue in *Deinococcus radiodurans*, *Plos One 3*, e1602.

209. Wang, L. Y., Xu, G. Z., Chen, H., Zhao, Y., Xu, N., Tian, B., and Hua, Y. J. (2008) DrRRA: a novel response regulator essential for the extreme radioresistance of *Deinococcus radiodurans*, *Mol Microbiol 67*, 1211-1222.

210. Yokoyama, H., and Fujii, S. (2014) Structures and Metal-Binding Properties of *Helicobacter pylori* Neutrophil-Activating Protein with a Di-Nuclear Ferroxidase Center, *Biomolecules 4*, 600-615.

211. Sun, H. X., Li, M. F., Xu, G. Z., Chen, H., Jiao, J. D., Tian, B., Wang, L. Y., and Hua, Y. J. (2012) Regulation of MntH by a Dual Mn(II)- and Fe(II)-Dependent Transcriptional Repressor (DR2539) in *Deinococcus radiodurans*, *Plos One 7*, e35057.

212. Shah, A. M. U., Zhao, Y., Wang, Y. F., Yan, G. Q., Zhang, Q. K., Wang, L. Y., Tian, B., Chen, H., and Hua, Y. J. (2014) A Mur Regulator Protein in the Extremophilic Bacterium *Deinococcus radiodurans*, *Plos One 9*, e106341.

213. Sun, H. X., Xu, G. Z., Zhan, H. D., Chen, H. A., Sun, Z. T., Tian, B., and Hua, Y. J. (2010) Identification and evaluation of the role of the manganese efflux protein in *Deinococcus radiodurans*, *Bmc Microbiol 10*.

214. Liu, Y., Zhou, J., Omelchenko, M. V., Beliaev, A. S., Venkateswaran, A., Stair, J., Wu, L., Thompson, D. K., Xu, D., Rogozin, I. B., Gaidamakova, E. K., Zhai, M., Makarova, K. S., Koonin, E. V., and Daly, M. J. (2003) Transcriptome dynamics of *Deinococcus radiodurans* recovering from ionizing radiation, *P Natl Acad Sci USA 100*, 4191-4196.

215. Huan Chen , Z. X., Bing Tian ,Weiwei Chen ,Songnian Hu,Yuejm Hua (2007) Transcriptional profile in response to ionizing radiation at low dose in *Deinococcus radiodurans*, In *Prog. Nat. Sci*, pp 529-536.

216. Chen, H. A., Wu, R. R., Xu, G. Z., Fang, X., Qiu, X. L., Guo, H. Y., Tian, B., and Hua, Y. J. (2010) DR2539 is a novel DtxR-like regulator of Mn/Fe ion homeostasis and antioxidant enzyme in *Deinococcus radiodurans*, *Biochem Bioph Res Co 396*, 413-418.

217. DeLano, W. L. (2002) The PyMOL Molecular Graphics System.

218. Schrodinger, L. L. C. (2010) The PyMOL Molecular Graphics System, Version 1.3r1.

219. Chiancone, E., and Ceci, P. (2010) The multifaceted capacity of Dps proteins to combat bacterial stress conditions: Detoxification of iron and hydrogen peroxide and DNA binding, *Biochimica et biophysica acta 1800*, 798-805.

220. Haikarainen, T., and Papageorgiou, A. C. (2010) Dps-like proteins: structural and functional insights into a versatile protein family, *Cellular and molecular life sciences : CMLS 67*, 341-351.

221. Hudson, A. J., Andrews, S. C., Hawkins, C., Williams, J. M., Izuhara, M., Meldrum, F. C., Mann, S., Harrison, P. M., and Guest, J. R. (1993) Overproduction, purification and characterization of the *Escherichia coli* ferritin, *Eur J Biochem 218*, 985-995.

222. Yariv, J., Kalb, A. J., Sperling, R., Bauminger, E. R., Cohen, S. G., and Ofer, S. (1981) The composition and the structure of bacterioferritin of *Escherichia coli*, *Biochem J 197*, 171-175.

223. Pandey, R., and Rodriguez, G. M. (2012) A ferritin mutant of *Mycobacterium tuberculosis* is highly susceptible to killing by antibiotics and is unable to establish a chronic infection in mice, *Infect Immun 80*, 3650-3659.

224. Almiron, M., Link, A. J., Furlong, D., and Kolter, R. (1992) A novel DNA-binding protein with regulatory and protective roles in starved *Escherichia coli*, *Genes Dev 6*, 2646-2654.

225. Martinez, A., and Kolter, R. (1997) Protection of DNA during oxidative stress by the nonspecific DNA-binding protein Dps, *J Bacteriol 179*, 5188-5194.

226. Haikarainen, T., Thanassoulas, A., Stavros, P., Nounesis, G., Haataja, S., and Papageorgiou, A. C. (2011) Structural and thermodynamic characterization of metal ion binding in *Streptococcus suis* Dpr, *J Mol Biol 405*, 448-460.

227. Kauko, A., Haataja, S., Pulliainen, A. T., Finne, J., and Papageorgiou, A. C. (2004) Crystal structure of *Streptococcus suis* Dps-like peroxide resistance protein Dpr: implications for iron incorporation, *J Mol Biol 338*, 547-558.

228. Wang, G., Hong, Y., Olczak, A., Maier, S. E., and Maier, R. J. (2006) Dual Roles of *Helicobacter pylori* NapA in inducing and combating oxidative stress, *Infect Immun 74*, 6839-6846.

229. Chen, L., and Helmann, J. D. (1995) *Bacillus subtilis* MrgA is a Dps(PexB) homologue: evidence for metalloregulation of an oxidative-stress gene, *Mol Microbiol 18*, 295-300.

230. Pesek, J., Buchler, R., Albrecht, R., Boland, W., and Zeth, K. (2011) Structure and mechanism of iron translocation by a Dps protein from *Microbacterium arborescens*, *J Biol Chem 286*, 34872-34882.

231. Thumiger, A., Polenghi, A., Papinutto, E., Battistutta, R., Montecucco, C., and Zanotti, G. (2006) Crystal structure of antigen TpF1 from *Treponema pallidum*, *Proteins 62*, 827-830.

232. Grant, R. A., Filman, D. J., Finkel, S. E., Kolter, R., and Hogle, J. M. (1998) The crystal structure of Dps, a ferritin homolog that binds and protects DNA, *Nat Struct Biol 5*, 294-303.

233. Zanotti, G., Papinutto, E., Dundon, W., Battistutta, R., Seveso, M., Giudice, G., Rappuoli, R., and Montecucco, C. (2002) Structure of the neutrophil-activating protein from *Helicobacter pylori*, *J Mol Biol 323*, 125-130.

234. Papinutto, E., Dundon, W. G., Pitulis, N., Battistutta, R., Montecucco, C., and Zanotti, G. (2002) Structure of two iron-binding proteins from *Bacillus anthracis*, *J Biol Chem 277*, 15093-15098.

235. Schonafinger, A., Morbitzer, A., Kress, D., Essen, L. O., Noll, F., and Hampp, N. (2006) Morphology of dry solid-supported protein monolayers dependent on the substrate and protein surface properties, *Langmuir 22*, 7185-7191.

236. Zeth, K., Offermann, S., Essen, L. O., and Oesterhelt, D. (2004) Iron-oxo clusters biomineralizing on protein surfaces: structural analysis of *Halobacterium salinarum* DpsA in its low- and high-iron states, *P Natl Acad Sci USA 101*, 13780-13785.

237. Calhoun, L. N., and Kwon, Y. M. (2011) Structure, function and regulation of the DNA-binding protein Dps and its role in acid and oxidative stress resistance in *Escherichia coli*: a review, *J Appl Microbiol 110*, 375-386.

238. Ardini, M., Fiorillo, A., Fittipaldi, M., Stefanini, S., Gatteschi, D., Ilari, A., and Chiancone, E. (2013) *Kineococcus radiotolerans* Dps forms a heteronuclear Mn-Fe ferroxidase center that may explain the Mn-dependent protection against oxidative stress, *Bioch Biophys Acta 1830*, 3745-3755.

239. Miyamoto, T., Asahina, Y., Miyazaki, S., Shimizu, H., Ohto, U., Noguchi, S., and Satow, Y. (2011) Structures of the SEp22 dodecamer, a Dps-like protein from *Salmonella enterica* subsp. enterica serovar Enteritidis, *Acta Cryst F 67*, 17-22.

240. Crichton, R. R., and Declercq, J. P. (2010) X-ray structures of ferritins and related proteins, *Biochim Biophys Acta 1800*, 706-718.

241. Castruita, M., Saito, M., Schottel, P. C., Elmegreen, L. A., Myneni, S., Stiefel, E. I., and Morel, F. M. (2006) Overexpression and characterization of an iron storage and DNA-binding Dps protein from *Trichodesmium erythraeum*, *Appl Environ Microbiol 72*, 2918-2924.

242. Ilari, A., Stefanini, S., Chiancone, E., and Tsernoglou, D. (2000) The dodecameric ferritin from *Listeria innocua* contains a novel intersubunit iron-binding site, *Nat Struct Biol 7*, 38-43.

243. Gupta, S., and Chatterji, D. (2003) Bimodal protection of DNA by *Mycobacterium smegmatis* DNA-binding protein from stationary phase cells, *J Biol Chem 278*, 5235-5241.

244. Hitchings, M. D., Townsend, P., Pohl, E., Facey, P. D., Jones, D. H., Dyson, P. J., and Del Sol, R. (2014) A tale of tails: deciphering the contribution of terminal tails to the biochemical properties of two Dps proteins from *Streptomyces coelicolor*, *Cellular and molecular life sciences : CMLS 71*, 4911-4926.

245. Stillman, T. J., Upadhyay, M., Norte, V. A., Sedelnikova, S. E., Carradus, M., Tzokov, S., Bullough, P. A., Shearman, C. A., Gasson, M. J., Williams, C. H., Artymiuk, P. J., and Green, J. (2005) The crystal structures of *Lactococcus lactis* MG1363 Dps proteins reveal the presence of an N-terminal helix that is required for DNA binding, *Mol Microbiol 57*, 1101-1112.

246. Kim, S. G., Bhattacharyya, G., Grove, A., and Lee, Y. H. (2006) Crystal structure of Dps-1, a functionally distinct Dps protein from Deinococcus radiodurans, *Journal of molecular biology 361*, 105-114.

247. Roy, S., Saraswathi, R., Gupta, S., Sekar, K., Chatterji, D., and Vijayan, M. (2007) Role of N and C-terminal tails in DNA binding and assembly in Dps: structural studies of *Mycobacterium smegmatis* Dps deletion mutants, *J Mol Biol 370*, 752-767.

248. Franceschini, S., Ceci, P., Alaleona, F., Chiancone, E., and Ilari, A. (2006) Antioxidant Dps protein from the thermophilic cyanobacterium *Thermosynechococcus elongatus*, *Febs J 273*, 4913-4928.

249. Zeth, K. (2012) Dps biomineralizing proteins: multifunctional architects of nature, *Biochem J 445*, 297-311.

250. Pulliainen, A. T., Kauko, A., Haataja, S., Papageorgiou, A. C., and Finne, J. (2005) Dps/Dpr ferritin-like protein: insights into the mechanism of iron incorporation and evidence for a central role in cellular iron homeostasis in *Streptococcus suis*, *Mol Microbiol 57*, 1086-1100.

251. Bellapadrona, G., Stefanini, S., Zamparelli, C., Theil, E. C., and Chiancone, E. (2009) Iron translocation into and out of *Listeria innocua* Dps and size distribution of the protein-enclosed nanomineral are modulated by the electrostatic gradient at the 3-fold "ferritin-like" pores, *J Biol Chem 284*, 19101-19109.

252. Zeth, K. (2012) Dps biomineralizing proteins: multifunctional architects of nature, *Biochem J 445*, 297-311.

253. Ilari, A., Latella, M. C., Ceci, P., Ribacchi, F., Su, M., Giangiacomo, L., Stefanini, S., Chasteen, N. D., and Chiancone, E. (2005) The unusual intersubunit ferroxidase center of *Listeria innocua* Dps is required for hydrogen peroxide detoxification but not for iron uptake. A study with site-specific mutants, *Biochemistry 44*, 5579-5587.

254. Liu, X. F., Kim, K., Leighton, T., and Theil, E. C. (2006) Paired *Bacillus anthracis* Dps (mini-ferritin) have different reactivities with peroxide, *J Biol Chem 281*, 27827-27835.

255. Alaleona, F., Franceschini, S., Ceci, P., Ilari, A., and Chiancone, E. (2010) *Thermosynechoccus elongatus* DpsA binds Zn(II) at a unique three histidine-containing ferroxidase center and utilizes O_2 as iron oxidant with very high efficiency, unlike the typical Dps proteins, *Febs J 277*, 903-917.

256. Ren, B., Tibbelin, G., Kajino, T., Asami, O., and Ladenstein, R. (2003) The multi-layered structure of Dps with a novel di-nuclear ferroxidase center, *J Mol Biol 329*, 467-477.

257. Granier, T., d'Estaintot, B. L., Gallois, B., Chevalier, J. M., Precigoux, G., Santambrogio, P., and Arosio, P. (2003) Structural description of the active sites of mouse L-chain ferritin at 1.2 angstrom resolution, *J Biol Inorg Chem 8*, 105-111.

258. Levi, S., Yewdall, S. J., Harrison, P. M., Santambrogio, P., Cozzi, A., Rovida, E., Albertini, A., and Arosio, P. (1992) Evidence That H-Chains and L-Chains Have Cooperative Roles in the Iron-Uptake Mechanism of Human Ferritin, *Biochem J 288*, 591-596.

259. Santambrogio, P., Levi, S., Cozzi, A., Corsi, B., and Arosio, P. (1996) Evidence that the specificity of iron incorporation into homopolymers of human ferritin L- and H-chains is conferred by the nucleation and ferroxidase centres, *Biochem J 314*, 139-144.

260. Desilva, D., Guo, J. H., and Aust, S. D. (1993) Relationship between Iron and Phosphate in Mammalian Ferritins, *Arch Biochem Biophys 303*, 451-455.

261. Trefry, A., and Harrison, P. M. (1978) Incorporation and release of inorganic phosphate in horse spleen ferritin, *Biochem J 171*, 313-320.

262. Treffry, A., Harrison, P. M., Cleton, M. I., de Bruijn, W. C., and Mann, S. (1987) A note on the composition and properties of ferritin iron cores, *J Inorg Biochem 31*, 1-6.

263. Ilari, A., Ceci, P., Ferrari, D., Rossi, G. L., and Chiancone, E. (2002) Iron incorporation into *Escherichia coli* Dps gives rise to a ferritin-like microcrystalline core, *J Biol Chem 277*, 37619-37623.

264. Williams, S. M., Chandran, A. V., Vijayabaskar, M. S., Roy, S., Balaram, H., Vishveshwara, S., Vijayan, M., and Chatterji, D. (2014) A Histidine Aspartate Ionic Lock Gates the Iron Passage in Miniferritins from *Mycobacterium smegmatis*, *J Biol Chem 289*, 11042-11058.

265. Ceci, P., Cellai, S., Falvo, E., Rivetti, C., Rossi, G. L., and Chiancone, E. (2004) DNA condensation and self-aggregation of *Escherichia coli* Dps are coupled phenomena related to the properties of the N-terminus, *Nucleic Acids Res 32*, 5935-5944.

266. Ceci, P., Ilari, A., Falvo, E., and Chiancone, E. (2003) The Dps protein of *Agrobacterium tumefaciens* does not bind to DNA but protects it toward oxidative cleavage: x-ray crystal structure, iron binding, and hydroxyl-radical scavenging properties, *J Biol Chem 278*, 20319-20326.

267. Ceci, P., Ilari, A., Falvo, E., Giangiacomo, L., and Chiancone, E. (2005) Reassessment of protein stability, DNA binding, and protection of *Mycobacterium smegmatis* Dps, *J Biol Chem 280*, 34776-34785.

268. Ceci, P., Mangiarotti, L., Rivetti, C., and Chiancone, E. (2007) The neutrophil-activating Dps protein of *Helicobacter pylori*, HP-NAP, adopts a mechanism different from *Escherichia coli* Dps to bind and condense DNA, *Nucleic Acids Res 35*, 2247-2256.

269. Nguyen, K. H., and Grove, A. (2012) Metal Binding at the *Deinococcus radiodurans* Dps-1 N-Terminal Metal Site Controls Dodecameric Assembly and DNA Binding, *Biochemistry 51*, 6679-6689.

270. Bhattacharyya, G., and Grove, A. (2007) The N-terminal Extensions of Deinococcus radiodurans Dps-1 Mediate DNA Major Groove Interactions as well as Assembly of the Dodecamer, *The Journal of biological chemistry 282*, 11921-11930.

271. Nguyen, K. H., Smith, L. T., Xiao, L. J., Bhattacharyya, G., and Grove, A. (2012) On the stoichiometry of *Deinococcus radiodurans* Dps-1 binding to duplex DNA, *Proteins 80*, 713-721.

272. Wolf, S. G., Frenkiel, D., Arad, T., Finkel, S. E., Kolter, R., and Minsky, A. (1999) DNA protection by stress-induced biocrystallization, *Nature 400*, 83-85.

273. Minsky, A., Shimoni, E., and Frenkiel-Krispin, D. (2002) Stress, order and survival, *Nat Rev Mol Cell Biol 3*, 50-60.

274. Tonello, F., Dundon, W. G., Satin, B., Molinari, M., Tognon, G., Grandi, G., Del Giudice, G., Rappuoli, R., and Montecucco, C. (1999) The *Helicobacter pylori* neutrophil-activating protein is an iron-binding protein with dodecameric structure, *Mol Microbiol 34*, 238-246.

275. Frenkiel-Krispin, D., Ben-Avraham, I., Englander, J., Shimoni, E., Wolf, S. G., and Minsky, A. (2004) Nucleoid restructuring in stationary-state bacteria, *Mol Microbiol 51*, 395-405.

276. Nair, S., and Finkel, S. E. (2004) Dps protects cells against multiple stresses during stationary phase, *J Bacteriol 186*, 4192-4198.

277. Nicodeme, M., Perrin, C., Hols, P., Bracquart, P., and Gaillard, J. L. (2004) Identification of an iron-binding protein of the Dps family expressed by *Streptococcus thermophilus*, *Curr Microbiol 48*, 51-56.

278. Malone, A. S., Chung, Y. K., and Yousef, A. E. (2006) Genes of *Escherichia coli* O157:H7 that are involved in high-pressure resistance, *Appl Environ Microbiol 72*, 2661-2671.

279. Choi, S. H., Baumler, D. J., and Kaspar, C. W. (2000) Contribution of dps to acid stress tolerance and oxidative stress tolerance in *Escherichia coli* O157:H7, *Appl Environ Microbiol 66*, 3911-3916.

280. Tsou, C. C., Chiang-Ni, C., Lin, Y. S., Chuang, W. J., Lin, M. T., Liu, C. C., and Wu, J. J. (2008) An iron-binding protein, Dpr, decreases hydrogen peroxide stress and protects *Streptococcus pyogenes* against multiple stresses, *Infect Immun 76*, 4038-4045.

281. Calhoun, L. N., and Kwon, Y. M. (2011) The ferritin-like protein Dps protects *Salmonella enterica* serotype *Enteritidis* from the Fenton-mediated killing mechanism of bactericidal antibiotics, *Int J Antimicrob Agents 37*, 261-265.

282. Ye, Y., Li, H., Ling, N., Han, Y., Wu, Q., Xu, X., Jiao, R., and Gao, J. (2016) Identification of potential virulence factors of *Cronobacter sakazakii* isolates by comparative proteomic analysis, *Int J Food Microbiol 217*, 182-188.

283. Theoret, J. R., Cooper, K. K., Zekarias, B., Roland, K. L., Law, B. F., Curtiss, R., 3rd, and Joens, L. A. (2012) The *Campylobacter jejuni* Dps homologue is important for in vitro biofilm formation and cecal colonization of poultry and may serve as a protective antigen for vaccination, *Clin Vaccine Immunol 19*, 1426-1431.

284. Satin, B., Del Giudice, G., Della Bianca, V., Dusi, S., Laudanna, C., Tonello, F., Kelleher, D., Rappuoli, R., Montecucco, C., and Rossi, F. (2000) The neutrophil-activating protein (HP-NAP) of *Helicobacter pylori* is a protective antigen and a major virulence factor, *J Exp Med 191*, 1467-1476.

285. Kawamura, N., Piao, H., Minohara, M., Matsushita, T., Kusunoki, S., Matsumoto, H., Ikenaka, K., Mizunoe, Y., and Kira, J. (2011) *Campylobacter jejuni* DNA-binding protein from starved cells in Guillain-Barre syndrome patients, *J Neuroimmunol 240-241*, 74-78.

286. Piao, H., Minohara, M., Kawamura, N., Li, W., Mizunoe, Y., Umehara, F., Goto, Y., Kusunoki, S., Matsushita, T., Ikenaka, K., Maejima, T., Nabekura, J., Yamasaki, R., and Kira, J. (2010) Induction of paranodal myelin detachment and sodium channel loss *in vivo* by *Campylobacter jejuni* DNA-binding protein from starved cells (C-Dps) in myelinated nerve fibers, *J Neurol Sci 288*, 54-62.

287. Olsen, K. N., Larsen, M. H., Gahan, C. G., Kallipolitis, B., Wolf, X. A., Rea, R., Hill, C., and Ingmer, H. (2005) The Dps-like protein Fri of Listeria monocytogenes promotes stress tolerance and intracellular multiplication in macrophage-like cells, *Microbiology 151*, 925-933.

288. Halsey, T. A., Vazquez-Torres, A., Gravdahl, D. J., Fang, F. C., and Libby, S. J. (2004) The ferritin-like Dps protein is required for *Salmonella enterica serovar Typhimurium* oxidative stress resistance and virulence, *Infect Immun 72*, 1155-1158.

289. Hanna, E. S., Roque-Barreira, M. C., Bernardes, E. S., Panunto-Castelo, A., Sousa, M. V., Almeida, I. C., and Brocchi, M. (2007) Evidence for glycosylation on a DNA-binding protein of *Salmonella enterica*, *Microb Cell Fact 6*.

290. Nothaft, H., and Szymanski, C. M. (2013) Bacterial protein N-glycosylation: new perspectives and applications, *J Biol Chem 288*, 6912-6920.

291. Paiva, C. N., and Bozza, M. T. (2014) Are Reactive Oxygen Species Always Detrimental to Pathogens?, *Antioxid Redox Sign 20*, 1000-1037.

292. Roy, S., Saraswathi, R., Chatterji, D., and Vijayan, M. (2008) Structural studies on the second *Mycobacterium smegmatis* Dps: invariant and variable features of structure, assembly and function, *J Mol Biol 375*, 948-959.

293. Facey, P. D., Hitchings, M. D., Saavedra-Garcia, P., Fernandez-Martinez, L., Dyson, P. J., and Del Sol, R. (2009) *Streptomyces coelicolor* Dps-like proteins: differential dual roles in response to stress during vegetative growth and in nucleoid condensation during reproductive cell division, *Molecular Microbiology 73*, 1186-1202.

294. Wei, X., Mingjia, H., Xiufeng, L., Yang, G., and Qingyu, W. (2007) Identification and biochemical properties of Dps (starvation-induced DNA binding protein) from cyanobacterium *Anabaena* sp. PCC 7120, *IUBMB Life 59*, 675-681.

295. Ghatak, P., Karmakar, K., Kasetty, S., and Chatterji, D. (2011) Unveiling the Role of Dps in the Organization of *Mycobacterial* Nucleoid, *Plos One 6*, e16019.

296. Facey, P. D., Hitchings, M. D., Williams, J. S., Skibinski, D. O., Dyson, P. J., and Del Sol, R. (2013) The evolution of an osmotically inducible dps in the genus *Streptomyces*, *Plos One 8*, e60772.

297. Sato, N., Moriyama, T., Toyoshima, M., Mizusawa, M., and Tajima, N. (2012) The *all0458/lti46.2* gene encodes a low temperature-induced Dps protein homologue in the cyanobacteria *Anabaena* sp. PCC 7120 and *Anabaena variabilis* M3, *Microbiology 158*, 2527-2536.

298. Oliveira, P., Martins, N. M., Santos, M., Couto, N. A., Wright, P. C., and Tamagnini, P. (2015) The *Anabaena* sp. PCC 7120 Exoproteome: Taking a Peek outside the Box, *Life (Basel) 5*, 130-163.

299. Ren, B., Tibbelin, G., Kajino, T., Asami, O., and Ladenstein, R. (2003) The multi-layered structure of Dps with a novel di-nuclear ferroxidase center, *Journal of Molecular Biology 329*, 467-477.

300. Codolo, G., Papinutto, E., Polenghi, A., D'Elios, M. M., Zanotti, G., and de Bernard, M. (2010) Structure and immunomodulatory property relationship in NapA of *Borrelia burgdorferi*, *Biochim Biophys Acta 1804*, 2191-2197.

301. Gauss, G. H., Reott, M. A., Rocha, E. R., Young, M. J., Douglas, T., Smith, C. J., and Lawrence, C. M. (2012) Characterization of the *Bacteroides fragilis bfr* Gene Product Identifies a Bacterial DPS-Like Protein and Suggests Evolutionary Links in the Ferritin Superfamily, *J Bacteriol 194*, 15-27.

302. Ishikawa, T., Mizunoe, Y., Kawabata, S., Takade, A., Harada, M., Wai, S. N., and Yoshida, S. (2003) The iron-binding protein Dps confers hydrogen peroxide stress resistance to *Campylobacter jejuni*, *J Bacteriol 185*, 1010-1017.

303. Huergo, L. F., Rahman, H., Ibrahimovic, A., Day, C. J., and Korolik, V. (2013) *Campylobacter jejuni* Dps protein binds DNA in the presence of iron or hydrogen peroxide, *J Bacteriol 195*, 1970-1978.

304. Thieme, D., and Grass, G. (2010) The Dps protein of *Escherichia coli* is involved in copper homeostasis, *Microbiol Res 165*, 108-115.

305. Bozzi, M., Mignogna, G., Stefanini, S., Barra, D., Longhi, C., Valenti, P., and Chiancone, E. (1997) A novel non-heme iron-binding ferritin related to the DNA-binding proteins of the Dps family in *Listeria innocua*, *J Biol Chem 272*, 3259-3265.

306. Bellapadrona, G., Chiaraluce, R., Consalvi, V., Ilari, A., Stefanini, S., and Chiancone, E. (2007) The mutations Lys 114 --> Gln and Asp 126 --> Asn disrupt an intersubunit salt bridge and convert *Listeria innocua* Dps into its natural mutant *Listeria monocytogenes dps*. Effects on protein stability at Low pH, *Proteins 66*, 975-983.

307. Dussurget, O., Dumas, E., Archambaud, C., Chafsey, I., Chambon, C., Hebraud, M., and Cossart, P. (2005) *Listeria monocytogenes* ferritin protects against multiple stresses and is required for virulence, *FEMS Microbiol Lett 250*, 253-261.

308. Ping, L., Buchler, R., Mithofer, A., Svatos, A., Spiteller, D., Dettner, K., Gmeiner, S., Piel, J., Schlott, B., and Boland, W. (2007) A novel Dps-type protein from insect gut bacteria catalyses hydrolysis and synthesis of N-acyl amino acids, *Environ Microbiol 9*, 1572-1583.

309. Roy, S., Gupta, S., Das, S., Sekar, K., Chatterji, D., and Vijayan, M. (2004) X-ray analysis of *Mycobacterium smegmatis* Dps and a comparative study involving other Dps and Dps-like molecules, *J Mol Biol 339*, 1103-1113.

310. Ushijima, Y., Ohniwa, R. L., Maruyama, A., Saito, S., Tanaka, Y., and Morikawa, K. (2014) Nucleoid compaction by MrgA(Asp56Ala/Glu60Ala) does not contribute to *Staphylococcal* cell survival against oxidative stress and phagocytic killing by macrophages, *FEMS Microbiol Lett 360*, 144-151.

311. Morikawa, K., Ohniwa, R. L., Kim, J., Maruyama, A., Ohta, T., and Takeyasu, K. (2006) Bacterial nucleoid dynamics: oxidative stress response in *Staphylococcus aureus*, *Genes Cells 11*, 409-423.

312. Horsburgh, M. J., Clements, M. O., Crossley, H., Ingham, E., and Foster, S. J. (2001) PerR controls oxidative stress resistance and iron storage proteins and is required for virulence in *Staphylococcus aureus*, *Infect Immun 69*, 3744-3754.

313. Haikarainen, T., Tsou, C. C., Wu, J. J., and Papageorgiou, A. C. (2010) Crystal structures of *Streptococcus pyogenes* Dpr reveal a dodecameric iron-binding protein with a ferroxidase site, *J Biol Inorg Chem 15*, 183-194.

314. Wiedenheft, B., Mosolf, J., Willits, D., Yeager, M., Dryden, K. A., Young, M., and Douglas, T. (2005) An archaeal antioxidant: characterization of a Dps-like protein from *Sulfolobus solfataricus*, *P Natl Acad Sci USA 102*, 10551-10556.

315. Babolin, C., Amedei, A., Ozolins, D., Zilevica, A., D'Elios, M. M., and de Bernard, M. (2011) TpF1 from *Treponema pallidum* activates inflammasome and promotes the development of regulatory T cells, *J Immunol 187*, 1377-1384.

316. Confalonieri, F., and Sommer, S. (2011) Bacterial and archaeal resistance to ionizing radiation, *J Phys Conf Ser 261*.

317. Chen, H., Huang, L. F., Hua, X. T., Yin, L. F., Hu, Y. H., Wang, C., Chen, W. W., Yu, X. M., Xu, Z. J., Tian, B., Hu, S. N., and Hua, Y. J. (2009) Pleiotropic effects of RecQ in *Deinococcus radiodurans*, *Genomics 94*, 333-340.

318. Gonzalez-Flecha, B., and Demple, B. (1995) Metabolic sources of hydrogen peroxide in aerobically growing *Escherichia coli*, *J Biol Chem 270*, 13681-13687.

319. Chiancone, E., Ceci, P., Ilari, A., Ribacchi, F., and Stefanini, S. (2004) Iron and proteins for iron storage and detoxification, *Biometals 17*, 197-202.

320. Stefanini, S., Ceci, P., Ardini, M., and Ilari, A. (2010) DNA-binding proteins from starved cells (Dps proteins), In *Handbook of Metalloproteins*, John Wiley & Sons, Ltd.

321. Brisslert, M., Enarsson, K., Lundin, S., Karlsson, A., Kusters, J. G., Svennerholm, A. M., Backert, S., and Quiding-Jarbrink, M. (2005) *Helicobacter pylori* induce neutrophil transendothelial migration: role of the bacterial HP-NAP, *FEMS Microbiol Lett 249*, 95-103.

322. Fu, H. W. (2014) *Helicobacter pylori* neutrophil-activating protein: from molecular pathogenesis to clinical applications, *World J Gastroenterol 20*, 5294-5301.

323. Polenghi, A., Bossi, F., Fischetti, F., Durigutto, P., Cabrelle, A., Tamassia, N., Cassatella, M. A., Montecucco, C., Tedesco, F., and de Bernard, M. (2007) The neutrophil-activating protein of *Helicobacter pylori* crosses endothelia to promote neutrophil adhesion in vivo, *J Immunol 178*, 1312-1320.

324. D'Elios, M. M., Montecucco, C., and de Bernard, M. (2007) VacA and HP-NAP, Ying and Yang of *Helicobacter pylori*-associated gastric inflammation, *Clin Chim Acta 381*, 32-38.

325. Piao, H., Minohara, M., Kawamura, N., Li, W., Matsushita, T., Yamasaki, R., Mizunoe, Y., and Kira, J. (2011) Tissue binding patterns and in vitro effects of *Campylobacter jejuni* DNA-binding protein from starved cells, *Neurochem Res 36*, 58-66.

326. Frenkiel-Krispin, D., Levin-Zaidman, S., Shimoni, E., Wolf, S. G., Wachtel, E. J., Arad, T., Finkel, S. E., Kolter, R., and Minsky, A. (2001) Regulated phase transitions of bacterial chromatin: a non-enzymatic pathway for generic DNA protection, *EMBO J 20*, 1184-1191.

327. Macedo, S., Romao, C. V., Mitchell, E., Matias, P. M., Liu, M. Y., Xavier, A. V., LeGall, J., Teixeira, M., Lindley, P., and Carrondo, M. A. (2003) The nature of the di-iron site in the bacterioferritin from *Desulfovibrio desulfuricans*, *Nat Struct Biol 10*, 285-290.

328. Gauss, G. H., Benas, P., Wiedenheft, B., Young, M., Douglas, T., and Lawrence, C. M. (2006) Structure of the DPS-like protein from *Sulfolobus solfataricus* reveals a bacterioferritin-like dimetal binding site within a DPS-like dodecameric assembly, *Biochemistry 45*, 10815-10827.

329. Toueille, M., Mirabella, B., Guerin, P., de la Tour, C. B., Boisnard, S., Nguyen, H. H., Blanchard, L., Servant, P., de Groot, A., Sommer, S., and Armengaud, J. (2012) A

comparative proteomic approach to better define Deinococcus nucleoid specificities, *J Proteomics 75*, 2588-2600.

330. Petersen, T. N., Brunak, S., von Heijne, G., and Nielsen, H. (2011) SignalP 4.0: discriminating signal peptides from transmembrane regions, *Nature methods 8*, 785-786.

331. Bradford, M. M. (1976) A rapid and sensitive method for the quantitation of microgram quantities of protein utilizing the principle of protein-dye binding, *Anal Biochem 72*, 248-254.

332. Yan, L. J., and Forster, M. J. (2009) Resolving mitochondrial protein complexes using nongradient blue native polyacrylamide gel electrophoresis, *Anal Biochem 389*, 143-149.

333. Nguyen, H. H., de la Tour, C. B., Toueille, M., Vannier, F., Sommer, S., and Servant, P. (2009) The essential histone-like protein HU plays a major role in *Deinococcus radiodurans* nucleoid compaction, *Molecular microbiology 73*, 240-252.

334. Winkler, W., Buhl, F., Arenhovel-Pacula, A., and Hachula, U. (2003) Spectrophotometric method for the determination of manganese with phenylfluorone in the presence of Triton X-100 and cetylpyridinium chloride in pharmacological preparations and vegetable fertilizers, *Anal Bioanal Chem 376*, 934-937.

335. Krissinel, E., and Henrick, K. (2007) Inference of macromolecular assemblies from crystalline state, *Journal of molecular biology 372*, 774-797.

336. McDonald, I. K., and Thornton, J. M. (1994) Satisfying hydrogen bonding potential in proteins, *Journal of molecular biology 238*, 777-793.

337. Baker, N. A., Sept, D., Joseph, S., Holst, M. J., and McCammon, J. A. (2001) Electrostatics of nanosystems: Application to microtubules and the ribosome, *Proceedings of the National Academy of Sciences of the United States of America 98*, 10037-10041.

338. Dolinsky, T. J., Nielsen, J. E., McCammon, J. A., and Baker, N. A. (2004) PDB2PQR: an automated pipeline for the setup of Poisson-Boltzmann electrostatics calculations, *Nucleic Acids Res 32*, W665-667.

339. Kim, D., Lee, Y. J., and Corry, P. M. (1992) Constitutive HSP70: oligomerization and its dependence on ATP binding, *J Cell Physiol 153*, 353-361.

340. Aprile, F. A., Dhulesia, A., Stengel, F., Roodveldt, C., Benesch, J. L., Tortora, P., Robinson, C. V., Salvatella, X., Dobson, C. M., and Cremades, N. (2013) Hsp70 oligomerization is mediated by an interaction between the interdomain linker and the substrate-binding domain, *Plos One 8*, e67961.

341. Giese, K. C., and Vierling, E. (2004) Mutants in a small heat shock protein that affect the oligomeric state. Analysis and allele-specific suppression, *J Biol Chem 279*, 32674-32683.

342. Giese, K. C., and Vierling, E. (2002) Changes in oligomerization are essential for the chaperone activity of a small heat shock protein *in vivo* and *in vitro*, *J Biol Chem 277*, 46310-46318.

343. Sharma, A., Gaidamakova, E. K., Matrosova, V. Y., Bennett, B., Daly, M. J., and Hoffman, B. M. (2013) Responses of Mn^{2+} speciation in *Deinococcus radiodurans* and *Escherichia coli* to gamma-radiation by advanced paramagnetic resonance methods, *P Natl Acad Sci USA 110*, 5945-5950.

344. Storz, G., and Imlay, J. A. (1999) Oxidative stress, *Curr Opin Microbiol 2*, 188-194.

345. Levin-Zaidman, S., Englander, J., Shimoni, E., Sharma, A. K., Minton, K. W., and Minsky, A. (2003) Ringlike structure of the *Deinococcus radiodurans* genome: A key to radioresistance?, *Science 299*, 254-256.

346. Frenkiel-Krispin, D., and Minsky, A. (2006) Nucleoid organization and the maintenance of DNA integrity in *E. coli*, *B. subtilis* and *D. radiodurans*, *Journal of structural biology 156*, 311-319.

347. Putnam, C. D., Hammel, M., Hura, G. L., and Tainer, J. A. (2007) X-ray solution scattering (SAXS) combined with crystallography and computation: defining accurate macromolecular structures, conformations and assemblies in solution, *Q Rev Biophys 40*, 191-285.

348. Wriggers, W., Milligan, R. A., Schulten, K., and McCammon, J. A. (1998) Self-organizing neural networks bridge the biomolecular resolution gap, *J Mol Biol 284*, 1247-1254.

349. Guinier, A., and Fournet, G. (1955) *Small-angle scattering of X-rays*, John Wiley New York.

350. Gao, J. L., Lu, Y., Browne, G., Yap, B. C., Trewhella, J., Hunter, N., and Nguyen, K. A. (2012) The role of heme binding by DNA-protective protein from starved cells (Dps) in the Tolerance of *Porphyromonas gingivalis* to heme toxicity, *J Biol Chem 287*, 42243-42258.

351. Santos, S. P., Mitchell, E. P., Franquelim, H. G., Castanho, M. A., Abreu, I. A., and Romao, C. V. (2015) Dps from *Deinococcus radiodurans*: oligomeric forms of Dps1 with distinct cellular functions and Dps2 involved in metal storage, *Febs J 282*, 4307-4327.

352. Pernot, P., Round, A., Barrett, R., De Maria Antolinos, A., Gobbo, A., Gordon, E., Huet, J., Kieffer, J., Lentini, M., Mattenet, M., Morawe, C., Mueller-Dieckmann, C., Ohlsson, S., Schmid, W., Surr, J., Theveneau, P., Zerrad, L., and McSweeney, S. (2013) Upgraded ESRF BM29 beamline for SAXS on macromolecules in solution, *J Synchrotron Radiat 20*, 660-664.

353. Round, A., Brown, E., Marcellin, R., Kapp, U., Westfall, C. S., Jez, J. M., and Zubieta, C. (2013) Determination of the GH3.12 protein conformation through HPLC-integrated SAXS measurements combined with X-ray crystallography, *Acta Crystallogr D Biol Crystallogr 69*, 2072-2080.

354. Round, A., Felisaz, F., Fodinger, L., Gobbo, A., Huet, J., Villard, C., Blanchet, C. E., Pernot, P., McSweeney, S., Roessle, M., Svergun, D. I., and Cipriani, F. (2015) BioSAXS Sample Changer: a robotic sample changer for rapid and reliable high-throughput X-ray solution scattering experiments, *Acta Crystallogr D Biol Crystallogr 71*, 67-75.

355. Brennich, M. E., Kieffer, J., Bonamis, G., De Maria Antolinos, A., Hutin, S., Pernot, P., and Round, A. (2016) Online data analysis at the ESRF bioSAXS beamline, BM29, *J Appl Crystallogr 49*, 203-212.

356. Incardona, M. F., Bourenkov, G. P., Levik, K., Pieritz, R. A., Popov, A. N., and Svensson, O. (2009) EDNA: a framework for plugin-based applications applied to X-ray experiment online data analysis, *J Synchrotron Radiat 16*, 872-879.

357. Konarev, P. V., Volkov, V. V., Sokolova, A. V., Koch, M. H. J., and Svergun, D. I. (2003) PRIMUS: a Windows PC-based system for small-angle scattering data analysis, *J Appl Cryst 36*, 1277-1282.

358. Svergun, D. I. (1992) Determination of the Regularization Parameter in Indirect-Transform Methods Using Perceptual Criteria, *J Appl Crystallogr 25*, 495-503.

359. Svergun, D., Barberato, C., and Koch, M. H. J. (1995) CRYSOL - A program to evaluate x-ray solution scattering of biological macromolecules from atomic coordinates, *J Appl Crystallogr 28*, 768-773.

360. Svergun, D. I., Petoukhov, M. V., and Koch, M. H. (2001) Determination of domain structure of proteins from X-ray solution scattering, *Biophys J 80*, 2946-2953.

361. Tria, G., Mertens, H. D., Kachala, M., and Svergun, D. I. (2015) Advanced ensemble modelling of flexible macromolecules using X-ray solution scattering, *IUCrJ 2*, 207-217.

362. Volkov, V. V., and Svergun, D. I. (2003) Uniqueness of *ab initio* shape determination in small-angle scattering, *J Appl Crystallogr 36*, 860-864.

363. Kozin, M. B., and Svergun, D. I. (2001) Automated matching of high- and low-resolution structural models, *J Appl Crystallogr 34*, 33-41.

364. Wriggers, W., and Chacon, P. (2001) Using Situs for the registration of protein structures with low-resolution bead models from X-ray solution scattering, *J Appl Crystallogr 34*, 773-776.

365. Wriggers, W., and Chacon, P. (2001) Modeling tricks and fitting techniques for multiresolution structures, *Structure 9*, 779-788.

366. Wriggers, W., and Birmanns, S. (2001) Using Situs for flexible and rigid-body fitting of multiresolution single-molecule data, *Journal of structural biology 133*, 193-202.

367. Wriggers, W., Milligan, R. A., and McCammon, J. A. (1999) Situs: A package for docking crystal structures into low-resolution maps from electron microscopy, *Journal of structural biology 125*, 185-195.

368. Pedersen, J. S. (2002) Modelling of Small-Angle Scattering Data from Colloids and Polymer Systems, In *Neutrons, X-Rays and Light*, pp 391-420, *Elsevier*.

369. Watters, C. (1978) A one-step biuret assay for protein in the presence of detergent, *Anal Biochem 88*, 695-698.

370. Valentini, E., Kikhney, A. G., Previtali, G., Jeffries, C. M., and Svergun, D. I. (2015) SASBDB, a repository for biological small-angle scattering data, *Nucleic Acids Res 43*, D357-363.

371. Koch, M. H. J., Vachette, P., and Svergun, D. I. (2003) Small-angle scattering: a view on the properties, structures and structural changes of biological macromolecules in solution, *Q Rev Biophys 36*, 147-227.

372. Schneidman-Duhovny, D., Hammel, M., Tainer, J. A., and Sali, A. (2013) Accurate SAXS profile computation and its assessment by contrast variation experiments, *Biophys J 105*, 962-974.

373. Jones, D. T. (1999) Protein secondary structure prediction based on position-specific scoring matrices, *J Mol Biol 292*, 195-202.

374. Bruch, E. M., de Groot, A., Un, S., and Tabares, L. C. (2015) The effect of gamma-ray irradiation on the Mn(II) speciation in *Deinococcus radiodurans* and the potential role of Mn(II)-orthophosphates, *Metallomics 7*, 908-916.

375. Tabares, L. C., and Un, S. (2013) In situ determination of manganese(II) speciation in *Deinococcus radiodurans* by high magnetic field EPR: detection of high levels of Mn(II) bound to proteins, *J Biol Chem 288*, 5050-5055.

376. Mennecier, S., Coste, G., Servant, P., Bailone, A., and Sommer, S. (2004) Mismatch repair ensures fidelity of replication and recombination in the radioresistant organism *Deinococcus radiodurans*, *Mol Genet Genomics 272*, 460-469.

377. Passot, F. M., Nguyen, H. H., Dard-Dascot, C., Thermes, C., Servant, P., Espeli, O., and Sommer, S. (2015) Nucleoid organization in the radioresistant bacterium *Deinococcus radiodurans*, *Mol Microbiol 97*, 759-774.

378. Kosako, H. (2009) Phos-tag Western blotting for detecting stoichiometric protein phosphorylation in cells, *Protocol Exchange*.

379. Beauchamp, C., and Fridovich, I. (1971) Superoxide dismutase: improved assays and an assay applicable to acrylamide gels, *Anal Biochem 44*, 276-287.

380. Fridovich, I. (1974) Superoxide dismutases, *Adv Enzymol Relat Areas Mol Biol 41*, 35-97.

381. Bannister, J. V., Bannister, W. H., and Rotilio, G. (1987) Aspects of the structure, function, and applications of superoxide dismutase, *CRC Crit Rev Biochem 22*, 111-180.

382. Weisiger, R. A., and Fridovich, I. (1973) Superoxide dismutase. Organelle specificity, *J Biol Chem 248*, 3582-3592.

383. Woodbury, W., Spencer, A. K., and Stahman, M. A. (1971) An improved procedure using ferricyanide for detecting catalase isozymes, *Anal Biochem 44*, 301-305.

384. Morawe, C., Barrett, R., Cloetens, P., Lantelme, B., Peffen, J. C., and Vivo, A. (2015) Graded multilayers for figured Kirkpatrick-Baez mirrors on the new ESRF end station ID16AProc. *SPIE Advances in X-Ray/EUV Optics and Components X 9588*, pp 958803-958807.

385. Cloetens, P., Ludwig, W., Baruchel, J., Dyck, D. V., Landuyt, J. V., Guigay, J. P., and Schlenker, M. (1999) Holotomography: Quantitative phase tomography with micrometer resolution using hard synchrotron radiation X-rays, *Applied Physics Letters 75*, 2912-2914.

386. Robinson, I., Yang, Y., Zhang, F., Lynch, C., Yusuf, M., and Cloetens, P. (2016) Nuclear incorporation of iron during the eukaryotic cell cycle, *J Synchrotron Radiat 23*, 1490-1497.

387. Solé, V. A., Papillon, E., Cotte, M., Walter, P., and Susini, J. (2007) A multiplatform code for the analysis of energy-dispersive X-ray fluorescence spectra, *Spectrochim Acta B Atom Spectrosc 62*, 63-68.

388. Webb, B., and Sali, A. (2014) Protein structure modeling with MODELLER, *Methods Mol Biol 1137*, 1-15.

389. Larkin, M. A., Blackshields, G., Brown, N. P., Chenna, R., McGettigan, P. A., McWilliam, H., Valentin, F., Wallace, I. M., Wilm, A., Lopez, R., Thompson, J. D., Gibson, T. J., and Higgins, D. G. (2007) Clustal W and Clustal X version 2.0, *Bioinformatics 23*, 2947-2948.

390. Roderic D. M. Page, G., Scotland, . TreeView [homepage on the Internet], *UK, 1998*.

391. Nicholas, K. B., Nicholas, H. B., and Deerfield, D. W. (1997) {GeneDoc: analysis and visualization of genetic variation}, *Embnew News 4*, 14.

392. Rajpurohit, Y. S., and Misra, H. S. (2013) Structure-function study of *Deinococcal* serine/threonine protein kinase implicates its kinase activity and DNA repair protein phosphorylation roles in radioresistance of *Deinococcus radiodurans*, *Int J Biochem Cell B 45*, 2541-2552.

393. Rajpurohit, Y. S., Bihani, S. C., Waldor, M. K., and Misra, H. S. (2016) Phosphorylation of *Deinococcus radiodurans* RecA Regulates Its Activity and May Contribute to Radioresistance, *J Biol Chem 291*, 16672-16685.

394. Misra, H. S., Rajpurohit, Y. S., and Kota, S. (2013) Physiological and molecular basis of extreme radioresistance in *Deinococcus radiodurans*, *Curr Sci 104*, 194-205.

395. Nguyen, K. H., and Grove, A. (2012) Metal binding at the Deinococcus radiodurans Dps-1 N-terminal metal site controls dodecameric assembly and DNA binding, *Biochemistry 51*, 6679-6689.

396. Eicken, C., Pennella, M. A., Chen, X., Koshlap, K. M., VanZile, M. L., Sacchettini, J. C., and Giedroc, D. P. (2003) A metal-ligand-mediated intersubunit allosteric switch in related SmtB/ArsR zinc sensor proteins, *J Mol Biol 333*, 683-695.

397. Busenlehner, L. S., Pennella, M. A., and Giedroc, D. P. (2003) The SmtB/ArsR family of metalloregulatory transcriptional repressors: structural insights into prokaryotic metal resistance, *Fems Microbiol Rev 27*, 131-143.

398. Eijkelkamp, B. A., McDevitt, C. A., and Kitten, T. (2015) Manganese uptake and streptococcal virulence, *Biometals 28*, 491-508.

399. Abate, F., Malito, E., Cozzi, R., Lo Surdo, P., Maione, D., and Bottomley, M. J. (2014) Apo, Zn^{2+}-bound and Mn^{2+}-bound structures reveal ligand-binding properties of SitA from the pathogen *Staphylococcus pseudintermedius*, *Biosci Rep 34*, e00154.

400. McDevitt, C. A., Ogunniyi, A. D., Valkov, E., Lawrence, M. C., Kobe, B., McEwan, A. G., and Paton, J. C. (2011) A molecular mechanism for bacterial susceptibility to zinc, *PLoS Pathog 7*, e1002357.

401. Lawrence, M. C., Pilling, P. A., Epa, V. C., Berry, A. M., Ogunniyi, A. D., and Paton, J. C. (1998) The crystal structure of pneumococcal surface antigen PsaA reveals a metal-binding site and a novel structure for a putative ABC-type binding protein, *Structure 6*, 1553-1561.

402. Gribenko, A., Mosyak, L., Ghosh, S., Parris, K., Svenson, K., Moran, J., Chu, L., Li, S., Liu, T., Woods, V. L., Jr., Jansen, K. U., Green, B. A., Anderson, A. S., and Matsuka, Y. V.

(2013) Three-dimensional structure and biophysical characterization of *Staphylococcus aureus* cell surface antigen-manganese transporter MntC, *J Mol Biol 425*, 3429-3445.